Fluctuation-induced phenomena in nanophotonic systems

Dissertation

zur Erlangung des akademischen Grades

doctor rerum naturalium

(Dr. rer. nat.)

im Fach Physik

Spezialisierung: Theoretische Physik

eingereicht an der

Mathematisch-Naturwissenschaftlichen Fakultät

der Humboldt-Universität zu Berlin

von

M.Sc. Marty Oelschläger

Präsidentin der Humboldt-Universität zu Berlin

Prof. Dr. Sabine Kunst

Dekan der Mathematisch-Naturwissenschaftlichen Fakultät

Prof. Dr. Elmar Kulke

GutachterInnen:

1. Prof. Dr. Kurt Busch
2. Prof. Dr. Stefan Scheel
3. Prof. Dr. Claudia Eberlein

Tag der mündlichen Prüfung: 6. März 2020

Ich erkläre, dass ich die Dissertation selbständig und nur unter Verwendung der von mir gemäß §7 Abs. 3 der Promotionsordnung der Mathematisch-Naturwissenschaftlichen Fakultät, veröffentlicht im Amtlichen Mitteilungsblatt der Humboldt-Universität zu Berlin Nr. 42/2018 am 11.07.2018 angegebenen Hilfsmittel angefertigt habe.

Weiterhin erkläre ich, dass ich mich nicht bereits anderwärts um einen Doktorgrad im Promotionsfach Physik beworben habe beziehungsweise einen entsprechenden Doktorgrad besitze.

Ich habe Kenntnis der dem Promotionsverfahren zugrunde liegenden Promotionsordnung der Mathematisch-Naturwissenschaftlichen Fakultät, veröffentlicht im Amtlichen Mitteilungsblatt der Humboldt-Universität zu Berlin Nr. 42/2018 am 11.07.2018.

Berlin, den 28. März 2020

Mathematisch-Naturwissenschaftliche Fakultät
Institut für Physik

Fluctuation-induced phenomena in nanophotonic systems

A study on nonequilibrium atom-surface interactions

picture by Gus Chan, The Plain Dealer

Ph.D. thesis
by Marty Oelschläger

Supervisor: Prof. Dr. Kurt Busch

Zusammenfassung

Die vorliegende Arbeit befasst sich mit dem Thema der Nichtgleichgewichts-Dispersionskräfte. Der Fokus liegt auf der kontroversen Casimir- bzw. Quantenreibung. Sie tritt auf, wenn sich zwei elektrisch neutrale Körper relativ zueinander bewegen. Vermittelt wird diese kontaktlose Reibungskraft über fluktuierende elektromagnetische (Quanten-) Felder und ist somit der Kategorie der fluktuationsinduzierten Phänome zuzuordnen, deren bekannte Beispiele die Van-der-Waals-Kraft und der Casimir-Effekt sind. Im Speziellen wurde die Situation eines mikroskopischen Objektes, welches sich mit einer festgelegten Geschwindigkeit und Höhe über eine makroskopische und flache Oberfläche beweget, untersucht. Um einen Zugang in das Themenfeld zu erlangen, wird eine kurze Einleitung in die Theorie der linearen Antwort und der Dynamik offener Systeme gegeben. Des Weiteren, werden unterschiedliche Modelle zur Beschreibung des mikroskopischen Objektes eingeführt und verschiedene Konfigurationen und Modelle bezüglich der makroskopischen Oberfläche berücksichtigt. Neben einem exakten, wenn auch komplexen, Integralausdruck werden diverse asymptotische Ausdrücke für verschiedene relevante Grenzfälle der kontaktlosen Reibung hergeleitet. Darüber hinaus, um die Asymptoten mit der exakten Lösung vergleichen zu können, wurde eine numerisch Auswertungsroutine des exakten Ausdrucks entwickelt und implementiert. Durch die Nutzung einer vollen Nichtgleichgewichtbeschreibung und das Einbeziehen sowohl der Rückwirkung des elektromagnetischen Feldes auf die Dynamik des mikroskopischen Objektes, als auch dessen Rotationsfreiheitsgrade, werden bestehende theoretische Beschreibungen erweitert. Abschließend wird ein Ausblick auf experimentelle Messungen der kontaktlosen Reibung gegeben.

Abstract

The present thesis addresses the topic of nonequilibrium dispersion forces. The focus lies on the controversial Casimir or quantum friction, which occurs when two electrically neutral bodies move at a relative velocity with respect to each other. The noncontact friction force is mediated by the fluctuations of the (quantum) electromagnetic field and therefore belongs to the category of fluctuation-induced phenomena, whose prominent examples are the van der Waals force and the Casimir effect. Especially, the setup of a microscopic object moving at a fixed velocity and height above a flat macroscopic surface is investigated. To access this topic, a brief introduction into linear response and open system dynamics is given. Moreover, different models for the description of the microscopic object are introduced and various setups and models of the flat macroscopic surface are considered. Besides an exact but rather involved integral expression, several asymptotic expressions of the noncontact friction for different relevant limits are derived. Furthermore, in order to compare the asymptotic with the exact expression, a numerical approach for its evaluation was developed and implemented. Using a full nonequilibrium approach, which includes the backaction of the electromagnetic field onto the microscopic object's dynamics, as well as its rotational degrees, existing theoretical descriptions are extended. Eventually, an outlook towards experimental measurements of the noncontact friction is given.

"It is probably fair comment to say that to many physicists the subject of fluctuations (or 'noise' to put it bluntly) appears rather esoteric and perhaps even pointless; spontaneous fluctuations seem nothing but an unwanted evil which only an unwise experimenter would encounter!"

MacDonald 1962,
Noise and Fluctuation

Preface

The present thesis aims to be instructive and understandable also for students who are non-experts in this area of physics. The author's hope is that the slightly confused student, who started this thesis in June 2016, could pick up this document and be at least a bit less confused about the heap of information which flows in the topic of nonequilibrium fluctuation-induced phenomena. Nonetheless, the thesis provides all scientific relevant information and does not oversimplify the complex and intriguing mechanisms behind this interdisciplinary topic. As a very first glimpse into the topic we recommend a short Science Slam[1] (in German) by the author, which was presented several times over the course of the thesis in order to make the topic accessible even for non-physicists. After few general remarks on the chosen structure of the thesis we will give a brief illustrative introduction of the covered physical phenomena in this thesis.

First of all we provide, after a short historical introduction into the topic, an overview over the mathematical notation used in this thesis. In order to keep the thesis lucid and easily accessible we do not introduce additional abbreviations, since we believe that they might unnecessarily obscure the content. Furthermore, we refrain from the use of subsections in order to reduce interruptions within one closed topic. Nevertheless, we make use of margin notes, which provide hints on the current topic and can be helpful when seeking a certain subtopic within the section. Another feature are small recaps after every section. These might be skipped by the experienced reader, since they provide no new insights.

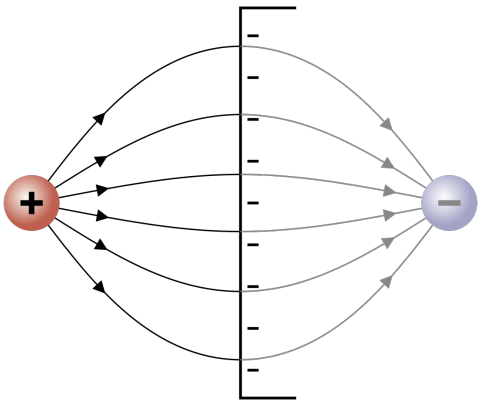

Figure 1: Sketch of a positively charged particle inducing a mirror charge into a metallic surface.[1]

In the following we like to give a short illustrative introduction into the topic by using solely basic physical principles. The first concept we employ are so-called mirror charges. When a charged particle approaches a conducting

[1] https://youtu.be/gJ9nsWLhyI8

neutral surface, the charges within the macroscopic surface will rearrange according to the influence of the charged particle. This rearrangement of surface charges can be described by an imaginary particle of opposite charge at the mirrored position of the actual particle, and is illustrated in figure 1. Therefore, if one lets loose the charged particle, it will be attracted towards the now negatively charged surface. This very concept can be extended to more complex objects consisting of more than just one charged particles, as for example atoms or molecules. However, atoms as well as molecules are neutral objects themselves. Nonetheless, the charge density carried within the neutral objects is fluctuating. The fluctuations allow for temporal charge imbalances, which again will be projected as an image of the opposite charge onto the surface. Thus, one finds an attractive force pulling the neutral atom or molecule towards the neutral surface.

This fluctuation-induced force is, depending on the context, called the van der Waals or Casimir-Polder force. This force is ubiquitous in nature as e.g. in the form of adhesion. This thesis is focused on a phenomenon related to the Casimir-Polder force. But before turning towards another fluctuation-induced phenomenon, we once more take the situation of one charged particle in front of a conducting surface. If the particle is set in constant relative motion parallel to the surface, the mirror charge will attempt to follow. However, due to resistivity within the conductor the image charge will lag behind. As in the static case the charge is pulled perpendicular towards the surface, the attraction between the actual and the lagging image charge exhibits additionally a parallel component. This parallel drag is opposing the motion of the charged particle and is known as Coulomb drag [2]. Substituting the charged particle with a neutral object the fluctuation of the charge density yields a similar mechanism as the Coulomb drag, which will be the focus of this thesis, the Casimir or quantum friction, which is illustrated in figure 2.

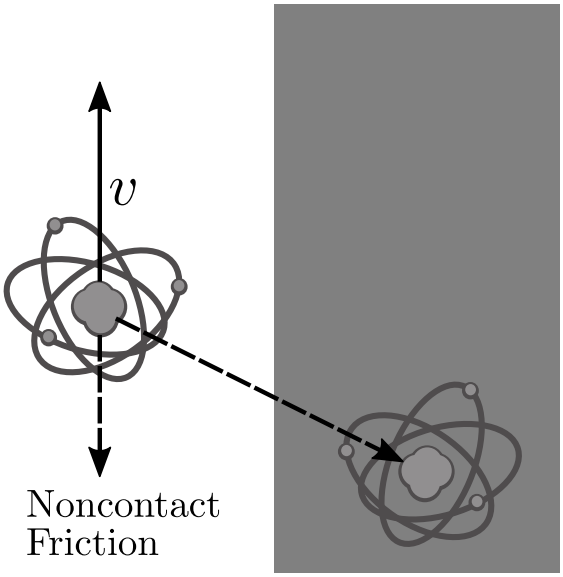

Figure 2: A neutral atom induces, caused by charge fluctuations, a mirror image into a metallic surface. When moving at a constant velocity v, the image lags behind the actual atom due to the resistivity within the metal. Besides an attraction towards the surface the actual atom additionally experiences a frictional drag which is opposing its motion.

With this illustrative explanation of the noncontact Casimir or quantum friction, we wish the reader a hopefully pleasant dive into the realm of nonequilibrium fluctuation-induced phenomena.

Introduction

As fluctuations are an omnipresent phenomenon in nature, they are often degraded to an annoyance. In experiments, they seem to obstruct the way to the "pure" results and in theory they are regularly omitted. Nonetheless, fluctuation-induced or even fluctuation-dominated phenomena are important in our daily lives and still raise questions on a fundamental scientific level. While we curiously observe how paint sticks to a wall [3], wonder about the gecko walking seemingly effortless upside-down on the ceiling [4–6], we also discuss the concept of virtual particles and the structure of the quantum vacuum [7, 8]. With the advent of quantum mechanics in the beginning of the 20$^{\text{th}}$ century [9] and the foundation of modern probability theory in the 1920s to 1930s [10], fluctuations became a profound concept in the physical description and interpretation of nature[1]. Probably the most common effect, which is dominated by fluctuations, is the attraction of neutral matter (for example molecules and atoms) on short length scales. Due to fluctuations of the electromagnetic field and the position of the charge carriers within neutral objects, these objects experience a fundamental (mostly) attractive force, which is long range and quantum in nature [14]. This effect was first noticed by van der Waals [15], theoretically explained by London [16] and later refined and extended by Casimir and Polder [17]. Furthermore, Casimir turned towards macroscopic objects and predicted an attraction of two perfectly conducting plates, which is commonly known as the Casimir effect [18]. Although Casimir's result was impressive and elegantly derived, it relied on the idealistic assumption of perfectly conducting plates. This idealization could be abandoned when Lifshitz developed his generalized theory of interacting macroscopic bodies [19]. While the van der Waals interaction and Lifshitz' theory were confirmed rather quickly in experiments by Tabor and Winterton [20] and Sabisky and Anderson [21], the macroscopic Casimir force lacked an

[1] In the illustrative path integral formulation developed by Wiener, Dirac and Feynman [11] the similarity between stochastic and quantum mechanics becomes probably most evident. While Wiener engaged this technique to solve problems concerning diffusion and Brownian motion, it was reinvented by Feynman as a new perspective on quantum theory. Fluctuations are divided into two categories: *quantum fluctuations* and *thermal fluctuations* [12]. While in classical mechanics a particle follows exclusively one path connecting a point A and a point B, i.e. the path where the action S has its extremum, a quantum particle takes virtually any path between those two points, with each path weighted by $\exp(-\mathrm{i}S/\hbar)$. The deviations from the classical trajectory, which scale by $\hbar$, represent quantum fluctuations. A similar concept can be used to describe a particle in a thermal environment performing a Brownian motion [13]. In equilibrium the location of the particle is characterized by its potential energy V, where each position is weighted by $\exp(-V/(k_{\mathrm{B}}T))$. The favorable position of the particle is in the minimum of the potential. Deviations from that minimum position scale by $k_{\mathrm{B}}T$. In both cases, the deviations significantly contribute, if they are on the scale of $\hbar$ or $k_{\mathrm{B}}T$, respectively.

experimental confirmation for a long time. After nearly five decades from its first theoretical prediction in 1948 by Casimir a reliable experimental measurement[2] was performed. Lamoreaux, who employed a torsion pendulum, finally presented the attraction of neutral macroscopic bodies, confirming accurately with the theoretical prediction, in a range of 0.6 to $6\,\mathrm{mm}$ [23] in 1997. One year later Mohideen and Roy followed up with precise measurements from 0.1 to $0.9\,\mu\mathrm{m}$ [24].

Besides the scientific journey of the static Casimir effect its intriguing quantum electrodynamical explanation sparked new ideas. One crucial prediction stems from Fulling and Davies [25], who investigated a dynamical pendant of the Casimir effect. One puzzling feature of their investigation was the creation of real particles from the vacuum, induced solely by the motion of the perfectly conducting plates. As striking as this theoretical result was, it took again several decades to its first experimental realization by Wilson et al. [26], who demonstrated the generation of photons by modulating the inductance of a superconducting quantum interference device. While both, the static and dynamical Casimir effect, succeeded in jumping from a theoretical *gedankenexperiment* (thought experiment) to measurable reality, another phenomenon in the realm of Casimir physics still requires experimental support: The nonequilibrium noncontact friction between neutral objects in relative motion to each other[3], which is the main topic of this thesis. The scientific history of the noncontact friction is filled with controversies and debates. Since it is usually discussed in two distinct setups, either two moving flat macroscopic surfaces or one microscopic object moving above a macroscopic surface (see figure 1), we like to split the brief introduction into the scientific history of the noncontact friction with respect to these two setups. In table 1 the reader finds a list of selected references of the controversial history for both setups.

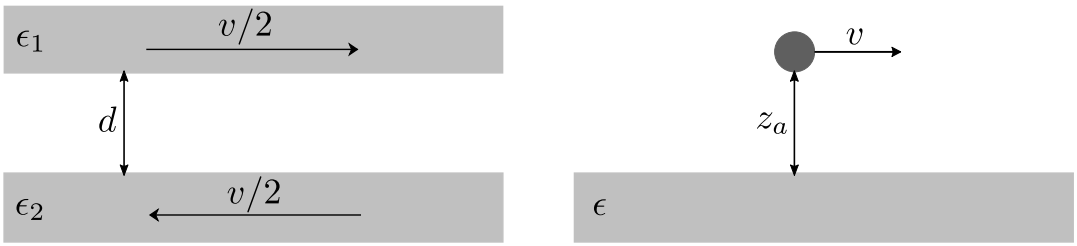

Figure 1: Depicted are the two common configurations in which various authors have theoretically studied noncontact friction. On the left, two plates at a distance d which are set in a relative motion to each other at a fixed velocity v. Their electrodynamic response is encoded in the macroscopic permittivity functions ϵ_1 and ϵ_2. On the right, a small object moving at fixed distance z_a and velocity v above a flat macroscopic surface, which again is described via its permittivity function ϵ.

[2] An early attempt of measuring the Casimir force by Sparnaay [22] remained, due to its high uncertainty, inconclusive.

[3] This phenomenon is called — depending on the exact context — by many names as e.g. van der Waals' friction [27], Casimir friction [28] or quantum friction [29].

Authors	Year of Publication	Low velocity dependency	Distance dependency
[30] Teodorovich & Tabor	1978	v	d^{-4}
[27] Levitov	1989	v^3	d^{-2}
[31] Polevoi	1990	v	d^{-1}
[32] Mkrtchian	1995	v	$d^{-6}, d^{-16/3}$
[29] Pendry	1997	v^3	d^{-6}
[33] Persson & Zhang	1998	v	d^{-4}, d^{-6}
[34] Volokitin & Persson	1999	v	d^{-4}
[35] Philbin & Leonhardt	2009	0	0
[36] Mahanty	1980	v	z_a^{-5}
[37] Schaich & Harris	1981	v	z_a^{-10}
[38] Thomassone & Widom	1997	v	z_a^{-5}
[39] Scheel & Buhmann	2009	v	z_a^{-8}
[40] Barton	2010	v	z_a^{-8}
[28, 41] Høye & Brevik	2011	v	z_a^{-8}
[42] Dedkov & Kyasov	2003	v^3	z_a^{-7}
[43] Intravaia et al.	2015	v^3	z_a^{-10}
[44] Reiche et al.	2017	v^3	z_a^{-10}
[45] Klatt et al.	2017	v^2	$z_a(t)^{-6}$
[46] Oelschläger et al.	2018	$v^{2\ldots3}$	$z_a^{-8\ldots-10}$
[47] Intravaia et al.	2019	v^3	z_a^{-10}

Table 1: An extensive (but potentially incomplete) overview over theoretical predictions concerning quantum friction's low velocity and distance dependency. The two given dependencies concerning velocity and distance are of course only a condensed fraction of the respective work. In the upper part (above the double line) we present various publications with respect to the two plate setup and in the lower part (below the double line) with respect to the setup of a microscopic object moving above a macroscopic surface (for a depiction of the setups see figure 1).

Starting with the two plate setup, one of the earliest work was carried out by Teodorovich and Tabor [30], who engaged Lifshitz' theory and predicted a frictional force between two parallel moving plates proportional to v/d^4. However, the prediction was strongly criticized by several authors [29, 37] especially in the limit of zero temperature. Further early works were done by Levitov [27], Polevoi [31] and Mkrtchian [32]. The suggestion of these three studies that the frictional force vanishes in the nonretarded regime, however, was again strongly debated [34]. Ever since Pendry's publication on "Shearing the vacuum" [29], the concept of noncontact friction established in the broader physics community. While Pendry considered zero temperature, Persson and Zhang [33], in agreement with Pendry's calculations, obtained results for finite temperature. Only one year later Volokitin and Persson [34] generalized the previous results — which neglected retardation effects and were partly restricted to small velocities — to arbitrary distance, velocity and temperature by applying the general theory of fluctuating fields pioneered by Rytov [48]. Although these results were accepted among the community,

Philbin and Leonhardt attacked the very existence of such a frictional force [35]. In spite of an effective defense by Pendry [14] and Volokitin and Persson [49], who pointed out the errors in the calculations of Philbin and Leonhardt, the lack of a confirmation in form of a meaningful experiment still haunts each and every new theoretical prediction on the noncontact friction.

The second setup of which we like to give a brief historical overview is that of a moving microscopic object, e.g. a nanoparticle, molecule or atom, above a macroscopic surface. One early work considering this setup was published my Mahanty [36]. By investigating the velocity dependence of the van der Waals force between molecules, Mahanty stated the implication that a molecule moving near a slab should experience a frictional drag proportional to v/z_a^5, where z_a is the perpendicular distance between the molecule and the flat macroscopic surface. While Mahanty's result was criticized for yielding a frictional force even for perfect conductors, many publications confirmed the linear behavior in v [28, 37, 39, 40], even though different dependencies on the distance were found (see table 1). In contrast, Thomassone and Widom [38] found a vanishing linear velocity dependence for temperatures approaching zero and pointed out that higher orders in velocity should be considered in this limit. Volokitin and Persson [50], Dedkov and Kyasov [51], and Golyk et al. [52, 53] agreed with this conclusion as well. On that note, further publications calculated the first non-vanishing contribution with respect to the velocity. Dedkov and Kyasov [54] extended their previous work to the zero temperature case stated a non-linear v^3 behavior of the frictional force. The cubic dependency on the velocity could be confirmed by Pieplow and Henkel [55, 56], who employed a covariant formulation in order to capture relativistic velocities. Furthermore, Intravaia et al. [57] used a generalized fluctuation-dissipation relation in order to correctly represent the nonequilibrium steady state of the system. In the following years, Intravaia et al. pointed out the peculiarity of this system and showed that common assumptions are not reasonable in the case of quantum friction, i.e. for temperatures approaching absolute zero. On the one hand, Intravaia et al. showed why the assumption of Markovianity is not adequate for this system [58] and on the other hand, they demonstrated that the local thermal equilibrium approximation mistreats the true nonequilibrium effect. Still in recent years the theoretical investigation with respect to the noncontact friction remains active: Reiche et al. [44] as well as Volokitin and Persson [59] presented effects of spatial correlation within the surface on the friction. Oelschläger et al. investigated how the alteration of the plasmonic density of states due to superlattice structures impacts the noncontact friction and presented tunable power-laws from $v^{2\ldots3}$. Additionally, Intravaia et al. included very recently the full rotational dynamics into their calculations [47], showing that quantum friction is a pure nonequilibrium effect, with a vanishing equilibrium contribution.

Notwithstanding, in spite of great progress with respect to the theoretical descriptions in the last decades, the crucial point of the noncontact friction remains that it could not yet be experimentally measured and thus neither one nor another theory could be tested. The reason behind this circumstance is that, under the current state of knowledge, the friction force is predicted to be very small and difficult to measure and was even declared to be "far beyond experimental reach" [60]. In this thesis we want to spark renewed optimism into the topic by investigating closely the mechanisms behind noncontact friction, which might be used to leverage this effect into the realm of experimental accessibility. Here, we focus on the setup of a microscopic object moving above a macroscopic surface. Hopefully, after few additional years also this fundamental and peculiar effect of noncontact friction steps in line with the

static and dynamic Casimir effect, which too were declared to be out of experimental reach once but, nonetheless, are confirmed experimental reality now.

After this brief historical overview we turn towards the structure of the thesis. In chapter 1 we build the theoretical foundation of our investigations. Based on linear response theory, as a profound analytical tool, we briefly revisit the open (quantum) system paradigm. In the last section of chapter 1 we apply the acquired mathematical and physical tools to Maxwell's equations of electromagnetic fields. In chapter 2 we outline the setup under scrutiny: The parallel dispersion force acting on a microscopic object moving above a flat macroscopic surface. First, we give a brief introduction to dispersion forces derived from the averaged Lorentz force acting on a neutral particle. Second, we model the dynamics of the dipole moment for different classes of small microscopic objects. To describe the electromagnetic field acting on the dipole moment, we consider the general impact of geometry on the structure of the electromagnetic field and show the connection to material properties of infinitely extended bulk materials. Finally, we introduce two established models for bulk materials, i.e. for dielectrics and metals. In chapter 3 we assemble the ingredients of chapter 2 to study the nonequilibrium noncontact friction. The aim of this chapter is to thoroughly examine the properties of the noncontact friction and in the end to give an explanation of the intertwined physical effects giving rise to several peculiar features. In order to not rely solely on asymptotic approximations as calculated in chapter 3, we develop numerical strategies to evaluate the derived expression for the noncontact friction in chapter 4. At the end of this chapter we briefly present the code used to perform the numerical calculations. Finally, in chapter 5 we conclude with a discussion of the insights gathered throughout the thesis. We point out several levers to enhance the noncontact friction and point towards an experimentally accessible realm.

Contents

Conventions and Notation

In order to ease the access to the mathematical formulae and their underlying meaning, we give a brief overview over the use of mathematical notation and further conventions in this thesis. All general meanings of different typography and garnish of symbols are given in following table

Symbol	Intended Meaning
$\mathbf{V}$ or $\boldsymbol{\mathcal{V}}$	Vector of a collection of related objects $\mathbf{V} = \left(V_1, \cdots, V_N\right)$
$\underline{G}$ or $\mathbb{G}$	Matrix with $N \times N$ elements
$\hat{a}$	Operator valued quantity
$\underline{G}^\dagger$ or $\hat{a}^\dagger$	Conjugate transposed of matrices or Hermitian conjugate of operators
$\underline{G}^\intercal$ or $\mathbf{d}^\intercal$	Transposed matrix or vector respectively
α^*	Complex conjugated quantity
$\mathbf{d}^\intercal\mathbf{d}$ or $\mathbf{d} \cdot \mathbf{d}$	Scalar product of vectors and/or matrices
$\mathbf{d}\mathbf{d}^\intercal$ or $\mathbf{d} \otimes \mathbf{d}$	Outer product of vectors and/or matrices
$\int \mathrm{d}x$	Integration without limits indicates an integration from $-\infty$ to $+\infty$
$\sim$ and $\approx$	*Asymptotic to* and *approximated*

Further, we use the same symbol for a function and its Fourier transformed pendant, but indicating the respective domain in the argument, as e.g.

$$\alpha(t) = \int \frac{\mathrm{d}\omega}{2\pi}\, \alpha(\omega)\, e^{-\mathrm{i}\omega t}. \tag{$*$}$$

As shown in equation ($*$) the normalization factor of 2π is introduced in the integration over reciprocal space. While the transformation from frequency to time is chosen to transform with $\exp(-\mathrm{i}\omega t)$ (see example in equation ($*$)), we consequently transform from wavevector k_x to the respective spatial coordinate x with $\exp(+\mathrm{i}kx)$, in order to obtain a wave propagating in positive spatial direction x while t proceeds in positive time direction. Furthermore, throughout this thesis three different representations, so-called *pictures*, with respect to the quantum mechanical treatment are used. Within the Schrödinger picture the time evolution is carried by the states, whereas the operators remain typically time-independent. However,

the operators might carry an explicit time-dependence. Contrary, in the Heisenberg picture the time-dependence is put into the operators, whereas the states remain time-independent. Furthermore, the interaction picture is used. Coming from the Schrödinger picture, the states and operators in the interaction picture transform as follows

$$|\psi_{\mathrm{I}}(t)\rangle = e^{\mathrm{i}\hat{H}_0 t/\hbar}|\psi_{\mathrm{S}}(t)\rangle, \qquad \hat{A}_{\mathrm{I}}(t) = e^{\mathrm{i}\hat{H}_0 t/\hbar}\hat{A}_{\mathrm{S}}\, e^{-\mathrm{i}\hat{H}_0 t/\hbar},$$

with the subscripts denoting the respective representation, and we used the bra-ket notation.

CHAPTER 1

Theoretical Background

In this first chapter we introduce the general concepts used throughout the whole thesis. More specific discussions of the different investigated systems will be the focus of the chapter 2. The chapter begins with section 1.1, a brief introduction into the linear response theory as a central and fundamental tool. This powerful tool allows to formulate the famous fluctuation-dissipation theorem. In section 1.2, the focus is shifted to the open system paradigm, making strong use of the schemes introduced in section 1.1 and discuss the terms *fluctuation* and *dissipation* in detail. While doing so, we introduce the concept of the Langevin equation and (quantum) heat baths. Eventually, in the section 1.3 the toolbox acquired over the course of the preceding two sections is set in the context of electrodynamics. Here, we outline the physical framework of electrodynamic fluctuation theory, which treats fluctuations and dissipation in a coherent description.

1.1 Linear Response Theory

Very often, a physical or mathematical problem cannot be solved exactly. But with help of perturbation theory and approximate calculus we can approach even a very hard problem by dividing it into many easy problems, i.e. a perturbation series. In a perturbation series one expands the hard problem at a local point with respect to a small parameter. Furthermore, the first few correction terms are usually sufficient to yield an accurate approximation of the local behavior [61]. Subsequently, we employ perturbation theory to develop a technique to solve the evolution of a quantum system, which experiences a small perturbation. The state of a quantum system is fully characterized by its density operator $\hat{\rho}(t)$. The general time evolution of $\hat{\rho}(t)$ is determined by the von Neumann equation [9, 62]

$$\partial_t \hat{\rho}(t) = \frac{1}{\mathrm{i}\hbar}\left[\hat{\mathcal{H}}(t),\, \hat{\rho}(t)\right], \tag{1.1}$$

where $\hat{\mathcal{H}}$ is the Hamilton operator (or Hamiltonian) of the total system, $[\hat{A}, \hat{B}] = \hat{A}\hat{B} - \hat{B}\hat{A}$ is the commutator and $\hbar$ is the reduced Planck constant. The total system is separated into a time-

independent unperturbed system $\hat{\mathcal{H}}_0$ and an explicitly time-dependent perturbation $\hat{\mathcal{H}}_{\mathrm{per}}(t)$

$$\hat{\mathcal{H}}(t) = \hat{\mathcal{H}}_0 + \hat{\mathcal{H}}_{\mathrm{per}}(t). \tag{1.2}$$

While equation (1.1) describes the evolution of the system, one has to specify an initial state. We choose to prepare our system at an initial time t_0 to be the unperturbed system in its thermal equilibrium at the temperature T. Hence, the density operator is given by the respective Gibbs state of the unperturbed system

$$\hat{\rho}(t_0) = \frac{e^{-\beta\hat{\mathcal{H}}_0}}{\mathcal{Z}}. \tag{1.3}$$

with the partition function $\mathcal{Z} = \mathrm{tr}[\exp(-\beta\hat{\mathcal{H}}_0)]$ and $\beta = 1/(k_{\mathrm{B}}T)$, where k_{B} is the Boltzmann constant, and $\mathrm{tr}[\cdot]$ refers to the trace over a complete set of states. With this initial condition equation (1.1) can formally be solved by inserting the time evolution operator $\hat{\mathcal{U}}(t, t_0)$. The unitary time evolution operator propagates the system from a time t_0 to t, i.e. $\hat{\rho}(t) = \hat{\mathcal{U}}^\dagger(t, t_0)\hat{\rho}(t_0)\hat{\mathcal{U}}(t, t_0)$, and fulfills the differential equation

$$\mathrm{i}\hbar\partial_t \hat{\mathcal{U}}_{\mathcal{H}}(t, t_0) = \hat{\mathcal{H}}(t)\hat{\mathcal{U}}_{\mathcal{H}}(t, t_0) \quad \text{where} \quad \hat{\mathcal{U}}_{\mathcal{H}}(t_0, t_0) = \mathbb{1}. \tag{1.4}$$

Solving the above equation formally, the time evolution operator can be expressed as

$$\hat{\mathcal{U}}_{\mathcal{H}}(t, t_0) = \hat{\mathcal{T}}\left\{\exp\left(-\frac{\mathrm{i}}{\hbar}\int_{t_0}^{t} \mathrm{d}t'\, \hat{\mathcal{H}}(t')\right)\right\}, \tag{1.5}$$

with the time ordering operator $\hat{\mathcal{T}}$, which defines the ordering of operators with respect to their time-dependence. For example applying $\hat{\mathcal{T}}$ on two operators $\hat{A}(t_A)$ and $\hat{B}(t_B)$ and their corresponding time-dependence, the ordering reads

$$\hat{\mathcal{T}}\left\{\hat{A}(t_A)\,\hat{B}(t_B)\right\} = \begin{cases} \hat{A}(t_A)\,\hat{B}(t_B), & \text{for} \quad t_A > t_B \\ \pm\hat{B}(t_B)\,\hat{A}(t_A), & \text{for} \quad t_A < t_B \end{cases}, \tag{1.6}$$

with $\pm$ depending on the bosonic or fermionic nature of the operators [63]. In the case of unperturbed time evolution the time-evolution operator can be written as

$$\hat{\mathcal{U}}_{\mathcal{H}_0}(t, t_0) = \exp\left(-\frac{\mathrm{i}}{\hbar}\hat{\mathcal{H}}_0(t - t_0)\right). \tag{1.7}$$

In the following, the unperturbed time evolution shall be drawn out of the full time evolution [64]

$$\hat{\mathcal{U}}_{\mathcal{H}}(t, t_0) = \hat{\mathcal{U}}_{\mathcal{H}_0}(t, t_0)\,\hat{\mathcal{U}}_{\mathcal{H}_{\mathrm{per}}}(t, t_0). \tag{1.8}$$

In search for a differential equation of the perturbed time evolution equation (1.8) is substituted into equation (1.4), which leads to

$$\mathrm{i}\hbar\partial_t \hat{\mathcal{U}}_{\mathcal{H}_{\mathrm{per}}}(t,t_0) = e^{\frac{\mathrm{i}}{\hbar}\hat{\mathcal{H}}_0(t-t_0)}\hat{\mathcal{H}}_{\mathrm{per}}(t)e^{-\frac{\mathrm{i}}{\hbar}\hat{\mathcal{H}}_0(t-t_0)}\,\hat{\mathcal{U}}_{\mathcal{H}_{\mathrm{per}}}(t,t_0) \tag{1.9}$$

$$\equiv \hat{\mathcal{H}}^{\mathcal{H}_0}_{\mathrm{per}}(t,t-t_0)\,\hat{\mathcal{U}}_{\mathcal{H}_{\mathrm{per}}}(t,t_0). \tag{1.10}$$

Again, this differential equation can be formally solved by

$$\hat{\mathcal{U}}_{\mathcal{H}_{\mathrm{per}}}(t,t_0) = \hat{\mathcal{T}}\left\{\exp\left(-\frac{\mathrm{i}}{\hbar}\int_{t_0}^{t}\mathrm{d}t'\,\hat{\mathcal{H}}^{\mathcal{H}_0}_{\mathrm{per}}(t',t'-t_0)\right)\right\} \quad \text{with} \quad \hat{\mathcal{U}}_{\mathcal{H}_{\mathrm{per}}}(t_0,t_0) = \mathbb{1}. \tag{1.11}$$

In order to proceed, we assume a perturbation of the form

$$\hat{\mathcal{H}}_{\mathrm{per}}(t) = -\epsilon(t)\hat{\mathcal{V}}, \quad \text{or} \quad \hat{\mathcal{H}}^{\mathcal{H}_0}_{\mathrm{per}}(t,t-t_0) = -\epsilon(t)\hat{\mathcal{V}}(t-t_0) \tag{1.12}$$

where we used the transformation $e^{\frac{\mathrm{i}}{\hbar}\hat{\mathcal{H}}_0 t}\,\hat{\mathcal{V}}\,e^{-\frac{\mathrm{i}}{\hbar}\hat{\mathcal{H}}_0 t} = \hat{\mathcal{V}}(t)$ from the Schrödinger picture to the interaction picture. The scalar dimensionless parameter $\epsilon(t)$ facilitates a neat perturbation approach. On the one hand, $\epsilon(t)$ enables to turn the perturbation operator $\hat{\mathcal{V}}$ on and off with time, i.e. the perturbation being finite in time. And on the other hand, we are in control of the term *small*, i.e. $|\epsilon(t)| \ll 1$. In this scheme we can expand the perturbed evolution in time in orders of $\epsilon(t)$

$$\hat{\mathcal{U}}_{\mathcal{H}_{\mathrm{per}}}(t,t_0) = \hat{\mathcal{T}}\left\{\exp\left(\frac{\mathrm{i}}{\hbar}\int_{t_0}^{t}\mathrm{d}t'\,\epsilon(t')\hat{\mathcal{V}}(t'-t_0)\right)\right\} \tag{1.13}$$

$$= \mathbb{1} + \frac{\mathrm{i}}{\hbar}\int_{t_0}^{t}\mathrm{d}t'\,\epsilon(t')\hat{\mathcal{V}}(t'-t_0) + \mathcal{O}(\epsilon^2). \tag{1.14}$$

While we restrict our investigation to the linear order, also higher orders can be evaluated within the very same scheme [65]. Employing the expansion of equation (1.14) and applying it to the density operator of the system leads to

$$\hat{\rho}(t) = \hat{\mathcal{U}}_{\mathcal{H}}(t,t_0)\hat{\rho}(t_0)\hat{\mathcal{U}}^{\dagger}_{\mathcal{H}}(t,t_0) \tag{1.15}$$

$$\overset{|\epsilon|\ll 1}{\approx} \hat{\rho}(t_0) + e^{-\frac{\mathrm{i}}{\hbar}\hat{\mathcal{H}}_0(t-t_0)}\frac{\mathrm{i}}{\hbar}\int_{t_0}^{t}\mathrm{d}t'\,\epsilon(t')\left[\hat{\mathcal{V}}(t'-t_0),\,\hat{\rho}(t_0)\right]e^{\frac{\mathrm{i}}{\hbar}\hat{\mathcal{H}}_0(t-t_0)}, \tag{1.16}$$

where we used that the perturbation is a Hermitian operator, i.e. $\hat{\mathcal{V}}^{\dagger} = \hat{\mathcal{V}}$. The truncation of the series in equation (1.16) after the linear order lends the name of the theory based on it, i.e. *linear response theory*[1]. With the expansion of equation (1.16), we are ready to compute expectation values of arbitrary operators $\hat{\mathcal{A}}$. For the expectation value with $t > t_0$, we find in

[1] It is worth pointing out that the relations derived within the linear response theory, as for example the later demonstrated fluctuation-dissipation theorem, are exact connections of well-defined quantities. For instance, the linear response of a maybe more general nonlinear response still has to fulfill the fluctuation-dissipation theorem.

linear order

$$\left\langle \hat{\mathcal{A}} \right\rangle_{\rho(t)} - \left\langle \hat{\mathcal{A}} \right\rangle_{\rho(t_0)} \approx \mathrm{tr}\left[\hat{\mathcal{A}}(t-t_0) \left(\frac{\mathrm{i}}{\hbar} \int_{t_0}^{t} \mathrm{d}t'\, \epsilon(t') \left[\hat{\mathcal{V}}(t'-t_0),\, \hat{\rho}(t_0) \right] \right) \right] \tag{1.17}$$

$$= \frac{\mathrm{i}}{\hbar} \int_{t_0}^{t} \mathrm{d}t'\, \epsilon(t') \left\langle \left[\hat{\mathcal{V}}(t'-t_0),\, \hat{\mathcal{A}}(t-t_0) \right] \right\rangle_{\rho(t_0)} \tag{1.18}$$

$$\overset{t'=t-\tau}{=} \frac{\mathrm{i}}{\hbar} \int_{0}^{t-t_0} \mathrm{d}\tau\, \epsilon(t-\tau) \left\langle \left[\hat{\mathcal{V}}(0),\, \hat{\mathcal{A}}(\tau) \right] \right\rangle_{\rho(t_0)}, \tag{1.19}$$

where the exponentials of equation (1.16) were absorbed by the change to interaction picture of the operators, and the stationarity was used to eliminate the t_0 in the commutator, i.e.

$$\left\langle \left[\hat{\mathcal{V}}(t'-t_0),\, \hat{\mathcal{A}}(t-t_0) \right] \right\rangle_{\rho(t_0)} = \left\langle \left[\hat{\mathcal{V}}(0),\, \hat{\mathcal{A}}(t-t') \right] \right\rangle_{\rho(t_0)}. \tag{1.20}$$

At this point we choose a perturbed and unperturbed region with respect to time. Assigning the time before t_0 as unperturbed and then switching on the perturbation, the response to the strength of the perturbation is defined via the retarded response function

$$\alpha_{\mathcal{A}\mathcal{V}}(\tau) = \frac{\mathrm{i}}{\hbar} \theta(\tau) \left\langle \left[\hat{\mathcal{V}}(0),\, \hat{\mathcal{A}}(\tau) \right] \right\rangle_{\rho(t_0)}. \tag{1.21}$$

Vice versa, one could decide to time-wise exchange perturbed and unperturbed regime and define the advanced response function, which differs from the retarded response just by $\theta(\tau) \to \theta(-\tau)$. Equation (1.19) fully expresses the response of the system through the state of the unperturbed system $\rho(t_0)$. In the following, a relaxed perturbed state of the system is considered. This means, that we are not concerned about any transient regime which might occur between the system being unperturbed and reaching a stationary but perturbed state. Assuming a finite life-time τ_{tr} of the transient regime, we investigate only points in time, where the difference between switching the perturbation on (at t_0) and probing the total system (at t) is much larger than the impact of the transient regime, i.e. $t - t_0 \gg \tau_{\mathrm{tr}}$. Formally, one can express this focus on the stationary regime via sending $t - t_0 \to \infty$, assuming it yields no relevant change when performing the integrations. With this last simplification we eventually arrive at the very condensed form

Expectation Value in Linear Response

$$\left\langle \hat{\mathcal{A}} \right\rangle_{\rho(t)} = \int_{-\infty}^{\infty} \mathrm{d}\tau\, \alpha_{\mathcal{A}\mathcal{V}}(\tau) \epsilon(t-\tau) + \mathcal{O}(\epsilon^2). \tag{1.22}$$

Fluctuation-Dissipation Theorem

The expectation value in linear response of equation (1.22) was derived for an arbitrary operator $\hat{\mathcal{A}}$. With this general and powerful tool, we can derive another highly relevant and powerful relation, the fluctuation-dissipation theorem. The fluctuation-dissipation theorem, originally proposed by Nyquist for classical systems [66] and extended for quantum systems

by Callen and Welton [67], points out the connection between a linear perturbation impinging an equilibrium system and the general response to it. In general the perturbation and the corresponding response function can be multidimensional, i.e. the perturbation might be written as a N-dimensional vector operator $\hat{\boldsymbol{\mathcal{O}}} = (\hat{\mathcal{O}}_1, \hat{\mathcal{O}}_2, \cdots, \hat{\mathcal{O}}_N)^\intercal$, with the $\intercal$ indicating the transpose of a vector or matrix. Consequently, the response function is a $N \times N$-dimensional matrix

$$\underline{\alpha}_{\boldsymbol{\mathcal{A}}\boldsymbol{\mathcal{V}}}(\tau) = \frac{\mathrm{i}}{\hbar}\theta(\tau)\left\langle \hat{\boldsymbol{\mathcal{V}}}(0)\hat{\boldsymbol{\mathcal{A}}}^\intercal(\tau) - \hat{\boldsymbol{\mathcal{A}}}(\tau)\hat{\boldsymbol{\mathcal{V}}}^\intercal(0)\right\rangle_{\rho(t_0)} \tag{1.23}$$

$$= \frac{\mathrm{i}}{\hbar}\theta(\tau)\Big[\underline{C}_{\boldsymbol{\mathcal{V}}\boldsymbol{\mathcal{A}}}(-\tau) - \underline{C}_{\boldsymbol{\mathcal{A}}\boldsymbol{\mathcal{V}}}(\tau)\Big]. \tag{1.24}$$

Here, we introduced the stationary correlation function

$$\underline{C}_{\boldsymbol{\mathcal{A}}\boldsymbol{\mathcal{V}}}(\tau) = \left\langle \hat{\boldsymbol{\mathcal{A}}}(\tau)\hat{\boldsymbol{\mathcal{V}}}^\intercal(0)\right\rangle_{\rho(t_0)} = \left\langle \hat{\boldsymbol{\mathcal{A}}}(0)\hat{\boldsymbol{\mathcal{V}}}^\intercal(-\tau)\right\rangle_{\rho(t_0)}, \tag{1.25}$$

where in the last line we employed the definition of the interaction picture and that $\hat{\rho}(t_0)$ and $\hat{\mathcal{H}}_0$ do commute. As stated earlier at t_0 the system is assumed to be in its equilibrium state $\rho(t_0)$ as defined by equation (1.3). In $\rho(t_0)$ following relation can be exploited

$$\begin{aligned}\underline{C}_{\boldsymbol{\mathcal{V}}\boldsymbol{\mathcal{A}}}(-\tau) &= \mathrm{tr}\left[\hat{\boldsymbol{\mathcal{V}}}(0)\,\hat{\boldsymbol{\mathcal{A}}}^\intercal(\tau)\,e^{-\beta\hat{\mathcal{H}}_0}\right]\frac{1}{\mathcal{Z}} \\ &= \mathrm{tr}\left[\hat{\boldsymbol{\mathcal{V}}}(0)\,e^{-\beta\hat{\mathcal{H}}_0}\,\hat{\boldsymbol{\mathcal{A}}}^\intercal(\tau - \mathrm{i}\hbar\beta)\right]\frac{1}{\mathcal{Z}} = \underline{C}^\intercal_{\boldsymbol{\mathcal{A}}\boldsymbol{\mathcal{V}}}(\tau - \mathrm{i}\hbar\beta)\,.\end{aligned} \tag{1.26}$$

This condition is also referred to as Kubo-Martin-Schwinger condition [68, 69]. Finally, we shift our discussion to frequency domain. The power spectrum is defined as the Fourier transform[2] of the stationary correlation function of two operators $\hat{\boldsymbol{\mathcal{A}}}$ and $\hat{\boldsymbol{\mathcal{B}}}$

$$\underline{S}_{\boldsymbol{\mathcal{A}}\boldsymbol{\mathcal{B}}}(\omega) \equiv \frac{1}{2\pi}\int \mathrm{d}\tau\, \underline{C}_{\boldsymbol{\mathcal{A}}\boldsymbol{\mathcal{B}}}(\tau)e^{\mathrm{i}\omega\tau}. \tag{1.27}$$

To retrieve the connection between the response function — or its pendant in frequency domain, the susceptibility — and the power spectrum, we calculate

$$\underline{\alpha}_{\boldsymbol{\mathcal{A}}\boldsymbol{\mathcal{V}}}(\omega) - \alpha^\dagger_{\boldsymbol{\mathcal{V}}\boldsymbol{\mathcal{A}}}(\omega) = \frac{1}{\mathrm{i}\hbar}\int \mathrm{d}\tau\, e^{\mathrm{i}\omega\tau}\Big(-\underline{C}_{\boldsymbol{\mathcal{A}}\boldsymbol{\mathcal{V}}}(\tau) + \underline{C}_{\boldsymbol{\mathcal{V}}\boldsymbol{\mathcal{A}}}(-\tau)\Big), \tag{1.28}$$

where we used $\underline{C}^\dagger_{\boldsymbol{\mathcal{A}}\boldsymbol{\mathcal{B}}}(\tau) = \underline{C}_{\boldsymbol{\mathcal{B}}\boldsymbol{\mathcal{A}}}(-\tau)$. Applying the Kubo-Martin-Schwinger condition to the previous equation, leads to the relation most often referred to as *fluctuation-dissipation*

[2] Please note the opposite placement of the normalization factor 2π in this definition. For all other Fourier transformed quantities we divide by 2π in the frequency integration, i.e.

$$x(t) = \int \frac{\mathrm{d}\omega}{2\pi}x(\omega)e^{-\mathrm{i}\omega t}.$$

theorem[3]

Fluctuation Dissipation Theorem

$$\underline{S}_{\boldsymbol{\mathcal{A}}\boldsymbol{\mathcal{V}}}(\omega) = \frac{\hbar}{1-\exp(-\beta\hbar\omega)} \frac{\underline{\alpha}_{\boldsymbol{\mathcal{A}}\boldsymbol{\mathcal{V}}}(\omega) - \underline{\alpha}^{\dagger}_{\boldsymbol{\mathcal{V}}\boldsymbol{\mathcal{A}}}(\omega)}{2\pi\mathrm{i}} \,. \tag{1.29}$$

Until now, $\hat{\boldsymbol{\mathcal{A}}}$ is a generic operator. Subsequently, $\hat{\boldsymbol{\mathcal{A}}}$ is set to be the perturbation operator $\hat{\boldsymbol{\mathcal{A}}} \equiv \hat{\boldsymbol{\mathcal{V}}}$. In this case equation (1.29) can be written as

$$\underline{S}_{\boldsymbol{\mathcal{V}}\boldsymbol{\mathcal{V}}}(\omega) = \frac{\hbar/\pi}{1-\exp(-\beta\hbar\omega)} \underline{\alpha}_{\Im}^{\boldsymbol{\mathcal{V}}\boldsymbol{\mathcal{V}}}(\omega) \,, \tag{1.30}$$

where the subscript $\Im$ is defined as $(\underline{\alpha} - \underline{\alpha}^{\dagger})/(2\mathrm{i})$ and the former subscript $\boldsymbol{\mathcal{V}}\boldsymbol{\mathcal{V}}$ was shifted to the superscript. The connection of the respective power spectrum to the autocorrelator $\langle \hat{\boldsymbol{\mathcal{V}}} \hat{\boldsymbol{\mathcal{V}}}^{\mathsf{T}} \rangle_{\rho(t_0)}$ in frequency domain reads [4]

$$\langle \hat{\boldsymbol{\mathcal{V}}}(\omega)\, \hat{\boldsymbol{\mathcal{V}}}^{\mathsf{T}}(\omega') \rangle_{\rho(t_0)} = 4\pi^2 \underline{S}_{\boldsymbol{\mathcal{V}}\boldsymbol{\mathcal{V}}}(\omega)\delta(\omega+\omega'), \tag{1.34}$$

which is a form of the Wiener-Khinchin theorem [71] for stationary processes.

Interestingly, in order to obtain the fluctuation-dissipation theorem of equation (1.29), no explicit connection between the perturbation $\hat{\boldsymbol{\mathcal{V}}}$ and the arbitrary operator $\hat{\boldsymbol{\mathcal{A}}}$ was assumed. Nonetheless, when evaluating the expectation value $\langle \hat{\boldsymbol{\mathcal{A}}}(t) \rangle_{\rho(t)}$ the connection becomes evident in the response function $\underline{\alpha}_{\boldsymbol{\mathcal{A}}\boldsymbol{\mathcal{V}}}$. The response function contains, in addition to the operator which shall be evaluated, the unperturbed density operator $\hat{\rho}(t_0)$ and the perturbation $\hat{\boldsymbol{\mathcal{V}}}$. Besides this implicit connection of the expectation value of $\hat{\boldsymbol{\mathcal{A}}}$ to the perturbation $\hat{\boldsymbol{\mathcal{V}}}$, $\hat{\boldsymbol{\mathcal{A}}}$ might be driven explicitly by the perturbation. In the case of a linear driving the operator $\hat{\boldsymbol{\mathcal{A}}}$ can be written in response to the perturbation

$$\hat{\boldsymbol{\mathcal{A}}}(t) = \int \mathrm{d}\tau\, \underline{\tilde{\alpha}}(\tau) \cdot \hat{\boldsymbol{\mathcal{V}}}(t-\tau). \tag{1.35}$$

[3] The first versions of this theorem were carried out by Nyquist [66] and Einstein [70], relating the fluctuation acting on the system to the respective dissipation. Thus, the historically grown name *fluctuation-dissipation theorem* is easily understandable and also proven by Callen and Welton [67]. Nonetheless, the name might seem a bit odd, when the reader, without that historical context, is confronted with the general linear response derivation as done by Kubo [62] and seeks in vain for fluctuations or dissipation in the first place. To lift this confusion we suggest to think of the theorem stated in equation (1.29) as *perturbation-response theorem*, since this is what Kubo and other authors are actually implying within their general derivation.

[4] Here, we insert the short proof

$$\langle \hat{\boldsymbol{\mathcal{V}}}(\omega)\, \hat{\boldsymbol{\mathcal{V}}}^{\mathsf{T}}(\omega') \rangle_{\rho(t_0)} = \int \mathrm{d}t \int \mathrm{d}t'\, \langle \hat{\boldsymbol{\mathcal{V}}}(t)\, \hat{\boldsymbol{\mathcal{V}}}^{\mathsf{T}}(t') \rangle_{\rho(t_0)} e^{\mathrm{i}(\omega t + \omega' t')} \tag{1.31}$$

$$= \frac{1}{2} \int \mathrm{d}\tau \int \mathrm{d}T\, \langle \hat{\boldsymbol{\mathcal{V}}}(\tau)\, \hat{\boldsymbol{\mathcal{V}}}^{\mathsf{T}}(0) \rangle_{\rho(t_0)} e^{\frac{1}{2}\mathrm{i}T(\omega+\omega')} e^{\frac{1}{2}\mathrm{i}\tau(\omega-\omega')} \tag{1.32}$$

$$= 2\pi\delta(\omega+\omega') \int \mathrm{d}\tau \langle \hat{\boldsymbol{\mathcal{V}}}(\tau)\, \hat{\boldsymbol{\mathcal{V}}}^{\mathsf{T}}(0) \rangle_{\rho(t_0)} e^{\frac{1}{2}\mathrm{i}\tau(\omega-\omega')} = 4\pi^2 \delta(\omega+\omega') \underline{S}_{\boldsymbol{\mathcal{V}}\boldsymbol{\mathcal{V}}}(\omega) \tag{1.33}$$

where we used the substitutions $\tau = t - t'$, $T = t + t'$ and consequently $2\mathrm{d}t\, \mathrm{d}t' = \mathrm{d}\tau\, \mathrm{d}T$.

To emphasize the difference between the response concerning the expectation value of $\hat{\boldsymbol{\mathcal{A}}}$, we introduced a new response function $\underline{\tilde{\alpha}}(\tau)$ with respect to the operator. When investigating the power spectrum of the respective $\hat{\boldsymbol{\mathcal{A}}}$ autocorrelator $\underline{S}_{\boldsymbol{\mathcal{A}}\boldsymbol{\mathcal{A}}}$, we are able to retrieve the autocorrelator of the perturbation $\underline{S}_{\boldsymbol{\mathcal{V}}\boldsymbol{\mathcal{V}}}$

$$\underline{S}_{\boldsymbol{\mathcal{A}}\boldsymbol{\mathcal{A}}}(\omega) = \underline{\tilde{\alpha}}(\omega) \cdot \underline{S}_{\boldsymbol{\mathcal{V}}\boldsymbol{\mathcal{V}}}(\omega) \cdot \underline{\tilde{\alpha}}^{\dagger}(\omega). \tag{1.36}$$

Substituting this relation into equation (1.28), we can derive the statement

$$\underline{\tilde{\alpha}}_{\Im}(\omega) = \underline{\tilde{\alpha}}(\omega) \cdot \underline{\alpha}_{\Im}^{\boldsymbol{\mathcal{V}}\boldsymbol{\mathcal{V}}}(\omega) \cdot \underline{\tilde{\alpha}}^{\dagger}(\omega). \tag{1.37}$$

In the literature, the last equation is often referred to as *fluctuation-dissipation theorem of second kind*, whereas the theorem of equation (1.29) is labeled the first kind. We like to stress that equation (1.37) depends on the fact that $\hat{\boldsymbol{\mathcal{A}}} \propto \hat{\boldsymbol{\mathcal{V}}}$. Otherwise, the statement of equation (1.37) would be incorrect (e.g. for $\hat{\boldsymbol{\mathcal{A}}} \propto \hat{\boldsymbol{\mathcal{V}}}^2$ this relation breaks down). Nonetheless, the relation in equation (1.22) remains valid since the expansion for a small perturbation is carried out within the density matrix.

Recap: Applying a perturbation approach to the evolution of the density operator $\hat{\rho}(t)$, we derived the first order correction to an unperturbed system in equilibrium. The consequences of this first correction are often summed up with the term *linear response theory*. Exploiting linear response theory we derived the famous fluctuation-dissipation theorem in its first and second kind in equations (1.29) and (1.37).

1.2 Open System Dynamics

In the last section, we established the connection between a perturbation and the corresponding response of the initially unperturbed system. However, it might not yet become clear why we and many other authors refer to the relation given in equation (1.29) as "fluctuation-dissipation" theorem. Both words of the theorem derive their meaning from the open system paradigm. Within this paradigm, the fact that one cannot entirely separate the dynamics of the system of interest (e.g. the dynamics of one single atom) from its environment has to be accepted. But instead of solving the dynamics of the whole universe at once, a compromise is chosen. As one continues to cover all detailed and relevant dynamics of the system of interest, the environment shall be described solely through its influence on the system. Physically, when coupling the system and the environment, energy can be exchanged between them. Especially, when assuming that the environment contains many more degrees of freedom than the investigated system, energy placed in the system is to be expected to be transferred to the environment, or in other words, to dissipate. Therefore, energy is not conserved when considering the system exclusively and it is called an open system. If we consider both, the system and its environment, the total system still conserves energy, i.e. it is a closed system. At this point, we recall a prototypical description of an environment. It is important to remember here that we do not

Independent Oscillator Model

aim to model the exact microscopic physics of the environment, but rather want to obtain a "basis set" from which we can construct nearly any macroscopic influence of the environment on the system in weak coupling. One very neat and practical scheme, namely the independent oscillator model, was proposed by Feynman and Vernon [72] and exhaustively studied by Ford et al. [73–75]. As the name suggests, the bath is modeled as an assembly of independent harmonic oscillators. The universality of this model comes with the fact that any robust and just weakly disturbed system may be, "to the extent that second order perturbation theory yields satisfactory accuracy, [...] considered as a sum of harmonic oscillators"[72]. Or as Anglin et al. put it: "[...] the independent oscillator model is therefore not entirely a toy, and represents a simplicity that is actually realized in nature."[76]. Motivated by this profound universality, we set up the Hamiltonian of the independent oscillator model coupled to the system.

The total system is divided into a sub-system we refer to as *system* S and the environment we refer to as *bath* B. Conclusively, a respective Hamiltonian divides into

$$\hat{\mathcal{H}} = \hat{\mathcal{H}}_S + \hat{\mathcal{H}}_{SB} + \hat{\mathcal{H}}_B, \tag{1.38}$$

where $\hat{\mathcal{H}}_S$ and $\hat{\mathcal{H}}_B$ represent the isolated subsystems and $\hat{\mathcal{H}}_{SB}$ the coupling between them. For a start, the system shall be a single particle of mass M moving in a potential V

$$\hat{\mathcal{H}}_S = \frac{\hat{p}^2}{2M} + V(\hat{x}). \tag{1.39}$$

The bath is modeled as an assembly of independent harmonic oscillators, which bilinearly couple to the system

$$\hat{\mathcal{H}}_{SB} + \hat{\mathcal{H}}_B = \sum_j \left[\frac{\hat{p}_j^2}{2m_j} + \frac{m_j}{2}\omega_j^2 \left(\hat{q}_j - \hat{x}\right)^2 \right], \tag{1.40}$$

where m_j and ω_j are the corresponding parameters of the oscillators of the environment with the spatial operator $\hat{q}_j$ and momentum operator $\hat{p}_j$. It is suggestive to interpret m_j as mass and ω_j as the central frequency of the respective jth oscillator. Since we use the independent oscillator model more as an approximation around the equilibrium position instead of an actual description of the physical mechanism within the bath, one could also simply refer to m_j and ω_j as expansion coefficients. As already mentioned, the linear coupling is justified for a weak coupling strength between the system and the environment, which is the exact regime we are interested in within this thesis. Nonetheless, there are of course also vivid investigations of the strong coupling regime by other authors [77–80]. The bilinear form, i.e. introducing the system-bath coupling via $(\hat{q}_j - \hat{x})^2$, results from a renormalization. The simple linear coupling scheme yields nonphysical effects for $V(\hat{x}) = 0$, i.e. no lower bound on the energy, meaning there is no equilibrium state and spatial non-invariance [73, 81]. With the bilinear form, these defects are remedied. A detailed discussion of the independent oscillator model and the connection to other models was done by Ford et al. [73]. Besides the simplicity and easy handling of the independent oscillators as bath model and the fundamental connection to any slightly disturbed robust equilibrium system, even more motivation can be found in real physical systems like the normal modes of the electromagnetic field or phonon modes in a

crystal [82, 83]. With this strong and broad motivation of the model Hamiltonian, we continue determining the dynamics of the system. Employing the Heisenberg picture and the resulting equation of motion for an arbitrary operator $\hat{\mathcal{A}}^{(\mathrm{H})}(t)$

$$\frac{\mathrm{d}\hat{\mathcal{A}}^{(\mathrm{H})}(t)}{\mathrm{d}t} = \frac{\mathrm{i}}{\hbar}[\hat{\mathcal{H}}, \hat{\mathcal{A}}^{(\mathrm{H})}(t)] + \frac{\partial \hat{\mathcal{A}}^{(\mathrm{H})}(t)}{\partial t}, \tag{1.41}$$

where the superscript (H) denotes the Heisenberg picture, the following equations of motion can be derived

$$M\ddot{\hat{x}}^{(\mathrm{H})}(t) + V'(\hat{x}^{(\mathrm{H})}(t)) = \sum_j m_j\omega_j^2 \left(\hat{q}_j^{(\mathrm{H})}(t) - \hat{x}^{(\mathrm{H})}(t)\right) \tag{1.42}$$

$$\ddot{\hat{q}}_j^{(\mathrm{H})}(t) + \omega_j^2\hat{q}_j^{(\mathrm{H})}(t) = \omega_j^2\hat{x}^{(\mathrm{H})}(t) \tag{1.43}$$

where the bosonic canonical commutator relations $[\hat{x}, \hat{p}] = \mathrm{i}\hbar$ for the system and bath variables were used. Due to their independence $[\hat{x}, \hat{p}_j] = 0$ as well as $[\hat{q}_j, \hat{p}_i] = \mathrm{i}\hbar\delta_{ij}$. The prime at the potential indicates the derivative with respect to $\hat{x}$, since $(\mathrm{i}/\hbar)\left[V(\hat{x}), \hat{p}\right] = V'(\hat{x})$. First, we construct the solution of the bath operators and find

$$\hat{q}_j^{(\mathrm{H})}(t) = \hat{q}_j^{(\mathrm{H})\,\mathrm{free}}(t) - \int_{t_0}^{t} \mathrm{d}t_1 \cos\left[\omega_j\,(t - t_1)\right] \dot{\hat{x}}^{(\mathrm{H})}\,(t_1)\,, \tag{1.44}$$

$$\hat{q}_j^{(\mathrm{H})\,\mathrm{free}}(t) = \hat{q}_j^{(\mathrm{H})}(t_0)\cos(\omega_j t) + \hat{p}_j^{(\mathrm{H})}(t_0)\frac{\sin(\omega_j t)}{m_j\omega_j}, \tag{1.45}$$

where $\hat{q}_j^{(\mathrm{H})\,\mathrm{free}}$, the homogeneous solution of equation (1.43), is solely dependent on the bath's quantities. Condensing the free part to one free bath operator

$$\hat{F}^{(\mathrm{H})}(t) = \sum_j m_j\omega_j^2\hat{q}_j^{(\mathrm{H})\,\mathrm{free}}(t) \tag{1.46}$$

and collecting the remaining bath quantities in

$$\mu(t) = \theta(t)\sum_j m_j\omega_j^2\cos(\omega_j t), \tag{1.47}$$

one retrieves the quantum version of the Langevin equation [84]

Quantum Langevin Equation

$$M\ddot{\hat{x}}^{(\mathrm{H})}(t) + \int_{t_{\mathrm{in}}}^{\infty} \mathrm{d}t_1\,\mu(t - t_1)\,\dot{\hat{x}}^{(\mathrm{H})}(t_1) + V'(\hat{x}^{(\mathrm{H})}(t)) = \hat{F}^{(\mathrm{H})}(t). \tag{1.48}$$

The classical Langevin equation, first proposed by Langevin [13], recasts the stochastic problem of a Brownian motion into a simple equation of motion with two additional terms. These two terms carry the experimentally observed effects of friction/dissipation and fluctuation. While the friction lowers the velocity of the particle, the fluctuation randomly pushes the particle

around. In this analogy we refer to μ as friction kernel and to $\hat{F}$ as fluctuation operator. The bath influences the system through μ and $\hat{F}$. Since the operators contained in $\hat{F}$ are not acting on the same Hilbert space as the system operators, $\hat{F}$ — from the system's point of view — is interpreted as an external fluctuation or driving force. If one takes a closer look at the definitions of μ and $\hat{F}$ in equation (1.46) and equation (1.47), one will already notice connections via the parameters m_j and ω_j. More generally, one can derive directly from the quantum Langevin equation that

$$\left[\hat{F}(t), \hat{F}(t')\right] = \frac{2}{\mathrm{i}\pi} \int_0^\infty \mathrm{d}\omega \, \mathrm{Re}\left\{\mu(\omega + \mathrm{i}0^+)\right\} \hbar\omega \sin(\omega\tau), \tag{1.49}$$

where $\mathrm{i}0^+$ shifts the frequency dependence infinitesimal into the upper complex half-plane in order to obey causality [73]. Moreover, we can use the tools of the previous section to make a general statement for stationary regimes. Let us assume, one perturbs the initial independent oscillator Hamiltonian of equation (1.38) with a small perturbation $\hat{\mathcal{H}}_{\mathrm{per}} = -\epsilon(t)\hat{x}$. Further, we assume that $\epsilon(t)$ was switched off long ago, such that the full system relaxed to its equilibrium. Under these assumptions, the Langevin equation of equation (1.48) is altered only by one additional term

$$M\ddot{\hat{x}}(t) + \int_{t_{\mathrm{in}}}^\infty \mathrm{d}t_1 \, \mu(t - t_1) \, \dot{\hat{x}}(t_1) + V'\left(\hat{x}(t)\right) = \hat{F}(t) + \epsilon(t). \tag{1.50}$$

Here, we dropped the superscript (H) since the former Heisenberg picture becomes the interaction picture of the new system, which contains the unperturbed system $\hat{\mathcal{H}}_0$ together with the attached perturbation, i.e. the former total Hamiltonian now only characterizes the unperturbed part of the total Hamiltonian ($\hat{\mathcal{H}} \to \hat{\mathcal{H}}_0$). With the aid of the fluctuation-dissipation theorem in the form of equation (1.30), we immediately know the form of the autocorrelator or the respective power spectrum

$$S_{xx}(\omega) = \frac{\hbar/\pi}{1 - \exp(-\beta\hbar\omega)} \alpha_I^{xx}(\omega), \tag{1.51}$$

where we used that for scalar response functions $\Im \to I$, with I being the imaginary part of the scalar susceptibility. In the following we assume a quadratic potential $V(\hat{x}) = M\hat{x}^2\omega_0^2/2$ with a central frequency ω_0. As long as the system possesses a robust equilibrium position, one can expand around this equilibrium position and achieves approximately a harmonic oscillator, i.e. a quadratic potential. Consequently, the differential equation is linear in $\hat{x}$ and with the following solution in frequency domain

$$\hat{x}(\omega)\tilde{\alpha}(\omega) = \hat{F}(\omega) + \epsilon(\omega) \quad \text{with} \quad \tilde{\alpha}(\omega) = \omega_0^2 - \omega^2 - \mathrm{i}\omega\mu(\omega). \tag{1.52}$$

When comparing with equation (1.35) we notice that we reproduced nearly the same structure of $\hat{x}(\omega)\tilde{\alpha}(\omega) = \hat{F}(\omega)$, but with an additional $\epsilon(\omega)$ term. Calculating the correlator also yields additional terms. However, if we take a closer look at the derivation of the fluctuation-dissipation theorem in equation (1.29), we notice that the derivation rests upon commutators when defining the response function. Thus, since $\epsilon(\omega)$ is a scalar function its contribution

vanishes as soon as the commutator is applied. Therefore, $\hat{F}$ and μ are connected by

$$S_{FF}(\omega) = \frac{\hbar/\pi}{1-\exp(-\beta\hbar\omega)}\tilde{\alpha}(\omega)\,\alpha^{xx}_{\Im}(\omega)\,\tilde{\alpha}^*(\omega) = \frac{\hbar/\pi}{1-\exp(-\beta\hbar\omega)}\mathrm{Im}\left[\mathrm{i}\omega\mu(\omega)\right], \tag{1.53}$$

where we engaged the fluctuation-dissipation theorem of second kind (see equation (1.37)). Finally, the name "fluctuation-dissipation" theorem becomes more evident. On the left-hand side only the fluctuation operator $\hat{F}$ is present, whereas on the right-hand side we find the friction kernel. In other words, fluctuation and dissipation are deeply connected. We emphasize, as mentioned earlier, that the chosen environment/bath model does not need to model the complete structure of the environment/bath in the first place but rather results from the expansion around the equilibrium to second order. However, from the system's point of view in weak coupling, one cannot distinguish the two situations. The system effectively senses solely the condensed quantities μ and $\hat{F}$. Remarkably, the independent oscillator model is capable of modeling the most general (linear) quantum Langevin equation (this strong statement is demonstrated by Ford and O'Connell [73]). Nevertheless, we should interpret both the classical and quantum Langevin equation more, as Van Kampen phrases it in [85], as a "pre-equation", since the statistical behavior of $\hat{F}$ and μ is not specified yet. From a quantum mechanical point of view, this can be done by tracing out all environmental degrees of freedom. This means that the full dynamics of environment are condensed to a stochastic processes acting on the system. Formally, the described approach is applied by the using the Nakajima-Zwanzig projection operator [86]

Stochastic Fluctuation

$$\hat{\mathcal{P}} = \mathrm{tr}_B[\hat{\rho}_B^{\mathrm{eq}}\cdots], \tag{1.54}$$

where the $\mathrm{tr}_B[\cdots] = \sum_i \langle B_i|\cdots|B_i\rangle$, with B_i being the ith bath state, traces out all degrees of freedom of the bath. The Nakajima-Zwanzig projection refers consequently to the exact equilibrium state of the full system,

$$\hat{\rho}_B^{\mathrm{eq}} = \frac{\mathrm{tr}_S\left[e^{-\beta\hat{\mathcal{H}}}\right]}{\mathcal{Z}}, \tag{1.55}$$

with tr_S being the system's analogue to tr_B. At this point, we introduce another important assumption, i.e. that we can approximate $\hat{\rho}_B^{\mathrm{eq}}$ by the uncoupled heat bath being at equilibrium. Thus, we are neglecting the impact of the system on the bath's equilibrium. Omitting the influence of the system on the bath is a crucial and sometimes inconsistent step to obtain the rather simple result of Gaussian noise, which is discussed by Geva et al. [87]. Nevertheless, as long as the coupling is weak and the bath's relaxation time τ_B is short compared to the system's relaxation time τ_S, we should not notice any relevant difference[5] in our results [88].

[5] In order to keep up the fast relaxation time of the bath we have to be aware of the fact, that the relaxation time of the bath may grows significantly for low temperatures as e.g. for a phononic heat bath [88, 89].

Under the preceding assumptions the bath's equilibrium density matrix takes the form

$$\hat{\rho}_B = \exp\left(-\beta \sum_j \frac{\hat{p}_j^2}{2m_j} + \frac{\omega_j^2 m_j}{2}\hat{q}_j^2\right)\frac{1}{\mathcal{Z}_B} = \frac{1}{\mathcal{Z}_B}\prod_j e^{-\beta\hbar\omega_j(\hat{n}_j+\frac{1}{2})} \tag{1.56}$$

where $\mathcal{Z}_B$ is again the remaining partition function of the bath's equilibrium and $\hat{n}_j$ the respective number operator of the jth harmonic bath oscillator. With this clear recipe the relevant system dynamics can be isolated. Due to the applied projection the fluctuation operator becomes a stochastic process defined by its moments. In order to determine the complete stochastic behavior of the fluctuations, one would have to know all its moments or its respective characteristic (or moment generating) function [90]

$$\mathcal{C}_F(k,t) = \sum_{n=1}^{\infty}\frac{(\mathrm{i}k)^n}{n!}\langle\hat{F}^n(t)\rangle, \tag{1.57}$$

At the first glance this might seem extremely cumbersome. Fortunately, $\hat{F}(t)$, as stated in equation (1.46), contains only the free position and momentum operators acting on the bath's degrees of freedom. When rewriting the fluctuation into annihilation and creation operators of the bath modes, we find

$$\hat{F}(t) = \sum_j c_j\hat{a}_j + c_j^*\hat{a}_j^\dagger, \tag{1.58}$$

with $c_j = \exp(-\mathrm{i}\omega_j t)\sqrt{\hbar\omega_j^3 m_j/2}$. Calculating the moments of the fluctuation now leads to a Gaussian statistic. Conveniently, this can be shown by tracing over the basis of all number states which immediately yields zero for all odd moments. The second moment is directly proportional to the number operator and all higher even moments of the order N can be represented by a superposition of $\hat{n}_j^i$ with $i = 1, \cdots, N/2$, or in other words, all higher even moments are represented by the second moment. Thus, one only needs to know the second moment and can derive the complete stochastic behavior of $\hat{F}$. Fortunately, the second moment is actually already known via the fluctuation-dissipation theorem in equation (1.53). Thus, solely the friction kernel $\mu(\omega)$ is needed to provide all information to fully characterize the stochastic process experienced by the system. At this point, we like to stress the assumption we made concerning the relaxation time of the bath and the system. If we cannot separate the timescales by the relation $\tau_S \gg \tau_B$, the back-action of the bath will become important, and we need to take care of the actual full equilibrium. Moreover, the simple Gaussian behavior is lost. However, in the scope of this thesis, we remain within the preceding assumptions which yields the very strong connection between the stochastic behavior of $\hat{F}$ and the knowledge about the dissipation $\mathrm{Im}\{\mu\}$. Besides referring to μ as friction kernel, the name "memory kernel" is also frequently used in the literature. This name becomes evident when translating the connection derived with the fluctuation-dissipation theorem (see equation (1.53)) back into time domain.

Memory Kernel

Assuming for a moment the classical limit ($\hbar\omega \ll k_\mathrm{B}T$) of the fluctuation-dissipation theorem[6]

$$S_{FF}(\omega) \overset{\hbar\omega \ll k_\mathrm{B}T}{=} \frac{\mathrm{Im}\left[\mathrm{i}\mu(\omega)\right]}{\pi\beta}, \tag{1.60}$$

and transforming back to time domain

$$\langle \hat{F}(0)\hat{F}(\tau)\rangle = \int \mathrm{d}\omega\, \underline{S}_{FF}(\omega) e^{-\mathrm{i}\omega\tau} \overset{\hbar\omega \ll k_\mathrm{B}T}{=} 2k_\mathrm{B}T \int \frac{\mathrm{d}\omega}{2\pi} \mathrm{Re}\left[\mu(\omega)\right] e^{-\mathrm{i}\omega\tau} \tag{1.61}$$

we notice, that μ completely governs how fluctuations separated by a time span τ are correlated. Since in the classical regime, we do not have the non-commutative algebra of quantum mechanics, the result becomes more evident for the symmetric correlator

$$\frac{1}{2}\left\langle \hat{F}(0)\hat{F}(\tau) + \hat{F}(\tau)\hat{F}(0)\right\rangle \overset{\text{classic}}{=} 2k_\mathrm{B}T\mu(\tau). \tag{1.62}$$

In other words, one could say that $\mu(t)$ encodes the memory of the bath coupled to the system. Most often, since the dynamics of the coupled bath evolve much faster than the dynamics of the system, authors (for example see [58, 82, 91]) assume an Ohmic[7] memory kernel, i.e. $\mu(\omega) = \mathrm{const.}$, which yields to the correlation being a delta peak at zero time difference between t and t'. These systems are called Markovian, which denotes a system that encounters a bath without memory. The name stems from the Markov approximation in the corresponding master equation and is named after Andrey Markov, who investigated memoryless stochastic processes [92]. Hence, when investigating classical stochastic processes the words 'Ohmic' and 'Markovian' are commonly used as interchangeable concepts. However, when going back to the quantum realm, we cannot not use 'Ohmic' equal to 'Markovian'. Even without memory ($\mu(\omega) = \gamma = \mathrm{const.}$) quantum fluctuations are inherently non-Markovian

$$\frac{1}{2}\left\langle \hat{F}(0)\hat{F}(\tau) + \hat{F}(\tau)\hat{F}(0)\right\rangle = k_\mathrm{B}\gamma \frac{\mathrm{d}}{\mathrm{d}\tau} \coth\left[\frac{\tau\pi k_\mathrm{B}T}{\hbar}\right] \tag{1.63}$$

This is a compulsory consequence of the uncertainty relation between time and frequency. If the temperature is high compared to the relevant frequencies, or the considered characteristic time span τ_ch is much smaller than $\hbar/(k_\mathrm{B}T)$, we can retrieve the classical Markovian result as we did in equation (1.62).

Finally, we like to point the interested reader to further highly fascinating topics which were

[6] In many textbooks the transition from quantum to classical is performed by the formal limit $\hbar \to 0$. This is not a proper limit, since $\hbar$ is not a simple number, but connected to units. Thus, the proper limit in this case would be $\hbar\omega\beta \ll 1$. By using de l'Hôspital's rule we therefore obtain

$$\frac{\hbar\beta\omega}{1-\exp(-\hbar\beta\omega)} \overset{\hbar\beta\omega \ll 1}{\sim} 1. \tag{1.59}$$

[7] The 'Ohmic' assumption relies on a damping force being linearly proportional to the instant velocity. The name refers to Ohm's law of electricity on which the first fluctuation-dissipation theorem by Nyquist [66] is based on.

excluded from the previous discussion. Extensions to the concepts introduced often suffer from "subtleties and pitfalls" [92, 93] when pushing towards e.g. non-linearity in coupling between the system and bath. But even in the linear regime, it can become challenging when departing from Gaussian fluctuations or white noise [94]. If we are not able to separate the time scales of the bath and system, respectively, we may already encounter relevant inconsistencies when assuming the bath's equilibrium being independent of the coupling terms [87]. This especially has to be treated with care when investigating strong coupling [77]. Also the interpretation within the classical regime can be very challenging [95]. Although many of the mentioned problems may be tackled for special realizations, the question arises: Is it reasonable to separate into system and bath? The more structured/detailed the bath is modeled, the more we depart from the initial effective description. Notwithstanding, there is a lot of fascinating physics within the above mentioned extensions.

Recap: In this section we demonstrated the paradigmatic shift from closed to open systems, which yields to the separation of a total system into a *system* and an *environment/bath*. By employing the independent oscillator model we derived the quantum Langevin equation, which shows prominently the impact of the environment on the system in the form of a fluctuation force and a memory kernel. Using the fluctuation-dissipation theorem of the previous section, we demonstrated the connection between the fluctuation force and the memory kernel. Finally, we analyzed some properties of the fluctuation and highlighted further paths, when turning towards a more complex interplay of the environment and the system.

1.3 Electromagnetic Fluctuation Theory

As the last two sections introduced general concepts independent of an actual physical setting, this section is about to provide that missing context in form of macroscopic (quantum) electrodynamics. First, we start by introducing the general classic concepts of macroscopic medium-assisted fields. Within this framework, we point out a consistent incorporation of losses and field fluctuations. Second, we employ the fluctuation-dissipation theorem to join the macroscopic theory with a quantum statistical description.

Classical Electrodynamics

We begin with the formulation of the microscopic Maxwell's equations in the SI unit system

Microscopic Maxwell's Equations

$$\nabla \cdot \mathbf{e}(\mathbf{r},t) = \frac{\varrho(\mathbf{r},t)}{\epsilon_0}, \quad \nabla \cdot \mathbf{b}(\mathbf{r},t) = 0, \tag{1.64}$$

$$\nabla \times \mathbf{e}(\mathbf{r},t) = -\partial_t\, \mathbf{b}(\mathbf{r},t), \quad \nabla \times \mathbf{b}(\mathbf{r},t) = \mu_0 \Big(\mathbf{j}(\mathbf{r},t) + \epsilon_0 \partial_t\, \mathbf{e}(\mathbf{r},t) \Big), \tag{1.65}$$

where $\mathbf{e}$ is the microscopic electric field and $\mathbf{b}$ the microscopic magnetic (induction) field, ϱ is the charge density and $\mathbf{j}$ the current density [96]. The charge and current density can be expressed through the elemental charges q_i, their corresponding position $\mathbf{r}_i$ and velocity $\mathbf{v}_i$

$$\varrho(\mathbf{r},t) = \sum_i q_i \delta(\mathbf{r}_i(t) - \mathbf{r}), \quad \mathbf{j}(\mathbf{r},t) = \sum_i q_i \mathbf{v}_i(t)\, \delta(\mathbf{r}_i(t) - \mathbf{r}). \tag{1.66}$$

Here, ϵ_0 is the vacuum permittivity and μ_0 the vacuum permeability, which are connected to the speed of light via $c = (\mu_0 \epsilon_0)^{-1/2}$. The $\nabla = (\partial_x\,, \partial_y\,, \partial_z\,)^\intercal$ operator contains the spatial derivatives. Furthermore, the microscopic electric and magnetic field can be expressed as

$$\mathbf{e}(\mathbf{r},t) = -\nabla\varphi(\mathbf{r},t) - \frac{\partial \mathbf{a}(\mathbf{r},t)}{\partial t} \quad \text{and} \quad \mathbf{b}(\mathbf{r},t) = \nabla \times \mathbf{a}(\mathbf{r},t), \tag{1.67}$$

with the electric scalar potential φ and the magnetic vector potential $\mathbf{a}$. Since the correspondence between the potentials and the fields is not unique, one requires a gauge in order to fix the potentials. We employ the widely used Coulomb gauge ($\nabla \cdot \mathbf{a} = 0$) [96, 97]. It is noteworthy that the Coulomb gauge is only a gauge fixing condition and not a full gauge condition, since further residual gauge transformation via an arbitrary scalar ψ field are possible ($\mathbf{a} \to \mathbf{a}' = \mathbf{a} + \nabla\psi$ and $\varphi \to \varphi' = \varphi - \frac{1}{c}\partial_t \psi$, where $\nabla^2 \psi = 0$). Within the Coulomb gauge, one obtains the solutions for the potentials [96]

$$\varphi(\mathbf{r},t) = \frac{1}{4\pi\epsilon_0} \int \frac{\varrho(\mathbf{r}',t)}{|\mathbf{r}-\mathbf{r}'|} \mathrm{d}^3\mathbf{r}', \tag{1.68}$$

$$\mathbf{a}(\mathbf{r},t) = \frac{1}{4\pi\epsilon_0} \nabla \times \int \left[\int_0^{|\mathbf{r}-\mathbf{r}'|/c} \tau \frac{\mathbf{j}\Big(\mathbf{r}', t-\tau\Big) \times (\mathbf{r}-\mathbf{r}')}{|\mathbf{r}-\mathbf{r}'|^3} \mathrm{d}\tau \right] \mathrm{d}^3\mathbf{r}' \tag{1.69}$$

where the integration over τ considers retardation effects due to the finite speed of light.

While the microscopic Maxwell's equations express the fundamental relations of the electric and magnetic field and charged particles, the described resolution includes too many details for our purpose. We are interested solely in a part of information about the system (e.g. the light propagation through a medium) and are not eager to resolve each and every particle motion in order to obtain the desired result. Thus, we aim to condense the many degrees of freedom of the system down to macroscopically relevant quantities as e.g. refractive indices or reflection coefficients. Hence, we employ macroscopic fields. Macroscopic fields are essentially spatially averages over a volume V of the respective microscopic field [97], i.e.

$$\mathbf{E}(\mathbf{r},t) = \overline{\mathbf{e}(\mathbf{r},t)} = \frac{1}{V(\mathbf{r})}\int_{V(\mathbf{r})} \mathrm{d}^3\mathbf{r}'\, \mathbf{e}(\mathbf{r}',t), \tag{1.70}$$

$$\mathbf{B}(\mathbf{r},t) = \overline{\mathbf{b}(\mathbf{r},t)} = \frac{1}{V(\mathbf{r})}\int_{V(\mathbf{r})} \mathrm{d}^3\mathbf{r}'\, \mathbf{b}(\mathbf{r}',t), \tag{1.71}$$

where the bar indicates the spatial average. Subsequently, the microscopic system is coarse-grained into larger — but macroscopically still small — units. This means that we restrict our description to the system dynamics occurring on a larger length scale than the extent of the unit cell we defined by the coarse-graining. If one desires to resolve finer structures or dynamics, one needs to refine the grains. As such a unit cell or grain, is defined as a macroscopically small but microscopically large volume $V(\mathbf{r})$, which shall be a sphere around the center at $\mathbf{r}$. We assume that the distance between all points $\mathbf{r}'$ (at which we evaluate the fields) and the center $\mathbf{r}$ of the coarse-grained volume $V(\mathbf{r})$ is much larger than the size of the volume, i.e. the radius of the sphere r_V. Thus, we can employ the multipole expansion of the respective fields or potentials [96–98]. Combining these two assumptions (the evaluation of the volume $V(\mathbf{r})$ covers all relevant dynamics, and $|\mathbf{r}' - \mathbf{r}| \gg r_V$) we obtain

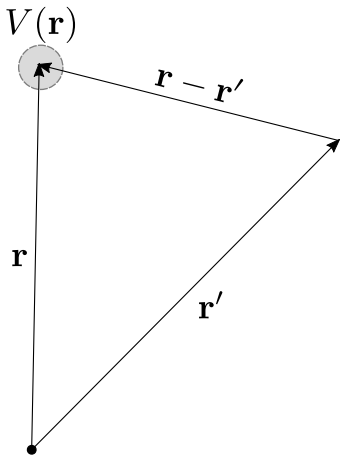

Figure 1.1: The radius of the coarse-grained volume is much smaller than the evaluated distance $|\mathbf{r} - \mathbf{r}'|$. In the limit $r_V \ll |\mathbf{r} - \mathbf{r}'|$ one can apply a multipole expansion.

$$\overline{\varphi(\mathbf{r},t)} = \frac{1}{4\pi\epsilon_0}\int_{V(\mathbf{r})} \mathrm{d}^3\mathbf{r}' \left[\frac{\varrho_{\text{free}}(\mathbf{r}',t)}{|\mathbf{r}-\mathbf{r}'|} + \mathbf{P}(\mathbf{r}',t)\cdot\frac{\mathbf{r}-\mathbf{r}'}{|\mathbf{r}-\mathbf{r}'|^3}\right] + \mathcal{O}\left(\left[\frac{r_V}{|\mathbf{r}-\mathbf{r}'|}\right]^3\right), \tag{1.72}$$

$$\overline{\mathbf{a}(\mathbf{r},t)} = \frac{\mu_0}{4\pi}\int_{V(\mathbf{r})} \mathrm{d}^3\mathbf{r}' \left[\frac{\mathbf{j}_{\text{free}}(\mathbf{r}',t)}{|\mathbf{r}-\mathbf{r}'|} + \mathbf{M}(\mathbf{r}',t)\times\frac{\mathbf{r}-\mathbf{r}'}{|\mathbf{r}-\mathbf{r}'|^3}\right] + \mathcal{O}\left(\left[\frac{r_V}{|\mathbf{r}-\mathbf{r}'|}\right]^3\right), \tag{1.73}$$

where the free charge and current density ϱ_{free} and $\mathbf{j}_{\text{free}}$ and the macroscopic polarization and

magnetization density $\mathbf{P}$ and $\mathbf{M}$,

$$\varrho_{\text{free}}(\mathbf{r},t) = \frac{1}{V(\mathbf{r})}\sum_{j\in V} q_j, \qquad \mathbf{P}(\mathbf{r},t) = \frac{1}{V(\mathbf{r})}\sum_{j\in V}\mathbf{r}_j q_j, \tag{1.74}$$

$$\mathbf{j}_{\text{free}}(\mathbf{r},t) = \frac{1}{V(\mathbf{r})}\sum_{j\in V} q_j\mathbf{v}_j, \quad \mathbf{M}(\mathbf{r},t) = \frac{1}{V(\mathbf{r})}\sum_{j\in V}\frac{q_j}{2}(\mathbf{r}_j\times\mathbf{v}_j), \tag{1.75}$$

were introduced. Each quantity above is an average over elemental charges q_j, currents $\mathbf{j}_j = q_j\mathbf{v}_j$, electric dipoles $\mathbf{p}_j = \mathbf{r}_j q_j$ and magnetic dipoles $\mathbf{m}_j = (\mathbf{r}_j\times\mathbf{v}_j)q_j/2$ contained within the coarse-grained volume respectively. Further, we omitted retardation effects, i.e. neglecting time scales smaller than $|\mathbf{r}-\mathbf{r}'|/c$. With this graining approach, we can reformulate Maxwell's equations in a macroscopic fashion

Macroscopic Maxwell's Equations

$$\nabla\cdot\mathbf{D}(\mathbf{r},t) = \varrho_{\text{free}}(\mathbf{r},t), \quad \nabla\cdot\mathbf{B}(\mathbf{r},t) = 0, \tag{1.76}$$

$$\nabla\times\mathbf{E}(\mathbf{r},t) = -\partial_t\mathbf{B}(\mathbf{r},t), \quad \nabla\times\mathbf{H}(\mathbf{r},t) = \mathbf{j}_{\text{free}}(\mathbf{r},t) + \partial_t\mathbf{D}(\mathbf{r},t). \tag{1.77}$$

Here, $\mathbf{D}$ the displacement and $\mathbf{H}$ the magnetizing field, with

$$\mathbf{D}(\mathbf{r},t) = \epsilon_0\mathbf{E}(\mathbf{r},t) + \mathbf{P}(\mathbf{r},t), \quad \mathbf{H}(\mathbf{r},t) = \frac{1}{\mu_0}\mathbf{B}(\mathbf{r},t) - \mathbf{M}(\mathbf{r},t), \tag{1.78}$$

were introduced in order to obtain similarly structured equations as for the microscopic case in equations (1.64) and (1.65). The macroscopic Maxwell's equations govern the macroscopic medium assisted propagation of the electromagnetic field. Combining equations (1.76) and (1.77) yields

$$\nabla\times\nabla\times\mathbf{E}(\mathbf{r},t) + \frac{1}{c^2}\partial_t^2\mathbf{E}(\mathbf{r},t) = -\mu_0\partial_t\left[\mathbf{j}_{\text{free}}(\mathbf{r},t) + \nabla\times\mathbf{M}(\mathbf{r},t) + \partial_t\mathbf{P}(\mathbf{r},t)\right], \tag{1.79}$$

$$\nabla\times\nabla\times\mathbf{B}(\mathbf{r},t) + \frac{1}{c^2}\partial_t^2\mathbf{B}(\mathbf{r},t) = \mu_0\nabla\times\left[\mathbf{j}_{\text{free}}(\mathbf{r},t) + \nabla\times\mathbf{M}(\mathbf{r},t) + \partial_t\mathbf{P}(\mathbf{r},t)\right], \tag{1.80}$$

Linear Response

which correspond to the equations of motion of the electromagnetic fields. However, in order to obtain a full solution also the equations of motion of the matter have to be considered. Once the equations of motion of the matter are solved with respect to the electromagnetic quantities, we are able to express the motion of the particles and thus ϱ_{free}, $\mathbf{j}_{\text{free}}$, $\mathbf{P}$ and $\mathbf{M}$ as functions of the macroscopic electric and magnetic field. Details on the description of the matter are given in section 2.4. We assume that the macroscopic electromagnetic fields acting as a small perturbation on the matter dynamics. Therefore, we can apply a perturbation approach to the quantities of interest and truncate at the linear term with respect to the electromagnetic field. The accuracy of this description strongly depends on the field strength and the matter dynamics. Nonetheless, for many materials the linear response description already yields very

accurate results [99]. Deviation in form of nonlinear contributions are vividly discussed in the literature [65, 100–105]. However, relevant nonlinear contributions most often rely on extreme intensity of the electromagnetic field, which are not of concern within the investigated setup of the current thesis and thus are not considered. In addition, we focus on neutral matter grains ($\varrho_{\text{free}} = 0$) and assume that magnetization effects can be neglected ($\mathbf{M} = 0$). Thus, we only have to expand the macroscopic polarization and free current density in response to the electric field[8]. Employing the definitions of $\mathbf{P}$ and $\mathbf{j}_{\text{free}}$, reveals the connection $\partial_t \mathbf{P} = \mathbf{j}_{\text{free}}$. Therefore, the response of $\mathbf{P}$ and $\mathbf{j}_{\text{free}}$ can be described analogously and $\mathbf{j}_{\text{free}}$ can be absorbed into $\mathbf{P}$, i.e. $\mathbf{j}_{\text{free}} + \partial_t \mathbf{P} \rightarrow \partial_t \mathbf{P}$. Assuming a weak coupling to the electromagnetic field, one finds the perturbation series

$$\mathbf{P}(\mathbf{r}, t) = \mathbf{P}_0(\mathbf{r}, t) + \epsilon_0 \int_{-\infty}^{t} \mathrm{d}t' \int \mathrm{d}^3\mathbf{r}' \underline{\chi}(\mathbf{r}, \mathbf{r}', t - t') \cdot \mathbf{E}(\mathbf{r}', t') + \mathcal{O}(|\mathbf{E}|^2), \tag{1.81}$$

with $\mathbf{P}_0$ representing the free fields — i.e. being independent of $\mathbf{E}$ — and the response tensor $\underline{\chi}$. The matter is assumed to be in a stationary state. In order to receive a suitable expression for the homogeneous part of the differential equation (1.79), the permittivity tensor is introduced

$$\underline{\epsilon}(\mathbf{r}, \mathbf{r}', \omega) \equiv \mathbb{1}\, \delta^{(3)}(\mathbf{r} - \mathbf{r}') + \underline{\chi}(\mathbf{r}, \mathbf{r}', \omega). \tag{1.82}$$

Combining the above assumptions and expressions, we arrive at the following partial differential equation in frequency domain

$$\nabla \times \nabla \times \mathbf{E}(\mathbf{r}, \omega) - \frac{\omega^2}{c^2} \int_V \mathrm{d}^3\mathbf{r}' \underline{\epsilon}(\mathbf{r}, \mathbf{r}', \omega) \cdot \mathbf{E}(\mathbf{r}', \omega) = \frac{\omega^2}{\epsilon_0 c^2} \mathbf{P}_0(\mathbf{r}, t). \tag{1.83}$$

This inhomogeneous linear differential equation can be solved by the Green's tensor formalism as done in many textbooks [96, 97]. We construct the electric Green's tensor via the differential equation[9]

$$\nabla \times \nabla \times \underline{G}(\mathbf{r}, \mathbf{r}', \omega) - \frac{\omega^2}{c^2} \int \mathrm{d}^3\mathbf{r}'' \underline{\epsilon}(\mathbf{r}, \mathbf{r}'', \omega) \cdot \underline{G}(\mathbf{r}'', \mathbf{r}', \omega) = \frac{\omega^2}{\epsilon_0 c^2} \mathbb{1}\, \delta^{(3)}(\mathbf{r} - \mathbf{r}'). \tag{1.85}$$

Similarly, we find a partial differential equation for the magnetic Green's tensor. The detailed construction of the Green's tensor is postponed to chapter 2. Nevertheless, we can formally write down the solution of the electric field simply by the convolution of the free polarization

[8] Since $\mathbf{E}$ and $\mathbf{B}$ are closely related, it is sufficient to choose one of them for the expansion.

[9] At this point we may have to remember, that there are various definitions of Green's tensors in the context of Maxwell's equations. In the above definition in equation (1.85), the electric field created by a polarization density reads

$$\mathbf{E}(\mathbf{r}, t) = \int_{-\infty}^{t} \mathrm{d}t' \int \mathrm{d}^3\mathbf{r}'\, \underline{G}(\mathbf{r}, \mathbf{r}', t - t') \mathbf{P}(\mathbf{r}', t') \tag{1.84}$$

This form is quite convenient in our calculations. In other contexts, the quantity of concern is maybe not a polarization density, but a current density. In order to obtain the same form as in equation (1.85) — but instead convolute with the current — we simply need to scale the Green's tensor by the factor $-\mathrm{i}\omega$, since $\mathbf{j}_{\text{free}}(\mathbf{r}, \omega) = -\mathrm{i}\omega \mathbf{P}(\mathbf{r}, \omega)$. Both, or even other scaling choices, are equally valid and can be chosen to shorten the notation.

density and the Green's tensor[10]

$$\mathbf{E}(\mathbf{r},t) = \int_{-\infty}^{t} \mathrm{d}t' \int \mathrm{d}^3\mathbf{r}'\, \underline{G}(\mathbf{r},\mathbf{r}',t-t') \cdot \mathbf{P}_0(\mathbf{r}',t'). \tag{1.86}$$

By substituting the above equation into the Maxwell–Faraday equation, we can derive the magnetic field as follows

$$\mathbf{B}(\mathbf{r},t) = \int \frac{\mathrm{d}\omega}{2\pi} \frac{e^{-\mathrm{i}\omega t}}{\mathrm{i}(\omega + \mathrm{i}0^+)} \nabla \times \mathbf{E}(\mathbf{r},\omega) \tag{1.87}$$

$$= \int \frac{\mathrm{d}\omega}{2\pi} \frac{e^{-\mathrm{i}\omega t}}{\mathrm{i}(\omega + \mathrm{i}0^+)} \nabla \times \int \mathrm{d}^3\mathbf{r}'\, \underline{G}(\mathbf{r},\mathbf{r}',\omega) \cdot \mathbf{P}_0(\mathbf{r}',\omega) \tag{1.88}$$

Noise Fields

where the $\mathrm{i}0^+$ ensures causality. Combining all the information above, we formally solved the classic electrodynamic problem. At this point, we emphasize the appearance of a field independent polarization density $\mathbf{P}_0$. Why should there be any fields independent of the electric or magnetic field? $\mathbf{P}_0$ becomes fundamentally important, when investigating open systems. In electrodynamics one is often confronted with losses, e.g. in reflection or transmission processes at or through a material. "Losses" refer to other degrees of freedom, which are not part of our investigated system (in this case the dynamics of the electromagnetic radiation). Consequently, as done in section 1.2 a bath or environment has to be introduced. The fluctuations, stemming from a physical region not accessible to the system, are represented by the zeroth term of the perturbation series of equation (1.81) and are a consequence of the open quantum system description. In order to emphasize this relation, we relabel the free polarization density as noise polarization density

$$\mathbf{P}_\mathrm{N}(\mathbf{r},t) \equiv \mathbf{P}_0(\mathbf{r},t). \tag{1.89}$$

The consequence of having a noise polarization density when treating losses was introduced by Rytov [48]. The noise introduces a stochastic process into the deterministic equations. In order to evaluate the electric field a "measuring" or time-wise averaging process has to be introduced. Again, not all dynamics of the matter shall be resolved, but rather the effective relevant information with respect to the system. Similar to the spatial graining of the matter, one can also apply a similar approach in time. Fragmenting time in larger bits is a very subtle process and by no means unique [95]. We express this "time graining" formally as $\langle \cdots \rangle_{\Delta t}$, where Δt shall be the time scale on which we measure the system dynamics. Thus, the measured result can be expressed with respect to the electric field as the electric noise field generated by the noise of the polarization density

$$\langle \mathbf{E}_\mathrm{N}(\mathbf{r},\omega) \rangle_{\Delta t} = \int \mathrm{d}^3\mathbf{r}'\, \underline{G}(\mathbf{r},\mathbf{r}',t) \cdot \langle \mathbf{P}_\mathrm{N}(\mathbf{r}',\omega) \rangle_{\Delta t}. \tag{1.90}$$

The Green's tensor, which is already formulated on the time scale of the system dynamics,

[10] At this point it is worth noting that it can be problematic to evaluate the Green's tensor at $\mathbf{r} = \mathbf{r}'$ due to its singular behavior. We comment on this when we are constructing the actual Green's tensor in section 2.3.

remains untouched by this averaging process. The dynamics happening on a shorter time scale than Δt are not resolved directly, but rather their averaged effect is sensed on the grained time-scale. For convenience, we assume $\langle \mathbf{E}_\mathrm{N} \rangle_{\Delta t} = \langle \mathbf{P}_\mathrm{N} \rangle_{\Delta t} = 0$. From an experimental point of view, one could also state that the measuring apparatus is calibrated by subtracting the noise off-set ($\hat{\mathbf{P}}_\mathrm{N} \to \hat{\mathbf{P}}_\mathrm{N} - \langle \hat{\mathbf{P}}_\mathrm{N} \rangle_{\Delta t}$). This does by no means state that there is no effect due to fluctuations. Before we investigate the effects of fluctuations more closely, we extend our formalism to the quantum regime.

Quantum Statistics

To perform a consistent transition from classic to quantum, two guiding principles shall be formulated [106]:

1. Validity of Maxwell's equations
2. A system in equilibrium must obey the fluctuation-dissipation theorem

We already relied on the first requirement by deriving all equations up to this point from the laws of electrodynamics. In order to understand the importance of the second requirement, we recall that the underlying key assumption of the fluctuation-dissipation theorem is that we can find an overall equilibrium. In our specific case, the field+matter system shall be in equilibrium. Thus, the (quantum) fluctuation-dissipation relation with respect to the electric noise field leads to[11]

Electric Noise Field Correlation

$$\langle \hat{\mathbf{E}}_\mathrm{N}(\mathbf{r},\omega)\, \hat{\mathbf{E}}_\mathrm{N}^\intercal(\mathbf{r}',\omega') \rangle = \frac{2\hbar}{1-\exp(-\beta\hbar\omega)} \frac{\underline{G}(\mathbf{r},\mathbf{r}',\omega) - \underline{G}^\dagger(\mathbf{r}',\mathbf{r},\omega)}{2\mathrm{i}} (2\pi)\delta(\omega-\omega'). \tag{1.93}$$

This result coincides with results from the literature [62, 106, 108, 109]. Despite achieving a statement which is also valid for the quantum realm, we refrain from displaying a distinct quantization here but refer to other authors [110–114]. Nonetheless, the result in equation (1.93) covers the correct statistics from the quantum to the classic regime [115]. In the very same manner, one can also extract the magnetic noise field correlation. Assuming the response to obey reciprocity, i.e. $\underline{G}(\mathbf{r},\mathbf{r}',\omega) = \underline{G}^\intercal(\mathbf{r}',\mathbf{r},\omega)$, the result of equation (1.93) can be written as

$$\langle \hat{\mathbf{E}}_\mathrm{N}(\mathbf{r},\omega)\, \hat{\mathbf{E}}_\mathrm{N}^\intercal(\mathbf{r}',\omega') \rangle = \frac{2\hbar}{1-\exp(-\beta\hbar\omega)} \mathrm{Im}\{\underline{G}(\mathbf{r},\mathbf{r}',\omega)\} (2\pi)\delta(\omega-\omega'). \tag{1.94}$$

In the case of three-dimensional homogeneous media, i.e. $\underline{G}(\mathbf{r},\mathbf{r}',\omega) = \underline{G}(\mathbf{r}-\mathbf{r}',\omega)$, one finds

[11] The connection to the spatial dependence can be shown by harnessing the space independent operator notation of the Green's tensor and the electric field [107]. The eigenvectors of the spatial coordinate can be written in bra-ket notation

$$\langle \mathbf{r}|\hat{\underline{G}}(\omega)|\mathbf{r}'\rangle = \underline{G}(\mathbf{r},\mathbf{r}',\omega), \tag{1.91}$$

$$\langle \mathbf{r}|\hat{\mathbf{E}}(\omega)|\mathbf{r}'\rangle = \langle \mathbf{r}|\mathbf{r}'\rangle \hat{\mathbf{E}}(\omega,\mathbf{r}') = \delta(\mathbf{r}-\mathbf{r}')\hat{\mathbf{E}}(\omega,\mathbf{r}'). \tag{1.92}$$

In this spatially independent formulation one can directly apply the fluctuation-dissipation theorem and afterwards project onto the spatial representation. After inserting a $1 = \int \mathrm{d}^3\mathbf{r}''|\mathbf{r}''\rangle\langle\mathbf{r}''|$ between the electric field operators and collapsing the integral due to the delta distribution, one obtains equation (1.93).

in the wavevector domain with $\mathbf{K} = (k_x,\, k_y,\, k_y)^\intercal$

$$\langle \hat{\mathbf{E}}_\mathrm{N}(\mathbf{K},\omega)\, \hat{\mathbf{E}}_\mathrm{N}^\intercal(\mathbf{K}',\omega')\rangle = \frac{2\hbar}{1-\exp(-\beta\hbar\omega)}\underline{G}_{\Im}(\mathbf{K},\omega)(2\pi)\delta(\omega-\omega')(2\pi)^3\delta(\mathbf{K}+\mathbf{K}'). \tag{1.95}$$

Recap: After a brief introduction into microscopic and macroscopic Maxwell's equations, we solved the latter by employing linear response theory and the Green's tensor technique. By doing so, we recovered the noise polarization density $\hat{\mathbf{P}}_\mathrm{N}$ which yields medium assisted fluctuations of the electromagnetic field. Finally, by solely relying on the validity of Maxwell's equations and the fluctuation-dissipation theorem we connected the autocorrelation of the electric noise field $\hat{\mathbf{E}}_\mathrm{N}$ to the Green's tensor and obtained the final result of this section in equation (1.93) (or in equations (1.94) and (1.95) depending on the material properties).

CHAPTER 2

Setup and Models

In this chapter we introduce the investigated setup. It consists, as illustrated in figure 2.1, of a charge neutral microscopic object, e.g. an atom, molecule or nanoparticle, moving through vacuum above a macroscopic non-magnetic flat surface. The microscopic object keeps a constant height z_a to the surface and moves with constant velocity v (without loss of generality) along the x axis. In section 2.1 we briefly outline the forces acting on a neutral microscopic object mediated by the electromagnetic field, i.e. dispersion forces. These forces can be identified as the averaged Lorentz force acting on the microscopic object. Within the sketch of figure 2.1 we identify three sub-systems and their respective interaction with each other: the microscopic object, the macroscopic surface and the electromagnetic fields. First, we have to choose a concrete microscopic object and model its internal dynamics. This is done in section 2.2, discussing different models used for a broad class of objects. Second, we specify the material model of the macroscopic surface and its interaction with the electromagnetic field. Before investigating the actual material models of a finitely extended body, we first address the impact of geometry in section 2.3. We briefly explain, how the dielectric functions of infinitely extended materials can be used for describing the response of finitely extended bodies. Furthermore, we elucidate how a finite spatial structuring along the z direction influences response quantities as e.g. the reflection coefficient. Finally, in section 2.4 we present the two major material models used in this thesis for infinitely extended materials, i.e. for dielectric and metallic materials.

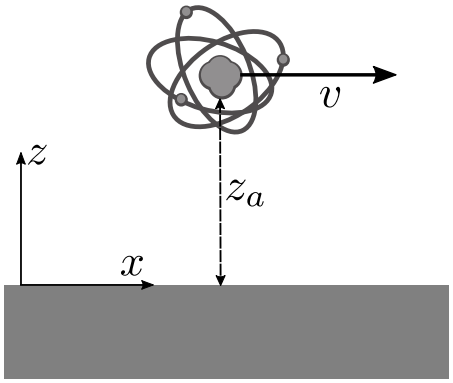

Figure 2.1: A sketch of the setup under investigation: A microscopic object (illustrated as an atom) moving at constant height z_a and with constant velocity v through vacuum and above a flat macroscopic surface.

2.1 Dispersion Forces

The main subject under investigation in this thesis are nonequilibrium dispersion forces[1] . Dispersion forces between electrically neutral objects are mediated by the fluctuations of the electromagnetic fields [116]. The most popular examples are the Casimir force between perfectly conducting plates [18] and the Casimir-Polder force. With the latter acting either between a neutral atom and — as initially calculated by Casimir and Polder — a perfectly conducting plate, or between two neutral atoms. The investigations of the force between two atoms are based on the work of London and van der Waals [15–17, 117]. Since the chosen setup (see figure 2.1) contains a neutral microscopic object and a macroscopic surface the phenomena we are interested in are highly related to the Casimir-Polder force. Nevertheless, there is a crucial property which keeps the system apart from the one studied by Casimir, Polder and many other authors [39, 118–122]. That is the nonequilibrium configuration which is characterizing the system. The detailed effect of the nonequilibrium situation compared to the quasi- and true equilibrium situation is considered in chapter 3. The force acting on a charged particle moving through an electromagnetic field is the well-known Lorentz force. Writing the Lorentz force in terms of charge density ϱ and current density $\mathbf{j}$ we find [96, 97]

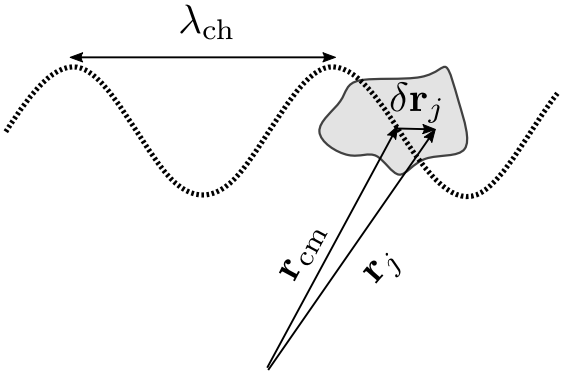

Figure 2.2: Illustration of the length scales within the dipole approximation. The displacement of the jth charge within a small object $\boldsymbol{\delta}\mathbf{r}_j$ is very small compared to the characteristic length scale of the electric field λ_{ch}.

Expansion of the Lorentz force

$$\mathbf{F}(t) = \int \mathrm{d}^3\mathbf{r} \left[\varrho(\mathbf{r},t)\mathbf{E}(\mathbf{r},t) + \mathbf{j}(\mathbf{r},t) \times \mathbf{B}(\mathbf{r},t)\right]. \tag{2.1}$$

Assuming the neutral (with an overall charge $Q = \sum_{j=1}^{N} q_j = 0$) microscopic object consists of N charged particles the densities can be written as

$$\varrho(\mathbf{r},t) = \sum_{j=1}^{N} q_j \delta(\mathbf{r} - \mathbf{r}_j(t)), \quad \mathbf{j}(\mathbf{r},t) = \sum_{j=1}^{N} q_j \mathbf{v}_j(t) \delta(\mathbf{r} - \mathbf{r}_j), \tag{2.2}$$

where $\mathbf{r}_j(t)$ and $\mathbf{v}_j(t)$ are the position and velocity and q_j the charge of the respective jth. In the following, we assume that the charges are rather localized compared to the characteristic wavelength of the electric field λ_{ch}. That means that the deviations $|\boldsymbol{\delta}\mathbf{r}_j|$ of the charges from

[1] The name *dispersion effect* or *dispersion force* was coined by London [16]. He realized that a static polarizability is not sufficient to describe these effects, but that one needs to know the contribution of the different frequency modes to the perturbation onto a neutral object. Thus, with dispersion being the dependence of a quantity on frequency, led to the name *dispersion effect*.

the microscopic object's center of mass, i.e.

$$\mathbf{r}_j(t) = \mathbf{r}_{\mathrm{cm}}(t) + \boldsymbol{\delta}\mathbf{r}_j(t) \quad \text{with} \quad \mathbf{r}_{\mathrm{cm}}(t) = \sum_{j=1}^{N} \frac{m_j}{M}\mathbf{r}_j(t), \tag{2.3}$$

where $M = \sum_{j=1}^{N} m_j$ and m_j is the respective mass of the charge carrier, are small compared to λ_{ch}. , i.e. $|\boldsymbol{\delta}\mathbf{r}_j| \ll \lambda_{\mathrm{ch}}$. For an illustration see figure 2.2. The corresponding multipole expansion of the electric contribution in equation (2.1) yields

$$\begin{aligned}\sum_{j=1}^{N}\sum_{i=x,y,z} q_j E_i(\mathbf{r}_{\mathrm{cm}} + \boldsymbol{\delta}\mathbf{r}_j, t)\mathbf{e}_i &= \sum_{j=1}^{N}\sum_{i=x,y,z} q_j \nabla E_i(\mathbf{r}_{\mathrm{cm}} + \boldsymbol{\delta}\mathbf{r}_j, t)\Big|_{\boldsymbol{\delta}\mathbf{r}_j=\mathbf{0}} \delta r_j^i + \mathcal{O}\left(\frac{|\boldsymbol{\delta}\mathbf{r}_j|^2}{\lambda_{\mathrm{ch}}^2}\right) \\ &= \sum_{i=x,y,z} d_i \nabla E_i(\mathbf{r}_{\mathrm{cm}}) + \mathcal{O}\left(\frac{|\boldsymbol{\delta}\mathbf{r}_j|^2}{\lambda_{\mathrm{ch}}^2}\right). \end{aligned} \tag{2.4}$$

where $\mathbf{e}_i$ is the respective Cartesian unit vector. The zeroth order has no contribution as long as the sum of all charges is equal to zero[2]. The overall dipole moment $\mathbf{d}$ is the sum of all microscopic dipole moments $\mathbf{d} = \sum_{j=1}^{N} q_j \boldsymbol{\delta}\mathbf{r}_j$. By truncating the series in equation (2.4) at the linear order, we obtain the dipole approximation of the electric contribution to the Lorentz force. In a similar scheme, we can implement the magnetic contribution. In leading order the Lorentz force on a neutral microscopic object is [123, 124]

$$\mathbf{F}(t) \overset{\delta r \ll \lambda_{\mathrm{ch}}}{\approx} \Big[\big(\mathbf{d}(t)\cdot\nabla_{\mathbf{r}}\big)\,\mathbf{E}(\mathbf{r},t) + \dot{\mathbf{d}}(t)\times\mathbf{B}(\mathbf{r},t)\Big]_{\mathbf{r}\to\mathbf{r}_{\mathrm{cm}}(t)}. \tag{2.5}$$

Even though we used a classical derivation, the quantum derivation can be carried out analogously, yielding the same result but the classical quantities replaced by quantum mechanical operators [39, 118]. Subsequently, we omit the magnetic contribution[3,4]

$$\hat{\mathbf{F}}(t) \overset{\delta r \ll \lambda_{\mathrm{ch}}}{\approx} \Big(\hat{\mathbf{d}}(t)\cdot\nabla_{\mathbf{r}}\Big)\,\hat{\mathbf{E}}(\mathbf{r},t)\Big|_{\mathbf{r}\to\mathbf{r}_{\mathrm{cm}}(t)}. \tag{2.6}$$

[2] For a microscopic object with an overall charge $Q \neq 0$ the zeroth order term would not vanish and yields the leading contribution. The resulting phenomenon in the context of a charged particle moving above a neutral macroscopic surface is known as Coulomb drag [2].

[3] Since $\hat{\mathbf{d}}$ and $\hat{\mathbf{E}}$ are operators associated with different Hilbert spaces, they do commute, i.e. $[\hat{d}_i, \hat{E}_j] = 0$. Thus, the ordering of the operators does not influence the end result. However, a different ordering can affect the interpretation of the resulting phenomena. For example considering radiative corrections to the atomic level shifts, Milonni et al. demonstrated [125] that a different ordering of the operators — while yielding the same final results — allows for different interpretations with respect to the origin of radiative corrections.

[4] As presented by Buhmann et al. [118], one can estimate the magnetic contribution to be subleading with respect to the — at least in the nonrelativistic regime — small prefactor v/c. Furthermore, in chapter 3 we demonstrate how a large resistivity, i.e. a low conductivity, of the macroscopic surface beneath the moving microscopic object leads to large values of the noncontact friction. Since we are interested in enhancing the noncontact friction, we preferably study materials with high resistivity. In this case, magnetic contributions can be safely neglected as demonstrated by several authors [126–128].

Here, we did not forget the operator hat over $\mathbf{r}$ or $\mathbf{r}_{\mathrm{cm}}(t)$, but used a semi-classical assumption with respect to the trajectory of the center of mass, i.e. we assumed that the uncertainty of $\mathbf{r}_{\mathrm{cm}}$ cannot be resolved by the characteristic wavelength of the electric field. To obtain a measurable quantity, the expectation value $\mathbf{F}(t) = \langle \hat{\mathbf{F}}(t) \rangle_{\rho(t)}$ with respect to a certain state, defined by the density operator $\hat{\rho}(t)$, has to be calculated. Before we elaborate on the state of the system, we will solve the equations of motion of the time-dependent operators $\hat{\mathbf{d}}(t)$ as well as $\hat{\mathbf{E}}(\mathbf{r}(t), t)$. The latter was already evaluated in chapter 1 by applying the concept of linear response (see section 1.1) and calculating the Green's tensor $\underline{G}$ (see section 1.3). The total electric field can be written as the sum of the free electric field $\hat{\mathbf{E}}_0(\mathbf{r}, t)$, which refers to the field in absence of the microscopic object, and the induced electric field $\hat{\mathbf{E}}_{\mathrm{ind}}(\mathbf{r}, t)$ originating from the dipole moment of the microscopic object

Constructing the total electric field

$$\hat{\mathbf{E}}(\mathbf{r}, t) = \hat{\mathbf{E}}_0(\mathbf{r}, t) + \int_{t_0}^{t} \mathrm{d}t' \, \underline{G}(\mathbf{r}, \mathbf{r}_{\mathrm{cm}}(t'), t - t') \, \hat{\mathbf{d}}(t') = \hat{\mathbf{E}}_0(\mathbf{r}, t) + \hat{\mathbf{E}}_{\mathrm{ind}}(\mathbf{r}, t) \, . \tag{2.7}$$

The setup presented in figure 2.1 is homogeneous and isotropic within the xy-plane. Thus, the Green's tensor's dependence on the spatial coordinates reduces to $\underline{G}(\mathbf{r}, \mathbf{r}', \tau) \to \underline{G}(\mathbf{R} - \mathbf{R}', z, z', \tau)$, where $\mathbf{R} = (x, \, y)^{\intercal}$. The Green's tensor itself has several characteristic properties stemming from basic physical principles. In time domain the Green's tensor obeys causality. Consequently, in frequency domain the Green's tensor is analytic in the upper half of the complex plane and thus fulfills the Kramers-Kronig relation. Using the Kramers-Kronig relation yields the compact form

$$\begin{aligned} \underline{G}(\mathbf{r}', \mathbf{r}', \tau) &= \int \frac{\mathrm{d}\omega}{2\pi} \left[\mathcal{P} \int \frac{\mathrm{d}\nu}{\pi} \frac{\underline{G}_I(\mathbf{r}, \mathbf{r}', \nu)}{\nu - \omega} + \mathrm{i} \underline{G}_I(\mathbf{r}, \mathbf{r}', \omega) \right] e^{-\mathrm{i}\omega\tau} \\ &= 2\mathrm{i} \int \frac{\mathrm{d}\omega}{2\pi} \underline{G}_I(\mathbf{r}, \mathbf{r}', \omega) e^{-\mathrm{i}\omega\tau} \\ &= 2\mathrm{i} \int \frac{\mathrm{d}\omega}{2\pi} \int \frac{\mathrm{d}^2\mathbf{k}}{(2\pi)^2} \underline{G}_{\Im}(\mathbf{k}, z, z', \omega) e^{\mathrm{i}\mathbf{k}^{\intercal}(\mathbf{R} - \mathbf{R}') - \mathrm{i}\omega\tau}, \end{aligned} \tag{2.8}$$

where $\underline{G}_{\Im}(\mathbf{k}, z, z', \omega) = \left[\underline{G}(\mathbf{k}, z, z', \omega) - \underline{G}^{\dagger}(\mathbf{k}, z, z', \omega) \right] / (2\mathrm{i})$. Employing the relation of equation (2.8), the induced part of the electric field can be rewritten as [5]

$$\begin{aligned} \hat{\mathbf{E}}_{\mathrm{ind}}(\mathbf{r}_{\mathrm{cm}}(t), t) = 2\mathrm{i} \int_0^{t - t_0} \mathrm{d}\tau \int \frac{\mathrm{d}\omega}{2\pi} \int \frac{\mathrm{d}^2\mathbf{k}}{(2\pi)^2} \underline{G}_{\Im}(\mathbf{k}, z_a, z_a, \omega) \hat{\mathbf{d}}(t - \tau) \\ \times \exp\left[\mathrm{i}\mathbf{k}^{\intercal} (\mathbf{R}_{\mathrm{cm}}(t) - \mathbf{R}_{\mathrm{cm}}(t - \tau)) - \mathrm{i}\omega\tau \right] \end{aligned} \tag{2.9}$$

$$= \hat{\mathbf{E}}^{\oplus}_{\mathrm{ind}}(\mathbf{r}_{\mathrm{cm}}(t), t) \, + \, \hat{\mathbf{E}}^{\ominus}_{\mathrm{ind}}(\mathbf{r}_{\mathrm{cm}}(t), t), \tag{2.10}$$

where the superscript $\oplus$ contains all contributions with $\omega \geq 0$ and $\ominus$ all contributions with $\omega < 0$. Here, $\hat{\mathbf{E}}^{\ominus}_{\mathrm{ind}}$ is the Hermitian conjugated operator to its $\oplus$ counterpart. Analogously to

[5] Here, we used that $\underline{G}^{\dagger}_{\Im} = \underline{G}_{\Im}$ and $\hat{\mathbf{d}} = \hat{\mathbf{d}}^{\dagger}$.

$\hat{\mathbf{E}}^{\oplus}_{\mathrm{ind}}$ one can define

$$\hat{\mathbf{E}}^{\oplus}_{0}(\mathbf{r}_{\mathrm{cm}}(t),t)=\int_0^\infty\frac{\mathrm{d}\omega}{2\pi}\int\frac{\mathrm{d}^2\mathbf{k}}{(2\pi)^2}\hat{\mathbf{E}}_0(\mathbf{k},z_a,\omega)e^{i\mathbf{k}^\intercal\mathbf{R}(t)-i\omega t}. \tag{2.11}$$

Despite the separation in positive and negative frequencies, one has to bear in mind that the motion of the object induces a Doppler shift, which enables a mixing of positive and negative frequency components. In other words, the usual splitting into annihilation and creation operators is the same as in a static case, but the Doppler shift mixes different frequency components. By using equation (2.10) the expectation value of the Lorentz force can be reformulated to

$$\begin{aligned}\mathbf{F}(t)&=\left\langle\left(\hat{\mathbf{d}}^\intercal(t)\nabla_{\mathbf{r}}\right)\hat{\mathbf{E}}^{\oplus}(\mathbf{r}(t),t)+\mathrm{h.c.}\right\rangle_{\rho(t)}\Big|_{\mathbf{r}=\mathbf{r}_{\mathrm{cm}}}\\&=2\mathrm{Re}\left\langle\left(\hat{\mathbf{d}}^\intercal(t)\nabla_{\mathbf{r}}\right)\hat{\mathbf{E}}^{\oplus}(\mathbf{r}(t),t)\right\rangle_{\rho(t)}\Big|_{\mathbf{r}=\mathbf{r}_{\mathrm{cm}}}.\end{aligned} \tag{2.12}$$

If the component perpendicular to the surface $F_\perp$ is calculated, we find the dynamic version of the Casimir-Polder force. The static Casimir-Polder force, i.e. for the case of the microscopic object being at rest, has been investigated massively in the literature [39, 118–122]. The dynamic version, i.e. the case of a moving microscopic object, in Markov approximation was investigated by Scheel and Buhmann [39] and without the Markov assumption by Dedkov and Kyasov [129]. In this thesis we focus on the parallel component $F_\parallel$. Without any static pendant, $F_\parallel$ represents the peculiar and controversially discussed phenomenon of Casimir or quantum friction [29, 57, 130]. Subsequently, $F_\parallel$ shall be reformulated into a more convenient form. The derivative is performed solely in the x direction, but can be carried out analogously in the y direction

Noncontact friction force

$$\begin{aligned}\partial_x\hat{\mathbf{E}}(\mathbf{r}(t),t)=\int\frac{\mathrm{d}\omega}{2\pi}\int\frac{\mathrm{d}^2\mathbf{k}}{(2\pi)^2}\,\mathrm{i}k_x\Big\{&\hat{\mathbf{E}}_0(\mathbf{k},z_a,\omega)e^{\mathrm{i}\mathbf{k}^\intercal\mathbf{R}(t)-\mathrm{i}\omega t}\\&+2\mathrm{i}\int_0^{t-t_0}\mathrm{d}\tau\,\underline{G}_{\Im}(\mathbf{k},z_a,z_a,\omega)\hat{\mathbf{d}}(t-\tau)\,e^{\mathrm{i}\mathbf{k}^\intercal(\mathbf{R}(t)-\mathbf{R}(t-\tau))-\mathrm{i}\omega\tau}\Big\},\end{aligned} \tag{2.13}$$

where we assumed that the object stays at constant height z_a. Further, the trajectory of the object's center-of-mass motion is fixed by $\mathbf{r}_{\mathrm{cm}}(t)\approx\mathbf{r}_{\mathrm{cm}}+\mathbf{v}t$, with an initial position $\mathbf{r}_{\mathrm{cm}}$ and a velocity vector $\mathbf{v}$. Even though there might be transient motions different from this given trajectory, at some point the particle will asymptotically move on the prescribed trajectory[6]. With the assumption of a classical trajectory we find

$$\begin{aligned}\partial_x\hat{\mathbf{E}}(\mathbf{r}(t),t)\Big|_{\mathbf{r}\to\mathbf{r}_{\mathrm{cm}}(t)}=\int\frac{\mathrm{d}\omega}{2\pi}\int\frac{\mathrm{d}^2\mathbf{k}}{(2\pi)^2}\,\mathrm{i}k_x\Big\{&\hat{\mathbf{E}}_0(\mathbf{k},z_a,\omega)e^{\mathrm{i}\mathbf{k}^\intercal(\mathbf{R}_a+\mathbf{v}t)-\mathrm{i}\omega t}\\&+2\mathrm{i}\int_0^{t-t_0}\mathrm{d}\tau\,\underline{G}_{\Im}(\mathbf{k},z_a,z_a,\omega)\hat{\mathbf{d}}(t-\tau)\,e^{\mathrm{i}(\mathbf{k}^\intercal\mathbf{v}-\omega)\tau}\Big\}.\end{aligned} \tag{2.14}$$

[6]This trajectory could be for example realized by an external trap which drags the particle at constant height and velocity over the surface. We expand on this topic in section 2.2.

Substituting the above expression for the x and y component back into equation (2.12) the parallel Lorentz force can be expressed as

Parallel Lorentz Force

$$\mathbf{F}_{\parallel}(t) = 2\mathrm{Re}\Bigg\langle \int_0^\infty \frac{\mathrm{d}\omega}{2\pi} \int \frac{\mathrm{d}^2\mathbf{k}}{(2\pi)^2}\, \mathrm{i}\mathbf{k} \Bigg(\hat{\mathbf{d}}^{\intercal}(t)\hat{\mathbf{E}}_0(\mathbf{k}, z_a, \omega) e^{i\mathbf{k}^{\intercal}(\mathbf{R}_a + \mathbf{v}t) - \mathrm{i}\omega t} + 2\mathrm{i}\int_0^{t-t_0} \mathrm{d}\tau\, \hat{\mathbf{d}}^{\intercal}(t)\underline{G}_{\Im}(\mathbf{k}, z_a, \omega)\hat{\mathbf{d}}(t-\tau)\, e^{\mathrm{i}(\mathbf{k}^{\intercal}\mathbf{v} - \omega)\tau} \Bigg) \Bigg\rangle_{\rho(t)} . \tag{2.15}$$

In order to continue, several quantities have to be specified. On the one hand we need a prescription for the dynamics concerning the dipole moment $\hat{\mathbf{d}}(t)$. And on the other hand, we need to construct the Green's tensor considering the macroscopic surface. This sets the guideline for the following sections.

Recap: Starting from the general Lorentz force acting on a charge and current density, we derived the leading contribution for a small neutral object by the means of its dipole moment in equation (2.5). After omitting the magnetic contribution, we refined our result employing besides the free electric field also the backaction of the dipole moment onto the electric field. Finally, by fixing the microscopic object's trajectory with a constant velocity parallel to the macroscopic surface, we arrived at the final result of this section in equation (2.15), which describes a force acting parallel to the surface onto a moving neutral object.

2.2 Modeling of the Microscopic Object

As described in the introduction of chapter 2, we aim to describe a macroscopically small object interacting with electromagnetic radiation. In the previous section we demonstrated that the light-object interaction in leading order is the electric field acting on the object's dipole moment. This approximation is valid for $\lambda_{\mathrm{ch}} \gg D$, where D is the extension of the object the electric field of a characteristic wavelength λ_{ch} is applied on. For extensions D equal or larger than λ_{ch}, the dipole approximation might not yield a sufficient description and higher orders of the multipole expansion and spatial size effects have to be considered [132]. In the following, we assume the validity of the dipole approximation with respect to the length scale of the electric field. From a microscopic point of view the object consists of N pairwise interacting particles. Omitting for a moment the energy carried by the electric field, the respective Hamiltonian reads

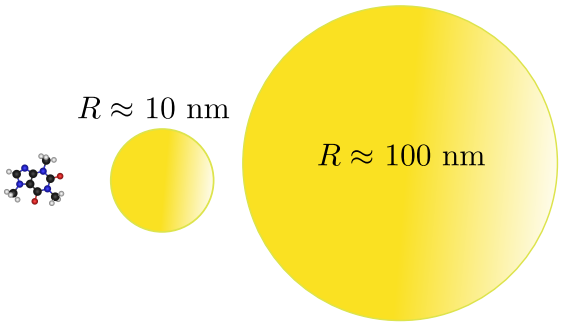

Figure 2.3: Depicted are candidates for the different models introduced within this section. From left to right: Atomic and molecular systems (represented by a caffeine molecule taken from [131]) and two gold spheres with different radii R.

$$\hat{\mathcal{H}} = \sum_{i=1}^{N} \frac{\hat{\mathbf{p}}_i^2}{2m_i} + \sum_{j \neq i} \hat{V}_{ij}(\hat{\mathbf{r}}_i - \hat{\mathbf{r}}_j) - \hat{\mathbf{d}}^{\mathsf{T}}(t)\hat{\mathbf{E}}(\mathbf{r}_{\mathrm{cm}}(t), t)\,, \tag{2.16}$$

with the interaction potential $\hat{V}_{ij}$ between the ith and jth particle. In order to isolate the dynamics of the center of mass, the coordinate system is transformed from a Cartesian to a center of mass coordinate system $\{\mathbf{r}_1, \mathbf{r}_2, \cdots, \mathbf{r}_N\} \rightarrow \{\mathbf{r}_{\mathrm{cm}}, \{\boldsymbol{\rho}_{\mathrm{rel}}\}\}$, where $\{\boldsymbol{\rho}_{\mathrm{rel}}\}$ refers to a complete basis set of relative coordinates perpendicular to $\mathbf{r}_{\mathrm{cm}}$. The construction of such a coordinate system is not unique, however, all possible configurations lead to a splitting of the kinetic energy into

$$\hat{\mathcal{T}} = \sum_{i=1}^{N} \frac{\hat{\mathbf{p}}_i^2(t)}{2m_i} = \frac{\mathbf{p}_{\mathrm{cm}}^2(t)}{2M} + \hat{\mathcal{T}}_{\mathrm{rel}}(\{\hat{\mathbf{p}}_{\mathrm{rel}}\})\,, \tag{2.17}$$

and to the interaction potential depending exclusively on the relative coordinates $\{\boldsymbol{\rho}_{\mathrm{rel}}\}$ [133]. The center of mass' equation of motion is therefore solely determined by the Lorentz force of equation (2.12) by

Center of Mass

$$M\ddot{\mathbf{r}}_{\mathrm{cm}}(t) = \left\langle \left(\hat{\mathbf{d}}^{\mathsf{T}}(t)^{\mathsf{T}} \nabla_{\mathbf{r}}\right) \hat{\mathbf{E}}(\mathbf{r}, t) \right\rangle_{\rho(t)} \Bigg|_{\mathbf{r} \rightarrow \mathbf{r}_{\mathrm{cm}}(t)} = \mathbf{F}(t)\,, \tag{2.18}$$

where $\mathbf{r}_{\mathrm{cm}}$ is assumed to be a classic macroscopic quantity. It is noteworthy, that $\mathbf{F}$ is not a conservative force as lossy systems are considered (for details see chapter 3). However, in section 2.1 we already demanded the trajectory $\mathbf{r}_{\mathrm{cm}}(t) = \mathbf{r}_0 + \mathbf{v}t$, which is the solution to $M\ddot{\mathbf{r}}_{\mathrm{cm}}(t) = 0$ with the boundary conditions $\mathbf{r}_{\mathrm{cm}}(0) = \mathbf{r}_0$ and $\dot{\mathbf{r}}_{\mathrm{cm}}(0) = \mathbf{v}$. In order to achieve this demanded trajectory, the Lorentz force has to be compensated. This can be achieved by introducing an additional external force $\mathbf{F}_{\mathrm{ext}}$, i.e. $\mathbf{F}(t) + \mathbf{F}_{\mathrm{ext}}(t) = 0$. Such an external driving force might be introduced by a magneto-optical trap [134, 135], by a rigid attachment to a cantilever [24], or another external agent. As it is shown in equation (2.18), the Lorentz force is acting on the motion of the center of mass. The force itself depends on the interaction of the dipole moment with the electric field. Thus, it is necessary to model the dynamics of the dipole moment when investigating dispersion forces. As long as the interaction between the dipole moment and the electric field is weak, the linear response of the dipole moment as presented in section 1.1 can be employed. Using equation (1.19) with $\hat{\mathbf{d}}^{\intercal}(t)\hat{\mathbf{E}}(t, \mathbf{r}_{\mathrm{cm}})$ as perturbation of the remaining system we find

Perturbation of the Dipole Moment

$$\langle\hat{\mathbf{d}}\rangle_{\rho(t)} - \langle\hat{\mathbf{d}}\rangle_{\rho(t_0)} \approx \frac{\mathrm{i}}{\hbar}\int_0^{t-t_0} \mathrm{d}\tau\, \epsilon(t-\tau)\Big\langle \hat{\mathbf{E}}^{\intercal}(0, \mathbf{r}_{\mathrm{cm}})\Big\rangle_{\rho(t_0)}\Big\langle \Big[\hat{\mathbf{d}}(0),\, \hat{\mathbf{d}}(\tau)\Big]\Big\rangle_{\rho(t_0)}, \tag{2.19}$$

where $\epsilon(t)$ is the switch, which enables or disables the interaction as explained in section 1.1. Here, the unperturbed initial state at $t = t_0$ of both systems, the microscopic object and the (medium assisted) electromagnetic field, is assumed to be separable in $\rho(t_0) = \rho_{\mathrm{mic}}(t_0) \otimes \rho_{\mathrm{f+m}}(t_0)$, i.e. both system are initially independent of each other. In a next step, we expand with respect to the eigenstates of the object's unperturbed state $|\varepsilon\rangle$ and find

$$\langle\hat{\mathbf{d}}\rangle_{\rho(t)} - \langle\hat{\mathbf{d}}\rangle_{\rho(t_0)} \approx \frac{2\langle\hat{\mathbf{E}}^{\intercal}(\mathbf{r}_{\mathrm{cm}})\rangle_{\rho(t_0)}}{\hbar}\int_0^{t-t_0} \mathrm{d}\tau\ \epsilon(t-\tau)\sum\!\!\!\!\!\!\int_{\varepsilon,\varepsilon'} \Big|\langle\varepsilon|\hat{\mathbf{d}}|\varepsilon'\rangle\Big|^2 \sin\left(\tau\frac{\varepsilon-\varepsilon'}{\hbar}\right)\frac{e^{-\beta\varepsilon}}{\mathcal{Z}}, \tag{2.20}$$

with $\mathcal{Z}$ being the partition function of the equilibrium state. Let ε_0 be the ground state of the unperturbed system. For low temperatures, i.e. $\beta\varepsilon_0 \gg 1$, solely the ground state yields a relevant contribution in the ε summation/integration

$$\langle\hat{\mathbf{d}}\rangle_{\rho(t)} - \langle\hat{\mathbf{d}}\rangle_{\rho(t_0)} \approx \frac{2\langle\hat{\mathbf{E}}^{\intercal}(\mathbf{r}_{\mathrm{cm}})\rangle_{\rho(t_0)}}{\hbar}\int_0^{t-t_0} \mathrm{d}\tau\ \epsilon(t-\tau)\sum\!\!\!\!\!\!\int_{\varepsilon'} \Big|\langle\varepsilon_0|\hat{\mathbf{d}}|\varepsilon'\rangle\Big|^2 \sin\left(\tau\frac{\varepsilon_0-\varepsilon'}{\hbar}\right). \tag{2.21}$$

Thus, the dynamics of the dipole moment — in linear order of the perturbation — follow the movement of a sum (or integral) of harmonic oscillators with frequencies $|\varepsilon_0 - \varepsilon'|/\hbar$ and corresponding transition probabilities $|\langle\varepsilon_0|\hat{\mathbf{d}}|\varepsilon'\rangle|^2$. For simplicity, we assume that the lowest transition ($\varepsilon_0 \leftrightarrow \varepsilon_1$) is dominant. Combining all mentioned approximations, the dynamics of the relative motion in linear order can be approximated as a single driven harmonic oscillator

$$\partial_t^2\hat{\mathbf{d}}(t) + \omega_a^2\hat{\mathbf{d}}(t) = \alpha_0\omega_a^2\hat{\mathbf{E}}(\mathbf{r}_{\mathrm{cm}}, t)\,, \tag{2.22}$$

where $\alpha_0 = \frac{2\hbar}{(\varepsilon_1-\varepsilon_0)^2}\left|\langle\varepsilon_0|\hat{\mathbf{d}}|\varepsilon_1\rangle\right|^2$ is the static polarizability and $\omega_a = (\varepsilon_1-\varepsilon_0)/\hbar$ the transition frequency. In frequency domain we find

$$\hat{\mathbf{d}}(\omega) = \frac{\alpha_0\omega_a^2}{\omega_a^2-\omega^2}\hat{\mathbf{E}}(\mathbf{r}_{\mathrm{cm}},\omega), \tag{2.23}$$

where one has to use $\omega \to \omega + \mathrm{i}0^+$ when applying the inverse Fourier transform in order to ensure causality. Until now, the derived scheme of equation (2.22) is generic for any slightly perturbed dipole moment as e.g. in atom-like or molecular structures with no intrinsic loss channels and a stable groundstate[7,8]. Besides atomic and molecular structures there is a recent intense research activity focusing on nanoparticles. Over the last decade the levitation of dielectric nanospheres surged high interest [142–149]. If a nanoparticle is small compared to the characteristic wavelength of the electromagnetic field $\lambda_{\mathrm{ch}} \gg D$ with D being the diameter of the nanoparticle, its interaction with the electromagnetic field can again be approximated by a dipole moment with the frequency dependent polarizability $\alpha_{\mathrm{NP}}(\omega)$ given by the Clausius-Mossotti relation [96, 150, 151]

Nanoparticles

$$\alpha_{\mathrm{NP}}(\omega) = 3\epsilon_0 V\frac{\epsilon(\omega)-1}{\epsilon(\omega)+2}, \tag{2.24}$$

where V is the volume of the nanoparticle and $\epsilon(\omega)$ a local dielectric function of the material of the nanoparticle[9]. In section 2.4 we show that $\epsilon(\omega)$ and therefore $\alpha_{\mathrm{NP}}(\omega)$ contain losses. As demonstrated in section 1.2, a loss channel inevitably leads to fluctuations stemming from the very same heat bath. Thus, the respective equation of motion of the dipole moment in frequency domain reads

$$\alpha_{\mathrm{NP}}^{-1}(\omega)\hat{\mathbf{d}}(\omega) = \hat{\mathbf{E}}(\omega,\mathbf{r}_{\mathrm{cm}}) + \hat{\mathbf{F}}(\omega), \tag{2.25}$$

where $\hat{\mathbf{F}}(\omega)$ is the fluctuation due to the internal heat bath of the nanoparticle. Furthermore, assuming that the nanoparticle is at equilibrium, we can use equation (1.53) to derive the relation between the polarizability of the nanoparticle and the power spectrum of the autocorrelator of

[7] When considering molecular structures also vibronic degrees of freedom have to be taken into account. Applying the Born-Oppenheimer approximation [136–138], electronic and nuclear motion can be separated due to their tremendous mass difference (for example the ratio of the proton to electron mass is $m_{\mathrm{p}}/m_{\mathrm{e}} = 1836.15$ [139]). In the lowest order Born-Oppenheimer approximation there is no energy transfer between the electronic and nuclear system. Thus, the vibronic degrees of freedom cannot — at this level — be assumed to provide an internal bath. The first corrections to the Born-Oppenheimer approximations are, however, on the order of $(m_{\mathrm{e}}/m_{\mathrm{nuc}})^{1/4} \approx 10^{-1}\cdots 10^{-2}$ [136, 137], where m_{nuc} is the mass of the nucleus.

[8] In atomic systems the extent is usually on the order of the Bohr radius $a_0 \approx 0.53\,\text{Å}$ [139]. As an estimate the model should thus be valid for $\lambda_{\mathrm{ch}} \gg a_0$, but might break down as soon as λ_{ch} approaches a_0 with the characteristic length scale of the electromagnetic field. Molecules can differ strongly in their extension. For example a water molecule has an approximated size of $2.8\,\text{Å}$ [140] whereas a human cell's DNA can stretch out up to meters in length [141].

[9] The Clausius-Mossotti relation can further be refined by extensions as given by Draine [152] considering radiative reaction or by Doyle [153] employing Mie theory. The first extension, however, will be implemented in chapter 3.

the fluctuation force $\hat{\mathbf{F}}$

$$\langle \hat{\mathbf{F}}(\omega)\hat{\mathbf{F}}^{\intercal}(\omega')\rangle_{\rho(t_0)} = \mathbb{1}\delta(\omega+\omega')\frac{4\hbar\pi}{1-\exp(-\beta\hbar\omega)}\frac{\mathrm{Im}\{\alpha_{\mathrm{NP}}(\omega)\}}{|\alpha_{\mathrm{NP}}(\omega)|^2}. \tag{2.26}$$

For simplicity, throughout this thesis we assume no interaction between the internal bath, and the electric field[10]. Defining a new quantity $\mu(\omega)$ as follows

$$\mathrm{Im}\{\mathrm{i}\omega\mu(\omega)\} \equiv \frac{\alpha_0\omega_a^2\mathrm{Im}\{\alpha_{\mathrm{NP}}(\omega)\}}{|\alpha_{\mathrm{NP}}(\omega)|^2}, \qquad \omega_a^2-\omega^2-\mathrm{Re}\{\mathrm{i}\omega\mu(\omega)\} \equiv \frac{\alpha_0\omega_a^2\mathrm{Re}\{\alpha_{\mathrm{NP}}(\omega)\}}{|\alpha_{\mathrm{NP}}(\omega)|^2}, \tag{2.27}$$

where ω_a shall be the dominant resonance frequency of the nanoparticle, the equation of motion of the dipole moment can be rearranged to a Langevin equation

$$\partial_t^2\hat{\mathbf{d}}(t) + \int_{t_{\mathrm{in}}}^{\infty}\mathrm{d}t_1\,\mu(t-t_1)\dot{\hat{\mathbf{d}}}(t) + \omega_a^2\hat{\mathbf{d}}(t) = \alpha_0\omega_a^2\hat{\mathbf{E}}(\mathbf{r}_{\mathrm{cm}}(t),t) + \hat{\mathbf{F}}(t)\,. \tag{2.28}$$

where μ can be interpreted as the memory kernel. Subsequently, we discuss two relevant examples of this memory kernel. Considering that the material of the nanoparticle can be described by the local Drude model $\epsilon(\omega) = 1-\omega_{\mathrm{p}}^2/[\omega(\omega+\mathrm{i}\gamma)]$ (see section 2.4), we find

$$\alpha_{\mathrm{NP}}(\omega) = \frac{\epsilon_0 V\omega_{\mathrm{p}}^2}{\omega_{\mathrm{p}}^2/3-\omega^2-\mathrm{i}\gamma\omega}., \tag{2.29}$$

with $\mathrm{Re}\{\mu(\omega)\}=\gamma$, $\mathrm{Im}\{\mu(\omega)\}=0$, $\omega_a=\omega_{\mathrm{p}}/\sqrt{3}$ and $\alpha_0 = 3\epsilon_0 V$. This phenomenological description coincides with an Ohmic spectral density. If the nanoparticle decreases in size it is known that their memory kernel differs significantly from a simple Ohmic heat bath [155, 156]. Especially the phononic modes of the nanoparticle become increasingly discretized. As a rough estimate, one can show that for spherical nanoparticle with a radius $R = 10\,\mathrm{nm}$ and a speed of sound within the particle's material of $c_{\mathrm{s}} \approx 10^3\,\mathrm{m/s}$ the phononic modes are found at integer multiples of $\omega_{\mathrm{phon}} \approx \pi c_{\mathrm{s}}/R \approx 2\pi\times 10^{11}\,\mathrm{Hz}$ [157]. Recently, López et al. [158] therefore argued to extend the model of an Ohmic heat bath by one additional phononic mode. This additional mode is assumed to couple much stronger to the dipole moment than the other bath modes due to the strong discretization of the phononic modes in very small nanoparticles. Furthermore, due to its weak coupling to the environment the phononic mode is assumed to have a very narrow linewidth γ_{phon} [159]. Employing this minimal model, we obtain the following memory kernel (for a detailed derivation see appendix E)

$$\mu(\omega) = \gamma + \frac{g^2}{\mathrm{i}\omega(\omega_{\mathrm{phon}}^2-\omega^2-\mathrm{i}\omega\gamma_{\mathrm{phon}})} \tag{2.30}$$

where g is the coupling constant between the dipole moment and the phonon mode. Typically, phononic modes are much lower in energy than the dipole resonance of the nanoparticle

[10] An internal bath driven by the electromagnetic field was incorporated by Grabert et al. [154].

$\omega_{\mathrm{phon}} \ll \omega_a$. Moreover, the coupling between the dipole moment and the phononic mode is assumed to be weak, i.e. $g \ll \omega_{\mathrm{phon}}$.

Recap: Throughout this section the microscopic object of the setup illustrated in figure 2.1 was under scrutiny. First, we decoupled the motion of the center of mass from the relative motion. Thereby, we highlighted the impact of the dipole moment's dynamic on the center of mass motion. Second, we discussed several possibilities of modeling the polarizability of the dipole moment. Besides the generic applicability of a harmonic oscillator model for atomic and molecular systems in equation (2.22), we also discussed phenomenological models in order to describe the dipole moment of a nanoparticle in equation (2.28). Lastly, we followed the argumentation of López [158] and presented a modified memory kernel by adding one single phononic mode, which is assumed to have a stronger coupling to the dipole moment than all other bath modes, in equation (2.30).

2.3 Geometry

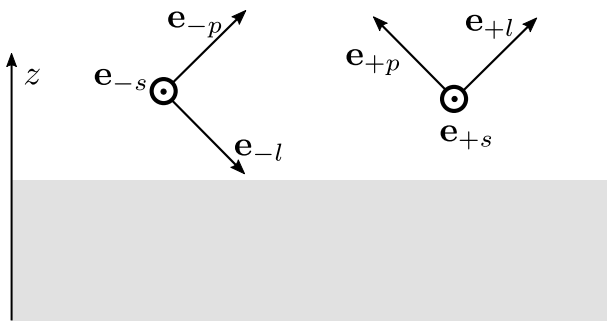

Figure 2.4: A sketch of the polarization basis vector for incident fields (on the left) and reflected fields (on the right) with respect to a flat macroscopic surface (gray area). The sign in the subscript indicates the propagation in z direction.

This section is devoted to the geometrical aspects of electromagnetic response of a macroscopic surface. The general Green's tensor, which was introduced in section 1.3, is refined to the situation of a flat surface. First, the free space Green's tensor is calculated, which then can be used to construct the part scattered by the surface. The latter step is formally done by introducing reflection coefficients. Furthermore, the macroscopic electromagnetic fields at the surface, under the assumption of hard-wall boundaries, are calculated. This enables us to directly derive surface impedances and reflection coefficients from given field ratios. Finally, the scattering and transfer formalism are employed to extend the description to finite single layer and multilayer systems.

Vacuum Green's tensor

As a very first step the free Green's tensor of infinitely extend vacuum is solved. Because of the vacuum being isotropic and homogeneous ($\underline{\epsilon} = \mathbb{1}\delta^{(3)}(\mathbf{r}-\mathbf{r}')$), the respective Green's tensor only depends on the distance between two points in space $\mathbf{r}-\mathbf{r}'$. As the case $\mathbf{r}=\mathbf{r}'$ yields a strong singular behavior, this point is treated separately [160]. In reciprocal space, with the corresponding wavevector $\mathbf{K} = (k_x,\, k_y,\, k_z)^\intercal$ to $\mathbf{r}-\mathbf{r}'$, we find

$$\mathbf{K}\times\mathbf{K}\times\underline{G}_0^{/V_\delta}(\mathbf{K},\omega) - \frac{\omega^2}{c^2}\underline{G}_0^{/V_\delta}(\mathbf{K},\omega) = \frac{\omega^2}{\epsilon_0 c^2}, \tag{2.31}$$

where the superscript $/V_\delta$ indicates that the infinitesimal volume V_δ at $\mathbf{r}=\mathbf{r}'$ is excluded. Using the vector triple product identity $\mathbf{A}\times(\mathbf{B}\times\mathbf{C}) = \mathbf{B}(\mathbf{A}^\intercal\mathbf{C}) - \mathbf{C}(\mathbf{A}^\intercal\mathbf{B})$ leads to

$$\underline{G}_0^{/V_\delta}(\mathbf{K},\omega) = \left(\mathbb{1}\frac{\omega^2}{c^2} - \mathbf{K}\mathbf{K}^\intercal\right)\frac{\epsilon_0^{-1}}{K^2-(\frac{\omega}{c}+\mathrm{i}0^+)^2} \tag{2.32}$$

where the $\mathrm{i}0^+$ ensures causality, and $K^2 = \mathbf{K}^\intercal\mathbf{K}$. In order to obtain the full free space Green's tensor, which is also covering $\mathbf{r}=\mathbf{r}'$, the small volume V_δ around the point source has to be added. This leads to an additional term $\underline{G}_0^{V_\delta}$. The total free space Green's tensor therefore reads

$$\underline{G}_0(\mathbf{r},\mathbf{r}',\omega) = \underline{G}_0^{/V_\delta}(\mathbf{r},\mathbf{r}',\omega) + \underline{G}_0^{V_\delta}(\mathbf{r},\mathbf{r}',\omega). \tag{2.33}$$

A very clear and detailed derivation of $\underline{G}_0^{V_\delta}$ is given in [161]. This term is in general shape-

dependent with respect to δV and can be written as

$$\underline{G}_0^{V_\delta}(\mathbf{r},\mathbf{r}',\omega) = \delta(\mathbf{r}-\mathbf{r}')\int_{\partial V_\delta(\mathbf{r})}\frac{\mathrm{d}^2\mathbf{r}''}{4\pi\epsilon_0}\frac{(\mathbf{r}-\mathbf{r}'')\otimes\mathbf{n}''}{|\mathbf{r}-\mathbf{r}''|^3} = \delta(\mathbf{r}-\mathbf{r}')\underline{\mathcal{S}}_{\partial V_\delta}, \tag{2.34}$$

where $\mathbf{n}''$ is an outward-pointing unit vector normal to the surface ∂V_δ of the infinitesimal volume V_δ. The shape-dependent part is condensed in $\underline{\mathcal{S}}_{\partial V_\delta}$. For instance for a spherical shape one finds $\underline{\mathcal{S}}^{\mathrm{sphere}}_{\partial V_\delta} = \mathbb{1}/(3\epsilon_0)$ [162]. Performing a back transformation with respect to the k_z component leads to a representation with only two dimensions expressed in reciprocal space. The respective integrals can be carried out via the residue theorem. Defining $\kappa = \sqrt{k^2-\omega^2/c^2}$ with $\mathrm{Im}\{\kappa\} < 0$ and $\mathrm{Re}\{\kappa\} > 0$, the enclosing contour in the upper half-plane for $z > 0$ and in the lower half-plane for $z < 0$ with respect to a complex k_z integral yields

$$\begin{aligned}\underline{G}_0(\mathbf{k},z-z',\omega) &= \frac{\omega^2}{\epsilon_0 c^2}\left(\mathbb{1}-\frac{c^2}{\omega^2}\begin{bmatrix}\mathbf{k}\\ \pm\mathrm{i}\kappa\end{bmatrix}\begin{bmatrix}\mathbf{k}^\intercal, & \pm\mathrm{i}\kappa\end{bmatrix}\right)\frac{e^{-\kappa|z-z'|}}{2\kappa} + \delta(z-z')\underline{\mathcal{S}}_{\partial V_\delta}\\ &= \frac{\omega^2}{c^2}\left(\mathbf{e}_s\otimes\mathbf{e}_s + \mathbf{e}_{\pm p}\otimes\mathbf{e}_{\pm p}\right)\frac{e^{-\kappa|z-z'|}}{2\epsilon_0\kappa} + \delta(z-z')\underline{\mathcal{S}}_{\partial V_\delta}\end{aligned} \tag{2.35}$$

where $\mathbf{k} = (k_x, k_y)^\intercal$ relates to $\mathbf{R} = (x-x', y-y')^\intercal$. The unit vectors $\mathbf{e}_{s/\pm p}$ refer to the s (transverse electric) or $\pm p$ (transverse magnetic) polarized radiation. The $\pm$ is connected to the sign of $z-z'$. For $z > z'$, an upward propagation, $+$ and for $z < z'$, a downward propagation, $-$ is used. In detail the unit vectors are

$$\mathbf{e}_s = \frac{\mathbf{k}}{k}\times\frac{\mathbf{z}}{z} = \Big(-\frac{k_y}{k},\ \frac{k_x}{k},\ 0\Big)^\intercal \tag{2.36}$$

$$\mathbf{e}_{\pm p} = \frac{c\kappa}{\omega}\left(\frac{\mathbf{z}}{z}\frac{k}{\kappa}\mp\mathrm{i}\frac{\mathbf{k}}{k}\right) = \frac{c\kappa}{\omega}\Big(\mp\mathrm{i}\frac{k_x}{k},\ \mp\mathrm{i}\frac{k_y}{k},\ \frac{k}{\kappa}.\Big)^\intercal. \tag{2.37}$$

With the additional unit vector $\mathbf{e}_{\pm l} = \mathbf{K}/K|_{k_z=\mathrm{sgn}(z-z')\mathrm{i}\kappa}$ of the longitudinal polarization, the three vectors form an orthogonal basis set with respect to the plane of incidence spanned by $\mathbf{k}$ and $\mathbf{z}$, as illustrated in figure 2.4. Here, $\mathbf{e}_{-s} = \mathbf{e}_{+s} = \mathbf{e}_s$ was used. In vacuum there is no longitudinal polarization as shown by Pieplow et al. [163].

Scattered Green's tensor

To derive the Green's tensor when adding a flat interface to a macroscopic material, one can utilize a scattering approach [164, 165]. The interface shall be placed at $z = 0$, and only the Green's tensor above the macroscopic material ($z, z' > 0$) shall be evaluated. Besides the free contribution additional scattered fields have to be included. The scattered Green's tensor $\underline{g}$ can be described via a free space solution, which accumulated the phase $\exp(2\mathrm{i}k_z z')$ and — due to the reflection at the surface — a reflection matrix $\underline{R}$

$$\underline{G}(\mathbf{K},\omega) = \underline{G}_0(\mathbf{K},\omega) + \underline{R}(\mathbf{K},\omega)\cdot\underline{G}_0(\mathbf{K},\omega)e^{2\mathrm{i}k_z z'} \tag{2.38}$$

$$= \underline{G}_0(\mathbf{K},\omega) + \underline{g}(\mathbf{K},\omega). \tag{2.39}$$

The reflection matrix is defined by the reflection coefficients $r^{s/p}$, with respect to their polar-

ization, and a diagonal mirror matrix $\underline{M} = \mathrm{diag}[1, 1, -1]$ representing the mirror reflection at the interface

$$\underline{R}(\mathbf{K}, \omega) = \underline{M} \cdot \Big(r^s(\mathbf{K}, \omega)\, \mathbf{e}_s \otimes \mathbf{e}_s - r^p(\mathbf{K}, \omega)\, \mathbf{e}_{-p} \otimes \mathbf{e}_{-p} \Big). \tag{2.40}$$

Applying the k_z integration and using contour integration leads to the scattered Green's tensor

$$\begin{aligned} \underline{g}(\mathbf{k}, z, z', \omega) &= \int \frac{\mathrm{d}k_z}{2\pi} \underline{R}(\mathbf{K}, \omega) \cdot \underline{G}_0(\mathbf{K}, \omega) e^{2\mathrm{i}k_z z'} e^{\mathrm{i}k_z (z - z')} \\ &= \frac{\omega^2}{c^2} \Big(r^s(\mathbf{k}, \omega)\, \mathbf{e}_s \otimes \mathbf{e}_s + r^p(\mathbf{k}, \omega)\ \cdot \mathbf{e}_{+p} \otimes \mathbf{e}_{-p} \Big) \frac{e^{-2\kappa(z+z')}}{2\epsilon_0 \kappa} \end{aligned} \tag{2.41}$$

where $k_z = \mathrm{i}\kappa$ was substituted in the reflection coefficients ($r(\mathbf{K}, \omega)|_{k_z = \mathrm{i}\kappa} = r(\mathbf{k}, \omega)$). The poles of the reflection coefficients do not contribute to the result [163]. Due to the accumulated phase and the restriction to the upper half-space above the surface, the $\underline{G}_0$ within the scattered Green's tensor is never evaluated at $z = z'$. Thus, solely the $\underline{G}_0^{/V\delta}$ part contributes to $\underline{g}$. This expression coincides with the work of other authors [58, 164, 166]. A very similar scheme can be used if $\underline{G}_0$ references to a different material than vacuum. Consequently, the permittivity of the respective material has to be considered, which might yield an additional non-vanishing longitudinal component. Again one would restrict the description to one side of the interface to another material, as for example to vacuum. To match the descriptions of both sides one has to determine the reflection coefficients as connecting piece between the two different material properties on each side.

Reflection Coefficients

The material enters the macroscopic description via the displacement field $\mathbf{D}$ and the magnetizing field $\mathbf{H}$, as shown in equation (1.78). For now, we assume an isotropic, homogeneous and non-magnetic material. To obtain the reflection coefficients, the fields in both half-spaces have to be solved and connected by boundary conditions at the interface. Although knowing the propagation of the electromagnetic fields in infinitely extended media (one can apply a similar scheme as for $\underline{G}_0$ in equation (2.35)), we only solved the semi-infinite system implicitly by introducing formally the concept of reflection coefficient. One common approach to match the fields of two interfacing materials A and B are Maxwell's boundary conditions [96], which read for the tangential components with respect to the surface

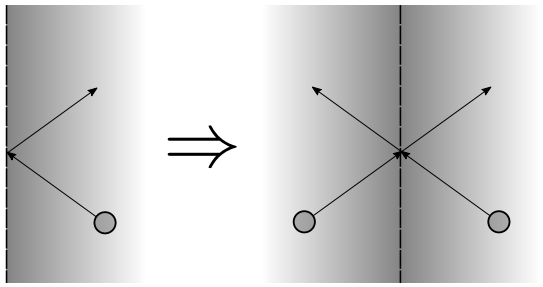

Figure 2.5: Mimicking scheme of the semi-infinitely extended material with hard-wall boundaries (the hard wall is represented by the dashed black line) to symmetrized situation within the infinitely extended material.

$$\mathbf{e_n} \times \mathbf{E}_\mathrm{B} = \mathbf{e_n} \times \mathbf{E}_\mathrm{A} \quad \text{and} \quad \mathbf{e_n} \times \mathbf{B}_\mathrm{B} = \mathbf{e_n} \times \mathbf{B}_\mathrm{A}, \tag{2.42}$$

where $\mathbf{e_n}$ is the normal vector perpendicular to the interface and we assumed non-magnetic materials with vanishing free surface charges and surface currents. While this prescription works properly for local interfacing materials, it becomes insufficient when considering non-local materials. The term *local* or *nonlocal* coins hereby the absence or presence of spatial correlation. This spatial correlation reflects itself in the dependence of the permittivities on the spatial coordinates. In nonlocal materials we encounter additional longitudinal modes, which in general cannot be considered solely by Maxwell's boundary conditions [167, 168]. Therefore, over the last decades schemes of additional boundary conditions were successfully developed [169–172]. However, their applicability has been a controverse subject [173–175]. Furthermore, for reciprocal media within the dielectric approximation no additional boundary conditions are required and a sufficient description is achieved by Huygen's principle and the extinction theorem [176, 177]. Despite the plethora of subtilities in the interface description, we want engage with the qualitatively successful description of a semi-classical infinite barrier, as for instance presented by Ford and Weber [172], which enables to directly elucidate the underlying phenomena in the surface's electromagnetic response. Here, we can comprehensibly establish the missing connection at the boundary via the sheet current technique[11] . In this technique the reflection of the charge carriers within the material at the interface is mapped to the situation, where charge carriers travel through the boundary in a symmetric fashion[12, 13], as is illustrated in figure 2.5. Thus, we can exploit the already available solutions of the infinitely extended media — i.e. $\underline{G}_0$ of the respective material, where V_δ is excluded — by replacing the interface by a sheet current along the interface[14] $\mathbf{J}(\omega, \mathbf{k})$ with $\mathbf{z} \cdot \mathbf{J}(\omega, \mathbf{k}) = 0$ (due to the fact, that $\mathbf{J}$ is located at a specific z coordinate, its Fourier transformed pendant is constant in k_z and therefore only dependent on $\mathbf{k}$). Within linear isotropic media the electromagnetic field can be split up into separate components, i.e. in transverse or longitudinal polarization with the respective permittivity $\epsilon_{t/l}$

$$\mathbf{D}(\omega, \mathbf{K}) = \left[\epsilon_l(K, \omega) \frac{\mathbf{K}\mathbf{K}^\intercal}{K^2} + \epsilon_t(K, \omega) \left(\mathbb{1} - \frac{\mathbf{K}\mathbf{K}^\intercal}{K^2} \right) \right] \mathbf{E}(\omega, \mathbf{K}). \tag{2.43}$$

Solving the electric and magnetic field in transverse and longitudinal polarization separately

[11] Hereby, we are neglecting spill-out effects. For a discussion on spill-out effects with a self-consistent hydrodynamic model see for example [178].

[12] A charge carrier being reflected at an interface leads to a change in momentum $\mathbf{p} = (p_x, p_y, p_z)^\intercal \rightarrow (p_x, p_y, -p_z)^\intercal = \mathbf{p}'$. Tantamount to the reflection, the charge carrier carrying $\mathbf{p}$ could pass through the barrier and another particle with $\mathbf{p}'$ could enter through the barrier. This alternative scheme allows to use the solutions for infinitely extended media. In order to comply with the requirement of the mirror symmetry along the interface, a surface current is introduced.

[13] Completely flat surfaces are only a theoretical idealization. The underlying assumption is that the surface roughness is negligible compared to the characteristic length scale of the electromagnetic field. However, there are possibilities to include surface roughness as for instance presented by Foreman [179].

[14] This solution is only valid within the respective media and not beyond the surface.

leads to the results

$$\mathbf{E}(\omega,\mathbf{k},z)=\frac{2}{\mathrm{i}\omega}\int \mathrm{d}k_z\left(\frac{\mathbb{1}-\frac{\mathbf{K}\mathbf{K}^\intercal}{K^2}}{\epsilon_t(K,\omega)-c^2K^2/\omega^2}+\frac{\mathbf{K}\mathbf{K}^\intercal}{K^2\epsilon_l(K,\omega)}\right)\mathbf{J}(\omega,\mathbf{k})e^{\mathrm{i}k_z(z-z_0)}, \tag{2.44}$$

$$\mathbf{B}(\omega,\mathbf{k},z)=\frac{2c}{\mathrm{i}\omega^2}\int \mathrm{d}k_z\frac{\mathbf{K}\times\mathbf{J}(\omega,\mathbf{k})}{\epsilon_t(K,\omega)-c^2K^2/\omega^2}e^{\mathrm{i}k_z(z-z_0)}, \tag{2.45}$$

where z_0 is the coordinate of the interface. We can engage this argumentation for both sides of the interface, only adapting the bulk permittivity of the respective material. The beauty of the sheet current technique is twofold. On the one hand, we are not restricted in our choice of $\mathbf{J}(\omega,\mathbf{k})$. Thus, we can emulate any field distribution possible for this setup. On the other hand, we notice, that any ratio of two fields is independent of the current itself, as all fields are linearly connected to the current. The current independent ratios can be depicted as a fundamental indication towards the formalisms in linear optics. Since we solved the fields at the inside and the outside of the medium, we are ready to solve for one specific ratio, namely the reflection coefficient. The reflection coefficients are quantities appearing in the scattering formalism. The scattering formalism relates in and out going fields with respect to a surface. While one could directly compute the reflection coefficients from equations (2.44) and (2.45), we want to take — in anticipation of further setups — a slight detour via a second formalism. Another way to categorize the fields is *in front* of and *beyond* the surface. This classification leads to the so-called transfer formalism. Both formalisms, scattering and transfer, have their advantages in different applications. In a field basis $\underline{\mathbf{F}}$ one can formulate a matrix notation for both approaches [180]

$$\mathbf{F}_{\mathrm{out}}=\mathbb{S}\cdot\mathbf{F}_{\mathrm{in}}\quad\text{and}\quad\mathbf{F}_{\mathrm{beyond}}=\mathbb{T}\cdot\mathbf{F}_{\mathrm{front}}. \tag{2.46}$$

The dimensionality of the matrices $\mathbb{S}$ and $\mathbb{T}$ depends on the number of independent field components. As shown in e.g. [163], there is no longitudinal polarization in free space. Thus, we only have two independent field components. For example in transverse magnetic or p polarization the magnetic field is chosen to be perpendicular to the plane of incidence, i.e. $B^p=(\mathbf{e_z}\times\mathbf{e_k})\cdot\mathbf{B}$, and consequently the electric field lies within the plane of incidence $E^p=\mathbf{e_k}\cdot\mathbf{E}$. Vice versa, one can construct the transverse electric or s polarization. In other media as e.g. in metals, the longitudinal polarization has to be considered [181]. These fields — being perpendicular to the transverse polarizations — can directly be engaged in the transfer matrix approach. However, using the scattering approach the direction of propagation is of interest. Hence, the fields would for example be notated as B^σ_+ and B^σ_-, where the sign indicates the direction of propagation and $\sigma=s,p$ the polarization. Nonetheless, we use the same field solutions of equations (2.44) and (2.45) to calculate the entries in either the scattering or transfer matrix. Therefore, as for instance demonstrated by Genet et al. [180], a direct connection

between the two formalisms can be established by

$$\mathbb{T} = -\left(\pi_- - \eta \cdot \mathbb{S} \cdot \pi_+\right)^{-1} \left(\pi_+ - \eta \cdot \mathbb{S} \cdot \pi_-\right), \tag{2.47}$$

$$\mathbb{S} = -\eta \cdot \left(\pi_- - \mathbb{T} \cdot \pi_+\right)^{-1} \left(\pi_+ - \mathbb{T} \cdot \pi_-\right), \tag{2.48}$$

with the aid of the matrices

$$\pi_+ = \begin{pmatrix} 1 & 0 \\ 0 & 0 \end{pmatrix}, \quad \pi_- = \begin{pmatrix} 0 & 0 \\ 0 & 1 \end{pmatrix}, \quad \eta = \begin{pmatrix} 0 & 1 \\ 1 & 0 \end{pmatrix}. \tag{2.49}$$

In the derivation of the Green's tensor we already harnessed the scattering concept when dividing into incident and reflected field. The full scattering matrix of some flat scatterer B cladded between another material A is described by

$$\mathbb{S} = \begin{pmatrix} r_{\mathrm{AB}} & t_{\mathrm{BA}} \\ t_{\mathrm{AB}} & r_{\mathrm{BA}} \end{pmatrix}, \tag{2.50}$$

where r_{XY} and t_{XY} are the reflection and transmission coefficient coming from material X and going to material Y. Considering a scattering process within the same material, i.e. $\mathrm{A} = \mathrm{B}$, we do not expect any reflection and obtain the propagation matrix $\mathbb{P} = t\eta$, where t governs the propagation through the medium. In order to obtain the required reflection coefficient demanded in equation (2.41), we take a small detour via the transfer formalism, as we believe that the calculation of the entries is more straightforward. To relate the fields directly at the interface we send $(z - z_0) \to 0^-$, i.e. the fields are evaluated still within the medium but infinitesimal close to the border. Thus, only the fields immediately inside and immediately outside are matched to each other via the usual interface conditions for electromagnetic fields ($\hat{\mathbf{z}} \times (\mathbf{E}_{\mathrm{in}} - \mathbf{E}_{\mathrm{out}}) = 0$ and $\hat{\mathbf{z}} \cdot (\mathbf{B}_{\mathrm{in}} - \mathbf{B}_{\mathrm{out}}) = 0$) [97]. In the case of two adjacent semi-infinite bulk media the reflected fields are caused solely by the single interface. The only non-zero quantities are the so-called surface impedances

$$Z^p(\omega, k) = -\frac{\mathbf{k} \cdot \mathbf{E}(\omega, k, z)}{(\mathbf{e_z} \times \mathbf{k}) \cdot \mathbf{B}(\omega, k, z)}\bigg|_{z \to z_0^-}, \quad Z^s(\omega, k) = \frac{(\mathbf{e_z} \times \mathbf{k}) \cdot \mathbf{E}(\omega, k, z)}{\mathbf{k} \cdot \mathbf{B}(\omega, k, z)}\bigg|_{z \to z_0^-}, \tag{2.51}$$

where the subscript z_0^- indicates that the fields shall be evaluated infinitesimal close to the surface, but still inside the respective material. As shown by Ford and Weber [172] the surface impedances in the case of hard-wall boundaries ($\mathbf{z} \cdot \mathbf{j} = 0$) can be analytically evaluated and yield the form

$$Z^s(\omega, k) = \frac{2\mathrm{i}\omega}{\pi} \int_0^\infty \mathrm{d}k_z \frac{1}{\epsilon_t(K, \omega)\omega^2 - K^2}, \tag{2.52}$$

$$Z^p(\omega, k) = \frac{2\mathrm{i}\omega}{\pi} \int_0^\infty \mathrm{d}k_z \frac{1}{K^2} \left(\frac{k_z^2}{\epsilon_t(K, \omega)\omega^2 - K^2} + \frac{k^2}{\epsilon_l(K, \omega)\omega^2} \right). \tag{2.53}$$

The assumption of a hard wall at which particles are specular reflected is a classical depiction

and is also referred to as semi-classical infinite barrier approximation. In quantum mechanics, i.e. in a wave picture, the electron density is zero at the boundary but increases over length-scales of the order of the respective Fermi length λ_F. However, as Ford and Weber showed [172], the main effect is a minor shift of the effective position of the boundary. Hence, we choose the semi-classical infinite barrier approximation as a simple and effective approximation, which is also confirmed by other authors [170]. Eventually, we can apply the transformation between the scattering and transfer matrix of equation (2.48) and find the relation between Z and r in the case of a single flat interface [182]

$$r^\sigma_{\mathrm{AB}}(\omega,k) = \delta^\sigma \frac{Z^\sigma_\mathrm{A}(\omega,k) - Z^\sigma_\mathrm{B}(\omega,k)}{Z^\sigma_\mathrm{A}(\omega,k) + Z^\sigma_\mathrm{B}(\omega,k)}, \tag{2.54}$$

where $\sigma = s,p$ and $\delta^p = 1$ and $\delta^s = -1$. This result is somehow remarkable, since the response of a surface is completely derived from the response functions of an infinitely extended bulk material in a compact and closed form. The results of $Z^{s/p}$ in equation (2.52) and (2.53) are valid for local as well as for nonlocal materials.

Structured Geometries

For more sophisticated geometries, as depicted in figure 2.6, the surface impedances or reflection coefficients are modified. To demonstrate this and also being capable of investigating the influence of geometry on dispersion forces later on, we give two further examples: A finite slab and multilayered superlattice. Starting with a finite slab of size d, the previous description has to be extended by another interface. The quintessence of the description of the fields inside the slab does not change. Another sheet current is introduced at the new interface and again a limiting procedure is performed. However, stemming from the backscattering of the second interface, this new contribution also depends on the adjacent medium (in our example again vacuum) at the second interface. Nevertheless, the fields and thus their respective ratios can be calculated. In order to keep a good overview, we can collect all ratios of the $\mathbf{E}$ and $\mathbf{B}$ fields in a respective transfer matrix

$$\mathbb{T}^\sigma_{\mathrm{slab}}(\omega,k,d) = \begin{pmatrix} \mathrm{cs}^\sigma(\omega,k,d) & \mathrm{i}\delta^\sigma \mathcal{Z}^\sigma_+(\omega,k,d) \\ \frac{\mathrm{i}\delta^\sigma}{\mathcal{Z}^\sigma_-(\omega,k,d)} & \mathrm{cs}^\sigma(\omega,k,d) \end{pmatrix}, \tag{2.55}$$

from which we can derive the respective reflection coefficient for a slab of material B cladded into a material A

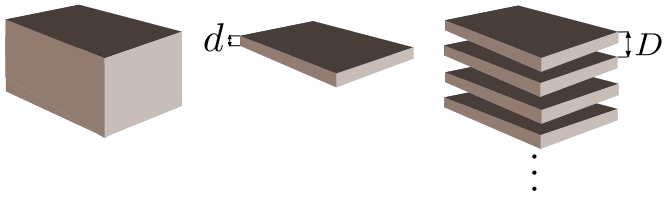

Figure 2.6: Displayed are the three different geometries we are going to consider. From left to right: A semi-infinite bulk, one finite slab and a superlattice structure.

$$r^{\sigma}_{\mathrm{ABA}}(\omega,k,d) = \frac{[Z^{\sigma}_{\mathrm{A}}(\omega,k)]^2 - \mathcal{Z}^{\sigma}_{\mathrm{B}+}(\omega,k,d)\mathcal{Z}^{\sigma}_{\mathrm{B}-}(\omega,k,d)}{[Z^{\sigma}_{\mathrm{A}}(\omega,k)]^2 + \mathcal{Z}^{\sigma}_{\mathrm{B}+}(\omega,k,d)\mathcal{Z}^{\sigma}_{\mathrm{B}-}(\omega,k,d) + 2\mathrm{i}\mathrm{cs}^{\sigma}_{\mathrm{B}}(\omega,k,d)Z^{\sigma}_{\mathrm{A}}(\omega,k)\mathcal{Z}^{\sigma}_{\mathrm{B}-}(\omega,k,d)}. \tag{2.56}$$

We refrain from displaying the full lengthy expressions of the quantities cs and $\mathcal{Z}_{\pm}$ here, but refer the interested reader to appendix D. In the case of local materials ($\epsilon_l(\omega) = \epsilon_t(\omega) = \epsilon(\omega)$), the poles in equations (2.44) and (2.45) can be easily evaluated and the transfer matrix reduces to

$$\mathbb{T}^{\sigma}_{\mathrm{lc}}(d) = \begin{pmatrix} \cos(\mathrm{i}\kappa_\epsilon d) & \mathrm{i}\delta^{\sigma}\sin(\mathrm{i}\kappa_\epsilon d)Z^{\sigma}_{\mathrm{lc}} \\ \mathrm{i}\delta^{\sigma}\sin(\mathrm{i}\kappa_\epsilon d)/Z^{\sigma}_{\mathrm{lc}} & \cos(\mathrm{i}\kappa_\epsilon d) \end{pmatrix}, \tag{2.57}$$

with $\kappa_\epsilon = \sqrt{k^2 - \epsilon(\omega)\omega^2/c^2}$, where $\mathrm{Re}\{\kappa_\epsilon\} > 0$ and $\mathrm{Im}\{\kappa_\epsilon\} < 0$. The local surface impedances yield

$$Z^{p}_{\mathrm{lc}} = \frac{\mathrm{i}c\kappa_\epsilon}{\omega\epsilon(\omega)} \quad \text{and} \quad Z^{s}_{\mathrm{lc}} = \frac{\omega}{\mathrm{i}c\kappa_\epsilon}. \tag{2.58}$$

In this case, the reflection coefficient takes the common form [165]

$$r_{\mathrm{ABA(lc)}}(\omega,k,d) = r^{\sigma}_{\mathrm{AB(lc)}}(\omega,k)\frac{1-\exp[2\mathrm{i}\kappa_\epsilon(\omega,k)d]}{1-\left(r^{\sigma}_{\mathrm{AB(lc)}}(\omega,k)\exp[\mathrm{i}\kappa_\epsilon(\omega,k)d]\right)^2}, \tag{2.59}$$

which can be understood by multiple internal reflection within the slab [183]. As final geometric extension, we introduce multilayer structures. In multilayered networks, we can harness the modularity of the transfer matrix formalism. Modularity means that one can express a network of layers by its N components, i.e.

$$\mathbb{T}_{\mathrm{mult}} = \prod_{j=1}^{N}\mathbb{T}_j = \cdots\mathbb{T}_3\cdot\mathbb{T}_2\cdot\mathbb{T}_1\,. \tag{2.60}$$

Despite having a direct formalism how to calculate the transfer matrix and afterwards extract the reflection coefficient, these structures can be arbitrarily complicated. Hence, we restrict ourselves to one specific class, namely superlattice structures. The word *superlattice* is inspired by the lattices of solid state physics. Superlattices describe macroscopic periodic structures $\mathbb{T}_{\mathrm{sup}}$ in which a certain pattern $\mathbb{T}_{\mathrm{pat}}$ is repeated over and over again, i.e.

$$\mathbb{T}_{\mathrm{sup}} = \prod_{j=1}^{\infty}\mathbb{T}_{\mathrm{pat}}. \tag{2.61}$$

For an infinite periodic structure, we can apply Floquet's [184] or Bloch's [185] theorem. This

means, we are allowed to rewrite the evolution along one pattern with the length D via

$$\begin{pmatrix} E \\ cB \end{pmatrix}^{\sigma}_{z'=z+D} = \mathbb{T}_{\mathrm{pat}}(D) \cdot \begin{pmatrix} E \\ cB \end{pmatrix}^{\sigma}_{z'=z} = e^{\mathrm{i}\beta^{\sigma} D} \begin{pmatrix} E \\ cB \end{pmatrix}^{\sigma}_{z'=z} \tag{2.62}$$

where β^{σ} is the one dimensional Bloch's wave vector. Such modes characterized by the Bloch's wave vector can only exist if $\mathbb{T}^{\sigma} - \mathbb{1}e^{\mathrm{i}\beta^{\sigma} D}$ is a singular matrix

$$\det\left[\mathbb{T}^{\sigma}_{\mathrm{pat}} - \mathbb{1}e^{\mathrm{i}\beta^{\sigma} D}\right] = 0. \tag{2.63}$$

Thus, if there exist normal modes in the structure, they are defined by the equation

$$e^{\mathrm{i}\beta^{\sigma} D} = \frac{\mathrm{tr}[\mathbb{T}_{\mathrm{pat}}]}{2} \pm \sqrt{\frac{\mathrm{tr}[\mathbb{T}_{\mathrm{pat}}]^2}{4} - \det[\mathbb{T}_{\mathrm{pat}}]}. \tag{2.64}$$

The two solutions stem from the fact that until now the superlattice is not truncated, i.e. it is infinitely extended along the z axis. However, with a truncation to a semi-infinite half-space, the symmetry is broken and one has to choose a physical solution. Allowing for losses (but not for gain) within the materials, the normal modes contain an imaginary part which either exponentially grows or decays, depending on the sign and propagation direction. Accordingly, one has to choose these normal modes, which fulfill $|\exp(\mathrm{i}\beta^{\sigma} D)| \leq 1$ in the direction of positive D. Since the superlattice is still infinitely extended when departing from the surface into the periodic material, we can again use the relation between r and Z as we did for the semi-infinitely extended bulk in equation (2.54). Furthermore, we can easily calculate the surface impedance $Z^{\sigma}_{\mathrm{sup}} = (E^{\sigma}/B^{\sigma})_{z\to z_0^-}$ via the eigenvector equation as demonstrated for instance by Mochán et al. [181]

$$\left(\mathbb{T}_{\mathrm{pat}} - \mathbb{1}e^{\mathrm{i}\beta^{\sigma} D}\right) \cdot \begin{pmatrix} E \\ cB \end{pmatrix}^{\sigma}_{z=z_0^-} = 0, \tag{2.65}$$

from which follows that

$$Z^{\sigma}_{\mathrm{sup}} = \frac{\mathbb{T}_{12}}{e^{\mathrm{i}\beta^{\sigma} D} - \mathbb{T}_{11}} = \frac{e^{\mathrm{i}\beta^{\sigma} D} - \mathbb{T}_{22}}{\mathbb{T}_{21}}. \tag{2.66}$$

Finally, one obtains the full reflection coefficient of the superlattice structure in complete analogy to the bulk reflection coefficient

$$r^{\sigma}_{\mathrm{Asup}}(\omega, k) = \delta^{\sigma} \frac{Z^{\sigma}_{\mathrm{A}}(\omega, k) - Z^{\sigma}_{\mathrm{sup}}(\omega, k)}{Z^{\sigma}_{\mathrm{A}}(\omega, k) + Z^{\sigma}_{\mathrm{sup}}(\omega, k)}. \tag{2.67}$$

Effective Medium Theory

The expression $Z^{\sigma}_{\mathrm{sup}}(\omega, k)$, however, is a mathematically rather involved expression. Therefore, physical information might not be extracted easily. In order to simplify the problem, one can perform a higher level coarse-graining method, commonly known as effective medium approximation introduces by Bruggeman [186]. In this approximation one assumes that the char-

acteristic length of the structure, i.e. D in superlattice system, is much smaller than the relevant wavelength of the electromagnetic radiation. For superlattices the permittivity tensor then becomes a diagonal matrix with two different entries $\underline{\epsilon}_{\mathrm{EMA}}(\omega) = \mathrm{diag}[\epsilon_\perp(\omega), \epsilon_\perp(\omega), \epsilon_\parallel(\omega)]$, with the subscript referring to the propagation direction with respect to the optical axis [46, 181, 187][15]. This mimics the permittivity tensor of an uniaxial crystal. The coarse-grained permittivities of a repeated AB pattern are

$$\epsilon_\perp(\omega) = \epsilon_\mathrm{A}(\omega)\, f + \epsilon_\mathrm{B}(\omega)\,(1-f) \quad \text{and} \quad \epsilon_\parallel(\omega) = \left[\frac{f}{\epsilon_\mathrm{A}(\omega)} + \frac{1-f}{\epsilon_\mathrm{B}(\omega)}\right]^{-1}, \tag{2.68}$$

where $f = d_\mathrm{A}/D$ is the filling factor with respect to material A. Since the optical axis coincides with the normal of the flat surface, one can deduce the surface impedances in p and s polarization

$$Z^s_{\mathrm{EMA}}(\omega, k) = \frac{\omega/c}{\sqrt{\frac{\omega^2}{c^2}\epsilon_\perp(\omega) - k^2}} \quad \text{and} \quad Z^p_{\mathrm{EMA}}(\omega, k) = \frac{\sqrt{\frac{\omega^2}{c^2}\epsilon_\parallel(\omega) - k^2}}{\frac{\omega}{c}\sqrt{\epsilon_\perp(\omega)\epsilon_\parallel(\omega)}}. \tag{2.69}$$

Nonetheless, the effective medium approximation has to be handled with care, since the coarse-graining is performed on a macroscopic level. Its range of validity is restricted to $k \ll 1/D$. Otherwise, one has to take into account the full nonlocal multilayer treatment, in order to receive a valid solution.

Recap: In this section we calculated the electromagnetic Green's tensor in different geometries. First, we derived the vacuum Green's tensor as a solution for a infinitely extended media in equation (2.35). In a next step, we derived the Green's tensor above a macroscopic surface with assigned reflection coefficients in equation (2.39). In order to connect the material properties, i.e. the bulk permittivities, to the reflection coefficients we employed the current-sheet technique. As an intermediate step, we calculated directly the surface impedances of different layered flat structured geometries and related them to the respective reflection coefficients. With this we obtained expressions of the reflection coefficients for a semi-infinite bulk, a finite slab and a superlattice configuration in equations (2.54), (2.56) and (2.67).

[15] Since the wavelength is assumed to be much larger than the macroscopic structuring, one can also apply local a material description of the components building the superlattice, which yields an overall effectively local model.

2.4 Bulk Material Models

In the previous section, we have shown that the permittivity of an infinitely extended bulk media is essential to determine the response of a macroscopic surface. Hence, subsequently we focus on the modeling of the material's response to macroscopic electromagnetic fields. The step from microscopic to macroscopic fields was demonstrated in section 1.3. While we defined various macroscopic quantities, e.g. ϱ_{free}, $\mathbf{P}$ or $\epsilon(\mathbf{r}, \mathbf{r}', \omega)$, we did not yet model their dynamics. In the following we are especially interested in the derivation of the permittivity $\epsilon(\mathbf{r}, \mathbf{r}', \omega)$. Thus, we introduce two different microscopic models, one for dielectrics and one for metals, and calculate their corresponding permittivity.

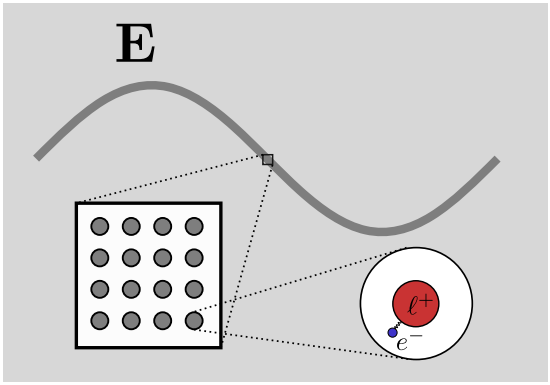

Figure 2.7: Illustration of the macroscopic description of a dielectric. One macroscopically small volume (black square) contains many independent lattice sides (gray circles) consisting of bound electrons and their respective screened nuclei. Here, the volume is small compared to the wavelength of the electric field.

The first material class we aim to model are dielectrics. Dielectric materials are non- or poorly conducting substances. The reason behind the poor conduction is the lack of free charge carriers. Therefore, the negatively charged electrons e^- as potential charge carriers are localized at the positively charged lattice sides ℓ^+ or bonds. This situation is analogous to the one discussed in section 2.2. The localized particles, which are situated in a stable equilibrium, are disturbed by an electric field. Confronted with a very large amount of degrees of freedom due to the many particles within the solid, we employ the Nakajima-Zwanzig projection (see equation (1.54)) to shift all less relevant degrees of freedom to a respective memory kernel γ_i and a microscopic fluctuation $\hat{\mathbf{f}}_i$, where i indicates the association with a respective frequency mode ω_i. The according Langevin equations read

$$\ddot{\hat{\mathbf{d}}}_i(t) + \omega_i^2 \hat{\mathbf{d}}_i(t) + \int_{-\infty}^{\infty} \mathrm{d}t' \gamma_i(t-t') \dot{\hat{\mathbf{d}}}_i(t') = \hat{\mathbf{f}}_i(t) + \alpha_i \omega_i^2 \hat{\mathbf{e}}(\mathbf{r}, t)\,, \tag{2.70}$$

where α_i is the respective static polarizability. Because the characteristic length scale of the electric field is already assumed to be much larger than the small macroscopic volume, the electric field is constant over the coarse-grained volume, i.e. $\mathbf{e}(\mathbf{r}_i, t) = \mathbf{e}(t)$. The remaining differential equation can be solved by

$$\hat{\mathbf{d}}_i(\omega) = \frac{\hat{\mathbf{f}}_i(\omega) + \alpha_i \omega_i^2 \hat{\mathbf{e}}(\omega)}{\omega_i^2 - \omega^2 - \mathrm{i}\omega\gamma_i(\omega)}. \tag{2.71}$$

When averaging over the macroscopic small volume $V(\mathbf{r})$, the polarization density can be

extracted by summing over all modes

$$\hat{\mathbf{P}}(\mathbf{r},\omega) = \frac{1}{V(\mathbf{r})}\int_{V(\mathbf{r})} \mathrm{d}^3\mathbf{r}' \sum_i \mathbf{d}_i(\omega) = \frac{1}{V(\mathbf{r})}\int_{V(\mathbf{r})} \mathrm{d}^3\mathbf{r}' \sum_i \frac{\hat{\mathbf{f}}_i(\omega) + \alpha_i\omega_i^2\hat{\mathbf{e}}(\omega)}{\omega_i^2 - \omega^2 - \mathrm{i}\omega\gamma_i(\omega)} \tag{2.72}$$

$$= \hat{\mathbf{P}}_\mathrm{N}(\mathbf{r},\omega) + \epsilon_0\chi(\omega)\hat{\mathbf{E}}(\mathbf{r},\omega), \tag{2.73}$$

where $\chi(\omega)$ is the spatially independent susceptibility. Eventually, we find the permittivity and the noise polarization density (see section 1.3) of a dielectric

$$\epsilon(\omega) = 1 - \sum_i \frac{\alpha_i\omega_i^2}{\omega_i^2 - \omega^2 - \mathrm{i}\omega\gamma_i(\omega)} \quad \text{and} \quad \hat{\mathbf{P}}_\mathrm{N}(\mathbf{r},\omega) = \sum_i \frac{\hat{\mathbf{f}}_i(\omega)}{\omega_i^2 - \omega^2 - \mathrm{i}\omega\gamma_i(\omega)}. \tag{2.74}$$

If one is only interested in the low-frequency behavior — for example one only considers frequencies lower than the first peak —, the other higher peaks might be approximated by their respective constant value for $\omega \ll \omega_i$ for $i > 0$. The resulting constant off-set is collected in a constant ϵ_∞

$$\epsilon(\omega) \overset{\omega\ll\omega_i}{\approx} \epsilon_\infty - \frac{\alpha_\mathrm{die}\omega_0^2}{\omega_0^2 - \omega^2 - \mathrm{i}\omega\gamma_0(\omega)}, \qquad \text{for} \quad i > 0. \tag{2.75}$$

Here, we named $\alpha_0 \equiv \alpha_\mathrm{die}$ in order to avoid confusion when considering the static polarizability of the dipole moment in section 2.2.

Semi-Classical Fermi Liquid

As second material model, we aim to describe metallic solids. In metals, in contrast to dielectrics, the electrons move freely against the positive background of the lattice sides. On the one hand, the density of conducting electrons is very high in metals, on the other hand the Coulomb interaction potential of the electrons is, compared to the distance between electrons, long range. Due to these two properties and the fact, that electrons are fermions, one refers to this system as *Fermi liquid*. Hence, one electron is not only interacting dominantly with its nearest neighbors, but rather with a very large number of other electrons. A usual approach towards interacting systems is a perturbation expansion with respect to the interaction. If one treats the Coulomb potential in such a perturbation approach, one finds logarithmic and higher order divergences in the perturbation series. This very problem in the modeling of Fermi liquids can be solved by introducing a more benign effective screening potential.

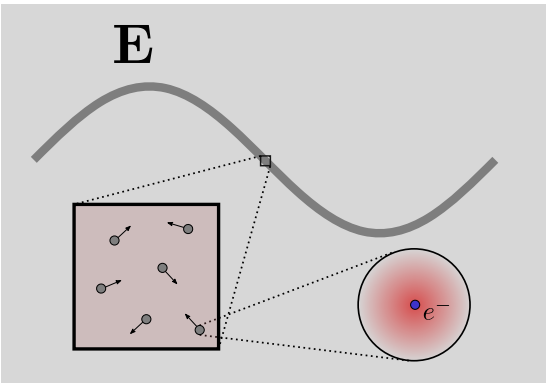

Figure 2.8: An illustration of a charged Fermi liquid. Within the macroscopic small volume (black square) Landau's quasi-particle concept is used, which describes the electron plus its screening hole as one quasi-particle (gray circles). Here, the volume is small compared to the wavelength of the electric field.

Historically, a static screening of the Coulomb interaction was introduced first by Debye and Hückel [188] and Mott and Jones [189]. But in order to derive the dynamics of the Fermi liquid, Silin generalized Landau's theory of the Fermi liquid by a dynamic screening [190]. In order to obtain a dynamic screening an external test electron with a velocity $\mathbf{v}_e$ and the elemental electron charge $-e$ is introduced into the densely packed Fermi liquid. Around the test charge the electrons in the liquid are repelled. Moving in front of a positive ionic background the repelling region around the test charge is defined as a positive screening hole. Solving for the modified effective electric potential one finds the Poisson equation

$$\nabla^2\varphi(\mathbf{r},t) = -4\pi e\left[\delta(\mathbf{r}-\mathbf{v}_e t) + \left\langle \varrho(\mathbf{r},t)\right\rangle\right], \tag{2.76}$$

where ϕ is the electric potential and $\langle\varrho\rangle$ is the averaged electron density. This effective potential yields a more short-range potential, usually on the scale of Bohr radius a_0. If one considers length scales much larger than a_0, the system of strongly interacting electrons can be rearranged into a system of weakly interacting quasi-particles, which contain an electron with its respective screening hole. Thus, the system of quasi-particles can be relabeled as Fermi gas. For such a system in equilibrium one can derive the probability of finding a single quasi-particle with effective mass m_{qua} and an energy $\varepsilon(\mathbf{p}) = \mathbf{p}^2/(2m_{\mathrm{qua}})$ [191, 192]

Fermi Gas

$$n_0(\varepsilon) = \frac{1}{\exp\left[\beta(\varepsilon(\mathbf{p})-\mu)\right]+1}, \tag{2.77}$$

with $\mu = \partial E/\partial N$ being the chemical potential of adding one quasi-particle to the system and $\beta^{-1} = k_{\mathrm{B}}T$. This result is the well-known Fermi-Dirac distribution. This quasi-particle picture has of course its restrictions. As discussed by Pines and Nozières [193] Landau's theory of quasi-particles applies for

$$\hbar\omega \ll \mu \quad \text{and} \quad \hbar K v_{\mathrm{F}} \ll \mu, \tag{2.78}$$

with $K = |\mathbf{K}|$ being the respective wavevector and $v_{\mathrm{F}} = \sqrt{2\varepsilon_{\mathrm{F}}/m_{\mathrm{qua}}}$ being the Fermi velocity. The latter derives from the Fermi energy ε_{F}. Keeping these restrictions in mind, we move towards a description of the dynamics of the system. To obtain a kinetic theory of the itinerant quasi-particles, the probability of a particle to be within the small volume of the phase space $\mathrm{d}^3\mathbf{r}\,\mathrm{d}^3\mathbf{p}$ is investigated. By means of the Liouville theorem of classical mechanics, the density within this small phase space volume is conserved [138]

$$\frac{\mathrm{d}n}{\mathrm{d}t} = \partial_t n + \frac{\mathrm{d}\mathbf{p}}{\mathrm{d}t}\cdot\nabla_{\mathbf{p}} n + \frac{\mathrm{d}\mathbf{r}}{\mathrm{d}t}\cdot\nabla_{\mathbf{r}} n = 0, \tag{2.79}$$

with $\mathrm{d}\mathbf{p}/\mathrm{d}t$ being a force acting on the particle. This differential equation is widely known as the classical Boltzmann transport equation. Again, we do not aim to give a full description of all microscopic dynamics, but project out less relevant information. This can be achieved by applying a Langevin-type treatment, as shown by Fox and Uhlenbeck [194] or Logan and Kac [195]. Thus, besides a collision term $I_{\mathrm{coll}}(n)$ also a fluctuation F enters the Boltzmann

equation

$$\partial_t n + \frac{\mathrm{d}\mathbf{p}}{\mathrm{d}t} \cdot \nabla_{\mathbf{p}} n + \frac{\mathrm{d}\mathbf{r}}{\mathrm{d}t} \cdot \nabla_{\mathbf{r}} n = I_{\mathrm{coll}}(n) + F\,. \tag{2.80}$$

Pioneering work in solving this differential equation for metals was done by Lindhard and Mermin [196, 197]. Following their work, the undisturbed state n_0 is assumed to be slightly disturbed by the electromagnetic field, causing a slight deviation in the probability distribution $n = n_0 + \delta n$. The electromagnetic field acts in form of the Lorentz force onto the probability density. Further, the behavior of the electrons shall be governed by the Pauli exclusion principle. Fortunately, if the exclusion principle is fulfilled in its initial state, it will be obeyed for any future time [196]. Substituting the Lorentz force[16] into the Boltzmann equation (2.80) and performing a linearization with respect to the perturbation leads to the expression

$$\partial_t \delta n + e\mathbf{e} \cdot \nabla_{\mathbf{p}} n_0 + \mathbf{v} \cdot \nabla_{\mathbf{r}} \delta n = I_{\mathrm{coll}}(n) + F\,. \tag{2.81}$$

Here, it was used that n_0 — as a homogeneous, isotropic distribution at equilibrium — , is independent of $\mathbf{r}$ and t. On the right-hand side we find the collision term, which carries the scattering processes of the quasi-particles with themselves, but as well the collisions with the lattice and scattering at impurities of the material. For an estimate, which processes are of relevance, Pines [198] gave exemplary an overview for sodium, displayed in table 2.1.

Collision Times	Characteristic Dependence	Temperature Regime
$\tau^{-1}_{\mathrm{e}^-\to\mathrm{ph}}$	$\propto k_{\mathrm{B}}T$	room temperature
	$\propto T^5 \times 10^4$	liquid helium temperatures
$\tau^{-1}_{\mathrm{e}^-\to\mathrm{imp}}$	$\propto \varrho_{\mathrm{imp}} \times 10^{15}$	temperature independent
$\tau^{-1}_{\mathrm{e}^-\to\mathrm{e}^-}$	$\propto (k_{\mathrm{B}}T/\varepsilon_{\mathrm{F}})^2 \times 10^{15}$	$k_{\mathrm{B}}T \ll \varepsilon_{\mathrm{F}}$

Table 2.1: List of inverse collision times τ^{-1} at different temperatures for sodium [198]. The three denoted scattering events are between an electron and a phonon, an electron and an impurity in the solid and an electron with another electron. Here, $\varrho_{\mathrm{imp}} = N_{\mathrm{imp}}/N$ is the concentration of impurities with respect to the number of itinerant electrons and ε_{F} the Fermi energy.

Of course, one has to modify the numbers given in table 2.1 for different metals. However, one often finds that the following relations hold: For higher temperatures the dominant contribution stems form electron-phonon collisions. At lower temperatures as for liquid helium temperatures ($\approx 4\,\mathrm{K}$) the electron-electron collision contribution is on the same order of magnitude as the electron-phonon collision contribution. Yet, the impurity concentration normally is dominating the electron-electron scattering, leading to basically no relevant contribution of the electron-electron scattering in most transport phenomena. At small deviations from the equilibrium distribution, collision integral can be estimated by a linearized relaxation-time ap-

[16] This is actually not so obvious as it might seem. A rather clear derivation can be found by Pines and Noziéres [193] in chapter 3.6.

proximation (for detailed discussion see [193, 198–201])

$$I_{\text{coll}}(n) \approx -(n - n_0)/\tau, \tag{2.82}$$

where the τ refers to an effective collision time including the relevant phenomena discussed above. Eventually, by the introduced assumptions, the transport equation can be solved by applying the Fourier transform with respect to $\mathbf{r}$ and t, which yields the resolvent

$$\delta n(\mathbf{p}, \mathbf{K}, \omega) \approx \mathrm{i}\frac{e\Big[\nabla_{\mathbf{p}} n_0(\mathbf{p})\Big] \cdot \mathbf{e}(\mathbf{K}, \omega) + F(\mathbf{K}, \omega)}{\mathbf{v} \cdot \mathbf{K} - \omega - \mathrm{i}/\tau} \tag{2.83}$$

$$= \boldsymbol{\alpha}(\mathbf{p}, \mathbf{K}, \omega) \cdot \mathbf{e}(\mathbf{K}, \omega) + \delta n_F(\mathbf{K}, \omega) \tag{2.84}$$

Landau damping

with $\boldsymbol{\alpha}$ being the momentum dependent response and δn_F being the density fluctuation. What attracts attention in equation (2.84) is the resonance of the system at $\mathbf{v} \cdot \mathbf{K} = \omega$. When considering a quasiparticle with a velocity $\mathbf{v}$ in $\mathbf{K}$ direction, the resonance occurs for the particle's velocity being equal to the phase velocity ω/K of the collective mode of the system. This resonance leads to an energy transfer between the quasiparticle and the collective mode. If the quasiparticle's velocity is slightly faster than the phase velocity, the quasiparticle is slowed down. Vice versa, if the quasiparticle moves slightly slower, the velocity of the quasiparticle increases. In a equilibrium situation, the distribution of quasiparticles is decreasing for higher velocities. Therefore, the energy transfer from the collective mode to the quasiparticles is preferred, i.e. the collective mode is damped. This damping mechanism is known as Landau damping and was proposed by Landau [202]. At this point, we like to emphasize that Landau damping differs from the above described collision induced damping mechanisms. As Landau damping represents a coherent energy transfer, which is enabled when fulfilling the above mentioned condition, collision induced damping mechanisms are incoherent scattering events. For more details about Landau damping, we refer the reader to [193, 203].

When assuming the temperature of the system being low compared to the degeneracy or Fermi temperature $T_{\text{F}} = \varepsilon_{\text{F}}/k_{\text{B}}$, the sharp edge of the Fermi distribution yields approximately a delta peak at the momentum of the Fermi surface $\nabla_{\mathbf{p}} n_0(\mathbf{p}) = -(\mathbf{p}/p)\delta(p - p_{\text{F}})$. Finally, in order to obtain macroscopic quantities, the density deviation of equation (2.84) is spatially averaged over a macroscopically small volume (an illustration of the coarse-graining scheme is given in figure 2.7)

$$\overline{\boldsymbol{\alpha}\mathbf{e}}(\mathbf{p}, \mathbf{r}, \omega) = \frac{1}{V(\mathbf{r})} \int_{V(0)} \mathrm{d}^3\mathbf{r}' \int \mathrm{d}^3\mathbf{r}'' \boldsymbol{\alpha}(\mathbf{p}, \mathbf{r} - \mathbf{r}' - \mathbf{r}'', \omega) \cdot \mathbf{e}(\mathbf{r}'', \omega) \tag{2.85}$$

$$\overset{r \gg r'}{\approx} \int \mathrm{d}^3\mathbf{r}'' \boldsymbol{\alpha}(\mathbf{p}, \mathbf{r} - \mathbf{r}'', \omega) \cdot \mathbf{E}(\mathbf{r}'', \omega), \tag{2.86}$$

where the extension of the coarse-grained volume is assumed to be much smaller than the distance between the coordinate of evaluation and the center of the volume. Similarly, the fluctuations can be averaged, too. From equation (2.86) the macroscopic quantities $\mathbf{P}$ and $\mathbf{j}_{\text{free}}$ can be constructed. Since polarization and free current density are connected through $\mathbf{j}_{\text{free}} =$

$\partial_t \mathbf{P}$, both can be used to extract the respective linear response function. The current density can derived by calculating the first moment with respect to the particle's velocity

$$\mathbf{j}_{\text{free}}(\mathbf{K},\omega) = 2e \int \mathrm{d}^3\mathbf{p}\, \mathbf{v}\, \overline{\delta n}(\mathbf{p},\mathbf{K},\omega), \tag{2.87}$$

where $\overline{\delta n}$ is the spatial average of δn, the prefactor 2 is due to the two different spin states, and $e\mathbf{v}$ is the current generated by a single electron. As the undisturbed distribution is even in the momentum, only the disturbance leads to an induced current. Besides the linear response to the electric field, which is governed by the conductivity tensor $\underline{\sigma}$, additionally the fluctuation stemming from the environmental degrees of freedom is included and yields a fluctuating noise current $\hat{\mathbf{j}}_{\text{N}}$. Rewriting the conductivity in terms of the permittivity we find

$$\begin{aligned} \mathbf{j}_{\text{free}}(\mathbf{K},\omega) &= \hat{\mathbf{j}}_{\text{N}}(\mathbf{K},\omega) + \underline{\sigma}(\mathbf{K},\omega)\cdot\mathbf{E}(\mathbf{K},\omega) && (2.88)\\ &= \hat{\mathbf{j}}_{\text{N}}(\mathbf{K},\omega) - \mathrm{i}\omega\epsilon_0\left[\underline{\epsilon}(\mathbf{K},\omega) + \mathbb{1}\right]\cdot\mathbf{E}(\mathbf{K},\omega). && (2.89)\end{aligned}$$

As indicated in section 1.3 the response may differ between transversal and longitudinal polarization. Thus, one can split the current into its transversal and its longitudinal part, which leads to a scalar $\sigma_{t/l}$ or $\epsilon_{t/l}$, where the subscripts refer to the transversal or longitudinal polarization respectively. While the path of achieving the macroscopic permittivities seems straightforward, the actual calculations are quite involved and shall not be displayed here. For the case of very low temperatures ($T \ll T_{\text{F}}$) we follow Lindhard [196] and find

$$\epsilon_l(\omega,\mathbf{K}) = 1 + \frac{\omega_p^2}{\omega + \mathrm{i}\gamma}\frac{3u^2 f_l(u)}{\omega + \mathrm{i}\gamma f_l(u)} \quad \text{and} \quad \epsilon_t(\omega,\mathbf{K}) = 1 - \frac{\omega_p^2 f_t(u)}{\omega(\omega+\mathrm{i}\gamma)} \tag{2.90}$$

where

$$f_l(u) = 1 - \frac{1}{2}u\ln\left[\frac{u+1}{u-1}\right] \quad \text{and} \quad f_t(u) = \frac{3}{2}u^2 - \frac{3}{4}\left(u^2-1\right)u\ln\left[\frac{u+1}{u-1}\right], \tag{2.91}$$

with $\gamma = 1/\tau$ being the dissipation rate, ω_p the plasma frequency, and $u = \frac{\omega+i\gamma}{v_{\text{F}}K}$. Two relevant asymptotic regimes of the Lindhard model of equation (2.90) are $|u| \to \infty$ and $u \to 0^+ + \mathrm{i}0^+$. The limits translate to a comparison of the material parameters γ and v_{F} with respect to ω and K. In detail, one compares ω to γ, the phase velocity $v_{\text{ph}} = \omega/K$ to the Fermi velocity v_{F} and the mean free path of the electrons $\ell = v_{\text{F}}/\gamma$ to the wavelength $\lambda = 2\pi/K$. The first case ($|u| \to \infty$) refers to a regime, where $v_{\text{ph}} \gg v_{\text{F}}$ and $\lambda \gg \ell$. In other words, the electromagnetic field averages over various scattering events and cannot access coherent collective interactions, as e.g. the collective effect of Landau damping. For $|u| \to \infty$, the logarithm can be expanded as

Drude Model

$$\ln\left[\frac{u+1}{u-1}\right] = \frac{2}{u} + \frac{2}{3u^2} + \mathcal{O}(1/u^5) \tag{2.92}$$

and yields in leading order to $f_l \approx -\frac{1}{3u^2}$ and $f_t \approx 1$. In this limit one can deduce the widely

used and much simpler local Drude model [204]

$$\epsilon_{l/t}(\omega, k) = \epsilon_{\mathrm{D}}(\omega) = 1 - \frac{\omega_p^2}{\omega(\omega + \mathrm{i}\gamma)}\,. \tag{2.93}$$

In the second limit $u \to 0^+ + \mathrm{i}0^+$ the wavelength becomes much larger than the electrons mean free path $\lambda \ll \ell$. This means the electric field can resolve the ballistic motion of the electrons and is enabled to coherently store energy in the electrons motion. Mathematically, one finds for $u \to 0^+ + \mathrm{i}0^+$

$$\ln\left[\frac{u+1}{u-1}\right] = -\mathrm{i}\pi + 2u + \mathcal{O}(u^3), \tag{2.94}$$

and consequently can derive the permittivities [205–207]

$$\epsilon_l(\omega, K) \approx 1 + \frac{3\omega_p^2}{v_{\mathrm{F}}^2 K^2} + \mathrm{i}\omega\frac{3\pi\omega_p^2}{2v_{\mathrm{F}}^3 K^3} \quad \text{and} \quad \epsilon_t(\omega, K) \approx 1 + \mathrm{i}\frac{3\pi\omega_p^2}{4v_{\mathrm{F}} K\omega}. \tag{2.95}$$

However, the Lindhard-Mermin model remains quite involved. Thus, in the following we point to other regularly used models. Skipping the already introduce Drude model, which could be assigned to be the simplest — yet often sufficient — models to describe the response of a metal, another often used model is the hydrodynamic model [101, 208–211]. In this model the metal's conduction electrons are described as a compressible fluid. The compressibility is governed by the constant parameter β, which takes different values depending on the studied frequency domain [212]. As the hydrodynamic model covers many interesting and physically relevant phenomena, it lacks for instance the effect of Landau damping. To include Landau damping and offer a more flexible description with respect to the investigated frequency domain, Halevi proposed an extended hydrodynamic model with a frequency dependent compressibility parameter $\beta(\omega)$ [213].

Recap: In this section we presented models for two material classes, i.e. dielectric and metallic materials. In both derivations we used phenomenological input to picture the mechanisms and motivate the assumptions. In the dielectric as well as in the metal, we applied a coarse-grain approach into macroscopic small volumes in order to derive macroscopic response to an electromagnetic field. Furthermore, we motivated losses as well as fluctuation via a Langevin-like treatment, i.e. via a Nakajima-Zwanzig projection, and the assumption of weak coupling to the environment. Eventually, we took a closer look at two opposite regimes present in the weakly disturbed Fermi liquid of metals and pointed out further models used in the literature.

CHAPTER 3

Analytical Investigations

While in chapters 1 and 2 we set up the framework for our study and already pointed out several interesting general properties of our system, in this chapter we perform the actual investigations of the nonequilibrium noncontact frictional force. In section 3.1 we solve the equation of motion of the microscopic object's dipole moment (see equation (2.28)) and extract — in anticipation of the calculations of the noncontact friction — required correlators, and respective power spectrum. In section 3.2 we use the previous groundwork to achieve a full analytical closed formula for the calculation of the noncontact friction. This general formula and its constituents are under scrutiny in section 3.3. We provide specialized formulae of the noncontact friction for the relevant asymptotic regimes. In the last section 3.4 we evaluate the asymptotic formulae for different situations and give insight into the physical mechanisms behind contributing to the noncontact friction. The asymptotic results are backed up by full numerical calculations, which we will introduce in chapter 4.

3.1 Solving the Equation of Motion

The total system under investigation (see figure 2.1) — within approximations introduced in chapter 2 — happens to be an exactly solvable physical system. The subsystem of interest is the moving dipole moment and its dynamics. As elaborated in section 2.2, one can use different models to describe the dynamics of the dipole moment. Since the model with an internal heat bath implicitly contains the model without an internal heat bath (by setting the bath quantities to zero), we are going to solve the equation of motion in the general case of additional internal bath degrees of freedom. For a better overview, we briefly recall the required equations. First, the equation of motion of the dipole moment was found in the form of a Langevin equation (see equation (2.28))

$$\partial_t^2 \hat{\mathbf{d}}(t) + \int_{-\infty}^{\infty} \mathrm{d}t_1 \, \mu(t - t_1) \dot{\hat{\mathbf{d}}}(t) + \omega_a^2 \hat{\mathbf{d}}(t) = \alpha_0 \omega_a^2 \hat{\mathbf{E}}(\mathbf{r}_a(t), t) + \hat{\mathbf{F}}(t) \,, \tag{3.1}$$

where $\hat{\mathbf{F}}$ is the Langevin force and μ the memory kernel stemming from the internal bath. In dipole approximation the microscopic object is externally only driven by the electric field $\hat{\mathbf{E}}$ evaluated at the microscopic object's center of mass coordinate $\mathbf{r}_a(t)$. Secondly, describing the electric field in linear response[1] to the dipole moment allows to employ the Green's tensor formalism (see section 1.3) and leads to the solution of the electrodynamical equation of motion as a linear combination of the free and induced part (see equation (2.7))

$$\hat{\mathbf{E}}(\mathbf{r}_a(t),t) = \hat{\mathbf{E}}_0(\mathbf{r}_a(t),t) + \int_{t_0}^{t} \mathrm{d}t' \int \frac{\mathrm{d}\omega}{2\pi}\, e^{-\mathrm{i}\omega(t-t')} \int \frac{\mathrm{d}^2\mathbf{k}}{(2\pi)^2} \underline{G}(\mathbf{k}, z_a, \omega)\, \hat{\mathbf{d}}(t')\, e^{\mathrm{i}\mathbf{k}^\intercal(\mathbf{r}_a(t)-\mathbf{r}_a(t'))}. \tag{3.2}$$

From here on, a shortened argument list of the Green's tensor $\underline{G}(\mathbf{k}, z_a, z_a, \omega) \to \underline{G}(\mathbf{k}, z_a, \omega)$ is used. As indicated by the hat symbol, all these quantities shall be read as operators. When substituting the electric field of equation (3.2) into the dipole moment's equation of motion of equation (3.1), one can apply a Fourier transform to obtain the respective resolvent, i.e. the dynamic susceptibility of the dipole moment with respect to the two Langevin forces $\hat{\mathbf{E}}_0$ and $\hat{\mathbf{F}}$. Furthermore, the relative motion of the microscopic object to the surface has to be taken into account. As imposed in section 2.2, the center of mass of the object moves on the classic trajectory $\mathbf{r}_a(t) \approx \mathbf{r}_a + \mathbf{v}t$ relatively to the surface. From the object's point of view the frequencies of the electromagnetic field, and vice versa, are thus Doppler shifted. This does not apply to the internal bath, since it moves with zero relative velocity to the center of mass of the microscopic object. Performing the previous mentioned steps leads to

$$\hat{\mathbf{d}}(\omega) = \underline{\alpha}(\omega) \left\{ \int \frac{\mathrm{d}^2\mathbf{k}}{(2\pi)^2} \hat{\mathbf{E}}_0(\mathbf{k}, z_a, \mathbf{k}^\intercal\mathbf{v} + \omega)\, e^{\mathrm{i}\mathbf{k}^\intercal\mathbf{r}_a} + \frac{1}{\alpha_0\omega_a^2} \hat{\mathbf{F}}(\omega) \right\}, \tag{3.3}$$

with the susceptibility or polarizability

$$\underline{\alpha}(\omega) = \alpha_0\omega_a^2 \left(\left[\omega_a^2 - \omega^2 - i\omega\mu(\omega)\right] \mathbb{1} - \alpha_0\omega_a^2 \int \frac{\mathrm{d}^2\mathbf{k}}{(2\pi)^2} \underline{G}(\mathbf{k}, z_a, \mathbf{k}^\intercal\mathbf{v} + \omega) \right)^{-1}. \tag{3.4}$$

From the preceding discussion, we can understand the frequency shift $\omega \to \omega + \mathbf{k}^\intercal\mathbf{v}$ in the argument of the electric field. In a next step, we impose an initial state of the full system, which can be factorized in its subsystems ($\hat{\rho}(t_0) = \hat{\rho}_{\mathrm{mic}}(t_0) \otimes \hat{\rho}_{\mathrm{f+m}}(t_0)$, where $\hat{\rho}_{\mathrm{mic}}(t_0)$ is the initial state of the microscopic object independent from the electromagnetic fields and $\hat{\rho}_{\mathrm{f+m}}$ is the initial state of the medium assisted electromagnetic fields), i.e. we assume initially independent subsystems. The interaction shall then be adiabatically switched on at t_0. At t_0 the two subsystems, i.e. the object and the medium assisted electromagnetic field, shall be separate in their respective equilibrium state. Due to the dissipation channels of the medium assisted electromagnetic fields and the internal bath, the system eventually relaxes to a stationary state,

[1] For linearly responding materials this formalism is exact. But even for not purely linear materials this might be a good approximation for weak field strength where nonlinear contributions are sub-leading in comparison to the linear order.

if $t - t_0$ is much larger than the life time of any transient dynamics[2] . Thus, due to used the Heisenberg picture (see section 1.2), the stationary state can be calculated by evaluating the initial factorized state. When aiming to calculate the dispersion forces acting on the dipole moment, as introduced in section 2.1, one can evaluate — by applying the fluctuation-dissipation theorem of equation (1.29) — the correlators of the fluctuation operators. As argued in section 2.2, the internal heat bath is assumed to effectively not interact with the electromagnetic field, i.e. $\langle \hat{\mathbf{E}}_0 \hat{\mathbf{F}} \rangle \approx \langle \hat{\mathbf{E}}_0 \rangle \langle \hat{\mathbf{F}} \rangle$. Therefore, assuming the first moments $\langle \hat{\mathbf{E}}_0 \rangle = \langle \hat{\mathbf{F}} \rangle = 0$, the $\langle \hat{\mathbf{E}}_0 \hat{\mathbf{F}} \rangle$ terms yield no contribution. The remaining terms, the autocorrelators, are evaluated by the fluctuation-dissipation theorem. Employing the Wiener-Khinchin theorem (see equation (1.34)) one finds

$$\left\langle \hat{\mathbf{F}}(\omega) \hat{\mathbf{F}}^{\intercal}(\omega') \right\rangle_{\rho_{\mathrm{mic}}(t_0)} = \mathbb{1} \frac{2\hbar \alpha_0 \omega_a^2 \omega \mu_R(\omega)}{1 - \exp(-\beta \hbar \omega)} (2\pi) \delta(\omega + \omega') \tag{3.6}$$

and

$$\left\langle \hat{\mathbf{E}}_0(\mathbf{k}, z_a, \omega) \hat{\mathbf{E}}_0^{\intercal}(\mathbf{k}', z_a, \omega') \right\rangle_{\rho_{\mathrm{f+m}}(t_0)} = \frac{2\hbar \underline{G}_{\Im}(\mathbf{k}, z_a, \omega)}{1 - \exp(-\beta \hbar \omega)} (2\pi)^3 \delta(\omega + \omega') \delta(\mathbf{k} + \mathbf{k}'), \tag{3.7}$$

where $\mu_R \equiv \mathrm{Re}\{\mu\}$. The two autocorrelators of equations (3.6) and (3.7) can further be utilized to calculate the autocorrelator of the dipole moment. However, many other authors [129, 214, 215] suggest to directly apply the fluctuation-dissipation theorem on the dipole moment's autocorrelator. This derives from the local thermal equilibrium approximation. This approximation assumes, that the system under investigation is effectively at equilibrium with its immediate surroundings. In local equilibrium the fluctuation-dissipation theorem can be applied directly on the dipole moment's autocorrelator

$$\langle \hat{\mathbf{d}}^{\intercal}(\omega) \hat{\mathbf{d}}(\omega') \rangle \overset{\mathrm{LTE}}{\approx} \frac{2\hbar \underline{\alpha}_{\Im}(\omega)}{1 - \exp(-\beta \hbar \omega)} (2\pi) \delta(\omega + \omega'). \tag{3.8}$$

Nonetheless, there is a conceptual problem as soon as the dipole is moving relatively to the surface. As shown in equation (3.3), the frequencies of the electric field and the polarizability are Doppler shifted. While the local equilibrium does implicitly account for the Doppler shift in the polarizability, it does not enter the equilibrium distribution. The justification in applying a local approximation can usually be found by rather short length scales of the mediating interaction [109, 216]. Although the use of the local approximation seems ubiquitous in the literature [28, 29, 215, 217–221], the quantitative justification of its validity is most often missing. As it was shown by Intravaia et al. [222], the assumption of local thermal equilibrium fails

[2] An effective estimate for the decay time of the transients is the inverse of the intrinsic plus the induced damping

$$\Gamma(\omega) \approx \mathrm{Re}\{\mu(\omega)\} + \frac{\alpha_0 \omega_a^2}{\omega} \int \frac{\mathrm{d}^2 \mathbf{k}}{(2\pi)^2} \mathrm{Im}\{\mathrm{Tr}\left[\underline{G}(\mathbf{k}, z_a, \mathbf{k}^{\intercal}\mathbf{v} + \omega)\right]\}. \tag{3.5}$$

For example, assuming an atom without an internal heat bath in the near-field (see appendix F), and assuming a local surface material ($\mathrm{Im}\{r(\omega)\} = 2\epsilon_0 \rho \omega$), on finds a constant decay rate of $\Gamma = \alpha_0 \omega_a^2 \rho / (4\pi z_a^3)$. In the case of an $^{87}\mathrm{Rb}$ atom at a distance of $z_a = 10\,\mathrm{nm}$ over a gold surface , the decay time is on the order of $\approx 20\,\mathrm{ns}$.

in the context of noncontact friction of an atomic system at absolute zero temperature. Calculating the dipole moment's autocorrelator by equations (3.6) and (3.7), we find two competing heat baths

$$\left\langle \hat{\mathbf{d}}(\omega)\hat{\mathbf{d}}^{\intercal}(\omega')\right\rangle = \underline{\alpha}(\omega)\Bigg\{ \int \frac{\mathrm{d}^2\mathbf{k}}{(2\pi)^2}\frac{4\pi\hbar}{1-\exp(-\beta\hbar[\mathbf{k}^{\intercal}\mathbf{v}+\omega])}\underline{G}_{\Im}(\mathbf{k},z_a,\mathbf{k}^{\intercal}\mathbf{v}+\omega) + \frac{1}{\alpha_0\omega_a^2}\frac{4\pi\hbar}{1-\exp(-\beta\hbar\omega)}\omega\mu_R(\omega)\Bigg\}\underline{\alpha}^{\intercal}(\omega')\delta(\omega+\omega'), \tag{3.9}$$

with $\beta = 1/(k_{\mathrm{B}}T)$ being the inverse temperature[3]. While the second term, which is connected to the internal heat bath, is in local thermal equilibrium — the interaction with the electromagnetic fields is assumed to be arbitrary short in length scale —, the interaction with the electric noise field is described in full nonequilibrium. Here, the latter does not reproduce the results of the local thermal equilibrium. The autocorrelator can be connected to its respective power spectrum $\underline{S}(\omega)$ (see equation (1.34))

Power Spectrum of the Dipole Moment's Autocorrelator

$$\underline{S}(\omega) = \frac{\hbar}{\pi}\underline{\alpha}(\omega)\Bigg\{ \int \frac{\mathrm{d}^2\mathbf{k}}{(2\pi)^2}\frac{\underline{G}_{\Im}(\mathbf{k},z_a,\mathbf{k}^{\intercal}\mathbf{v}+\omega)}{1-e^{-\beta\hbar[\mathbf{k}^{\intercal}\mathbf{v}+\omega]}} + \frac{1}{\alpha_0\omega_a^2}\frac{\omega\mu_R(\omega)}{1-e^{-\beta\hbar\omega}}\Bigg\}\underline{\alpha}^{\dagger}(\omega). \tag{3.10}$$

where we used the crossing relation of the susceptibility $\underline{\alpha}(-\omega) = \underline{\alpha}^*(\omega^*)$. The power spectrum $S_{ij}(\omega)$ gives a measure of how much energy is stored per frequency within the correlation of the ith dipole component and jth dipole component. In comparison to the result of equation (3.10) the local thermal equilibrium approximation yields

$$\underline{S}_{\mathrm{LTE}}(\omega) = \frac{\hbar}{\pi}\frac{\underline{\alpha}_{\Im}(\omega)}{1-\exp(-\beta\hbar\omega)} \tag{3.11}$$

$$= \frac{\hbar}{\pi}\underline{\alpha}(\omega)\Bigg\{ \int \frac{\mathrm{d}^2\mathbf{k}}{(2\pi)^2}\frac{\underline{G}_{\Im}(\mathbf{k},z_a,\mathbf{k}^{\intercal}\mathbf{v}+\omega)}{1-\exp(-\beta\hbar\omega)} + \frac{1}{\alpha_0\omega_a^2}\frac{\omega\mu_R(\omega)}{1-\exp(-\beta\hbar\omega)}\Bigg\}\underline{\alpha}^{\dagger}(\omega), \tag{3.12}$$

which is lacking the Doppler shift in the equilibrium distribution of the medium assisted fields, i.e. $\exp(-\beta\hbar[\omega+\mathbf{k}^{\intercal}\mathbf{v}]) \overset{\mathrm{LTE}}{\to} \exp(-\beta\hbar\omega)$. In order to quantify the deviation of the local thermal equilibrium approximation compared to the full nonequilibrium treatment, one can split the power spectrum in a local thermal equilibrium part and a nonequilibrium correction current $\underline{J}$

[3] Here, we assume that the temperature of the internal heat bath and the external heat bath (i.e. the medium assisted electromagnetic fields) have the same temperature.

[222]

$$\underline{S}(\omega) = \frac{\hbar}{\pi}\left(\frac{\underline{\alpha}_{\Im}(\omega)}{1-\exp(-\beta\hbar\omega)} + \underline{J}(\omega)\right), \tag{3.13}$$

where

$$\underline{J}(\omega) = \underline{\alpha}(\omega)\int \frac{\mathrm{d}^2\mathbf{k}}{(2\pi)^2}\underline{G}_{\Im}(\mathbf{k}, z_a, \mathbf{k}^\intercal\mathbf{v}+\omega)\left(\frac{1}{1-e^{-\beta\hbar[\mathbf{k}^\intercal\mathbf{v}+\omega]}} - \frac{1}{1-e^{-\beta\hbar\omega}}\right)\underline{\alpha}^\dagger(\omega) \tag{3.14}$$

and the relation[4]

$$\underline{\alpha}_{\Im}(\omega) = \underline{\alpha}(\omega)\int \frac{\mathrm{d}^2\mathbf{k}}{(2\pi)^2}\left(\underline{G}_{\Im}(\mathbf{k}, z_a, \mathbf{k}^\intercal\mathbf{v}+\omega) + \mathbb{1}\frac{\omega\mu_R(\omega)}{\alpha_0\omega_a^2}\right)\underline{\alpha}^\dagger(\omega) \tag{3.16}$$

was used. The nonequilibrium correction $\underline{J}$ contains solely the contribution of the induced Doppler shifted electromagnetic field. We emphasize that $\underline{S}(\omega \to 0)$ does, due to the Doppler shift, not vanish. This is true for the diagonal elements, as well as for the off-diagonal elements (or more specific, the antisymmetric part of $\underline{S}$). The $\underline{S}_{\mathrm{LTE}}(\omega \to 0)$ in contrast only yields non-vanishing contributions in the off-diagonal elements. In section 3.3 we will relate the off-diagonal/antisymmetric terms to the rotation of the dipole moment. Due to this relation to the rotational degrees of freedom, we recognize that, within the local thermal equilibrium approximation, the only available degrees of freedom for a vanishing frequency are rotations, whereas the full power spectrum of the moving dipole still allows for oscillations, i.e. non-vanishing diagonal elements.

Recap: Over the course of this section we investigated the dynamics of a moving dipole moment coupled to the heat bath of the electromagnetic field as well as to internal degrees of freedom. First, we solved the dipole moment's equation of motion in a formal operator valued manner in equation (3.3). We proceeded to calculate the second moment of the randomly driven statistical (quantum) operator $\hat{\mathbf{d}}$ and retrieved the nonequilibrium power spectrum in equation (3.10). Additionally, we set up the local thermal equilibrium version of the power spectrum in equation (3.12).

[4] This relation can briefly be derived by using the definition of the $\Im$ subscript

$$\underline{\alpha}_{\Im} = \frac{1}{2\mathrm{i}}\left(\underline{\alpha} - \underline{\alpha}^\dagger\right) = \frac{1}{2\mathrm{i}}\left(\underline{\alpha}\left(\underline{\alpha}^\dagger\right)^{-1}\underline{\alpha}^\dagger - \underline{\alpha}\left(\underline{\alpha}\right)^{-1}\underline{\alpha}^\dagger\right) = -\underline{\alpha}\,\underline{\alpha}_{\Im}^{-1}\underline{\alpha}^\dagger, \tag{3.15}$$

with $-\underline{\alpha}_{\Im}^{-1}(\omega) = \int \mathrm{d}^2\mathbf{k}\,\underline{G}_{\Im}(\mathbf{k}, z_a, \mathbf{k}^\intercal\mathbf{v}+\omega)/(2\pi)^2 + \mathbb{1}\omega\mu_R(\omega)/(\alpha_0\omega_a^2)$.

3.2 Noncontact Friction

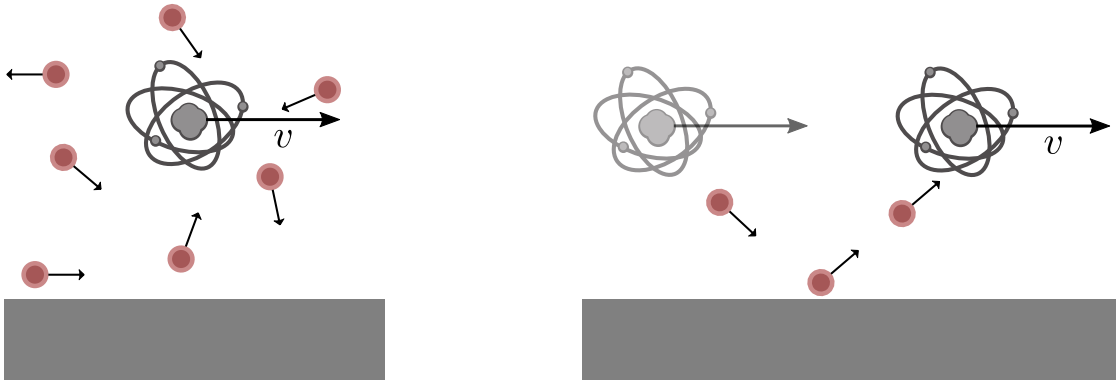

Figure 3.1: Depicted are the two mechanisms contributing to the noncontact friction. On the left the microscopic object is situated in a similar situation as in the Brownian motion [13]. Many small quasi-particles of the electromagnetic radiation scatter randomly with the object, which therefore experiences a friction opposing its directed motion. On the right the coherent backaction is illustrated. At a past time the object generated electromagnetic quasi-particles, which later on again scatter with the object.

In the last section we found the full solution of the dipole moment's equation of motion. Within the derivation we imposed a fixed trajectory ($\mathbf{r}_a(t) \approx \mathbf{r}_a + \mathbf{v}t$) on the microscopic object's center of mass. Without an external energy drive the directed motion of the center of mass would decelerate and eventually the full system would reach its equilibrium. This is not the case, if a constant external energy drive is applied on the system to keep the prescribed trajectory[5]. Despite a fixed trajectory the averaged Lorentz force is still acting on the neutral object. In this section, we calculate this fluctuation-induced force. While we focus mainly on the parallel component, i.e. the noncontact friction, the concepts presented in this section also apply to the perpendicular component, i.e. the dynamical Casimir-Polder force, which was investigated in a similar manner by Reiche et al. [223].

When recalling equation (2.15), where the Lorentz force acting on a neutral small object was calculated, we notice two additive contributions $F = F^{\mathbf{dE}_0} + F^{\mathbf{dd}}$. One contains the correlator $\langle \hat{\mathbf{d}}(t)\hat{\mathbf{E}}_0(t)\rangle$ and the other the autocorrelator $\langle \hat{\mathbf{d}}(t)\hat{\mathbf{d}}(t-\tau)\rangle$. The latter one is caused by the backaction of the dipole moment onto the electric field. The first term describes the force acting on a dipole moment due to the interaction with electric noise field. A randomly driven system without backaction on the environment is often referred to as Brownian motion and represents a fundamental and well studied system [84, 92, 224, 225]. The physical picture of these two mechanisms is illustrated in figure 3.1. The dipole moment is influenced by the electric field as well as the internal degrees of freedom, as shown in the previous section. In the following, we aim to calculate the two additive contributions connected to their respective

[5]The assumption of a constantly moving center of mass might also be sufficient when analyzing dynamics on time scales shorter than the relaxation time of the directed motion.

correlators $\langle\hat{\mathbf{d}}(t)\hat{\mathbf{E}}_0(t)\rangle$ and $\langle\hat{\mathbf{d}}(t)\hat{\mathbf{d}}(t-\tau)\rangle$. Without loss of generality $\mathbf{v} = v\,\mathbf{e}_x$ and one finds

Random Field Scattering

$$F_{\parallel}^{\mathbf{dE}_0} = 2\mathrm{Re}\left\langle \hat{\mathbf{d}}^{\intercal}(t)\int_0^{\infty}\frac{\mathrm{d}\omega}{2\pi}\int\frac{\mathrm{d}^2\mathbf{k}}{(2\pi)^2}\mathrm{i}k_x\,\hat{\mathbf{E}}_0(\mathbf{k},\omega)e^{\mathrm{i}\mathbf{k}^{\intercal}(\mathbf{r}_a+\mathbf{v}t)-\mathrm{i}\omega t}\right\rangle. \tag{3.17}$$

Inserting the Fourier transformed expression of equation (3.3) yields two terms. One contains the electric noise field $\hat{\mathbf{E}}_0$ and one contains the internal noise force $\hat{\mathbf{F}}$. Since, we imposed that $\langle\hat{\mathbf{F}}\hat{\mathbf{E}}_0\rangle \approx 0$ the latter term vanishes. This leads to

$$\begin{aligned} F_{\parallel}^{\mathbf{dE}_0} = 2\mathrm{Re}\Big\langle &\int\frac{\mathrm{d}\omega'}{2\pi}\int\frac{\mathrm{d}^2\mathbf{k}'}{(2\pi)^2}\hat{\mathbf{E}}_0^{\intercal}(\mathbf{k}',z_a,\mathbf{k}'^{\intercal}\mathbf{v}+\omega')\,e^{i\mathbf{k}'^{\intercal}\mathbf{r}_a} \\ &\times\underline{\alpha}^{\intercal}(\omega')\int_0^{\infty}\frac{\mathrm{d}\omega}{2\pi}\int\frac{\mathrm{d}^2\mathbf{k}}{(2\pi)^2}\mathrm{i}k_x\,\hat{\mathbf{E}}_0(\mathbf{k},\omega)e^{\mathrm{i}\mathbf{k}^{\intercal}(\mathbf{r}_a+\mathbf{v}t)-\mathrm{i}(\omega'+\omega)t}\Big\rangle. \end{aligned} \tag{3.18}$$

By applying a coordinate transformation one can achieve a more convenient form

$$\begin{aligned} F_{\parallel}^{\mathbf{dE}_0} \overset{\omega'=\tilde{\omega}-\mathbf{k}'^{\intercal}\mathbf{v}}{=} 2\mathrm{Re}\Big\langle &\int\frac{\mathrm{d}\tilde{\omega}}{2\pi}\int\frac{\mathrm{d}^2\mathbf{k}'}{(2\pi)^2}\hat{\mathbf{E}}_0^{\intercal}(\mathbf{k}',\tilde{\omega})\underline{\alpha}^{\intercal}(\tilde{\omega}-\mathbf{k}'^{\intercal}\mathbf{v}) \\ &\times\int_0^{\infty}\frac{\mathrm{d}\omega}{2\pi}\int\frac{\mathrm{d}^2\mathbf{k}}{(2\pi)^2}\mathrm{i}k_x\,\hat{\mathbf{E}}_0(\mathbf{k},\omega)e^{\mathrm{i}(\mathbf{k}+\mathbf{k}')^{\intercal}(\mathbf{r}_a+\mathbf{v}t)-\mathrm{i}(\tilde{\omega}+\omega)t}\Big\rangle, \end{aligned}$$

$$\begin{aligned} &= 2\mathrm{Re}\int\frac{\mathrm{d}\tilde{\omega}}{2\pi}\int\frac{\mathrm{d}^2\mathbf{k}'}{(2\pi)^2}\int_0^{\infty}\frac{\mathrm{d}\omega}{2\pi}\int\frac{\mathrm{d}^2\mathbf{k}}{(2\pi)^2}\mathrm{i}k_x\,e^{\mathrm{i}(\mathbf{k}+\mathbf{k}')^{\intercal}(\mathbf{r}_a+\mathbf{v}t)-\mathrm{i}(\tilde{\omega}+\omega)t} \\ &\quad\times\mathrm{Tr}\left[\left\langle\hat{\mathbf{E}}_0(\mathbf{k}',\tilde{\omega})\hat{\mathbf{E}}_0^{\intercal}(\mathbf{k},\omega)\right\rangle\underline{\alpha}(\tilde{\omega}-\mathbf{k}'^{\intercal}\mathbf{v})\right], \end{aligned} \tag{3.19}$$

with $\mathrm{Tr}[\underline{A}] = \sum_{j=x,y,z}\mathbf{e}_j^{\intercal}\cdot\underline{A}\cdot\mathbf{e}_j$ being the trace over the spatial coordinates. Using the fluctuation-dissipation theorem draws the connection to the Green's tensor (see equation (3.7)). Eventually, one obtains

$$\begin{aligned} F_{\parallel}^{\mathbf{dE}_0} &= -2\mathrm{Im}\int\frac{\mathrm{d}\tilde{\omega}}{2\pi}\int\frac{\mathrm{d}^2\mathbf{k}'}{(2\pi)^2}\int_0^{\infty}\frac{\mathrm{d}\omega}{2\pi}\int\frac{\mathrm{d}^2\mathbf{k}}{(2\pi)^2}k_x\,e^{i(\mathbf{k}+\mathbf{k}')^{\intercal}(\mathbf{r}_a+\mathbf{v}t)-i(\tilde{\omega}+\omega)t} \\ &\quad\times\mathrm{Tr}\left[\underline{\alpha}^{\intercal}(\tilde{\omega}-\mathbf{k}'^{\intercal}\mathbf{v})\frac{2\hbar(2\pi)^3}{1-\exp(-\beta\hbar\tilde{\omega})}\underline{G}_{\Im}(\mathbf{k},z_a,\tilde{\omega})\delta(\omega+\tilde{\omega})\delta(\mathbf{k}+\mathbf{k}')\right] \\ &= -2\int_0^{\infty}\frac{\mathrm{d}\omega}{2\pi}\int\frac{\mathrm{d}^2\mathbf{k}}{(2\pi)^2}k_x\,\frac{2\hbar}{1-\exp(\beta\hbar\omega)}\mathrm{Tr}\left[\underline{\alpha}_{\Im}^{\intercal}(\mathbf{k}^{\intercal}\mathbf{v}-\omega)\underline{G}_{\Im}(\mathbf{k},z_a,-\omega)\right]. \end{aligned} \tag{3.20}$$

Employing $\underline{G}_{\Im}(\mathbf{k},z_a,-\omega) = -\underline{G}_{\Im}(\mathbf{k},z_a,\omega)$ leads to the compact expression

Noncontact Friction: Random Field Scattering

$$F_{\parallel}^{\mathbf{dE}_0} = -2\int_0^{\infty}\frac{\mathrm{d}\omega}{2\pi}\int\frac{\mathrm{d}^2\mathbf{k}}{(2\pi)^2}k_x\,\frac{2\hbar}{\exp(\beta\hbar\omega)-1}\mathrm{Tr}\left[\underline{\alpha}_{\Im}^{\intercal}(\mathbf{k}^{\intercal}\mathbf{v}-\omega)\underline{G}_{\Im}(\mathbf{k},z_a,\omega)\right]. \tag{3.21}$$

The derived term of equation (3.21) is under scrutiny later in this chapter. However, we already point out that this contribution vanishes in the limit of $\hbar\omega \gg k_\mathrm{B}T$.

Backaction

The second term of equation (2.15) is the dipole moment's autocorrelator, which represents the retarded backaction of the dipole moment onto itself via the electric field. With equation (3.3) and $\underline{C}(\tau) = \langle \hat{\mathbf{d}}(t)\hat{\mathbf{d}}^\intercal(t-\tau)\rangle$ one derives

$$\begin{aligned} F_\parallel^{\mathbf{dd}}(t) &= -4\mathrm{Re}\int_0^{t-t_0}\mathrm{d}\tau\int_0^\infty\frac{\mathrm{d}\omega}{2\pi}\int\frac{\mathrm{d}^2\mathbf{k}}{(2\pi)^2}\,k_x \\ &\quad\times\sum_{i,j}\left[\underline{G}_\Im(\mathbf{k},z_a,\omega)\right]_{ij}\underbrace{\left\langle\left[\hat{\mathbf{d}}(t)\right]_i\left[\hat{\mathbf{d}}(t-\tau)\right]_j\right\rangle}_{=[\underline{C}(\tau)]_{ij}}e^{\mathrm{i}(\mathbf{k}^\intercal\mathbf{v}-\omega)\tau} \\ &= -4\mathrm{Re}\int_0^{t-t_0}\mathrm{d}\tau\int_0^\infty\frac{\mathrm{d}\omega}{2\pi}\int\frac{\mathrm{d}^2\mathbf{k}}{(2\pi)^2}\,k_x\,\mathrm{Tr}\left[\underline{G}_\Im(\mathbf{k},z_a,\omega)\underline{C}^\intercal(\tau)\right]\,e^{\mathrm{i}(\mathbf{k}^\intercal\mathbf{v}-\omega)\tau}. \end{aligned} \tag{3.22}$$

Similar to the first term $F_\parallel^{\mathbf{dE}_0}$, the second term $F_\parallel^{\mathbf{dd}}$ is not explicitly dependent on the time t. However, one still has to integrate over all time differences τ in order to receive a result. Since the integration over the time differences represents the contributions of the past, one finds a dependence on the initial time t_0, which marks the start of the interaction of the subsystems. Analogously to the discussion with respect to the general retarded response function around equation (1.21), we assume that all artifacts of the transient regime, i.e. effects due to the switching-on[6] the interaction process, have vanished. The underlying assumption is again, that the decay time of the transients is much smaller than the time span integrated, i.e. $\tau_\mathrm{tran} \ll t - t_0$. In other words, on the time scale of transient decay the initial time t_0 is in far past compared to the point in time t. Accordingly, one can formally extend the integration limit $t - t_0 \to \infty$. Within this approximation and by using the relations $\underline{C}^\dagger(\tau) = \underline{C}(-\tau)$ and $\underline{G}_\Im^* = \underline{G}_\Im^\intercal$ one finds

$$F_\parallel^{\mathbf{dd}} \overset{t-t_0\gg\tau_\mathrm{trans}}{=} -2\int\mathrm{d}\tau\int_0^\infty\frac{\mathrm{d}\omega}{2\pi}\int\frac{\mathrm{d}^2\mathbf{k}}{(2\pi)^2}\,k_x\,\mathrm{Tr}\left[\underline{G}_\Im^*(\mathbf{k},z_a,\omega)\underline{C}^\dagger(\tau)\right]\,e^{-\mathrm{i}(\mathbf{k}^\intercal\mathbf{v}-\omega)\tau}\,. \tag{3.23}$$

Exploiting the relation between the correlator and its power spectrum then leads to

Noncontact Friction: Backaction

$$F_\parallel^{\mathbf{dd}} = -\,2\int_0^\infty\mathrm{d}\omega\int\frac{\mathrm{d}^2\mathbf{k}}{(2\pi)^2}\,k_x\,\mathrm{Tr}\left[\underline{S}^\intercal(\mathbf{k}^\intercal\mathbf{v}-\omega)\underline{G}_\Im(\mathbf{k},z_a,\omega)\right]. \tag{3.24}$$

This result coincides with the work of other authors [47, 57, 222]. Besides the full results of equations (3.21) and (3.24), the respective local thermal equilibrium approximation can be achieved by substituting $\underline{S} \to \underline{S}^\mathrm{LTE}$ (see equation (3.12)). Combining the two terms $F^{\mathbf{dE}_0}$ and

Local Thermal Equilibrium

[6] One possible way to imagine the switching-on process in this setup is to bring the dipole from far distance to proximity to the surface. Another way is to start with the dipole at rest above the surface. In this situation one can define the whole system being at equilibrium. From here the dipole can be accelerated to the demanded constant velocity v as was described in [43].

$F^{\mathbf{dd}}$ in local thermal equilibrium leads to

$$F_{\parallel}^{\mathrm{LTE}} = -2\int_0^\infty \frac{\mathrm{d}\omega}{2\pi}\int \frac{\mathrm{d}^2\mathbf{k}}{(2\pi)^2} k_x \,\mathrm{Tr}\left[\underline{\alpha}_{\Im}^{\intercal}(\mathbf{k}^{\intercal}\mathbf{v}-\omega)\underline{G}_{\Im}(\mathbf{k},z_a,\omega)\right] \times\left(\frac{2\hbar}{\exp(\beta\hbar\omega)-1}+\frac{2\hbar}{1-\exp(-\beta\hbar(\mathbf{k}^{\intercal}\mathbf{v}-\omega))}\right)$$

$$= -2\hbar\int_0^\infty \frac{\mathrm{d}\omega}{2\pi}\int \frac{\mathrm{d}^2\mathbf{k}}{(2\pi)^2} k_x \,\mathrm{Tr}\left[\underline{\alpha}_{\Im}(\mathbf{k}^{\intercal}\mathbf{v}+\omega)\underline{G}_{\Im}^{\intercal}(\mathbf{k},z_a,\omega)\right] \times\left(\coth\left(\frac{\beta\hbar\omega}{2}\right)-\coth\left(\frac{\beta\hbar(\omega+k_x v)}{2}\right)\right) \tag{3.25}$$

which includes and confirms with the results of Dedkov and Kyasov [129] concerning nonrelativistic noncontact friction in the local thermal equilibrium approximation[7].

Recap: In this section we derived a compact form of the two components of the noncontact friction $F_{\parallel}^{\mathbf{dE}_0}$ and $F_{\parallel}^{\mathbf{dd}}$ in equations (3.21) and (3.24) in the stationary limit.

3.3 Asymptotic Analyses

In this section we investigate various asymptotic regimes of the complete solution given in equations (3.21) and (3.24) of the previous section. As a first step, we restrict our investigation to low temperatures, i.e. $k_{\mathrm{B}}T \ll \hbar|\omega|$, with ω being the dominant frequencies contributing to the noncontact friction. In a second step, expanding the expressions of equations (3.21) and (3.24) to the second leading order in $k_{\mathrm{B}}T \ll \hbar|\omega|$ yields the possibility to study the transition from a realm purely dominated by quantum fluctuations into a regime where both, thermal and quantum fluctuations, are relevant. In order to identify the dominant frequencies contributing to the noncontact friction, we focus onto two general parameters, the velocity v and the distance z_a of the microscopic object with respect to the surface. Eventually, by the comparison of T, v and z_a to the microscopic object's and macroscopic surface's immanent parameters (as e.g. resonance frequency of the dipole moment or the surface plasmon polariton frequency) we distinguish different regimes and characteristics of the noncontact friction.

Low Temperatures

We start the investigation by extracting the asymptotic behavior for low temperatures, which means $k_{\mathrm{B}}T \ll \hbar|\omega|$. When performing this limit we have to bear in mind that, at low temperatures as $T \ll T_{\mathrm{F}}$, the relaxation time of the heat bath might drastically increase, as e.g.

[7] Equation (3.25) represents a more general form compared to the result of Dedkov and Kyasov [129]. In contrast to their result it does not rely on near-field approximation (see appendix F) and considers a polarizability which includes induced frequency shifts, losses and a full tensorial structure instead of a scalar polarizability.

for a perfect crystal[8]. Fortunately, in realistic materials impurities are always present. Impurities lead to defects within the periodicity of the material and thus provide a temperature independent relaxation time which is proportional to the inverse of the impurity concentration $\tau_{e^-\to\mathrm{imp}} \propto \varrho_{\mathrm{imp}}^{-1}$. At low temperatures this provides the dominant relaxation channel in single quasi-particle excitations [226] (see also table 2.1). Here, we like to mention that besides the described single quasi-particle relaxation channels the collective damping mechanism of Landau damping (see section 2.4) can also yield an even faster relaxation channel. In conclusion, as long as we stay below the Fermi-temperature $T \ll T_{\mathrm{F}}$ the modeling in section 2.4 is sufficient, with usual Fermi-temperatures for metals being in the range of $T_{\mathrm{F}} \approx 10^4 - 10^5\,\mathrm{K}$ [138, 227]. Bearing this prologue in mind, we begin with the investigation. The temperature enters the friction in both contributions, i.e. $F_{\parallel}^{\mathbf{dE}_0}$ and $F_{\parallel}^{\mathbf{dd}}$, via the Bose-Einstein distribution (see equations (3.10) and (3.21))

$$n(\omega) = \frac{1}{\exp(\hbar\beta\omega) - 1} \quad \text{or with} \quad n(\omega) + 1 = \frac{1}{1 - \exp(-\hbar\beta\omega)} \tag{3.26}$$

respectively. Subsequently, the singular distribution $n(\omega)$ is expanded for low temperatures, i.e. $|\hbar\beta\omega| \gg 1$. By using the formalism presented Estrada and Fulling [228] the expansion reads (see appendix A)

$$n(\omega) \overset{|\hbar\beta\omega|\gg 1}{\sim} -\theta(-\omega) - \frac{\pi^2}{3}\left(\frac{k_{\mathrm{B}}T}{\hbar}\right)^2 \delta^{(1)}(\omega) + \mathcal{O}(T^4)\,, \tag{3.27}$$

with $\theta(\omega)$ being the Heaviside step function and $\delta^{(n)}(\omega)$ indicates a Dirac delta distribution, with a preceding nth distributional derivative with respect to ω performed on the function the distribution is applied on. The first term of the expansion in equation (3.27) is temperature independent. Since it represents the behavior at effectively zero temperature (on the scale of $\hbar|\omega|/k_{\mathrm{B}}$), this term is solely influenced by quantum fluctuations. The second term slightly departs from absolute zero and thermal fluctuation at the order of $\propto (k_{\mathrm{B}}T)^2/(\hbar\omega)^2$ become relevant. In the temperature independent limit the power spectrum reads (for comparison see [58, 222])

$$\underline{S}(\omega) \overset{T=0}{\sim} \frac{\hbar}{\pi}\,\underline{\alpha}(\omega)\left\{\int \frac{\mathrm{d}^2\mathbf{k}}{(2\pi)^2}\underline{G}_{\Im}(\mathbf{k}, z_a, \mathbf{k}^{\mathsf{T}}\mathbf{v} + \omega)\theta(\mathbf{k}^{\mathsf{T}}\mathbf{v} + \omega) + \frac{\omega\mu_R(\omega)}{\alpha_0\omega_a^2}\theta(\omega)\right\}\underline{\alpha}^{\dagger}(\omega)\,. \tag{3.28}$$

The temperature independent backaction contribution of the force $F^{\mathbf{dd}}$ then follows accordingly by inserting $\underline{S}(\omega)$ as shown in equation (3.24). The frictional force contribution, stemming of the direct scattering with the random electric field $F^{\mathbf{dE}_0}$, yields in the temperature

[8] For instance at $T \ll T_{\mathrm{F}}$ in an ideal metal, i.e. perfectly aligned lattice without any defects, the relaxation time stemming from the electron-phonon scattering is $\tau_{e^-\to\mathrm{ph}} \propto T^{-5}$ and the relaxation time with respect to the electron-electron scattering with $\tau_{e^-\to e^-} \propto T^{-(2\cdots 3)}$ [226].

independent limit

$$F^{\mathbf{dE}_0} \overset{T=0}{\sim} 4\int_0^\infty \frac{\mathrm{d}\omega}{2\pi}\int \frac{\mathrm{d}^2\mathbf{k}}{(2\pi)^2} k_x\, \hbar\theta(-\omega)\mathrm{Tr}\left[\underline{\alpha}_{\Im}^{\intercal}(\mathbf{k}^{\intercal}\mathbf{v}-\omega)\underline{G}_{\Im}(\mathbf{k},\omega)\right] = 0\,. \tag{3.29}$$

From here on we conveniently drop the subscript $\|$. The $\langle\hat{\mathbf{d}}\hat{\mathbf{E}}_0\rangle$ contribution vanishes for $T\to 0$ due to the integration limits introduced by the Heaviside function that only allow the contribution $\omega = 0$, which vanishes, due to $\underline{G}_{\Im}(\mathbf{k},0) = 0$, too. Thus, the dipole moment's autocorrelator is the only relevant contribution for the $T\to 0$ limit. At the second order one finds

$$\underline{S}(\omega) \overset{\mathcal{O}(T^2)}{\sim} \frac{\pi(k_\mathrm{B}T)^2}{3\hbar}\underline{\alpha}(\omega)\left\{\int \frac{\mathrm{d}^2\mathbf{k}}{(2\pi)^2}\underline{G}'_{\Im}(\mathbf{k},z_a,0)\delta(\mathbf{k}^{\intercal}\mathbf{v}+\omega) + \frac{\mu_R(0)}{\alpha_0\omega_a^2}\delta(\omega)\right\}\underline{\alpha}^{\dagger}(\omega) \tag{3.30}$$

and

$$F^{\mathbf{dE}_0} \overset{\mathcal{O}(T^2)}{\sim} -\frac{\pi(k_\mathrm{B}T)^2}{3\hbar}\int \frac{\mathrm{d}^2\mathbf{k}}{(2\pi)^2} k_x\,\mathrm{Tr}\left[\underline{\alpha}_{\Im}^{\intercal}\left(\mathbf{k}^{\intercal}\mathbf{v}\right)\underline{G}'_{\Im}\left(\mathbf{k},z_a,0\right)\right], \tag{3.31}$$

where the prime indicates the derivative with respect to ω before setting $\omega\to 0$. Here we used the fact, that due to reality of the response in time all response functions, e.g. $\underline{G}$ or μ, have to fulfill $\mathcal{R}(\omega) = \mathcal{R}(-\omega)^*$. Therefore, their imaginary part, which is uneven in frequency, has to vanish at zero frequency [73].

Rather than calculating higher orders in the limit $\hbar|\omega| \gg k_\mathrm{B}T$, we turn towards the behavior in the classic limit $\hbar|\omega| \ll k_\mathrm{B}T$. In the classic limit the quantumness of the system is expected to lose its importance. The respective expression was already derived in section 1.2 and reads

$$\frac{1}{1-\exp(-\hbar\omega\beta)} \overset{\hbar|\omega|\ll k_\mathrm{B}T}{\sim} \frac{k_\mathrm{B}T}{\hbar\omega}\,. \tag{3.32}$$

However, as elaborated at the beginning of this section, the validity of the derived material model in section 2.4 has the upper bound $T \ll T_\mathrm{F}$. In proximity or even beyond T_F, the temperature dependent shape of the Fermi-Dirac distribution (see equation (2.77)) has to be considered. Furthermore, at high temperatures ($T > T_\mathrm{F}$) one also has to reevaluate the hierarchy of collision times (see table 2.1), since electron-phonon scattering usually provides the dominant mechanism in this regime. Nevertheless, if remaining in the realm of $T \ll T_\mathrm{F}$, the classical results reads

$$\underline{S}(\omega) \overset{\hbar|\omega|\ll k_\mathrm{B}T}{\sim} \frac{k_\mathrm{B}T}{\pi}\,\underline{\alpha}(\omega)\left\{\int \frac{\mathrm{d}^2\mathbf{k}}{(2\pi)^2}\frac{\underline{G}_{\Im}(\mathbf{k},z_a,\mathbf{k}^{\intercal}\mathbf{v}+\omega)}{\omega+\mathbf{k}^{\intercal}\mathbf{v}} + \frac{\mu_R(\omega)}{\alpha_0\omega_a^2}\right\}\underline{\alpha}^{\dagger}(\omega) \tag{3.33}$$

and

$$F^{\mathbf{dE}_0} \overset{\hbar|\omega|\ll k_\mathrm{B}T}{\sim} -2\int_0^\infty \frac{\mathrm{d}\omega}{2\pi}\int \frac{\mathrm{d}^2\mathbf{k}}{(2\pi)^2} k_x\,\frac{2k_\mathrm{B}T}{\omega}\mathrm{Tr}\left[\underline{\alpha}_{\Im}^{\intercal}(\mathbf{k}^{\intercal}\mathbf{v}-\omega)\underline{G}_{\Im}(\mathbf{k},z_a,\omega)\right]. \tag{3.34}$$

As expected, the "quantum indicator" $\hbar$ vanishes in this limit. Both limits, i.e. $k_\mathrm{B}T \ll \hbar|\omega|$ and

$k_\mathrm{B}T \gg \hbar|\omega|$, were achieved by comparing the temperature to a dominant contribution at ω. In the following we identify the dominant frequency regime and relate it to general parameters of the system, i.e. the velocity v and the distance z_a of the microscopic object from the surface.

Dominant Frequencies

Within the noncontact friction (see equations (3.21) and (3.24)) three quantities are intertwined: the Bose-Einstein distribution $n(\omega)$, the polarizability $\underline{\alpha}$ of the dipole moment and the electric Green's tensor $\underline{G}$. The interplay of these three quantities determines the relevant frequencies contributing to the noncontact friction. As we already know from the discussion above, $n(\omega)$ does either yield a sharply truncated distribution in the case of $k_\mathrm{B}T \ll \hbar|\omega|$, or a smooth $1/\omega$ distribution in the case of $k_\mathrm{B}T \gg \hbar|\omega|$. In the subsequent considerations, we investigate the two remaining quantities, i.e. $\underline{\alpha}$ and $\underline{G}$, under the assumption that we can impose either $k_\mathrm{B}T \ll \hbar|\omega|$ or $k_\mathrm{B}T \gg \hbar|\omega|$. As denoted in equation (2.39), the Green's tensor can be separated into a free vacuum part $\underline{G}_0$ and a scattered part $\underline{g}$ (see also equation (2.41)). Despite operating within non-relativistic framework, the chosen description has to preserve Lorentz invariance in the vacuum. By demanding Lorentz invariance to be preserved for the vacuum part, the moving microscopic object can effectively be boosted in its respective rest frame, where it experiences non-Doppler shifted vacuum fluctuations. This allows to omit the Doppler shift in each appearance of $\underline{G}_0$. Thus, with respect to noncontact friction the contribution of the vacuum part is sub-leading[9] [10] . This is not true for the scattered part. Here, Lorentz invariance is broken due to the losses at the surface. Therefore, the Doppler shift in $\underline{g}$ has to be considered even at $T = 0$. In the limit of $k_\mathrm{B}T \ll \hbar|\omega|$ only the backaction term contributes to the noncontact friction, which leads to

$$F = -2\int_0^\infty \mathrm{d}\omega \int \frac{\mathrm{d}^2\mathbf{k}}{(2\pi)^2}\, k_x \,\mathrm{Tr}\left[\underline{S}^\intercal(\mathbf{k}^\intercal\mathbf{v}-\omega)\underline{g}_{\Im}(\mathbf{k}, z_a, \omega)\right]. \tag{3.35}$$

Since the chosen geometry of the setup is symmetric in y direction (see section 2.3), all odd terms in k_y vanish under a symmetric integration. When omitting the odd k_y terms, the scattered Green's tensor splits into two terms

$$\underline{g}(\mathbf{k}, z_a, \omega) = \underline{\sigma}(\mathbf{k}, z_a, \omega) - \phi_y(\mathbf{k}, z_a, \omega)\underline{L}_y \tag{3.36}$$

where $\underline{\sigma}$ is a diagonal matrix and $\underline{L}_y$ is the yth component of the 3D rotation group's Lie algebra $\mathfrak{so}(3)$ (where $[\underline{L}_i]_{jk} = -\mathrm{i}\epsilon_{ijk}$ and ϵ_{ijk} is the Levi-Civita symbol). The function ϕ_y collects the prefactor of the skew symmetric matrix. Since $\underline{L}_y^\dagger = \underline{L}_y$, we can write $\underline{g}_{\Im} = \mathrm{Im}\{\underline{\sigma}\} - \mathrm{Im}\{\phi\}\underline{L}_y$. Due to the applied trace the force splits up into two additive contributions, where one contains

[9] However, in the polarizability the vacuum Green's tensor in general has to be considered to cover spontaneous decay and frequency shift in empty space [229–231].

[10] This statement is only true in the limit of $\hbar|\omega| \gg k_\mathrm{B}T$. Especially in the opposite case $\hbar|\omega| \gg k_\mathrm{B}T$ the vacuum contribution must not be neglected.

the symmetric parts of $\underline{S}$ and $\underline{g}$ and the other contains the antisymmetric parts [58]

$$F^{(\mathrm{s})} = -2\int_0^\infty \mathrm{d}\omega \int \frac{\mathrm{d}^2\mathbf{k}}{(2\pi)^2}\, k_x \,\mathrm{Tr}\left[\underline{S}^{(\mathrm{s})}(\mathbf{k}^\intercal\mathbf{v}-\omega)\mathrm{Im}\{\underline{\sigma}(\mathbf{k},z_a,\omega)\}\right] \tag{3.37}$$

$$F^{(\mathrm{a})} = -2\int_0^\infty \mathrm{d}\omega \int \frac{\mathrm{d}^2\mathbf{k}}{(2\pi)^2}\, k_x \,\mathrm{Im}\{\phi_y(\mathbf{k},z_a,\omega)\}\mathrm{Tr}\left[\underline{S}^{(\mathrm{a})}(\mathbf{k}^\intercal\mathbf{v}-\omega)\underline{L}_y\right], \tag{3.38}$$

where the superscripts (a) and (s) denote the antisymmetric and symmetric part, respectively. A separation into a symmetric and antisymmetric part of the force is true in general and not only for low temperatures. The power spectrum for $k_\mathrm{B}T \ll \hbar|\omega|$ (see equations (3.28) and (3.30)) is truncated by either a Heaviside function or a Dirac delta distribution (see equations (3.28) and (3.30)). The power spectrum within the backaction contribution carries the Doppler-shifted frequency $\mathbf{k}^\intercal\mathbf{v}-\omega$. Therefore, the truncation yields two inequalities (for details see appendix F)

$$\frac{\omega}{c} \ll \frac{\omega}{v} \leq \begin{cases} k & \text{local thermal contribution} \\ k+k' & \text{nonlocal contribution} \end{cases} \tag{3.39}$$

The two cases result from either the local thermal contributions which contain frequency distributions without Doppler shift or nonlocal contributions with Doppler-shifted distributions. Here, the k' denotes the wavevector integration within the power spectrum. The first relation in equation (3.39) stems from restriction to non-relativistic velocities $v \ll c$ and solely positive frequencies. In the following we restrict our calculations to the near-field contribution of the scattered Green's tensor (for more details see appendix F). In the near-field limit $\kappa = \sqrt{k^2-\omega^2/c^2} \sim k$ and thus prominently evanescent waves contribute to the interaction between the moving object and the surface. Additionally, the scattered Green's tensor, in the near-field limit, sets an upper bound $k \lesssim 1/(2z_a)$ to the wavevector integration by the exponential decay $\exp(-2\kappa z_a)$ away from the surface. Combining equation (3.39) with this upper bound yields an estimate for the frequencies contributing to the noncontact friction

$$\omega \lesssim \frac{v}{z_a}. \tag{3.40}$$

In order to be compatible with the low temperature limit one can extract a threshold temperature of the dominant regime $T_\mathrm{th} = \frac{\hbar v}{k_\mathrm{B} z_a}$. Thus, at e.g. $v = 10^{-5}c$ (as for instance presented in [232] for Li atoms) and $z_a = 20\,\mathrm{nm}$ (as for example in a slit experiment with $50\,\mathrm{nm}$ slit width [233]) one would need to cool down the system to $T \ll T_\mathrm{th} \approx 100\,\mathrm{K}$ to apply a low temperature analysis as shown above. This does not mean, that above T_th there is no noncontact friction. It only states, that above that point we might need further correction terms concerning the temperature. The previous line of argumentation changes when turning towards higher temperatures, since the power spectrum is not sharply truncated for $k_\mathrm{B}T \gg \hbar|\omega|$. However, before commenting on the high-temperature limit we focus on the polarizability.

Polarizability

We derived the polarizability from the dipole moment's equation of motion (see equation (3.3)). In order to derive the equation of motion a weak coupling to an internal bath as well as to the

electric field was assumed. In the following the polarizability is expanded with respect to the weak coupling. As long as one investigates frequencies far below the resonance frequency ω_a, i.e. $|\omega| \ll \omega_a$, the expansion to the first leading order simply yields

$$\underline{\alpha}(|\omega| \ll \omega_a) \sim \alpha_0 \mathbb{1} + \mathcal{O}(\alpha_0^2). \tag{3.41}$$

If one evaluates the polarizability far above ω_a, i.e. $|\omega| \gg \omega_a$, one will find a strongly decreasing polarizability[11]

$$\underline{\alpha}(|\omega| \gg \omega_a) \sim -\alpha_0 \frac{\omega_a^2}{\omega^2} \mathbb{1} + \mathcal{O}(\alpha_0^2). \tag{3.42}$$

When approaching $\omega \approx \omega_a$ the Sokhotski–Plemelj theorem [234] can be used to evaluate the different elements of the polarizability (for the calculation of the elements see appendix B). For the diagonal elements this directly leads to

$$\lim_{\alpha_0, \mu \to 0} [\underline{\alpha}(\omega)]_{ii} = \lim_{\epsilon_{ii} \to 0^+} \frac{\alpha_0 \omega_a^2}{\omega_a^2 - \omega^2 - \mathrm{i}\epsilon_{ii}} = \alpha_0 \omega_a^2 \left(\mathcal{P}\left(\frac{1}{\omega_a^2 - \omega^2} \right) + \mathrm{i}\pi \delta(\omega_a^2 - \omega^2) \right) \tag{3.43}$$

where $\mathcal{P}$ denotes the Cauchy principal value, and ϵ_{ii} collects all small contributions with respect to the iith element of the polarizability. Here, the small frequency shift induced by the Green's tensor is omitted compared to the much larger ω_a. The off-diagonal terms are higher order in α_0 and are thus neglected. The polarizability contributes to the noncontact friction via the power spectrum $\underline{S}$ and $\underline{\alpha}_{\Im}$. In the case of $\omega \ll \omega_a$ in both expressions $\underline{\alpha} \to \alpha_0 \mathbb{1}$ can be substituted. In the case of $\omega \approx \omega_a$ we find

$$\underline{S}(\omega \approx \omega_a) = \hbar \alpha_0 \omega_a^2 \delta(\omega_a^2 - \omega^2) \sum_{j=x,y,z} \mathbf{e}_j \otimes \mathbf{e}_j \frac{\mathrm{Im}\{\Sigma_j^{n+} + \mathrm{i}n(\omega)\frac{\mu\omega}{\alpha_0 \omega_a^2}\}}{\mathrm{Im}\{\Sigma_j + \mathrm{i}\frac{\mu\omega}{\alpha_0\omega_a^2}\}}, \tag{3.44}$$

where

$$\Sigma_j = \int \frac{\mathrm{d}^2\mathbf{k}}{(2\pi)^2} \sigma_j(\mathbf{k}, k_x + \omega), \qquad \Pi_i = \int \frac{\mathrm{d}^2\mathbf{k}}{(2\pi)^2} \phi_i(\mathbf{k}, k_x + \omega). \tag{3.45}$$

and the superscript $n+$ indicates that the respective integration is weighted by $n(\omega + k_x v) + 1$. Here, we did not yet specify the ratio between $\alpha_0 \omega_a^2$ and $\mu\omega$. If we choose a setup with a dominant coupling to the internal bath — compared to the coupling to the electric field — the power spectrum simplifies to

$$\underline{S}(\omega \approx \omega_a) = \hbar \alpha_0 \omega_a^2 \delta(\omega_a^2 - \omega^2)[n(\omega) + 1]\mathbb{1}, \tag{3.46}$$

which coincides with the local thermal equilibrium approximation. This result is expected, as long as the coupling to the internal bath — which is described in local thermal equilibrium —

[11] In this limit we might have to reconsider the validity of the harmonic oscillator model presented in section 2.2, as higher energies might lead to relevant anharmonicity of the restoring potential.

is dominant. In the opposite case, i.e. the coupling to the field is dominant compared to the coupling to the internal bath, the diagonal matrix reads (see appendix B)

$$\underline{S}(\omega \approx \omega_a) = \hbar\alpha_0\omega_a^2\delta(\omega_a^2 - \omega^2) \sum_{j=x,y,z} \mathbf{e}_j \otimes \mathbf{e}_j \frac{\mathrm{Im}\{\Sigma_j^{n+}\}}{\mathrm{Im}\{\Sigma_j\}}, \tag{3.47}$$

which does not resemble the local equilibrium result due to its Doppler-shifted frequency distribution $n(\omega + k_x v)$. Surprisingly, Intravaia et al. [222] found that the resulting noncontact force for a non-rotating dipole moment coincides again with its result obtained using the local thermal equilibrium approximation. This coincidence is elaborated in appendix B. Essentially, we found that the low-temperature distribution $n(\omega + k_x v) \overset{T\to 0}{\to} \theta(\omega + k_x v)$ in the limit of $\frac{v}{2z_a} \geq \omega_a$ can be approximated by $\theta(\omega + k_x v) \approx \theta(k_x)$. While this seems to be in stark contrast to the local thermal equilibrium approximation, where $\theta(\omega + k_x v) \approx \theta(k_x)$, interestingly — due to the high symmetry of the according integrands — both expressions yield the very same result in the limit of $\frac{v}{2z_a} \leq \omega_a$.

Concluding Estimates and Remarks

On the previous detour with respect to the polarizability, we showed that the resonant frequency strongly determines the power spectrum and effectively restricts[12] it to $\omega \leq \omega_a$. Applying this knowledge to the $k_\mathrm{B}T \ll \hbar|\omega|$ case, where we found the relation $\omega \lesssim v/z_a$, we can identify two regimes: the nonresonant regime, where $\omega_a \gg v/z_a$ and the resonant regime, where $\omega_a \leq v/z_a$. While the nonresonant regime features a broad band of low frequencies $\lesssim v/z_a$ contributing to the noncontact friction, the resonant regime is dominated by the resonant frequency ω_a. To account some numbers to the point at which we expect the resonant regime to dominate, we estimate the resonance frequency with a usual atomic dipole transition, as e.g. for ^{87}Ru [235], with $\omega_a \approx 1.3\,\mathrm{eV}$. When choosing nanometres as length scale, we find

$$\frac{v}{c} \approx z_a[\mathrm{nm}]\frac{1.3}{1.97} \times 10^{-2}. \tag{3.48}$$

For example, at an already experimentally challenging distance of $1\,\mathrm{nm}$, we would expect to enter the resonant regime at the order of $v \approx 10^{-2}c$, which is on the one hand experimentally challenging and on the other hand at the border of the validity of a non-relativistic theory. For larger distances the resonant velocity would be even closer to c. Thus, in realistic and experimentally accessible scenarios, one rather operates in the regime $\omega_a \gg v/z_a$. Nonetheless, one can use lower resonance frequencies to lower this restriction. Finally, we turn to the high temperature limit $k_\mathrm{B}T \gg \hbar|\omega|$. Here, there is no sharp truncation of the frequency and a broad spectrum of frequencies is relevant. However, the distribution $n(\omega) + 1 \approx k_\mathrm{B}T/(\hbar\omega)$ still favors predominantly low frequencies. Therefore the high temperature regime noncontact friction is again dominated by the strong peak at ω_a. Converting the resonance frequency at e.g. $\omega_a \approx 1.3\mathrm{eV}$ to the corresponding temperature $T_a = \hbar\omega_a/k_\mathrm{B}$, we find $T_a \approx 10^4\,\mathrm{K}$, which is in the regime of the Fermi temperature. Consequently, the high temperature limit is dominant for $T \gg T_a$. As T_a is on the order of usual Fermi temperatures, an adapted mate-

[12] The restriction only applies to $\underline{G}_\Im \propto \omega^m$ with $m < 2$. Otherwise, for $m \geq 2$, the Green's tensor compensates the decay for higher frequencies and also higher frequencies have to be considered.

rial model for temperatures around or above T_F might be used in this high temperature regime.

Recap: Within this section we discussed the relevant contributions to the noncontact friction concerning temperature, velocity and distance. The relevant contributions are determined by the Bose-Einstein distribution $n(\omega)$, the Green's tensor $\underline{G}(\mathbf{k}, z_a, \omega)$ and the polarizability $\alpha(\omega)$. Furthermore, we derived several asymptotic expressions for the respective regimes of T, v and z_a.

3.4 Asymptotic Results

The discussion of the previous section highlighted the characteristic behavior of the quantities $n(\omega)$, $\underline{G}(\mathbf{k}, z_a, \omega)$, and $\alpha(\omega)$ with respect to T, v, z_a, and ω_a. In the current section this knowledge is applied to obtain respective asymptotic results of the noncontact friction. For the sake of brevity some lengthy calculations are shifted into the respective appendices. We derive the asymptotes in the low temperature case ($\hbar|\omega| \gg k_\mathrm{B}T$, for more details see section 3.3) in the first two leading orders. The high temperature case $\hbar|\omega| \ll k_\mathrm{B}T$ is currently under investigation and will not be elaborated further within this thesis. The first (temperature-independent) order is identified with the so-called *quantum friction* [45, 57, 130], since it is governed by quantum fluctuations. Within the low temperature limit we distinguished earlier the cases $v/z_a \ll \omega_a$ and $v/z_a \gg \omega_a$. However, as argued with the relation presented in equation (3.48) we identified the case $v/z_a \ll \omega_a$ to be more relevant in actual realizable experiments. Therefore, we move the discussion concerning the resonant regime, i.e. $v/z_a \gg \omega_a$, to appendix B. In a first step, we discuss the impact of nonlocality and non-Ohmicity on the temperature independent quantum friction. In a second step, we turn towards the first temperature correction and elucidate the competing mechanisms of thermal and quantum fluctuations in the context of the low-temperature noncontact friction. Finally, we elaborate on connections of the noncontact friction to the spin-momentum locking of light and the anomalous Doppler effect of surface plasmon polaritons.

Quantum Friction

As it was shown in section 3.3, of the two contributions of noncontact friction, i.e. $F^{\mathbf{dE}_0}$ and $F^{\mathbf{dd}}$, only the latter contributes in the lowest order of $\hbar|\omega| \gg k_\mathrm{B}T$. In order to perform the calculations of the noncontact friction as lucid as possible, we use the following expression of equation (3.24) (a short derivative is given in chapter 4)

$$F_{T=0} = -2\int \mathrm{d}\omega \int \frac{\mathrm{d}^2\mathbf{k}}{(2\pi)^2}\, k_x\, \mathrm{Tr}\left[\underline{S}(\omega)\underline{G}_{\Im}(\mathbf{k}, z_a, k_x v + \omega)\right]\, \theta(-k_x v - \omega)\,. \tag{3.49}$$

In a next step the power spectrum is separated with respect to the internal and induced bath

$$\underline{S}(\omega) = \underline{S}^{\mu}(\omega) + \underline{S}^{G}(\omega), \tag{3.50}$$

where the superscript μ indicates the internal bath, and G the induced bath of the medium

assisted electromagnetic field. For the two terms we find

$$\underline{S}^{\mu}(\omega) = \frac{\hbar}{\pi}\frac{\omega\mu_R(\omega)}{\alpha_0\omega_a^2}\underline{\alpha}(\omega)\underline{\alpha}^{\dagger}(\omega)\theta(\omega)\,, \tag{3.51}$$

$$\underline{S}^{G}(\omega) = \frac{\hbar}{\pi}\underline{\alpha}(\omega)\int\frac{\mathrm{d}^2\mathbf{k}}{(2\pi)^2}\underline{G}_{\Im}(\mathbf{k}, z_a, k_x v+\omega)\theta(k_x v+\omega)\underline{\alpha}^{\dagger}(\omega)\,, \tag{3.52}$$

and the corresponding force contributions

$$\begin{aligned} F^{\mu}_{T=0} = &-\frac{2\hbar}{\pi}\int\frac{\mathrm{d}^2\mathbf{k}}{(2\pi)^2}\,k_x\,\theta(-k_x)\int_0^{-k_x v}\mathrm{d}\omega\,\frac{\omega\mu_R(\omega)}{\alpha_0\omega_a^2} \\ &\times\mathrm{Tr}\left[\underline{\alpha}(\omega)\underline{\alpha}^{\dagger}(\omega)\underline{G}_{\Im}(\mathbf{k}, z_a, k_x v+\omega)\right]\,, \end{aligned} \tag{3.53}$$

$$\begin{aligned} F^{G}_{T=0} = &-\frac{2\hbar}{\pi}\int\frac{\mathrm{d}^2\mathbf{k}}{(2\pi)^2}\,k_x\int\frac{\mathrm{d}^2\mathbf{k}'}{(2\pi)^2}\theta(k_x'-k_x)\int_{-k_x' v}^{-k_x v}\mathrm{d}\omega \\ &\times\mathrm{Tr}\left[\underline{\alpha}(\omega)\underline{G}_{\Im}(\mathbf{k}', k_x' v+\omega)\underline{\alpha}^{\dagger}(\omega)\underline{G}_{\Im}(\mathbf{k}, k_x v+\omega)\right]\,. \end{aligned} \tag{3.54}$$

In the following we focus on the nonresonant regime ($\omega_a \gg v/z_a$). The detailed discussion of the resonant regime is shifted to appendix B. In the nonresonant regime the polarizability reduces to $\underline{\alpha}(\omega) \sim \alpha_0\mathbb{1}$. The respective noncontact friction reduces consequently to

$$F^{\mu}_{T=0} \overset{\omega_a\gg v/z_a}{=} -\alpha_0\frac{2\hbar}{\pi}\int\frac{\mathrm{d}^2\mathbf{k}}{(2\pi)^2}\,k_x\,\theta(-k_x)\int_0^{-k_x v}\mathrm{d}\omega\,\frac{\omega\mu_R(\omega)}{\omega_a^2}\mathrm{Tr}\left[\mathrm{Im}\{\underline{\sigma}(\mathbf{k}, k_x v+\omega)\}\right] \tag{3.55}$$

and

$$\begin{aligned} F^{G}_{T=0} \overset{\omega_a\gg v/z_a}{=} &-\alpha_0^2\frac{2\hbar}{\pi}\int\frac{\mathrm{d}^2\mathbf{k}}{(2\pi)^2}\,k_x\int\frac{\mathrm{d}^2\mathbf{k}'}{(2\pi)^2}\theta(k_x'-k_x)\int_{-k_x' v}^{-k_x v}\mathrm{d}\omega \\ &\times\Big\{\mathrm{Tr}\left[\mathrm{Im}\{\underline{\sigma}(\mathbf{k}, k_x v+\omega)\}\mathrm{Im}\{\underline{\sigma}(\mathbf{k}', k_x' v+\omega)\}\right] \\ &+2\mathrm{Im}\{\phi_y(\mathbf{k}, k_x v+\omega)\}\mathrm{Im}\{\phi_y(\mathbf{k}', k_x' v+\omega)\}\Big\}, \end{aligned} \tag{3.56}$$

where $\underline{g} = \underline{\sigma} - \phi_y\underline{L}_y$ was used, with $\underline{\sigma}$ being the diagonal part and $-\phi_y\underline{L}_y$ being the antisymmetric part of the scattered Green's tensor. The two force contributions carry a different orders in α_0. While F^{μ} includes processes with one interaction with the internal bath and one to the external bath of the electromagnetic field, F^{G} includes processes interacting twice with the electric field. Furthermore, we notice two additive contributions in the F^{G} term. One including twice the diagonal elements of the Green's tensor and the other containing twice the off-diagonal contribution. To understand the separation into diagonal and off-diagonal contribution, we recall the associated electric fields. The diagonal matrix $\underline{\sigma}$ is associated with linear polarized electric fields and the $-\phi_y\underline{L}_y$ term is associated with circular polarized electric

fields. Similar to $\underline{g}$, the dipole moment's dynamic can be separated into linear oscillations and rotation, too. When the dipole moment absorbs or emits excitations of the electric fields, the different polarizations, i.e. linear and circular, account for different degrees of freedom in the dipole moment, i.e. oscillation or rotation.

Internal Bath

In order to perform further calculations, on the one hand the frequency distribution of the internal bath and on the other hand the frequency distribution of the electric field have to be considered. The latter is determined by the reflection coefficients. In section 2.2 an unstructured internal bath as well as a structured bath, where one specific bath mode to couples significantly stronger than every other bath mode, were considered. As the unstructured case is contained within the structured case (in the limit of the coupling to the distinct mode $g \to 0$), only the latter is considered. With ω_{phon} being the resonance frequency of the single distinct bath mode, an additional frequency scale is introduced. Analogously to the polarizability (for details see appendix E) we find

$$\begin{aligned} &\mu_R(\omega \ll \omega_{\mathrm{phon}}) \sim \gamma + \gamma_{\mathrm{phon}} \frac{g^2}{\omega_{\mathrm{phon}}^2}, \quad \mu_R(\omega \gg \omega_\mu) \sim \gamma, \\ &\text{and} \quad \mu_R(\omega \approx \omega_{\mathrm{phon}}) \sim \gamma + \pi g^2 \delta(\omega_{\mathrm{phon}}^2 - \omega^2), \end{aligned} \tag{3.57}$$

where γ is the decay rate of the dipole resonance and γ_{phon} is the decay rate of the distinct internal mode with respect to the internal bath. The structured model can, for instance, be used to model a small nanoparticle. In the case of a gold nanosphere López et al. [158] related the distinct bath mode frequency to the dipole resonance by $\omega_{\mathrm{phon}} \approx 1.8 \times 10^{-3} \omega_a$, where $\omega_a \approx 1\,\mathrm{eV}$. Thus, ω_{phon} yields an additional energy scale to consider within the $\omega_a \gg v/z_a$ limit. With ω_{phon} being magnitudes smaller than ω_a, the resonance of the distinct bath mode can relevantly contribute to the noncontact friction (see equation (3.48)). The F^μ contribution accordingly divides into a nonresonant and a resonant contribution with respect to ω_{phon}

$$F^\mu_{T=0} \overset{\omega_{\mathrm{phon}} \gg v/z_a}{=} -\alpha_0 \frac{2\hbar}{\pi} \int \frac{\mathrm{d}^2\mathbf{k}}{(2\pi)^2}\, k_x\, \theta(-k_x) \int_0^{-k_x v} \mathrm{d}\omega\, \frac{\omega \mu_R(0)}{\omega_a^2} \mathrm{Tr}\left[\mathrm{Im}\{\underline{\sigma}(\mathbf{k}, k_x v + \omega)\}\right], \tag{3.58}$$

$$\begin{aligned} F^\mu_{T=0} \overset{\omega_{\mathrm{phon}} \ll v/z_a}{=}\ & -\alpha_0 \frac{2\hbar}{\pi} \int \frac{\mathrm{d}^2\mathbf{k}}{(2\pi)^2}\, k_x\, \theta(-k_x) \int_0^{-k_x v} \mathrm{d}\omega\, \frac{\omega \gamma_{\mathcal{B}}}{\omega_a^2} \mathrm{Tr}\left[\mathrm{Im}\{\underline{\sigma}(\mathbf{k}, k_x v + \omega)\}\right] \\ & - \alpha_0 2\hbar \int \frac{\mathrm{d}^2\mathbf{k}}{(2\pi)^2}\, k_x\, \theta(-\omega_{\mathrm{phon}} - k_x v) \frac{g^2}{\omega_a^2} \mathrm{Tr}\left[\mathrm{Im}\{\underline{\sigma}(\mathbf{k}, k_x v + \omega_{\mathrm{phon}})\}\right]. \end{aligned} \tag{3.59}$$

Dissipative Reflection

To finish the calculations, we turn towards the frequency distribution of the electric Green's tensor. In the near-field limit the scattered Green's tensor takes the form [47]

$$\underline{g}(\mathbf{k}, \omega) = \frac{k e^{-2 z_a k}}{2\epsilon_0} \begin{pmatrix} k_x^2/k^2 & 0 & -\mathrm{i} k_x/k \\ 0 & k_y^2/k^2 & 0 \\ \mathrm{i} k_x/k & 0 & 1 \end{pmatrix} r^p(\omega, k). \tag{3.60}$$

Here, we already dropped the odd orders of k_y in anticipation that they vanish concerning the

symmetric integration. For $\underline{g}_{\Im}$ we find $\underline{g}_{\Im} \propto \mathrm{Im}\{r^p(\omega,k)\}$, i.e $\mathrm{Im}\{\underline{\sigma}\} \propto \mathrm{Im}\{r^p(\omega,k)\}$ and $\mathrm{Im}\{\phi_y\} \propto \mathrm{Im}\{r^p(\omega,k)\}$. Thus, the imaginary part of the p (transverse magnetic) polarized reflection coefficient encodes the relevant information about the frequency distribution of the scattered Green's tensor and can be used as a lever to alter noncontact friction. The impact of this lever and the possibility to tailor the noncontact friction through it, was demonstrated by Oelschläger et al. [46, 236]. Similarly to the discussion concerning the distinct resonance of the internal bath, the reflection coefficient's frequency distribution is determined by a characteristic frequency. The most prominent might be the surface plasmon polariton frequency ω_{sp}. Surface plasmon polaritons — mixed quasi-particles of plasma oscillations and the electric field at an interface — have already been on their own a topic of high interest for a long period of time [124, 237–241]. In semi-infinite bulk geometries (see section 2.3) with local material models (see section 2.4) surface plasmon polaritons can be found as poles of the near-field p polarized reflection coefficient

$$r^p(\omega) \overset{\text{near}}{\sim} \frac{\epsilon(\omega)-1}{\epsilon(\omega)+1} \qquad \Rightarrow \qquad \epsilon(\omega_{\mathrm{sp}}) = -1. \tag{3.61}$$

Usually at vacuum material interfaces these excitations are on the same order of magnitude or even larger than the atomic resonances $\omega_{\mathrm{sp}} \approx 1 \cdots 10\,\mathrm{eV}$ [200][13]. Considering "usual" bulk materials, one can expand the reflection coefficient on the scale $\omega \ll \omega_{\mathrm{sp}}$ and obtains

$$r^p(\omega) = r^p(0) + r^{p\prime}(0)\omega + \mathcal{O}(\frac{\omega^2}{\omega_{\mathrm{sp}}^2}) = r^p(0) + 2\mathrm{i}\epsilon_0\rho_{\mathrm{loc}}\omega + \mathcal{O}(\frac{\omega^2}{\omega_{\mathrm{sp}}^2}), \tag{3.62}$$

where local resistivity $\rho_{\mathrm{loc}} = r^{p\prime}(0)/(2\mathrm{i}\epsilon_0)$ was introduced. Due to reality of the response in time ($r(-\omega) = r^*(\omega)$) the even orders in ω appear as purely real quantities and the odd orders as purely imaginary quantities. Such a linear regime in ω is called Ohmic in analogy to an Ohmic heat bath (see section 1.2). The two local models introduced in section 2.4, are the Drude model and the dielectric Lorentz peaks. For a local Drude model we find $\rho_{\mathrm{loc}} = \gamma_{\mathrm{D}}/(\epsilon_0\omega_{\mathrm{p}}^2)$ with ω_{p} being the plasma frequency and γ_{D} the respective damping. For a dielectric with a single resonance frequency ω_0 with damping γ_0 and static polarizability α_{die} we find $\rho_{\mathrm{loc}} = \gamma_0\alpha_{\mathrm{die}}/([2+\alpha_{\mathrm{die}}]^2\omega_0^2)$. Employing local materials in Ohmic approximation, the noncontact friction above a semi-infinite bulk yields

$$F_{T=0}^{G} \approx -(63-45)\frac{\hbar\alpha_0^2\rho_{\mathrm{loc}}^2}{\pi^3}\frac{v^3}{(2z_a)^{10}} \tag{3.63}$$

$$F_{T=0}^{\mu} \overset{\omega_{\mathrm{phon}}\gg v/z_a}{\approx} -45\frac{\hbar\alpha_0\rho_{\mathrm{loc}}}{\pi^2}\frac{\mu_R(0)}{\omega_a^2}\frac{v^3}{(2z_a)^7} \tag{3.64}$$

$$F_{T=0}^{\mu} \overset{\omega_{\mathrm{phon}}\ll v/z_a}{\approx} -45\frac{\hbar\alpha_0\rho_{\mathrm{loc}}}{\pi^2}\frac{\gamma}{\omega_a^2}\frac{v^3}{(2z_a)^7} - 4\hbar\alpha_0\frac{g^2}{\omega_a^2}\frac{v}{(2z_a)^5}\mathcal{K}_{0,1,1}^{\theta-}\left(\frac{\omega_{\mathrm{phon}}z_a}{v}\right) \tag{3.65}$$

where the function $\mathcal{K}_{m,n,l}^{\theta\pm}$ is given in appendix C. In the results of equations (3.63) to (3.65),

[13] An exception are for example doped materials [240, 242] with surface plasmon polariton frequencies far below usual atomic resonance.

we highlight the proportionality to v^3. The first order in v vanishes[14]. Furthermore, in F^G we denoted the difference $(63 - 45)$, where the first term stems from the oscillatory degrees of freedom and the second from the rotational degrees of freedom[15]. This means, that involving rotational degrees of freedom decreases the noncontact friction.

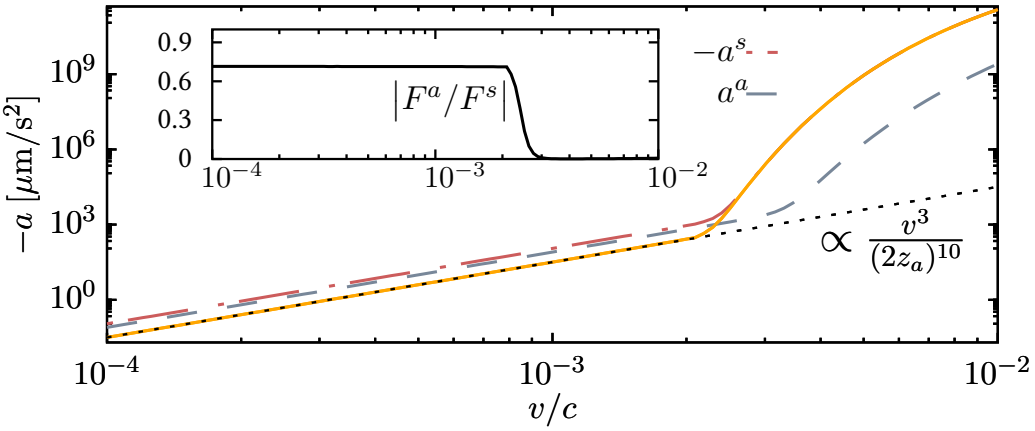

Figure 3.2: Frictional acceleration $a = F/m_{\mathrm{Rb}} = a^{\mathrm{s}} + a^{\mathrm{a}}$, on a ^{87}Rb atom ($\alpha_0 = 4\pi\epsilon_0 \times 47.28\,\text{Å}^3$, $\omega_a = 1.3\,\mathrm{eV}$ and $m_{\mathrm{Rb}} = 86.9\,\mathrm{u}$ [235]) as a function of its velocity. The atom without an internal heat bath moves at $z_a = 5\,\mathrm{nm}$ from a gold surface, described by a local Drude permittivity ($\omega_{\mathrm{p}} = 9\,\mathrm{eV}$ and $\gamma = 35\,\mathrm{meV}$ [247]). The two competing contributions a^{s} (dash-dotted line) and a^{a} (dashed line) stem from the interaction with linear polarized radiation or circular polarized radiation, respectively. Furthermore, the low velocity asymptote (black dotted line) was calculated (see equation (3.63)). In the inset the modulus of the ratio of the symmetric and antisymmetric force is shown. While at low velocities the ratio is constant at $\approx 70\%$ it decreases rapidly in the resonant regime.

This might be understood intuitively by its classic analogue. While the mechanisms behind the noncontact friction presented here and a classic contact friction are different, the effect of friction reduction by incorporating rotational degrees of freedom is similar in both systems. Nonetheless, we come back to the reduction by incorporating rotational degrees of freedom in the end of this section. The difference in power laws with respect to α_0, z_a and ρ between the internal and induced part of the noncontact friction can be understood by the different underlying processes. While the induced part relies on twice an interaction with the electromagnetic field, the internal part only interacts once with the electromagnetic field and once

[14]This result led to several controversies in the past, since several authors obtained a linear v dependence in leading order [39, 45, 243–245]. The linear velocity dependence is linked to the assumption of Markovianity of the system, which is equivalent with using Fermi's golden rule [246]. But as explained in section 1.2 the assumption of Markovianity can be difficult when it comes to quantum statistics, since in the quantum regime even an Ohmic heat bath does not yield a Markovian stochastic process in the case of $\hbar\omega \gg k_{\mathrm{B}}T$.

[15]Recently, the impact of rotation on the noncontact friction was investigated by Zhao et al. [126]. However, the difference to our treatment lies in the fact that they impose a rotation of a small sphere, whereas in our scheme the rotation solely stems from the friction itself.

with the internal bath. With this comprehension one can also explain why this term is less sensitive on the distance to the surface z_a. Especially noteworthy is the fact that, in the case without internal bath, the local thermal equilibrium approximation leads to a compensation of oscillatory and rotational contribution in the quantum friction [47]. That means, in local thermal equilibrium $F^G_{\mathrm{LTE}} = 0$ and thus quantum friction is a pure nonequilibrium phenomenon without an equilibrium pendant.

Nonlocality

Going beyond Ohmic and local materials, the characteristic behavior of the quantum friction is altered. First we consider nonlocality which enters when the length scale of the electric fields, i.e. $k \lesssim 1/(2z_a)$, can resolve spatial correlation. Such a correlation can stem from the material model itself, as e.g. shown in section 2.4 on the example in certain regimes of the Lindhard-Mermin model, or by macroscopic structures, as e.g. a finite slab or superlattice as presented in section 2.3.

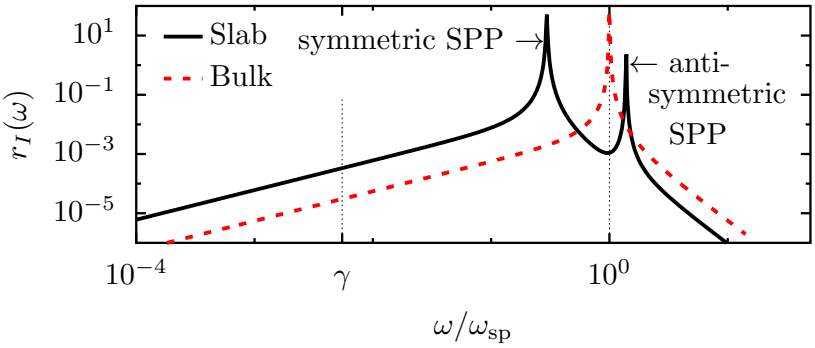

Figure 3.3: Frequency dependence of the imaginary part of the reflection coefficient in the near-field limit. Two geometries with the same local Drude material of equation (2.93) are considered: A semi-infinite bulk (dotted red line) and a finite slab (solid black line). As parameters we chose typical values for gold [247] $\omega_{\mathrm{p}} = 9\,\mathrm{eV}$ and $\gamma = 35\,\mathrm{meV}$, a slab thickness of $d = 2\,\mathrm{nm} \approx 10^{-3}\,c/\omega_{\mathrm{p}}$ and $k = \omega_{\mathrm{p}}/c$. For the half-space case one resonance of the surface plasmon polariton appears at the frequency $\omega_{\mathrm{sp}} \approx \omega_{\mathrm{p}}/\sqrt{2}$, while for the slab two resonances are visible, one below and another above ω_{sp}. These two modes correspond to the symmetric and antisymmetric coupled mode of the two interface plasmon polaritons.

In the case of a single slab with thickness d cladded in vacuum two interfaces between vacuum and the material have to be considered. Consequently, this system exhibits two surface plasmon polariton modes (see figure 3.3). Using the given reflection coefficient in equation (2.59) in the near-field limit the two modes can be found at [237, 248]

$$\epsilon(\omega) = -\begin{cases} \coth(kd/2), & \text{symmetric} \\ \tanh(kd/2), & \text{antisymmetric} \end{cases}. \tag{3.66}$$

The symmetric mode is lower in frequency and the antisymmetric mode at a higher frequency

compared to the surface plasmon polariton in semi-infinite bulk setup. As the bulk result for $kd \gg 1$ is retrieved, the two modes split into a symmetric and antisymmetric coupled surface plasmon polariton for values $kd < 1$. This can be understood by the penetration depth of the fields into the slab

$$\delta_{\mathrm{pen}}(\omega, k) = \mathrm{Im}\Big\{\sqrt{\frac{\omega^2}{c^2}\epsilon(\omega) - k^2}\Big\}^{-1} \overset{\mathrm{near}}{\sim} k^{-1}, \tag{3.67}$$

which in the near-field limit is dominated by k (for details see appendix F). If the penetration depth is smaller than the thickness of the slab, the electric field effectively cannot distinguish between a bulk and a finite slab. If the penetration depth exceeds the thickness, the two surface modes will couple to each other. Since in the context of the low temperature noncontact friction $k \lesssim 1/(2z_a)$, one retrieves the local bulk result of equations (3.63) to (3.65) if $d \gg 2z_a$, i.e. the spatial extension is not resolved. In the opposite case of $d \ll 2z_a$, the behavior of the noncontact friction is altered, as was shown by Oelschläger et al. [46], which manifests directly in a changed z_a dependence of the force. The slab's reflection coefficient in the near-field and Ohmic approximation reads

$$\mathrm{Im}\Big\{r_{\mathrm{slab}}(\omega, k)\Big\} \approx 2\epsilon_0\omega\rho_{\mathrm{bulk}}\coth[dk] = \begin{cases} 2\epsilon_0\omega\rho_{\mathrm{bulk}}(kd)^{-1}, & \text{for} \quad kd \ll 1 \\ 2\epsilon_0\omega\rho_{\mathrm{bulk}}, & \text{for} \quad kd \gg 1 \end{cases}, \tag{3.68}$$

where ρ_{bulk} is the resistivity of the corresponding semi-infinite bulk. In other words, the expansion coefficient ρ of equation (3.68) becomes k dependent. In the case of a finite slab one finds $\rho(k) = \rho_{\mathrm{bulk}}\coth[dk]$. We refrain from restating all results obtained in equations (3.63) to (3.65) for a finite slab (for detail results see [46]). Nonetheless, by an analysis of the length scales, i.e. by using dimensionless integration variables, one can derive the parameter dependent proportionality when comparing the bulk to the slab result

$$\frac{F^G_{\mathrm{slab}}}{F^G_{\mathrm{bulk}}} \propto \begin{cases} z_a^2/d^2, & \text{for} \quad d \ll 2z_a \\ 1, & \text{for} \quad d \gg 2z_a \end{cases}, \qquad \frac{F^\mu_{\mathrm{slab}}}{F^\mu_{\mathrm{bulk}}} \propto \begin{cases} z_a/d\,, & \text{for} \quad d \ll 2z_a \\ 1, & \text{for} \quad d \gg 2z_a \end{cases}. \tag{3.69}$$

When going to larger distances compared to the thickness of the slab, the participating electric field can resolve the finite thickness of the slab, i.e. access the symmetric coupling between the two surface plasmon polaritons. This coupled mode has an enhanced dissipation, i.e. $\rho(k)$, for low wavevectors, which yields a linear or quadratic enhancement of the respective friction component, as shown in equation (3.69).

While the previous example of nonlocality was introduced by structuring a local material, it can also be achieved by considering spatial correlation effects within the material model. In the case of the presented Lindhard-Mermin model of equation (2.90) the effect of spatial correlation on noncontact friction was studied extensively by Reiche et al. [44, 207]. In this case— still relying on Ohmicity — the resistivity, yields [236]

$$\rho(k) = \frac{2}{\pi\epsilon_0}\int_0^\infty \mathrm{d}k_z \frac{k}{K^2}\,\mathrm{Im}\left\{\frac{\partial_\omega \epsilon_l(\omega,K)_{\omega=0}}{\left[\epsilon_l(0,K)\right]^2}\right\}\left(\left[1+\frac{2}{\pi}\int_0^\infty \mathrm{d}k_z \frac{k}{K^2\epsilon_l(0,K)}\right]^2\right)^{-1}. \tag{3.70}$$

The presented expression of equation (3.70) contains the intrinsic length scales of the material, i.e. the Thomas-Fermi screening length $\lambda_{\mathrm{TF}} = v_{\mathrm{F}}/(\sqrt{3}\omega_{\mathrm{p}})$ and the mean free path of the quasi-particles $\ell = v_{\mathrm{F}}/\gamma$ (see section 2.4). Typically $\lambda_{\mathrm{TF}} \approx 10^{-1}\,\mathrm{nm}$ whereas $\ell \approx 100\,\mathrm{nm}$ [227]. Comparing ℓ to the wavevector k and the γ to the frequency ω yields two regimes. For $k\ell \ll |\omega/\gamma + \mathrm{i}|$ we retrieve the local Drude model we already discussed above. In the limit $k\ell \gg |\omega/\gamma + \mathrm{i}|$ spatial correlation is strongly relevant. Using $v \ll v_{\mathrm{F}}$, with usual Fermi-velocities around $10^{-2}c$ [138], the wavevector dependent resistivity reads [44]

$$\rho(k) \approx \frac{1}{\epsilon_0 k\lambda_{\mathrm{TF}}}\frac{Q(k\lambda_{\mathrm{TF}}, \frac{\pi^2-4}{2\pi k\ell})}{\left(k\lambda_{\mathrm{TF}} + \sqrt{1+k^2\lambda_{\mathrm{TF}}^2}\right)^2}, \tag{3.71}$$

where the dimensionless function $Q(a,b)$ is not displayed in this thesis, but can be found in the appendix of [44]. The nonlocal resistivity in the Lindhard-Mermin model grows $\propto |k\lambda_{\mathrm{TF}}\ln(k\lambda_{\mathrm{TF}})|$ for $k \ll \lambda_{\mathrm{TF}}$, features a maximum at $k \sim 1/(5\lambda_{\mathrm{TF}})$ and then decreases with $\propto k\lambda_{\mathrm{TF}}$. In the local model, collision induced damping constitutes the dominant dissipation channel, where the electric field effectively averages over a multitude of scattering event. On the contrary, in the nonlocal limit, incoherent scattering becomes less important and the ballistic motion of the quasi-particles is resolved. Here, the quasi-particle's velocity becomes comparable to the phase velocity of the electromagnetic radiation, allowing for a coherent energy transfer from the field to the quasi particle, i.e. Landau damping [202, 203, 249]. With the upper bound $k \lesssim 1/(2z_a)$, going close or beyond $k\lambda_{\mathrm{TF}}$ would tantamount with unrealistic distances on the order of angstrom and further could not be described within the current theoretical framework[16]. Thus the regime $\lambda_{\mathrm{TF}} \ll z_a$ is more relevant in real experimental setups. The additional loss channel of Landau damping, which enters at distances $z_a < \ell$, yields an enhancement of the noncontact friction. This deviation from the local model manifests in the distance dependence. For the fully detailed results of noncontact friction in the Lindhard-Mermin model we refer to [44, 236].

These two examples, i.e. a finite slab and the spatially correlated Lindhard-Mermin model, demonstrate how nonlocality can alter the distance dependence of the noncontact friction at low-temperatures. In both cases, the crucial length scales connect to their respective access to additional dissipation channels. In the slab configuration the coupling of the two surface plasmon polaritons — and thus their enhanced dissipation — is only accessed for distances larger than the slab thickness. In the spatially correlated Lindhard-Mermin bulk material the additional loss channel via Landau damping can only be accessed by the distances below the

[16] A breakdown of the theoretical description would for example occur in the dipole approximation of the microscopic object, as well as in semi-classical infinite barrier approximation.

mean free path of the quasi-particles. When turning towards a finite slab of a solid material described by the Lindhard-Mermin model, these two additional channels, i.e. the second surface plasmon polariton and Landau damping, can be even combined, as shown by Reiche et al. [236].

Non-Ohmicity

As the previous two examples illustrated the impact of nonlocality, until now only Ohmic materials, i.e. $\mathrm{Im}\{r\} \propto \omega$, were considered. Considering non-Ohmicity, there are examples with a leading order lower (sub-Ohmic) or higher (super-Ohmic) with respect to ω. One example, studied by Oelschläger et al. [46], are superlattice structures, built of a repeating pattern with thickness $D = d_\mathrm{A} + d_\mathrm{B}$, which consists of alternating metal and vacuum layers with thicknesses d_A and d_B, respectively. In the regime of $kD \ll 1$, the longitudinal and transversal permittivity can be approximated by the effective medium approximation, as shown in equation (2.68). This approximation is restricted by the penetration depth. If the electric field does not penetrate beyond the first pattern, it cannot resolve the superlattice structure and effectively senses the top-most slab or — if the slab cannot be resolved — even a bulk (see equation (3.68)). In the range of validity of the effective medium approximation one finds a certain regime where the imaginary part of the reflection coefficient exhibits a leading order $\mathrm{Im}\{r_\mathrm{EMA}(\omega)\} \approx \sqrt{2\epsilon\rho\omega(d_\mathrm{B}/d_\mathrm{A})}$. The explanation behind this sub-Ohmic behavior lies in the mode structure of the superlattice. Similar to the example of a single slab, the infinitely many surface modes couple to a symmetric and an antisymmetric mode band, as shown in figure 3.4. When considering lossy materials the lower symmetric mode band exhibits a region of overdamped modes, which is shown in figure 3.5. These overdamped modes yield an altered loss channel, where the energy is not solely dissipated in the first layer, but is distributed over many superlattice sites. The transition, where the superlattice structure changes from Ohmic — which coincides with the slab description — to a sub-Ohmic behavior of the effective medium approximation, can be found by calculating the point of intersection of the respective asymptotics. This leads to the transition wavevector $k_\mathrm{t} \approx \sqrt{\omega\epsilon}\sqrt{2\rho_\mathrm{loc}/(d_\mathrm{A}d_\mathrm{B})}$, where ρ_loc is again the local resistivity of the dissipative slab. For $k \gg k_\mathrm{tr}$ the Ohmic single slab description and for $k \ll k_\mathrm{tr}$ the sub-Ohmic effective medium approximation is retrieved. The altered frequency dependence impacts the distance dependence as well as the velocity dependence of the noncontact friction. In comparison to a local Drude slab of thickness d_A we find (for detailed results see [46])[17]

$$\frac{F^G_\mathrm{EMA}}{F^G_\mathrm{slab}} \propto \begin{cases} \frac{d_\mathrm{A}d_\mathrm{B}}{2z_a|v|\rho_\mathrm{loc}\epsilon_0}, & \text{for} \quad vz_a \gg \frac{d_\mathrm{A}d_\mathrm{B}}{2\rho_\mathrm{loc}\epsilon_0} \\ 1, & \text{for} \quad vz_a \ll \frac{d_\mathrm{A}d_\mathrm{B}}{2\rho_\mathrm{loc}\epsilon_0} \end{cases} \tag{3.72}$$

$$\frac{F^\mu_\mathrm{EMA}}{F^\mu_\mathrm{slab}} \propto \begin{cases} \sqrt{\frac{d_\mathrm{A}d_\mathrm{B}}{2z_a|v|\rho_\mathrm{loc}\epsilon_0}}, & \text{for} \quad vz_a \gg \frac{d_\mathrm{A}d_\mathrm{B}}{2\rho_\mathrm{loc}\epsilon_0} \\ 1, & \text{for} \quad vz_a \ll \frac{d_\mathrm{A}d_\mathrm{B}}{2\rho_\mathrm{loc}\epsilon_0} \end{cases} . \tag{3.73}$$

[17] We emphasize that, despite seemingly even orders in velocity, the symmetry $F(-v) = -F(v)$ is still preserved. Thus, the second order velocity dependence reads $F(v) \propto v|v|$.

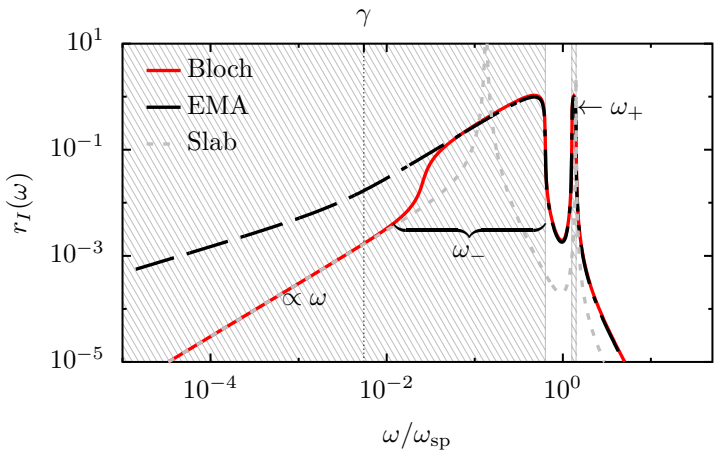

Figure 3.4: The imaginary part of the reflection coefficient is plotted as a function of ω at $k = 10^{-1}c/\omega_{\mathrm{p}}$. Two materials A with $\epsilon_{\mathrm{A}}(\omega)$, a Drude model with the same parameters as in figure 3.3, and B, with $\epsilon_{\mathrm{B}} = 1$, are considered. For a superlattice of a repeating AB pattern with a filling factor $f = d_{\mathrm{A}}/D = 0.2$ is chosen. The exhibited features can be directly connected to the continuous of mode branches $\omega_{\pm}$. For frequencies ω higher than the lower bound of the ω_--branch, the effective medium calculation (dashed black line) shows a very good agreement with the full transfer-matrix calculation (solid red line). At small frequencies ω, the full calculation is equivalent to the behavior of the very first conducting layer of the structure (gray dotted line). The shaded areas represent the hyperbolic regime with $\mathrm{Re}\{\epsilon_{\perp}(\omega)\}\mathrm{Re}\{\epsilon_{\parallel}(\omega)\} < 0$ (for an overview over hyperbolic metamaterials see [187]).

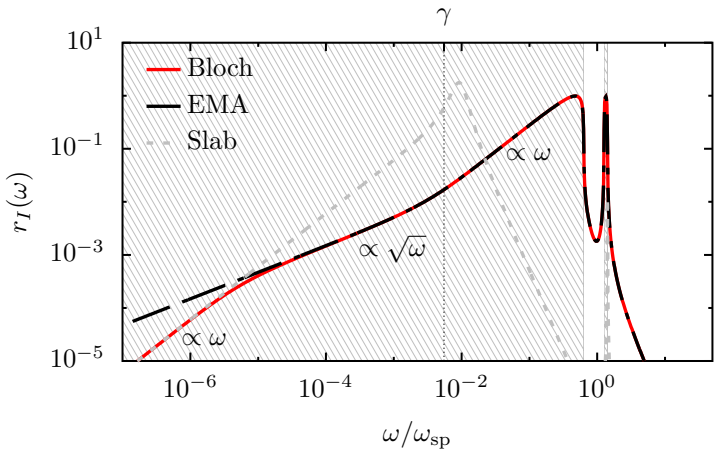

Figure 3.5: Analogous plot as in figure 3.4 for $k = 10^{-3}c/\omega_{\mathrm{p}}$. The effective medium approximation holds over a larger frequency range and for lower frequencies ω. A sub-Ohmic behavior ($r_{\mathrm{I}} \propto \sqrt{\omega}$) is visible in the full calculations. At low frequencies, the effective medium approximation breaks down and quintessentially only the first slab is responsible for the scattering properties of the entire structure.

In order to classify the impact of nonlocality and non-Ohmicity on the noncontact friction, one can derive the general connection between the order of ω and k dependence of the leading $\mathrm{Im}\{r\}$ term and the respective distance and velocity dependence of the low-velocity quantum friction

$$\mathrm{Im}\{r\} \propto \omega^n k^m \quad \Rightarrow \quad \begin{cases} F^G(v, z_a) \propto \dfrac{v^{2n+1}}{z_a^{2n+1}} \dfrac{1}{z_a^{7+2m}}, \\ F^\mu(v, z_a) \propto \dfrac{v^{n+2}}{z_a^{n+2}} \dfrac{1}{z_a^{4+m}} \end{cases} . \tag{3.74}$$

Nonetheless, the validity of the respective regime has to be evaluated for each physical system individually.

Temperature Correction

With this general connection, we finish the discussions in lowest order of $\hbar|\omega| \ll k_\mathrm{B}T$ and like to consider thermal corrections. As many features of the zeroth order analogously reoccur in the first thermal correction, we restrict the subsequent calculations to the local and Ohmic calculations, but highlight the impact of the entering temperature dependence. First of all, the $F^{\mathbf{dE}_0}$ term must not be neglected anymore and yields a significant contribution to the noncontact friction. Performing the calculation for the low-velocity case, i.e. $\omega_a \gg v/(2z_a)$, leads to the following results

$$F^\mu \overset{\mathcal{O}(T^2)}{\sim} -v\frac{\hbar}{\pi}\frac{\alpha_0}{\omega_a^2}\frac{2\pi^2\mu_R(0)}{3(\beta\hbar)^2}\int \frac{\mathrm{d}^2\mathbf{k}}{(2\pi)^2}k_x^2\,\mathrm{Tr}\left[\underline{\sigma}_I'(\mathbf{k},0)\right], \tag{3.75}$$

$$F^G \overset{\mathcal{O}(T^2)}{\sim} -v\frac{\hbar\pi}{3}\left(\frac{2\alpha_0}{\beta\hbar}\right)^2\int\frac{\mathrm{d}^2\mathbf{k}}{(2\pi)^2}\int_0^\infty\frac{\mathrm{d}^2\mathbf{p}}{(2\pi)^2} \tag{3.76}$$

$$\times\left\{\mathrm{Tr}\left[\underline{\sigma}_I'(\mathbf{p},0)\underline{\sigma}_I'(\mathbf{k},0)\right] + 2\phi_I'(\mathbf{p},0)\phi_I'(\mathbf{k},0)\right\}\left(k_x+p_x\right)^2. \tag{3.77}$$

While in the lowest temperature-independent order the linear order in velocity vanished and a leading order in v^3 was found, the first thermal correction exhibits a leading linear order in v. Assuming a local and Ohmic material model, one finds the respective expressions

$$F^G \approx -(6-3)\frac{\alpha_0^2\rho^2}{\pi\beta^2\hbar}\frac{6v}{(2z_a)^8}, \qquad F^\mu \approx -\frac{\hbar\pi\mu_R(0)}{(\hbar\beta)^2}\frac{v\alpha_0\rho}{\omega_a^2}\frac{8}{(2z_a)^5}, \tag{3.78}$$

where the difference $(6-3)$ refers to the rotational contribution diminishing the oscillatory contribution of the noncontact friction. When the terms are rearranged and separated into $\mathbf{dd}$ and $\mathbf{dE}_0$ contributions instead, one retrieves following ratios for the first thermal corrections in $\hbar|\omega| \gg k_\mathrm{B}T$

$$2[F^G]_{\mathbf{dd}} = [F^G]_{\mathbf{dE}_0} \quad \text{and} \quad \left[F^\mu\right]_{\mathbf{dd}} = \left[F^\mu\right]_{\mathbf{dE}_0}, \tag{3.79}$$

which highlights the importance of incorporating the $F^{\mathbf{dE}_0}$ term, since it contributes — at this order — two thirds to F^G and one half to F^μ. Moreover, even without an internal heat bath,

the frictional force does not vanish within the local thermal equilibrium approximation

$$F^G_{\mathrm{LTE}} \approx -\frac{\alpha_0^2\rho^2}{\pi\beta^2\hbar}\frac{6v}{(2z_a)^8}\,, \tag{3.80}$$

contrary to the zero temperature case, where the oscillatory and rotational contribution canceled equally. However, comparing the local equilibrium result to the full calculation it still only covers a third, whereas nonequilibrium corrections contribute two thirds. Similar to the considerations with respect to the dependence on velocity and distance, as shown in equation (3.74) for nonlocal and non-Ohmic materials, in the first thermal corrections one finds

$$\mathrm{Im}\{r\} \propto \omega^n k^m \quad \overset{\mathcal{O}(T^2)}{\Rightarrow} \quad \begin{cases} F^G(v,z_a) \propto \dfrac{v^{2n-1}}{z_a^{2n-1}}\dfrac{1}{z_a^{7+2m}} \\ F^\mu(v,z_a) \propto \dfrac{v^n}{z_a^n}\dfrac{1}{z_a^{4+m}} \end{cases}. \tag{3.81}$$

Comparing the temperature independent term to the to the first thermal correction, one can derive a general statement with respect to proportionality

$$\frac{F^G_{T=0}}{F^G_{T^2}} \propto \frac{v^2}{z_a^2} \quad \text{and} \quad \frac{F^\mu_{T=0}}{F^\mu_{T^2}} \propto \frac{v^2}{z_a^2}\,. \tag{3.82}$$

To understand the meaning behind this proportionality, we calculate the point of intersection between the temperature-independent contribution and the T^2 term in the example of Ohmic and local materials. Here, we find

$$\hbar\frac{v}{z_a} = \pi\sqrt{\frac{2}{3}}k_{\mathrm{B}}T. \tag{3.83}$$

The transition at this point is shown in figure 3.6. Employing again that $k \lesssim 1/(2z_a)$ fixes the length scale of relevant wavevectors. If we interpret $z_a^{-1} \equiv \overline{k}$, where $\overline{k}$ is some weighted relevant wavevector, we can rewrite the transition point as

$$\hbar\overline{k}v \propto k_{\mathrm{B}}T. \tag{3.84}$$

On the left-hand-side of equation (3.84) we find the decrease of the object's kinetic energy, i.e. the recoil, which occurs when emitting/absorbing a quanta of energy [250]. On the right-hand-side we find the thermal energy. Both sides represent different mechanisms to reduce kinetic energy: Recoil by emitting/absorbing quanta of radiation, or random scattering with an electric field at temperature T. Since solely one asymptotic, either the zeroth or second order in temperature, is dominant beyond or below the point of intersection, the transition from pure quantum friction to a thermal friction is marked by a change in the dominant friction mechanism.

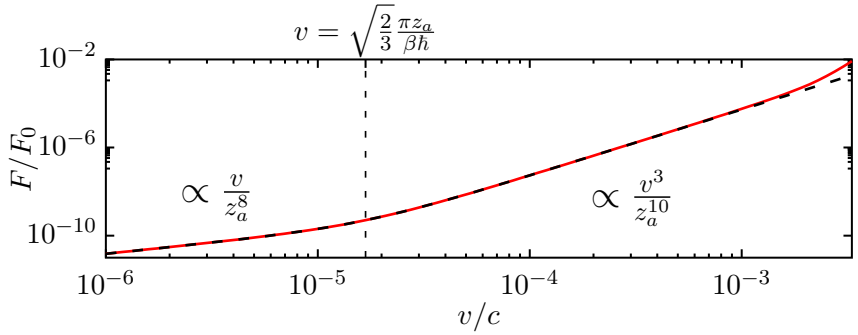

Figure 3.6: The noncontact friction for finite temperatures transitions for small velocities from the quantum friction ($\propto v^3/z_a^{10}$) to a thermal friction ($\propto v/z_a^8$). The two lines refer to the full numerical calculation (solid red) and the analytical asymptote (dashed black). For the analytical curve the temperature-independent term of equation (3.63) and the first thermal correction of equation (3.78) are summed up. The following parameters were used: $z_a = 5\,\mathrm{nm}$, $\omega_\mathrm{p} = \omega_a = 1.3\,\mathrm{eV}$, $\gamma = 0.12\,\mathrm{eV}$, $\epsilon_\infty = 3.7$, $\alpha_0 = 4\pi\epsilon_0 \times 47.28\ \text{Å}^3$ and $T = 3\,\mathrm{K}$ (which complies with a rubidium atom above a doped silicon surface [242]). Furthermore, the constant $F_0 = 3\hbar(\omega_\mathrm{p}/\sqrt{2})^5\alpha_0/(2\pi\epsilon_0 c^4)$ was defined.

Anomalous Doppler Effect

The first mechanism is related to the anomalous Doppler effect. The anomalous Doppler effect describes the peculiar situation that a moving object with velocity $\mathbf{v}$ emitting a quanta of energy $\hbar\omega$ with an momentum $\hbar\mathbf{K}$, as e.g. a photon or surface plasmon polariton, into the electric field reduces the kinetic energy of the object via recoil by $|\Delta E| = \hbar\mathbf{K}^\intercal\mathbf{v} = \hbar|\mathbf{v}||\mathbf{K}|\cos\theta$, which is larger than the amount of energy used to generate the quanta, i.e. $|\Delta E| > \hbar\omega$. This situation is only possible, if the object has internal degrees of freedom to store the excess energy. Otherwise, as for example seen with fast electrons at velocities higher than the phase velocity of light within the material they are passing through, the emission happens along the Cherenkov cone with an opening angle θ_C around the direction of motion. This phenomenon is known as Vavilov–Cherenkov radiation [252]. The opening angle of the Cherenkov cone is determined by the velocity of the emitted particle/quasi-particle v_qp via $\cos\theta_\mathrm{C} = v_\mathrm{qp}/v$. The region of the anomalous Doppler effect is inside the Cherenkov cone as illustrated in figure 3.7. Emitting a particle or quasi-particle within the region of the anomalous Doppler effect yields the strong recoil but leads automatically to an excitation of the internal degrees of freedom.

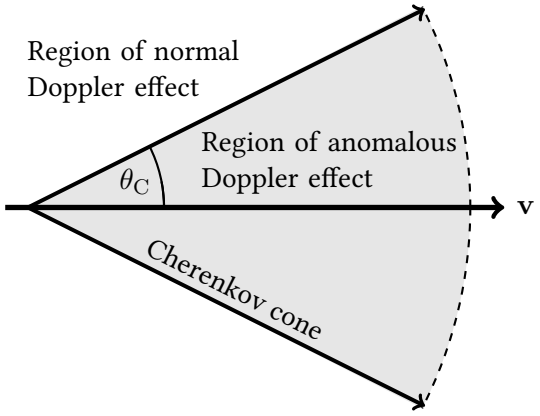

Figure 3.7: Sketch illustrating the regions of normal and anomalous Doppler effect, separated by the Cherenkov cone with an opening angle of θ_C centered along the direction of motion [250, 251].

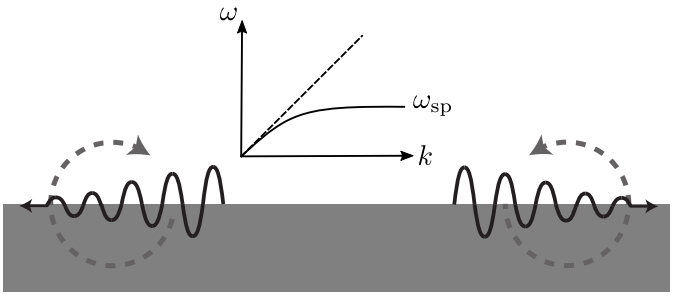

Figure 3.8: Depicted are important physical features of surface plasmon polaritons: The dispersion relation of a single surface plasmon polariton (solid line) compared to the light line (dashed line) an the locking of momentum and angular momentum [253–255].

In the context of quantum friction the emitted quasi-particles are surface plasmon polaritons. As illustrated in figure 3.8 the dispersion relation of surface plasmon polaritons bends off the light line ($\omega = ck$) and asymptotically approaches the constant surface plasmon polariton frequency ω_{sp} for large k. The velocity of the surface plasmon polariton v_{sp} is ω dependent. However, in the near-field limit it approaches $v_{\mathrm{sp}} \to 0$, which leads to an opening angle of the Cherenkov cone of $\theta_{\mathrm{C}} \to 90°$. Consequently, each emission in the near-field limit in the direction of motion causes an excitation of the dipole moment, which can yield further emissions or decays internally. In the zero temperature limit the recoil of the emitted surface plasmon polaritons in the direction of motion is the sole channel to reduce the kinetic energy. Thus, one can only describe this process properly by considering the backaction [222]. In this framework the reduction of friction by incorporating rotational degrees of freedom can be understood. As illustrated in figure 3.8, the direction of momentum and the direction of angular momentum of surface plasmon polaritons are locked [253, 255]. Hence, emitting a surface plasmon polariton in a certain direction yields the accumulation of rotational energy. To lose the accumulated rotational energy the object has to emit a surface plasmon polariton in the opposite direction. This process however reduces the initial recoil and thus the frictional force [47]. In the first thermal correction this effect becomes less relevant and random scattering with the thermally distributed surface plasmon polaritons takes over to be the dominant friction mechanism. For different setups with respect to nonlocality or non-Ohmicity the tipping point from quantum to thermal can vary, but — since stemming from the expansion of the Bose-Einstein distribution — is fundamental. It is very important to not mistake the first thermal correction as classical limit. The first thermal correction is situated within the quantum-classical cross-over regime, however, close to the quantum limit since we expanded around $\hbar\omega \gg k_{\mathrm{B}}T$.

Recap: Within this section we discussed several asymptotic properties of the low-temperature noncontact friction. Here, we incorporated a full nonequilibrium description concerning the interaction of the dipole moment with the electric field as well as an full treatment of the rotational degrees of freedom. We highlighted the impact of nonlocality and non-Ohmicity on the friction. Furthermore, we elaborated on the transition from quantum to thermal friction and the underlying processes. Eventually, we concluded by interweaving the gathered information to explain the underlying physical processes behind the nonequilibrium phenomenon of the noncontact friction friction.

CHAPTER 4

Numerical Investigations

While in chapter 3 we were mainly concerned with an analytical analysis of asymptotic behaviors, this chapter is dedicated to the full numerical treatment of the noncontact friction of a neutral microscopic object moving above a flat neutral macroscopic surface, as it was introduced in section 2.1. A careful investigation of dispersion forces has to include full numerical calculations in order to acquire a complete picture. On the one hand, such a numerical tool serves as confirmation of the analytical results (and vice versa). And on the other hand, it enables the access to regimes, where clear analytical results are not available. Despite the fact that we can write down a closed analytical expression for the noncontact frictional force (see equations (3.21) and (3.24)), the full numerical calculation remains challenging. In order to tackle this challenge, we present in section 4.1 a useful rearranging of the expressions of noncontact friction (see equations (4.3) and (4.5)), which yields an efficient integration scheme. Moreover, we highlight crucial obstacles for the numerical integration and how they can be overcome. In section 4.2, we briefly introduce the C code, which was developed during the thesis, as an implementation of the numerical scheme of section 4.1.

4.1 Numerical Suitable Reformulation

The evaluation of the analytical expressions of equation (3.21) and equation (3.24) are, from a numerical point of view, very challenging. We emphasize especially the five fold integration. Such a high nesting of integrals is a very expensive task for a numerical integration routine, as it leads to a tremendous amount of function evaluations. Furthermore, the numerical implementation of the improper integrals (reaching from $-\infty$ to ∞) has to be handled with care in order to include all relevant contributions. In a first step we rearrange the five fold nested integration. As was shown in section 3.2 the noncontact friction is described by two contributions: The autocorrelation of the dipole moment $\langle \mathbf{d}(t)\mathbf{d}(t-\tau)\rangle$ and the correlation of the dipole moment with the electric noise field $\langle \mathbf{d}(t)\mathbf{E}_0(t)\rangle$. These two terms can be rearranged

Integration Depth

as follows

$$\begin{aligned} F^{\mathbf{dd}} &= -2\int_{-\infty}^{\infty} \mathrm{d}\omega \int \frac{\mathrm{d}^2\mathbf{k}}{(2\pi)^2}\, k_x \,\mathrm{Tr}\left[\underline{S}^{\intercal}(\mathbf{k}^{\intercal}\mathbf{v}-\omega)\underline{G}_{\Im}(\mathbf{k},z_a,\omega)\right]\,\theta(\omega) \\ &= -2\int_{-\infty}^{\infty} \mathrm{d}\omega \int \frac{\mathrm{d}^2\mathbf{k}}{(2\pi)^2}\, k_x \,\mathrm{Tr}\left[\underline{S}(\omega)\underline{G}_{\Im}(\mathbf{k},z_a,k_xv+\omega)\right]\,\theta(-k_xv-\omega)\,, \end{aligned} \tag{4.1}$$

where the x axis is defined along the movement of the microscopic object, i.e. $\mathbf{k}^{\intercal}\mathbf{v} = k_x v$. Here, two consecutive variable transformation have been used, first $\omega \to \omega + k_x v$ and second $\omega \to -\omega$ and $k_x \to -k_x$. By splitting the frequency integral in positive and negative contributions one finds

$$\begin{aligned} F^{\mathbf{dd}} = &-2\int_{0}^{\infty} \mathrm{d}\omega \int \frac{\mathrm{d}^2\mathbf{k}}{(2\pi)^2}\, k_x \,\mathrm{Tr}\left[\underline{S}(\omega)\underline{G}_{\Im}(\mathbf{k},z_a,k_xv+\omega)\right] \\ &+2\int_{0}^{\infty} \mathrm{d}\omega \int \frac{\mathrm{d}^2\mathbf{k}}{(2\pi)^2}\, k_x \,\mathrm{Tr}\left[\frac{\hbar}{\pi}\underline{\alpha}_{\Im}(\omega)\underline{G}_{\Im}(\mathbf{k},z_a,k_xv+\omega)\right]\,\theta(k_xv+\omega)\,, \end{aligned} \tag{4.2}$$

where the relation[1] $\underline{S}^{\intercal}(-\omega) = \underline{S}(\omega) - \frac{\hbar}{\pi}\underline{\alpha}_{\Im}(\omega)$ was exploited. Performing similar steps for the $\langle \mathbf{d}(t)\mathbf{E}_0(t)\rangle$ contribution and add both terms eventually leads to the expression

Numerically Suitable Form №1

$$\begin{aligned} F = &-2\int_{0}^{\infty} \mathrm{d}\omega \,\mathrm{Tr}\left[\underline{S}(\omega)\int \frac{\mathrm{d}^2\mathbf{k}}{(2\pi)^2}\, k_x\, \underline{G}_{\Im}(\mathbf{k},z_a,k_xv+\omega)\right] \\ &+2\frac{\hbar}{\pi}\int_{0}^{\infty} \mathrm{d}\omega \,\mathrm{Tr}\left[\underline{\alpha}_{\Im}(\omega)\int \frac{\mathrm{d}^2\mathbf{k}}{(2\pi)^2}\, k_x\, \frac{\underline{G}_{\Im}(\mathbf{k},z_a,k_xv+\omega)}{1-\exp(-\beta\hbar[\omega+k_xv])}\right]. \end{aligned} \tag{4.3}$$

With the derivation of equation (4.3) the effective integration depth of the nested integrals was reduces from five to three. Schematically speaking the transformation rearranged

$$\int_{\omega}\int_{k_x}\int_{k_y}\left(\int_{k_x'}\int_{k_y'}\right) \quad\to\quad \int_{\omega}\left(\int_{k_x}\int_{k_y}\right)\left(\int_{k_x'}\int_{k_y'}\right), \tag{4.4}$$

where the subscript indicates the respective integration variable. The reduction in the nested integration depth strongly reduces the number of function evaluations. While the form in

[1] For a brief derivation, one splits up the power spectrum into the LTE and non-LTE contribution, as is done in equation (3.13), and uses the identity $(1-\exp(-x))^{-1} = 1-(1-\exp(x))^{-1}$. This leads to

$$\underline{S}^{\intercal}(-\omega) = \frac{\hbar}{\pi}\left(-\underline{\alpha}_{\Im}(\omega)\left[1-\frac{1}{1-\exp(-\beta\hbar\omega)}\right]+\underline{J}^{\intercal}(-\omega)\right) = \underline{S}(\omega) - \frac{\hbar}{\pi}\underline{\alpha}_{\Im}(\omega)\,,$$

where $\underline{\alpha}_{\Im}^{\intercal}(-\omega) = -\underline{\alpha}_{\Im}(\omega)$, $\underline{G}_{\Im}(-\mathbf{k},z_a,-\omega) = -\underline{G}_{\Im}^{\intercal}(\mathbf{k},z_a,\omega)$ and therefore $\underline{J}^{\intercal}(-\omega) = \underline{J}(\omega)$ was utilized.

equation (4.3) is already condensed and easily implementable,[2] the integration exhibits a crucial problem when it reaches regimes, where the resonant contributions are dominant (see section 3.2). As discussed in appendix B, the resonant contribution coincides with a local thermal equilibrium approximation. If the local equilibrium is dominant, the two terms in equation (4.3) will have a very similar value. The evaluation of the force thus amounts to numerically subtract nearly similar numbers, which leads to high inaccuracy known as the catastrophic cancellation. In order to lift this problem, the contributions of the local thermal equilibrium can be separated of the two terms in equation (4.3). Therefore, the large nearly similar contributions can be canceled analytically and solely the numerically stable difference remains with

Numerically Suitable Form №2

$$\begin{aligned} F = &-2\frac{\hbar}{\pi}\int_0^\infty \mathrm{d}\omega\,\mathrm{Tr}\left[\underline{J}(\omega)\int\frac{\mathrm{d}^2\mathbf{k}}{(2\pi)^2}\,k_x\,\underline{G}_\Im(\mathbf{k},z_a,k_xv+\omega)\right] \\ &+2\frac{\hbar}{\pi}\int_0^\infty \mathrm{d}\omega\,\mathrm{Tr}\left[\underline{\alpha}_\Im(\omega)\int\frac{\mathrm{d}^2\mathbf{k}}{(2\pi)^2}\,k_x\,\underline{G}_\Im(\mathbf{k},z_a,k_xv+\omega)\right]\Theta_T(\omega+k_xv,\omega)\,, \end{aligned} \tag{4.5}$$

where

$$\Theta_T(\omega+k_xv,\omega)=\frac{1}{1-e^{-\beta\hbar[\omega+k_xv]}}-\frac{1}{1-e^{-\beta\hbar\omega}}=n(\omega+k_xv,T)-n(\omega,T)\,. \tag{4.6}$$

A illustration of the behavior of $\Theta_T(\omega+k_xv,\omega)$ is given in figure 4.1.

Numerical Integration Cut-off

Another challenge for an efficient numerical calculation is the large integration domain. Even though the infinite limits can be mapped onto a finite domain, there is still the risk of omitting relevant areas in the integration when numerically estimating the results. In order to identify the relevant contributions, we investigate the equations with respect to strongly enhanced areas as well as significantly damped areas. The latter is found in the exponential damping term of the scattered Green's tensor $\propto \exp(-2z_a\kappa)$ (see equation (2.41)). Consequently, under the reasonable assumption, that the reflection coefficients do not increase faster than the exponential decreases, a cutoff can be introduced at $\kappa_{\mathrm{cut}}=\delta_{\mathrm{cut}}/(2z_a)$, where $\delta_{\mathrm{cut}}>1$ will be used as an

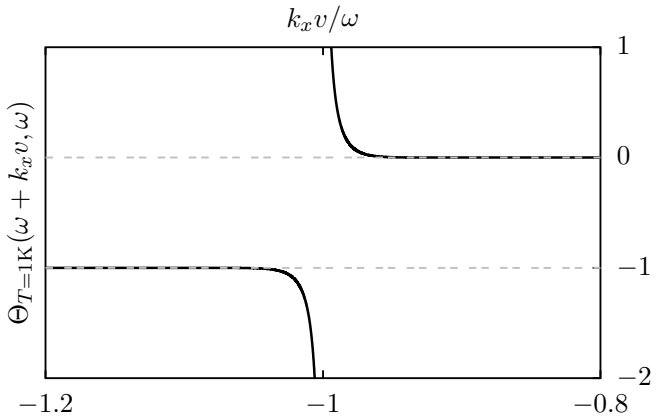

Figure 4.1: The $\Theta_T(\omega+k_xv,\omega)$ distribution at $T=1\,\mathrm{K}$ and $\omega=0.01\,\mathrm{eV}$.

[2] All k integrations yield a similar structure, which is the integration over the Green's tensor with different additions, i.e. a k_x and/or a $(1-\exp(-\beta\hbar[\omega+k_xv]))^{-1}$.

input parameter to the numerical calculations. With respect to computational resources, e.g. calculation time, a smaller δ_{cut} probably leads to a faster integration. Nevertheless, is has to be ensured, that resonant contributions, which maybe already lie outside the "obvious relevant domain" around $\delta_{\text{cut}} \approx 1$, are still captured. Before investigating the resonances, we consider a second damping mechanism: The above introduced $\Theta_T(\omega + k_x v, \omega)$ of equation (4.6). This distribution stems from the used fluctuation-dissipation relations and indicates the contributing states with respect to their temperature as weight. Keeping in mind that the models used within this thesis (see chapter 2) are focusing on low temperatures ($k_{\text{B}}T \ll \hbar|\omega|$), an expansion of $\Theta_T(\omega + k_x v, \omega)$ around zero temperature (see equation (3.27)) can be considered to gain further insight and leads to

$$\Theta_{T\to 0}(\omega + k_x v, \omega) = \theta(\omega + k_x v) - \theta(\omega) + \mathcal{O}(T^2) \tag{4.7}$$

$$\overset{\omega\geq 0}{=} -\theta(-\omega - k_x v) + \mathcal{O}(T^2). \tag{4.8}$$

In lowest order $\Theta_T(\omega + k_x v, \omega)$ sets the relevant contributions to fulfill the relation $-\omega \geq k_x v$, which was already visual suggested in figure 4.1. When rewriting this with polar coordinates $k_x = k\cos\varphi$ and $k_y = k\sin\varphi$ and in terms of $\kappa = \sqrt{k^2 - (\omega + k\cos\varphi)^2/c^2}$ one finds the similar relation

$$-\omega \geq \kappa v \cos\varphi = \begin{cases} 0, & \text{for } \cos\varphi > 0 \\ \frac{\omega}{v|\cos\varphi|} \leq \kappa, & \text{for } \cos\varphi \leq 0 \end{cases}, \quad \text{for } \mathrm{Re}\{\kappa\} \geq 0\,. \tag{4.9}$$

Combined with the introduced cutoff δ_{cut} one can therefore derive

$$\frac{\omega}{v} \leq \frac{\omega}{|\cos\varphi| v} \leq \kappa \leq \frac{\delta_{\text{cut}}}{2z_a} \equiv \frac{\omega_{\text{cut}}}{v}\,, \tag{4.10}$$

which yields a soft upper bound for the ω integration. *Soft* means in this context that values beyond ω_{cut} still have to be considered, but that the relevance of those terms strongly decreases as long as one considers low temperatures (for a clearer context, what *low temperatures* with respect to the systems parameters mean, see section 3.2). If the two "damping mechanisms", i.e. the exponential of the Green's tensor and the Θ_T distribution, are combined, the relevant integration domains can be fixed, as is illustrated in figure 4.2. The estimate of the range of the relevant contribu-

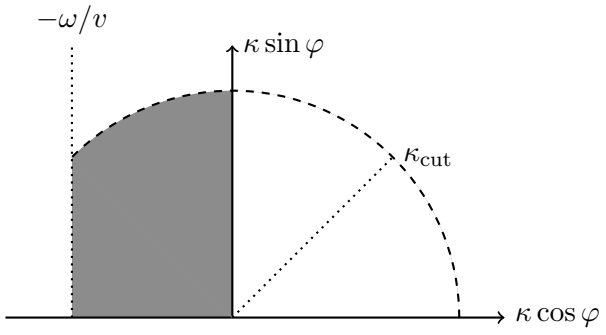

Figure 4.2: The sketch illustrates the relevant domains (marked in gray) of the κ related real part integrations given in equation (4.5). This domain is determined by the cutoff at $\kappa = \kappa_{\text{cut}}$ and the relation $\kappa\cos\varphi\, v = -\omega$.

tions allows a strong simplification of our numerical approach. It is noteworthy, that these estimates are — besides v and z_a — neither dependent on the parameters of the material or the object. As mentioned earlier, also the resonances of the subsystems have to be carefully considered. Resonances which lie outside the region of $\omega \leq \omega_{\mathrm{cut}}$ might be nonetheless relevant. Therefore, one has to determine at least the rough position of the resonances to cover its contribution properly. In this way, the material and object parameters influence the determination of the relevant domain. Since the resonances depend on the different models of the material or object, their evaluation has to be investigated separately, as shown in chapter 2. A roughly determined resonance (e.g. at $\omega \approx \omega_a$ for the harmonic dipole oscillator) with its respective width can then be used as additional information to make sure that even very narrow resonances are not accidentally omitted by the integration routine. In contrast to the investigations of chapter 3, which are mainly performed in the near-field limit, with $\kappa \approx k$, the numerical routine shall be able to calculate beyond the near-field and to include retardation effects. Unpleasantly, there is an — even if analytically removable — singularity $1/\kappa$ appearing in the retarded Green's tensor, which makes the numerical calculation prone to inaccuracies. To lift this singularity one performs a change of the integration variable $k \to \kappa$, where the Doppler shift has to be taken into account accordingly,

Including Retardation

$$\kappa = \sqrt{k^2 - \frac{(\omega + k_x v)^2}{c^2}} \quad \text{and} \quad \mathrm{d}\kappa\, \kappa = \mathrm{d}k \left(k - \frac{\cos\varphi\, v(\omega + k\cos\varphi\, v)}{c^2} \right). \tag{4.11}$$

Using $k > 0$ one expresses k in terms of the remaining integration variables

$$k(\omega, \kappa, \cos\varphi) = \frac{c\sqrt{\kappa^2(c^2 - v^2\cos^2\varphi) + \omega^2} + v\omega\cos\varphi}{c^2 - v^2\cos^2\varphi}\,. \tag{4.12}$$

Consequently, the integration path splits up into a purely imaginary and purely real κ

$$k \in [0, \infty[\quad \to \quad \kappa \in [-\mathrm{i}\frac{\omega}{c}, -\mathrm{i}0] \cup [0, \infty[\,. \tag{4.13}$$

Here, the purely imaginary part refers to the propagating contributions, whereas the purely real part refers to the evanescent fields. Performing the above transformation of the variables yields the following integration scheme for the scattered Green's tensor

$$\begin{aligned} \int \frac{\mathrm{d}^2\mathbf{k}}{(2\pi)^2} \underline{g}(\omega_+, k) = \frac{1}{4\pi^2\epsilon_0} \int_0^\pi \mathrm{d}\varphi \left\{ \int_{-\mathrm{i}\omega/c}^{-\mathrm{i}0} + \int_0^\infty \right\} \mathrm{d}\kappa\, e^{-2z_a\kappa} \left(1 - \frac{\cos\varphi\, v\omega_+}{kc^2} \right)^{-1} \\ \times \left\{ \kappa^2 r^p(\omega_+, k) \left(\mathrm{diag} \begin{bmatrix} \cos^2\varphi \\ \sin^2\varphi \\ k^2/\kappa^2 \end{bmatrix} - \frac{k}{\kappa}\cos\varphi\, \underline{L}_y \right) \right. \\ \left. + \frac{\omega_+^2}{c^2} r^s(\omega_+, k) \mathrm{diag} \begin{bmatrix} \sin^2\varphi \\ \cos^2\varphi \\ 0 \end{bmatrix} \right\}, \end{aligned} \tag{4.14}$$

where $\omega_+ = \omega + k_x v$ and we already canceled the antisymmetric k_y terms due to the symmetric integration.

Recap: After highlighting the obstacles in implementing a numerical evaluation of the expressions of the noncontact friction, these were rearranged into numerically better suited forms in equations (4.3) and (4.5). Furthermore, we determined the relevant integration domain, the treatment of resonances, and the inclusion of retardation effects.

4.2 An Implementation in C: QuaCa

As the reader might feel a bit exhausted by the thought on a section devoted to a numerical implementation of the integrals shown above, we like to introduce our C implementation QuaCa (named according to its eponym the quokka, depicted in figure 4.3). Currently, the code is available under following link[3], together with a detailed documentation. QuaCa was set up by the author and the support of Christoph Egerland and calculates the expression given in equation (4.5). Since the documentation is available under the above mentioned address, we forego the technical details and proceed with the scientific usability. After QuaCa is installed, the program can be used with a simple bash command

```
>> quaca data.in
```

It reads the data of an input file, e.g. *data.in*, and writes into a respective output file different components of the force and the respective asymptotic results. The user can choose between different material models (Drude, Drude-Lorentz, hydrodynamic model, extended hydrodynamic model) as well as between different geometries (semi-infinite bulk, slab, superlattice), which were introduced in chapter 2. Further, an internal can be disabled (atom-like systems) or enabled (as in nanoparticles). The program is stable, however, extensions are ongoing. As for any numerical calculation it is of great importance that the numerical results reliably converge to a distinct and correct value. In order to assure convergence, one has two test options: First, in asymptotic regimes, the numerical results have to coincide with the analytical results of chapter 3. And second, numerical inaccuracies or estimations respectively should not diverge, but converge in general to a

Convergence Study

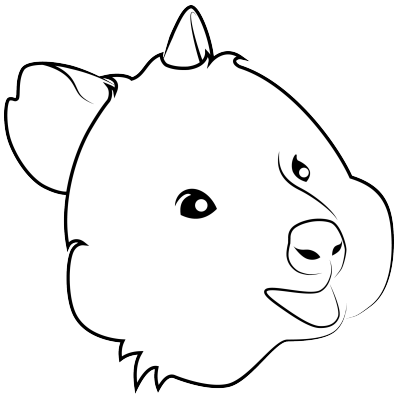

Figure 4.3: The quokka, a small and often happy looking mammal living in the southwest of Australia. It is the eponym and logo of the C code QuaCa, and mainly depicted to brighten up the reader's eyes. The illustration was drawn by Gerda Wolf.

[3] https://git.physik.hu-berlin.de/top/codeprojects/quaca.git

distinct value. The criteria can be categorized as *hard* and *soft* convergence study. A hard convergence study compares the numerical calculations to a fixed analytical result, whereas a soft convergence study demonstrates that the numerical results converge (or diverge) compared to previously obtained numerical results. As was shown in chapter 3, the numerical and analytical asymptotes coincide. Nonetheless, a soft convergence study is necessary to be confident that also in analytically inaccessible regimes the numerical results remain reliable. This is shown in figure 4.4, where the convergence behavior in terms of the introduced parameter δ_{cut} is investigated[4] .

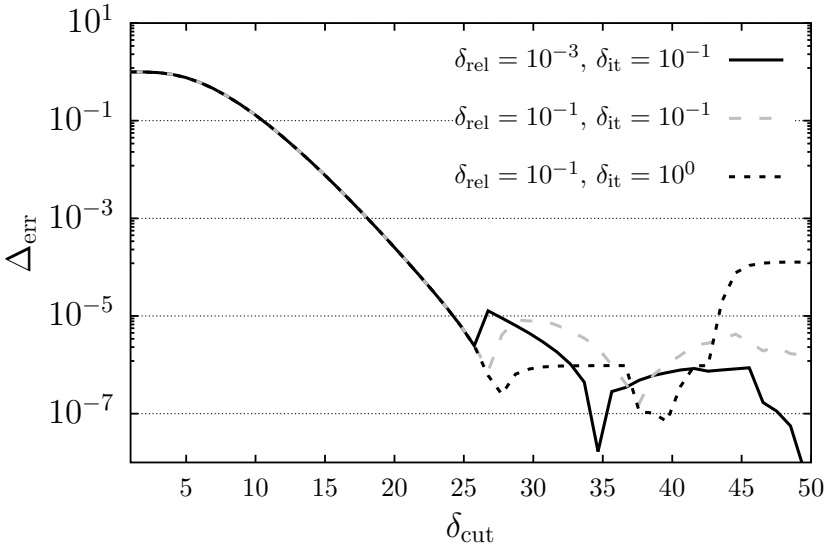

Figure 4.4: Soft convergence study concerning the introduced cutoff δ_{cut}. Besides the cutoff, also an error by the interpolation of the numerical integration is encountered. For all graphs a microscopic object without internal heat bath (see section 2.2) and a semi-infinite bulk configuration with a Drude model for the macroscopic surface is used. The respective parameters are $v = 10^{-5}c$, $z_a = 10\,\mathrm{nm}$, $T = 1\,\mu\mathrm{K}$, $\omega_a = 1.3\,\mathrm{eV}$, $\alpha_0 = 6 \times 10^{-9}\,\mathrm{eV}^{-3}$, $\gamma = 0.035\,\mathrm{eV}$, and $\omega_{\mathrm{p}} = 9\,\mathrm{eV}$. Where $\Delta_{\mathrm{err}} = |F - F_{\mathrm{conv}}|/F_{\mathrm{conv}}$ and F_{conv} refers to the most converged value ($\delta_{\mathrm{rel}} = 10^{-3}$, $\delta_{\mathrm{it}} = 10^{-1}$ and $\delta_{\mathrm{cut}} = 50$). As a pathologic case also $\delta_{\mathrm{it}} = 1$ is included, which is expected to accumulate numerical error due to the nested integration.

In order to estimate the numerical error we focus on the integrations. The numerical routines themselves aim to arrive at a given accuracy $\delta_{\mathrm{rel/abs}}$, either in relative or in absolute accuracy. For our purpose, we are mainly concerned with the relative accuracy. As already presented in equation (4.3), for the noncontact friction a triple nested integration has to be performed. It is faithful to use a higher accuracy when going deeper in nesting depth. Otherwise, the results might hardly converge or even diverge. Therefore, if the last integration (in equation (4.3)

[4]Since we are using commonly established integration routines of the GNU Scientific Library [256], we refrain from fundamental testing these routines and trust the work of the many developers and users. Thus, we restrict our investigations to the integration scheme and the parameters which were introduced in this thesis.

the ω integration) shall reach a relative accuracy of δ_{rel}, the accuracy will be iteratively set higher by δ_{it} with each additional nesting. This means, one sets $\delta_{\mathrm{n,rel}} = \delta_{\mathrm{rel}}(\delta_{\mathrm{it}})^n$, where n is the nesting depth and δ_{it} must be chosen smaller 1. As numerical integration routine CQUAD, which harnesses a Clenshaw-Curtis quadrature, is used for the determined relevant domain. The remaining less relevant regime is integrated by QAGI, which employs a Gauss-Kronrod quadrature[5] . Since multiple nested numerical integrals are performed, one can estimate the overall accuracy by the propagation of uncertainty. When fixing the relative precision, the accuracy of a threefold integration is just the sum of the relative errors. Because the precision of the deeper integrations should be chosen significantly higher, one can simply estimate the total relative precision with δ_{rel}. As shown in figure 4.4, the relative accuracy is even better than the estimated one, as long as $\delta_{\mathrm{it}} \ll 1$. The instability at large values of δ_{cut} is expected, since the most top integral has to deal with small but inaccurate values. However, the exponential decay nicely leads to a better convergence for higher δ_{cut}. Unfortunately, at some point the numerical error of the calculation prevents even better convergence. Nevertheless, figure 4.4 underlines the proper function of QuaCa in addition to the analytical analyses.

Recap: We very briefly introduced and outlined the developed C code QuaCa, which was used to fully evaluate the calculations of the noncontact friction without further approximation. Additionally, we demonstrated a soft convergence study, which complements the accordance to the asymptotic calculation of the previous chapter.

[5]For a detailed documentation of CQUAD and QAGI of the GNU Scientific Library see [256].

CHAPTER 5

Conclusion, Discussion & Outlook

At the beginning of this thesis, we highlighted the importance of fluctuation-induced, or even fluctuation-dominated, phenomena and gave a brief historical overview over important milestones achieved in predicting and measuring effects such as the static and dynamical Casimir and the Casimir-Polder effect. The aforementioned forces were confirmed experimentally, whereas the noncontact friction is still lacking an experimental realization. Thus, in this closing chapter we like to contemplate on our results, discuss the presented theory compared to other authors and give suggestions towards experimental realizations.

Conclusion

Over the course of this thesis we investigated nonequilibrium dispersion forces, in particular the noncontact friction of neutral small objects moving with constant velocity above a macroscopic surface. In chapters 1 and 2 we set the framework of our calculations, where the fundamental foundation rests on the linear response theory and a detailed understanding of the constituents of the total system. In chapters 3 and 4 we presented analytical and numerical approaches to calculate this peculiar nonequilibrium force caused by the interplay of quantum and thermal fluctuations. What distinguishes our approach from many other studies is the full consideration of the backaction of the dipole moment onto the electromagnetic field and the inclusion of rotational degrees of freedom. In the context of table 1 this means that we are neither relying on the assumption of Markovianity, as e.g. [39–41, 45], nor do we assume a local thermal equilibrium, as e.g. in [42, 43, 58]. By abandoning these two common but — for

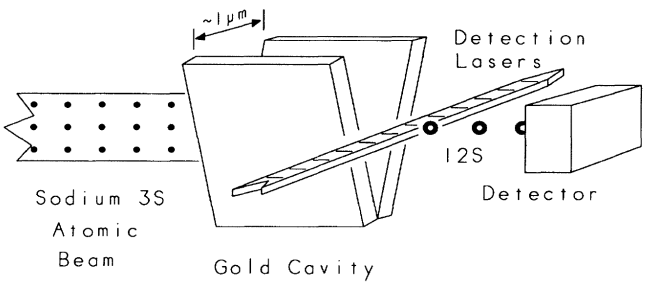

Figure 5.1: The experimental setup Sukenik et al. used to measure the Casimir-Polder force [257]. The deflection of the atom beam due to the walls of the wedge-shaped cavity and the according loss in contrast at the detector was used to deduce the strength of the force.

this specific system — invalid assumptions[1] , we provide a self-consistent solution in linear response. Our full and self-consistent treatment does not rely on perturbation scheme but yields a complete nonperturbative inclusion of the backaction of the electromagnetic field onto the dipole moment, and vice versa. The configuration was extended to a non-static dipole angle [2] and published in [47]. Last but not least, the formalism was extended to finite temperatures. While the extension to finite temperatures was already included in other formalisms, as e.g. in [42, 50], the combination of a state-of-the-art full nonequilibrium treatment of the given system at finite temperatures is — to the best of our knowledge — a novel achievement.

By employing the full nonequilibrium description we gave a broad overview over the various configurations and quantities, which have an impact on the noncontact friction. In chapter 3 we highlighted the influence of an internal heat bath, spatial correlation within the material and in general the effect of different dissipation channels on the characteristic behavior of the noncontact friction. Moreover, we presented the first thermal correction to the zero temperature noncontact friction, i.e. quantum friction. At this point we underline that these thermal corrections must not be mistaken to represent a classical result (we still expand around the limit $\hbar\omega \gg k_{\mathrm{B}}T$). Therefore, the correction terms lie within the quantum-classical crossover regime [259], however, still close to the "pure" quantum realm.

Material	ρ in $[\Omega\mathrm{m}]$	**Ref.**
Au	3.2×10^{-8}	[247]
Na	8×10^{-7}	[260]
n-Si	1.5×10^{-2}	[261]
Ge	0.5×10^{-1}	[262]

Atom	$^{87}\mathrm{Rb}$	$^{11}\mathrm{Na}$	$^{7}\mathrm{Li}$	$^{1}\mathrm{H}$
m in [u]	86.9	22.99	7.02	1.01
α_0 in $[4\pi\epsilon_0\text{Å}^3]$	47.3	24.1	24.3	0.67
v in [km/s]	0.12	1	1.5	30
Ref.	[263]	[264]	[265]	[266]

Table 5.1: The left table assembles resistivities of various materials. The right table collects different experimental data concerning various atoms. Here, all polarizabilities can be found in the overview of Schwerdtfeger and Nagle [267] and all atom masses in the technical report of Wieser and Coplen [268]. The references given in the right tables refer to experimentally realized beam velocities.

Calculating Deceleration

As already quoted in the introduction, Milton et al. declared the "inescapable truth" of experimental measurements of the noncontact friction being far beyond reach [60]. Nonetheless, we like to have a fresh and optimistic reevaluation of this fundamentally interesting problem. In order to demonstrate where this sobering evaluation stems from, we first revisit the examples of other authors. Thereafter, we point out the important mechanisms behind the friction and demonstrate how quantum friction can be strongly enhanced to experimentally accessible regimes.

[1] As it was shown by Intravaia et al. [47, 57, 58, 222], omitting the backaction and/or the nonequilibrium currents leads to a qualitatively different behavior of the quantum friction.

[2] At this point, we have to distinguish our treatment from existing publications as [126, 127, 258], where the rotation of the dipole moment was assumed to be fixed. In our work, we consider the backaction of the electromagnetic field onto the angular momentum of the dipole moment, which induces the rotation. In the nonequilibrium steady-state, however, the angular momentum reaches a determined value prominently connected to the velocity and the distance of the microscopic object (see [47]).

As we saw in figure 3.2, when moving a rubidium atom at $v \gtrsim 30\,\mathrm{km/s}$ at a distance of $5\,\mathrm{nm}$ from a gold surface the deceleration is $|a^{\mathrm{Rb}}_{\mathrm{Au}}| \gtrsim 3 \times 10^{-2}\,\mu\mathrm{m/s^2}$. In principle, this deceleration could lay within an experimentally accessible range [269], whereas both, the velocity and the distance, are experimentally very challenging. Going to larger separations or lower velocities, the frictional force dwindles rapidly $\propto v^3/z_a^{10}$. When engaging this configuration for reasonable velocities and distances, it is understandable that one probably surrenders, as an experimental realization seems indeed to be far beyond reach. However, if we choose different atoms and a surface material with a higher dissipation rate, i.e. resistivity, the situation brightens up drastically. Choosing experimental reasonable values as e.g. $v = 1.5\,\mathrm{km/s}$ for ^{7}Li atoms [265] (with $m_{\mathrm{Li}} = 7.02\,\mathrm{u}$ and $\alpha_0 = 4\pi\epsilon_0 \times 24.33\text{Å}^3$ [270]) and distances of $20\,\mathrm{nm}$ [271], but still choose the surface to be a gold bulk, we arrive again at a very tiny deceleration of $|a^{\mathrm{Li}}_{\mathrm{Au}}| \approx 1.3 \times 10^{-11}\,\mu\mathrm{m/s^2}$, which we would again confirm to be currently far beyond experimental reach. Nevertheless, we demonstrated in section 3.2, the crucial ingredients in quantum friction are the dissipation channels, which lead to a loss of kinetic energy. If we employ for example a strong absorber as doped silicon with $\rho = 1.5 \times 10^{-2}\,\Omega\mathrm{m}$ [261][3] , the deceleration is strongly enhanced $|a^{\mathrm{Li}}_{\mathrm{d-Si}}| \approx 2.8\,\mu\mathrm{m/s^2}$ and thus jumps back into experimental accessible regimes. These promising numbers get even more enhanced when we consider first thermal corrections. Using equation (3.78) and assuming room temperature of $T = 300\,\mathrm{K}$, we find

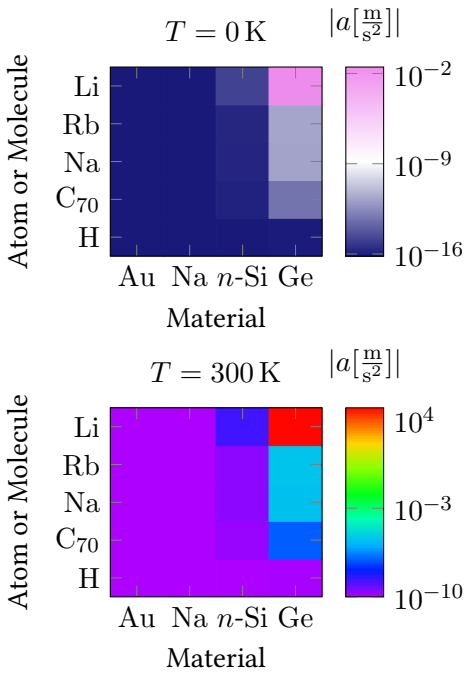

Figure 5.2: Deceleration due to the noncontact friction at $T = 0\,\mathrm{K}$ (top panel) and $T = 300\,\mathrm{K}$ (bottom panel) of various atom/molecule-surface combinations. Here, we chose $z_a = 10\,\mathrm{nm}$ and $v = 1.5\,\mathrm{km/s}$. The polarizability and mass of C_{70} can be found in [266]. All other parameters can be taken from table 5.1.

$$a^{\mathrm{Li}}_{\mathrm{d-Si}} \approx -30\,\frac{\mathrm{m}}{\mathrm{s}^2}. \tag{5.1}$$

To emphasize the importance of choosing a faithful configuration, we calculate the thermal

[3] We are aware that doped silicon might not fully act as a normal conductor [272]. However, depending on the concentration of the doping, in the low-frequency domain $\omega \lesssim v/z_a$, for the given velocity and distance, this approximation probably is still sufficient. For further details see [272–275].

correction of rubidium over gold and find

$$a_{\mathrm{Au}}^{\mathrm{Rb}} \approx -4.2 \times 10^{-11}\,\frac{\mathrm{m}}{\mathrm{s}^2}. \tag{5.2}$$

In order to develop a better intuition, we collected the decelerations of several setups in figure 5.2 [4]. Assuming for example the configuration of lithium over a doped silicon surface at $v = 1.5\,\mathrm{km/s}$ and $z_a = 20\,\mathrm{nm}$, we turn towards possible experimental realizable setups.

Atom beam deflection

One way to investigate the impact of the noncontact friction could be atomic beam deflection. This technique was successfully used to measure Casimir-Polder force acting on a beam of sodium atoms. In their experiment Sukenik et al. [257] sent the atomic beam through a micron-sized gold cavity (see figure 5.1). The closer the atoms travel to the surface of the wedge-shaped cavity, the more atoms are deflected. Consequently, the intensity of the outgoing atom beam, which then is measured with the aid of an detection laser, is reduced according to the strength of the attractive Casimir-Polder force. Similarily to the work done by Klatt in her PhD thesis [279], we are going to estimate the prolonged interaction time with the surface, due to the noncontact friction. The cavity Sukenik et al. [257, 280] used in their deflection experiment is $10\,\mathrm{mm}$ in length. The sodium beam with $v = 500\,\mathrm{m/s}$ experiences an interaction with the surface for roughly $20\,\mu\mathrm{s}$. Using a beam of lithium atoms at $v = 1.5\,\mathrm{km/s}$ would shorten the interaction time, when employing the same cavity length. In order to keep the interaction time fixed, we assume a tripeled cavity length of $30\,\mathrm{mm}$. Using the above parameters for lithium propelled to $z_a = 20\,\mathrm{nm}$ and $z_a = 10\,\mathrm{nm}$ distance at room temperature above a doped silicon surface leads to

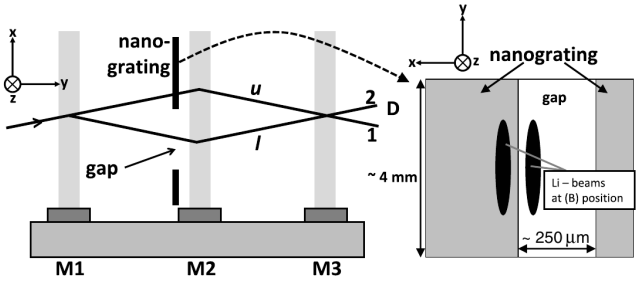

Figure 5.3: The sketch of an atom interferometric experiment performed by Lepoutre et al. in order to measure phase shifts induced by atom-surface interactions [278]. They use a supersonic beam of lithium (with velocities ranging from 700 to 3400 m/s), which is diffracted by three lasers (also known as Mach-Zehnder atom interferometer). One path of the diffracted atom beam passes a nanograting with 53 nm wide windows.

$$\Delta v(z_a = 20\,\mathrm{nm}) \approx -6 \times 10^{-4}\,\frac{\mathrm{m}}{\mathrm{s}} \qquad \text{and} \qquad \Delta v(z_a = 10\,\mathrm{nm}) \approx -1.5 \times 10^{-1}\,\frac{\mathrm{m}}{\mathrm{s}}\,. \tag{5.3}$$

[4] Concerning the drastic decrease in distance (For $T = 0\,\mathrm{K}$ we found $\propto z_a^{-10}$ for atoms above a semi-infinite bulk and $\propto z_a^{-7}$ for a nanoparticle above a semi-infinite bulk) in the noncontact friction one can also find better suited experimental setups. As we pointed out in section 3.4, spatial correlation can be used advantageously. For instance, using an ultra thin metallic slab, which was recently fabricated down to a thickness of 1 nm [276], can compensate for two orders in distance in the atomic case ($z_a^{-10} \to z_a^{-8}$) or for one order in the case of a nanoparticle ($z_a^{-7} \to z_a^{-6}$). Furthermore, recent studies suggest, that at such thin layers quantum spill-out effects would even enhance the plasmonic absorption [277].

These results reveal a way more optimistic perspective with respect to an experimental realization than the ones by Klatt [279] or Milton et al. [60]. However, it might still be challenging to measure this minute change in interaction time due to the frictional force. This does not mean, that we discard this experimental setup, however, we want to continue determining further possible experimental setups. Another promising experimental technique is atom interferometry (as for example shown in figure 5.3). With an accuracy up to $10^{-2}\,\mu\mathrm{m/s^2}$, experimental measurements of the controversial subject of noncontact friction should be within reach in near future [281]. For instance, one could operate neutralized ion beams with velocities of $\approx 100\,\mathrm{km/s}$ passing through a grating with very small aperture of $\approx 45 - 50\,\mathrm{nm}$ [266, 271, 282–284]. In this context other more optimistic voices see a potential for a possible experimental success in measuring the noncontact friction [47, 126, 130, 285].

Atom interferometry

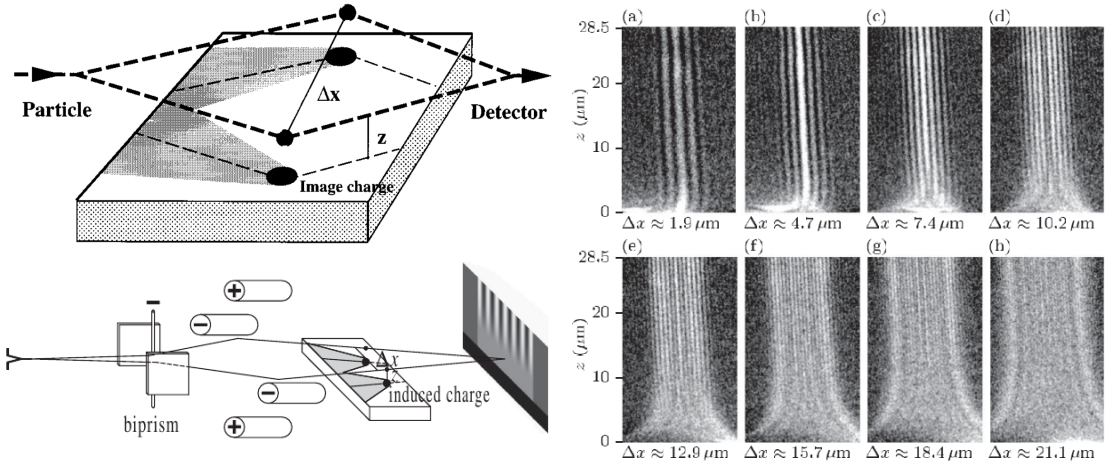

(a) Setup

(b) Electron interferograms

Figure 5.4: On the left in **(a)**, we show two sketches of the electron decoherence measurement. The upper sketch was proposed as a potential experimental setup by Anglin and Zurek [76, 286] in 1997. This proposal was successfully realized by Sonnentag and Hasselbach [261] in 2007. Their actual setup sketch is shown in the lower picture. On the right in **(b)** we reprinted the detected electron interferograms of Sonnentag and Hasselbach [261]. Here one sees impressively and clearly demonstrated, how the contrast of the interference fringes decreases when approaching the surface.

As Viotti et al. showed recently, noncontact friction enhances the decoherence of the moving atom [287]. Thus, they suggest that measuring decoherence times could indirectly demonstrate the existence of quantum friction. Similar suggestions have been made earlier by other authors [243, 288, 289]. This signature would be visible in atom interferometry experiments, too. As Anglin et al. show in their work on "deconstructing decoherence" [76], decoherence should not be observed as an annoying phenomenological disturbance, but rather as a possibility to access the quantum-classical-crossover regime. In conclusion of [76] they propose an experimental setup in order to demonstrate the continuous transition from a purely quantum to an effec-

tively classical regime (see figure 5.4a). This very experimental setup was realized a decade later by Sonnentag and Hasselbach [261], who showed — in agreement with the theory —, the impact of a macroscopic surface consisting of doped silicon[5] on the decoherence of electron beams. An initial electron beam is split up via an electron-optical biprism, similarly to Young's pin-holes experiment [293]. Brought together, the different trajectories interfere and one can detect the usual interference fringes. These interference fringes demonstrate the quantum nature of the electron, which was firstly demonstrated by Jösson [294]. If the trajectories are chosen in proximity to a macroscopic surface, the contrast of the interference pattern reduces with decreasing distance. This decrease in visibility can be assigned to decoherence which is mediated through the interaction with the surface as an environment. While we are very much aware that the interaction between charged particles and a surface is in fact different to the interaction of neutral particles with a surface, we acknowledge the line of thought behind this experiment as a possible experimental setup with respect to quantum friction. As Anglin et al. pointed out [76], especially a non-Ohmic environment, as in the case of the noncontact friction, might lead to characteristic signatures in the decoherence. Such signatures are vividly discussed in the literature [243, 287–289, 295] and may lead to an indirect demonstration of quantum friction effects in the near future.

We argued in this last chapter that there is a concrete hope — based on our theoretical investigations — that quantum/Casimir friction can be experimentally accessible, employing already available experimental techniques. As announced in the introduction, we hope that with our work we sparked renewed optimism to the topic of noncontact friction and looking forward that also this peculiar nonequilibrium phenomenon can be sighted in measurable reality soon.

Recap: After a brief review on the content of this thesis, we highlighted the distinguishing elements of this work compared to others in the context of noncontact friction. Afterwards, we discussed possible experimental setups in order to measure this frictional force or its signatures. Here, we come to the rather bright and optimistic conclusion that from our point of view the actual measurement should be possible by already currently available experimental techniques.

[5] Despite reasonable agreement with the theory based on the assumption of Ohmic damping of the surface presented by Anglin et al. [76], Howie's treatment [290, 291] of the doped semi-conductor — which essentially introduces a THz cut-off frequency to restrict the linear regime — seems to be more viable and confirms with the experimental results carried out by Sonnentag and Hasselbach [261] as well as with the more recent results obtained by Beierle et al. [292]. The adaptation with respect to doped silicon, are for example presented in [272]. This adaptation might be also viable for decoherence calculation with respect to quantum friction.

APPENDIX A

Distributions of singular functions

The $\coth(x)$ can be expanded by its moments [228, 296] [1]

$$\coth(\lambda x) \overset{\lambda\to+\infty}{=} \operatorname{sgn}(x) + \sum_{n=0}^{\infty} \frac{(-1)^n \tilde{\mu}_n \, \delta^{(n)}(x)}{n! \lambda^{n+1}} \tag{A.1}$$

with

$$\tilde{\mu}_n = \int_{-\infty}^{\infty} \mathrm{d}x \, \frac{2\operatorname{sgn}(x)\, x^n}{e^{2|x|} - 1} = \begin{cases} 0 & n \text{ even} \\ \neq 0 & n \text{ odd} \end{cases} . \tag{A.2}$$

The first momenta are

$$\tilde{\mu}_1 = \frac{\pi^2}{6}, \quad \tilde{\mu}_3 = \frac{\pi^4}{60}, \tag{A.3}$$

and $\delta^{(n)}$ acting as

$$\delta^{(n)}[f] = (-1)^n \delta[\partial^n f] \, . \tag{A.4}$$

Besides the $\coth$, another distribution appears in our calculations

$$\frac{1}{1 - e^{-\lambda x}} = \frac{e^{\lambda x}}{e^{\lambda x} - 1} \, . \tag{A.5}$$

Fortunately, we can relate this to the $\coth$ by

$$1 + \coth(\frac{\lambda}{2} x) = \frac{e^{\lambda x} - 1}{e^{\lambda x} - 1} + \frac{e^{\lambda x} + 1}{e^{\lambda x} - 1} = \frac{2 e^{\lambda x}}{e^{\lambda x} - 1} . \tag{A.6}$$

Thus, we obtain the following limiting distribution

$$\frac{2}{1 - e^{-\lambda x}} \overset{\lambda\to\infty}{=} 1 + \operatorname{sgn}(x) + \sum_{n=0}^{\infty} \frac{(-1)^n \tilde{\mu}_n \, \delta^{(n)}(x)}{n! (\lambda/2)^{n+1}} = 2\theta(x) + \sum_{n=0}^{\infty} \frac{(-1)^n \tilde{\mu}_n \, \delta^{(n)}(x)}{n! (\lambda/2)^{n+1}} . \tag{A.7}$$

[1] Please note that in [228] the $(-1)^n$ is missing.

APPENDIX B

Polarizability & Resonant Noncontact Friction

First, the polarizabilty of a freely rotating dipole moment above a macroscopic surface is investigated. To keep the notation lucid, we introduce

$$\int \frac{\mathrm{d}^2\mathbf{k}}{(2\pi)^2}\underline{G}(\mathbf{k}, k_x v+\omega) = \mathrm{diag}[\boldsymbol{\Sigma}(\mathbf{k}, k_x v+\omega)] - \Pi_y(\mathbf{k}, k_x v+\omega)\underline{L}_y, \tag{B.1}$$

with $\boldsymbol{\Sigma} = (\Sigma_x, \Sigma_y, \Sigma_z)$. Due to the Lorentz invariance of the free space Green tensor, one can shift $\underline{G}_0(\omega_\pm) \to \underline{G}_0(\omega)$. Since the off-diagonal terms of the free space Green tensor are then solely odd in k_x and k_y only diagonal terms remain under the symmetric integration. The elements of polarizability then read

$$[\underline{\alpha}(\omega)]_{xx} = \frac{\alpha_0\omega_a^2\left(\omega_a^2-\omega^2-\mathrm{i}\omega\mu-\alpha_0\omega_a^2\Sigma_z\right)}{\left(\omega_a^2-\omega^2-\mathrm{i}\omega\mu-\alpha_0\omega_a^2\Sigma_z\right)\left(\omega_a^2-\omega^2-\mathrm{i}\omega\mu-\alpha_0\omega_a^2\Sigma_x\right)-\left(\alpha_0\omega_a^2\Pi_y\right)^2}, \tag{B.2}$$

$$[\underline{\alpha}(\omega)]_{yy} = \frac{\alpha_0\omega_a^2}{\omega_a^2-\omega^2-\mathrm{i}\omega\mu-\alpha_0\omega_a^2\Sigma_y}, \tag{B.3}$$

$$[\underline{\alpha}(\omega)]_{zz} = \frac{\alpha_0\omega_a^2\left(\omega_a^2-\omega^2-\mathrm{i}\omega\mu-\alpha_0\omega_a^2\Sigma_x\right)}{\left(\omega_a^2-\omega^2-\mathrm{i}\omega\mu-\alpha_0\omega_a^2\Sigma_z\right)\left(\omega_a^2-\omega^2-\mathrm{i}\omega\mu-\alpha_0\omega_a^2\Sigma_x\right)-\left(\alpha_0\omega_a^2\Pi_y\right)^2}, \tag{B.4}$$

$$[\underline{\alpha}(\omega)]_{xz} = \frac{\mathrm{i}\alpha_0\omega_a^2\left(\alpha_0\omega_a^2\Pi_y\right)}{[\omega_a^2-\omega^2-\mathrm{i}\omega\mu-\alpha_0\omega_a^2\Sigma_z][\omega_a^2-\omega^2-\mathrm{i}\omega\mu-\alpha_0\omega_a^2\Sigma_x]-\left(\alpha_0\omega_a^2\Pi_y\right)^2}. \tag{B.5}$$

Further, $[\underline{\alpha}(\omega)]_{xz} = -[\underline{\alpha}(\omega)]_{zx}$ while all remaining not noted elements are zero. In the context of the power spectrum this yields important implications. Using the diagonal tensor structure of $\underline{\alpha}$ in the $\omega \approx \omega_a$ limit, one obtains the following result for the induced part of the power spectrum

$$\underline{\alpha} \cdot \overline{\underline{G}}^{\theta+}_{\Im} \cdot \underline{\alpha}^{\dagger} = \begin{pmatrix} |\alpha_{xx}|^2 \mathrm{Im}\{\Sigma_x^{\theta+}\} & 0 & \mathrm{i}\alpha_{xx}\alpha_{zz}^* \mathrm{Im}\{\phi_y^{\theta+}\} \\ 0 & |\alpha_{yy}|^2 \mathrm{Im}\{\Sigma_y^{\theta+}\} & 0 \\ -\mathrm{i}\alpha_{xx}^*\alpha_{zz} \mathrm{Im}\{\phi_y^{\theta+}\} & 0 & |\alpha_{zz}|^2 \mathrm{Im}\{\Sigma_z^{\theta+}\} \end{pmatrix}, \tag{B.6}$$

where the $\overline{\underline{G}}^{\theta+}_{\Im} = \int \frac{\mathrm{d}^2\mathbf{k}}{(2\pi)^2} \underline{G}_{\Im}(\mathbf{k}, k_x v + \omega)\theta(k_x v + \omega)$ (for the calculation of $\overline{\underline{G}}^{\theta}_{\Im}$ see appendix C). The polarizability enters into non-contact friction via the power spectrum $\underline{S}$ and $\underline{\alpha}_{\Im}$. In the case of $\omega \ll \omega_a$ one can simply substitute in both expressions $\underline{\alpha} \to \alpha_0 \mathbb{1}$. In the case of $\omega \approx \omega_a$ one finds

$$\underline{\alpha} \cdot \overline{\underline{G}}^{\theta+}_{\Im} \cdot \underline{\alpha}^{\dagger} \overset{\alpha_0, \omega\mu \to 0}{=} \alpha_0 \omega_a^2 \pi \delta(\omega_a^2 - \omega^2) \tag{B.7}$$

$$\times \, \mathrm{diag}\left[\frac{\mathrm{Im}\{\Sigma_x^{\theta+}\}}{\mathrm{Im}\{\Sigma_x + \mathrm{i}\frac{\mu\omega}{\alpha_0\omega_a^2}\}}, \frac{\mathrm{Im}\{\Sigma_y^{\theta+}\}}{\mathrm{Im}\{\Sigma_y + \mathrm{i}\frac{\mu\omega}{\alpha_0\omega_a^2}\}}, \frac{\mathrm{Im}\{\Sigma_z^{\theta+}\}}{\mathrm{Im}\{\Sigma_z + \mathrm{i}\frac{\mu\omega}{\alpha_0\omega_a^2}\}} \right], \tag{B.8}$$

Resonant velocities

where $\lim_{\epsilon \to 0} \frac{\epsilon}{x^2+\epsilon^2} = \pi\delta(x)$ was used and the subleading off-diagonal terms were omitted. The power spectrum around ω_a behaves therefore quite differently compared to its low-frequency counterpart. As it was shown by Intravaia et al. [222], the resonant power spectrum coincides in good approximation with that of the local thermal equilibrium approximation (see equation (3.12)). While the local equilibrium description in general fails to give correct results for the investigated system, due to the missing Doppler shift in the induced part of the power spectrum, it nevertheless yields a sufficient result in the regime $\omega_a \ll v/z_a$. As it was shown in equation (3.44) the resonant power spectrum compares the weighted integration of the Green tensor elements ($\int \frac{\mathrm{d}^2\mathbf{k}}{(2\pi)^2} \underline{G}_{\Im}(\mathbf{k}, k_x v + \omega)[n(k_x v + \omega) + 1]$, with $n(\omega, T) + 1 \overset{k_\mathrm{B}T \ll \hbar|\omega|}{\sim} \theta(\omega)$) with its unweighted pendant. Consequently, we find

$$F_{\mathrm{reso}}^{\mathrm{osc}} = -2\hbar\alpha_0\omega_a \int \frac{\mathrm{d}^2\mathbf{k}}{(2\pi)^2} \sum_{j=x,y,z} k_x \sigma_j(\mathbf{k}, \omega_a + k_x v)$$

$$\times \, \theta(\omega_a + k_x v) \left[\frac{\mathrm{Im}\{\Sigma_j^{\theta+}\big|_{\omega=\omega_a} + \mathrm{i}\frac{\mu}{\alpha_0\omega_a}\}}{\mathrm{Im}\{\Sigma_j\big|_{\omega=\omega_a} + \mathrm{i}\frac{\mu}{\alpha_0\omega_a}\}} - 1 \right], \tag{B.9}$$

where we used equation (4.2). In the case of $\omega_a \ll v/(2z_a)$ and $k \lesssim 1/(2z_a)$, the Doppler shift is much larger than the resonance frequency. With respect to the truncation of the integration this means that one can approximate $\theta(\omega_a \pm k_x v) \approx \theta(\pm k_x)$ up to a certain order in $\omega_a \ll v/(2z_a)$ (for more details see appendix C). This seems, on the first glance, contrary to the result of Intravaia et al. [222]. But in the case of the diagonal elements both approximations, i.e. $\theta(\omega_a \pm k_x v) \approx \theta(\pm k_x)$ and $\theta(\omega_a \pm k_x v) \approx \theta(\omega_a)$, yield the very same results. More details

concerning the actual calculations are given in appendix C. In conclusion we can state, that in the regime of $\omega_a \ll v/(2z_a)$ the complete Doppler shifted power spectrum yields the very same result as the local thermal equilibrium approximation. Due to the resonant character of this regime, the losses within the scattering process at the dipole are negligible. Thus, the dominant dissipation is — due to the lossy reflection of the electromagnetic field— at the macroscopic surface. Further, we have to be careful concerning the boundaries of our model. Despite our claim $2z_a\omega_a \ll v$ we still have to ensure, that $v \ll c$ in order to remain in a non-relativistic framework, where the used model is justified. Thus, our asymptotic result shall be trusted, as long as $2\frac{z_a\omega_a}{c} = 2\frac{z_a}{\lambda\!\!\!^{-}_a} \ll 1$, with $\omega_a = c/\lambda\!\!\!^{-}_a$.

APPENDIX C

Integration of the Truncated Scattered Green Tensor

In this appendix, we aim to obtain an analytical expression for the integration over the truncated scattered Green tensor in the near-field regime , i.e.

$$\int \frac{\mathrm{d}^2\mathbf{k}}{2\pi} \underline{g}(\mathbf{k}, z_a, k_x v + \omega)\theta(\pm[k_x v + \omega]). \tag{C.1}$$

In order to do so, we introduce the following function

$$\mathcal{K}^{\theta\pm}_{m,n,l}(\eta) = \int \mathrm{d}x\, x^m \theta(\pm[x+\eta]) \int_0^\infty \mathrm{d}y\, \frac{y^{2n} e^{-z}}{z^l}, \tag{C.2}$$

where $z = \sqrt{x^2+y^2}$ and η is a dimensionless input variable. The direct connection between $\mathcal{K}^{\theta\pm}_{m,n,l}(\eta)$ to the different elements of the integrated Green's tensor will become clear later in this appendix. In the following we make repeatedly use of various Bessel integrals, which can be found in [297]. To retrieve this structure we first reformulate the truncated Green's tensor. Assuming a local material ($r(\omega,k) = r(\omega)$), we find by using $k_s = s/(2z_a)$ with $s = x$ or y

$$2\int \mathrm{d}k_x f(k_x) \int_0^\infty \mathrm{d}k_y\, \frac{k_y^{2n} e^{-2z_a\sqrt{k_x^2+k_y^2}}}{(k_x^2+k_y^2)^{l/2}} = \frac{2}{(2z_a)^{2(n+1)-l}} \int \mathrm{d}x f(\frac{x}{2z_a}) \int_0^\infty \mathrm{d}y\, \frac{y^{2n} e^{-\sqrt{x^2+y^2}}}{(x^2+y^2)^{l/2}} \tag{C.3}$$

with $n = 0$ an 1 for $l = 1$ and $n = 0$ for $l = 0, -1$. Performing a substitution with $z^2 = x^2+y^2$ and the respective line element $\mathrm{d}z(z/y) = \mathrm{d}y$ we find

$$\frac{2}{(2z_a)^{2(n+1)-1}} \int \mathrm{d}x f(\frac{x}{2z_a}) \int_{|x|}^\infty \mathrm{d}z\, z^{1-l} \frac{(z^2-x^2)^n}{\sqrt{z^2-x^2}} e^{-z}. \tag{C.4}$$

This integral can be solved by

$$\int_{|x|}^{\infty} \mathrm{d}z\, z^{1-l} \frac{(z^2-x^2)^n}{\sqrt{z^2-x^2}} e^{-z} = \begin{cases} K_0(|x|) & \text{, for} \quad n=0 \quad \text{and} \quad l=1 \\ |x|K_1(|x|) & \text{, for} \quad n=1 \quad \text{and} \quad l=1 \\ |x|K_1(|x|) & \text{, for} \quad n=0 \quad \text{and} \quad l=0 \\ x^2K_0(|x|)+|x|K_1(|x|) & \text{, for} \quad n=0 \quad \text{and} \quad l=-1 \end{cases} \tag{C.5}$$

with the two lower cases being linked via the derivative of the root $\frac{z}{\sqrt{z^2-x^2}} = \partial_z \sqrt{z^2-x^2}$. In a next step, we perform the integration over the k_x component. Besides the near-field approximation, we restrict ourselves to a regime, where $r(\omega) = \text{const.} + \mathrm{i}2\epsilon_0\rho\omega$. Since, for the different elements of the Green tensor we find $f(k_x) \propto k_x^m$ with $m = 0, 1, 2, 3$, we solve for

$$\int \mathrm{d}x\, \theta(\pm[x+\eta]) x^m \begin{cases} K_0(|x|) & \text{, for} \quad n=0 \\ |x|K_1(|x|) & \text{, for} \quad n=1 \end{cases}. \tag{C.6}$$

Assuming $\eta \geq 0$, one can rewrite the two case of truncation as

$$\int \mathrm{d}x\, \theta(\pm[x+\eta]) x^m = \begin{cases} \int_0^{\infty} \mathrm{d}x\, \left[1+(-1)^m \theta(\eta-x)\right] x^m & \text{, for} \quad \theta(x+\eta) \\ \int_0^{\infty} \mathrm{d}x\, (-1)^m \theta(x-\eta) x^m & \text{, for} \quad \theta(-x-\eta) \end{cases} \tag{C.7}$$

where the second case can be represented by the first with $\theta(x-\eta) = 1-\theta(\eta-x)$. This leads to the following three integrations

$$\int_0^{\infty} \mathrm{d}x\, x^m \begin{cases} K_0(|x|) \\ |x|K_1(|x|) \end{cases} = \begin{cases} 2^{m-1}\Gamma\left(\frac{m+1}{2}\right)^2 \\ 2^m \Gamma\left(\frac{m+1}{2}\right)\Gamma\left(\frac{m+3}{2}\right) \end{cases} \tag{C.8}$$

$$\int_0^\eta \mathrm{d}x\, x^m K_0(|x|) = \begin{cases} \frac{1}{2}\pi\eta(K_0(\eta)\mathbf{L}_{-1}(\eta) + K_1(\eta)\mathbf{L}_0(\eta)) & ,m=0 \\ -\eta K_1(\eta) + 1 & ,m=1 \\ \frac{1}{6}\eta(3\pi K_2(\eta)\mathbf{L}_1(\eta) + K_1(\eta)(3\pi\mathbf{L}_2(\eta) - 4\eta)) & ,m=2 \\ \eta^3(-K_1(\eta)) - 2\eta^2 K_2(\eta) + 4 & ,m=3 \\ \frac{\eta}{2}\Big[K_1(\eta)\left(9\pi\mathbf{L}_0(\eta) - 2\eta\left(\eta^2+9\right)\right) & \\ -3K_0(\eta)\left(2\eta^2 - 3\pi\mathbf{L}_{-1}(\eta) + 6\right)\Big] & ,m=4 \end{cases} \tag{C.9}$$

$$\int_0^\eta \mathrm{d}x\, x^{m+1} K_1(x) = \begin{cases} \frac{\pi\eta}{2}\left[\mathbf{L}_0(\eta)K_1(\eta) + \mathbf{L}_1(\eta)K_0(\eta)\right] & ,m=0 \\ -\eta\left[\eta K_0(\eta) + 2K_1(\eta)\right] + 2 & ,m=1 \\ -3\eta^2 K_1(\eta) - \eta^3 K_0(\eta) & ,m=2 \\ +3\left(\frac{\pi\eta}{2}\left[\mathbf{L}_0(\eta)K_1(\eta) + \mathbf{L}_1(\eta)K_0(\eta)\right]\right) & \\ -\eta\left[\left(\eta^3+8\eta\right)K_0(\eta) + \left(4\eta^2+16\right)K_1(\eta)\right] + 16 & ,m=3 \end{cases} \tag{C.10}$$

with $\Gamma(\frac{1}{2}) = \sqrt{\pi}$, $\Gamma(\frac{3}{2}) = \frac{\sqrt{\pi}}{2}$, $\Gamma(\frac{5}{2}) = \frac{3\sqrt{\pi}}{4}$ and $\Gamma(n+1) = n!$ for $n > 0$ and $n \in \mathbb{N}$. Here, $\mathbf{L}_\nu$ is the modified Struve function. The remaining integration can be constructed by the displayed results (by $\theta(x-\eta) = 1-\theta(\eta-x)$). While these results may also be of broader interest, we are more interested in asymptotic results. In the actual calculation of the Green's tensor elements the parameter $\eta = \omega(2z_a)/v$. For the special case of $\omega \approx \omega_a$ and the dipole resonance ω_a being much smaller than the frequencies upper bound $v/(2z_a)$, i.e. $\omega_a \ll v/(2z_a)$, we can approximate the above expressions for $\eta = 2\omega_a z_a/v \ll 1$. This leads to

$$\int_0^\eta \mathrm{d}x\, x^m K_0(|x|) = \begin{cases} -\eta\left[\ln(\frac{\eta}{2}) + \gamma - 1\right] + \mathcal{O}(\eta^2) & , m = 0 \\ -\frac{\eta^2}{4}\left[2\ln(\frac{\eta}{2}) + 2\gamma - 1\right] + \mathcal{O}(\eta^3) & , m = 1 \\ -\frac{\eta^3}{9}\left[3\ln(\frac{\eta}{2}) + 3\gamma - 1\right] + \mathcal{O}(\eta^4) & , m = 2 \\ -\frac{\eta^4}{16}\left[4\ln(\frac{\eta}{2}) + 4\gamma - 1\right] + \mathcal{O}(\eta^5) & , m = 3 \end{cases} \tag{C.11}$$

with $\gamma \approx 0.5772$. Thus, for those integrals evaluated and demanded for later calculations one finds the expression

$$\int_0^\eta \mathrm{d}x\, x^m K_0(|x|) \overset{\eta \ll 1}{=} -\frac{\eta^{m+1}}{m+1}\left[\ln(\frac{\eta}{2}) + \gamma - \frac{1}{m+1}\right] + \mathcal{O}(\eta^{m+2}) \tag{C.12}$$

$$\int_0^\eta \mathrm{d}x\, x^{m+1} K_1(x) = \begin{cases} \eta + \frac{\eta^3}{6}\left[\ln(\frac{\eta}{2}) + \gamma - \frac{5}{6}\right] + \mathcal{O}(\eta^4) & , m = 0 \\ \frac{\eta^2}{2} + \frac{\eta^4}{8}\left[\ln(\frac{\eta}{2}) + \gamma - \frac{3}{4}\right] + \mathcal{O}(\eta^5) & , m = 1 \\ \frac{\eta^3}{3} + \frac{\eta^5}{10}\left[\ln(\frac{\eta}{2}) + \gamma - \frac{7}{10}\right] + O\left(\eta^6\right) & , m = 2 \\ \frac{\eta^4}{4} + \frac{\eta^6}{12}\left[\ln(\frac{\eta}{2}) + \gamma - \frac{2}{3}\right] + \mathcal{O}(\eta^7) & , m = 3 \end{cases} \tag{C.13}$$

Here, the evaluated terms lead to the expression

$$\int_0^\eta \mathrm{d}x\, x^{m+1} K_1(x) \overset{\eta \ll 1}{=} \frac{\eta^{m+1}}{m+1} + \frac{\eta^{m+2}}{2(m+3)}\left[\ln(\frac{\eta}{2}) + \gamma - \frac{m+5}{2(m+3)}\right] + \mathcal{O}(\eta^{m+4}). \tag{C.14}$$

With the expressions of equations (C.12) and (C.14) we can evaluate the truncated Green tensor at ω_a and extract the asymptote for $\omega_a \ll v/(2z_a)$. By using again, that $\underline{g} = \underline{\sigma} - \phi\underline{L}_y$ and assuming $r(\omega + k_x v) \approx r^0 + 2\mathrm{i}\epsilon_0\rho(\omega + k_x v)$, we find for the different components

$$\int \frac{\mathrm{d}^2\mathbf{k}}{(2\pi)^2}\mathrm{Im}\{\sigma_{xx}(\mathbf{k}, z_a, \omega + k_x v)\}\theta(\omega + k_x v)$$

$$=\frac{\rho v}{(2z_a)^4}\frac{2}{(2\pi)^2}\int \mathrm{d}x \int_0^\infty \mathrm{d}y \frac{x^2}{\sqrt{x^2+y^2}} e^{-\sqrt{x^2+y^2}} \left(\eta + x\right) \theta(x+\eta) \tag{C.15}$$

$$= \frac{\rho v}{(2z_a)^4}\frac{2}{(2\pi)^2}\int_0^\infty \mathrm{d}x\, x^2 K_0(|x|) \left(\eta[1+\theta(\eta-x)] + x[1-\theta(\eta-x)]\right) \tag{C.16}$$

$$= \frac{\rho v}{(2z_a)^4}\frac{2}{(2\pi)^2}\left(\frac{\pi}{2}\eta + \frac{\eta^2}{2}K_2(\eta)\left(\pi \mathbf{L}_1(\eta)+4\right) + \frac{\eta^2}{6}K_1(\eta)\left(2\eta + 3\pi \mathbf{L}_2(\eta)\right)\right) \tag{C.17}$$

$$= \frac{\rho v}{(2z_a)^4}\frac{2}{(2\pi)^2}\left[\left(\frac{\pi}{2}\eta + 4\right) - \frac{\eta^4}{12}\left[\ln\left(\frac{\eta}{2}\right) + \gamma - \frac{7}{12}\right]\right] + \mathcal{O}(\eta^5). \tag{C.18}$$

Thus, we find in leading zeroth order

$$\int \frac{\mathrm{d}^2\mathbf{k}}{(2\pi)^2}\mathrm{Im}\{\sigma_{xx}(\mathbf{k}, z_a, \omega + k_x v)\}\theta(\omega + k_x v) \overset{\eta\ll 1}{=} \frac{\rho v}{(2z_a)^4}\frac{8}{(2\pi)^2}\left(\frac{\pi}{2}\eta + 4\right) + \mathcal{O}(\eta^4). \tag{C.19}$$

Interestingly, up to the fourth order this result would be the same, when exchanging $\theta(\omega + k_x v) \to \theta(k_x v)$. In contrast we find for the opposite truncation

$$\int \frac{\mathrm{d}^2\mathbf{k}}{(2\pi)^2}\mathrm{Im}\{\sigma_{xx}(\mathbf{k}, z_a, \omega + k_x v)\}\theta(-\omega - k_x v)$$

$$=\frac{\rho v}{(2z_a)^4}\frac{2}{(2\pi)^2}\int \mathrm{d}x \int_0^\infty \mathrm{d}y \frac{x^2}{\sqrt{x^2+y^2}} e^{-\sqrt{x^2+y^2}} \left(\eta + x\right) \theta(-x-\eta) \tag{C.20}$$

$$= \frac{\rho v}{(2z_a)^4}\frac{2}{(2\pi)^2}\int_0^\infty \mathrm{d}x\, x^2 K_0(|x|)(\eta - x)[1-\theta(\eta-x)] \tag{C.21}$$

$$= \frac{\rho v}{(2z_a)^4}\frac{2}{(2\pi)^2}\left(\frac{\pi}{2}\eta - \frac{\eta^2}{2}K_2(\eta)\left(\pi \mathbf{L}_1(\eta)+4\right) - \frac{\eta^2}{6}K_1(\eta)\left(2\eta + 3\pi \mathbf{L}_2(\eta)\right)\right) \tag{C.22}$$

$$= \frac{\rho v}{(2z_a)^4}\frac{2}{(2\pi)^2}\left[\left(\frac{\pi}{2}\eta - 4\right) + \frac{\eta^4}{12}\left[\ln\left(\frac{\eta}{2}\right) + \gamma - \frac{7}{12}\right]\right] + \mathcal{O}(\eta^4) \tag{C.23}$$

and at the leading order

$$\int \frac{\mathrm{d}^2\mathbf{k}}{(2\pi)^2}\mathrm{Im}\{\sigma_{xx}(\mathbf{k}, z_a, \omega + k_x v)\}\theta(\omega + k_x v) \overset{\eta\ll 1}{=} \frac{\rho v}{(2z_a)^4}\frac{8}{(2\pi)^2}\left(\frac{\pi}{2}\eta - 4\right) + \mathcal{O}(\eta^4). \tag{C.24}$$

Up to the fourth order this result would be the same, if $\theta(-\omega - k_x v) \to \theta(-k_x v)$. Let us continue with the yy element

$$\int \frac{\mathrm{d}^2\mathbf{k}}{(2\pi)^2}\mathrm{Im}\{\sigma_{yy}(\mathbf{k}, z_a, \omega + k_x v)\}\theta(\omega + k_x v)$$

$$= \frac{\rho v}{(2z_a)^4}\frac{2}{(2\pi)^2}\int \mathrm{d}x \int_0^\infty \mathrm{d}y \frac{y^2}{\sqrt{x^2+y^2}} e^{-\sqrt{x^2+y^2}} \left(\eta + x\right)\theta(-x-\eta) \tag{C.25}$$

$$= \frac{\rho v}{(2z_a)^4}\frac{2}{(2\pi)^2}\int_0^\infty \mathrm{d}x\, x K_1(x) \left(\eta[1+\theta(\eta - x)] + x[1-\theta(\eta-x)]\right) \tag{C.26}$$

$$= \frac{\rho v}{(2z_a)^4}\frac{2}{(2\pi)^2}\left[\left(\frac{\pi}{2}\eta + 2\right) - \frac{\eta^2}{2}\left[\ln\left(\frac{\eta}{2}\right) + \gamma - \frac{3}{2}\right]\right] + \mathcal{O}(\eta^3). \tag{C.27}$$

Analogously we find

$$\int \frac{\mathrm{d}^2\mathbf{k}}{(2\pi)^2}\mathrm{Im}\{\sigma_{yy}(\mathbf{k}, z_a, \omega + k_x v)\}\theta(-\omega - k_x v)$$

$$= \frac{\rho v}{(2z_a)^4}\frac{2}{(2\pi)^2}\left[\left(\frac{\pi}{2}\eta - 2\right) + \frac{\eta^2}{2}\left[\ln\left(\frac{\eta}{2}\right) + \gamma - \frac{3}{2}\right]\right] + \mathcal{O}(\eta^3). \tag{C.28}$$

Up to third order in η the results can be reproduced by $\theta(\pm k_x v \pm \omega) \to \theta(\pm k_x)$. Finally, the zz component can be expressed as the sum of the xx and yy component. Hence, we find

$$\int \frac{\mathrm{d}^2\mathbf{k}}{(2\pi)^2}\mathrm{Im}\{\sigma_{zz}(\mathbf{k}, z_a, \omega + k_x v)\}\theta(\pm\omega \pm k_x v)$$

$$= \frac{\rho v}{(2z_a)^4}\frac{2}{(2\pi)^2}\left[\left(\pi\eta \pm 6\right) \mp \frac{\eta^2}{2}\left[\ln\left(\frac{\eta}{2}\right) + \gamma - \frac{3}{2}\right]\right] + \mathcal{O}(\eta^3). \tag{C.29}$$

Again up to second order with the same symmetry properties as found for σ_{yy} and σ_{zz}, i.e. $\theta(\pm k_x v \pm \omega) \to \theta(\pm k_x)$. Lastly, we calculate the off-diagonal contribution

$$\int \frac{\mathrm{d}^2\mathbf{k}}{(2\pi)^2}\mathrm{Im}\{\phi_y(\mathbf{k}, z_a, \omega + k_x v)\}\theta(\omega + k_x v)$$

$$= \frac{\rho v}{(2z_a)^4} \frac{2}{(2\pi)^2} \int \mathrm{d}x\, x \int_0^\infty \mathrm{d}y\, e^{-\sqrt{x^2+y^2}} \left(\eta + x\right) \theta(x+\eta) \tag{C.30}$$

$$= \frac{\rho v}{(2z_a)^4} \frac{2}{(2\pi)^2} \int_0^\infty \mathrm{d}x\, x^2 K_1(|x|) \left(\eta[1-\theta(\eta-x)] + x[1+\theta(\eta-x)]\right) \tag{C.31}$$

$$= \frac{\rho v}{(2z_a)^4} \frac{2}{(2\pi)^2} \left[\left(\frac{\pi}{2}\eta + 4\right) + \frac{\eta^3}{6}\left[\ln\left(\frac{\eta}{2}\right) + \gamma - \frac{5}{6}\right]\right] + \mathcal{O}(\eta^5) \tag{C.32}$$

and

$$\int \frac{\mathrm{d}^2\mathbf{k}}{(2\pi)^2} \mathrm{Im}\{\phi_y(\mathbf{k}, z_a, \omega + k_x v)\}\theta(-\omega - k_x v)$$

$$= \frac{\rho v}{(2z_a)^4} \frac{2}{(2\pi)^2} \left[\left(-\frac{\pi}{2}\eta + 4\right) - \frac{\eta^3}{6}\left[\ln\left(\frac{\eta}{2}\right) + \gamma - \frac{5}{6}\right]\right] + \mathcal{O}(\eta^4) \tag{C.33}$$

Again, up to the third order we can retrieve $\theta(\pm k_x v \pm \omega) \to \theta(\pm k_x)$.

APPENDIX D

Reflection Coefficients of Non-local Materials

As already stated in equation (2.56) we can calculate the reflection coefficient of a nonlocal material B of thickness d cladded in another local material A with the formula

$$r^{\sigma}_{\mathrm{ABA}}(\omega,k,d) = \frac{[Z^{\sigma}_{\mathrm{A}}(\omega,k)]^2 - \mathcal{Z}^{\sigma}_{\mathrm{B}+}(\omega,k,d)\mathcal{Z}^{\sigma}_{\mathrm{B}-}(\omega,k,d)}{[Z^{\sigma}_{\mathrm{A}}(\omega,k)]^2 + \mathcal{Z}^{\sigma}_{\mathrm{B}+}(\omega,k,d)\mathcal{Z}^{\sigma}_{\mathrm{B}-}(\omega,k,d) + 2\mathrm{i}\mathrm{cs}^{\sigma}_{\mathrm{B}}(\omega,k,d)Z^{\sigma}_{\mathrm{A}}(\omega,k)\mathcal{Z}^{\sigma}_{\mathrm{B}-}(\omega,k,d)}. \tag{D.1}$$

The local surface impedances Z were already displayed in the main text in equation (2.58). The remaining coefficients can for example be found in the work of Intravaia and Busch [298]

$$\mathrm{cs}^{\sigma}_{\mathrm{B}}(d) = \frac{\beta(0^+)\eta^{\sigma}(0) + \beta(d)\eta^{\sigma}(d)}{\beta(d)\eta^{\sigma}(0) + \beta(0^+)\eta^{\sigma}(d)} \tag{D.2}$$

$$\mathcal{Z}_{\mathrm{B}-}(d) = -\mathrm{i}\frac{(\eta^{\sigma}(d))^2 - (\eta^{\sigma}(0))^2}{\beta(d)\eta^{\sigma}(0) + \beta(0^+)\eta^{\sigma}(d)}, \quad \mathcal{Z}^{\sigma}_{\mathrm{B}+}(d) = \mathrm{i}\frac{\beta(d)\eta^{\sigma}(0) + \beta(0^+)\eta^{\sigma}(d)}{\beta^2(d) - \beta^2(0^+)} \tag{D.3}$$

where following quantities are introduced

$$\eta^{p}(z) = \frac{\omega}{c}\int_{-\infty}^{\infty}\frac{\mathrm{d}k_z}{2\pi\mathrm{i}}\left(\frac{2\frac{k_z^2}{K^2}e^{\mathrm{i}k_z z}}{K^2 - \frac{\omega^2}{c^2}\epsilon_t(K,\omega)} - \frac{2\frac{k^2}{K^2}e^{\mathrm{i}k_z z}}{\frac{\omega^2}{c^2}\epsilon_l(K,\omega)}\right), \tag{D.4}$$

$$\eta^{s}(z) = \frac{\omega}{c}\int_{-\infty}^{\infty}\frac{\mathrm{d}k_z}{2\pi\mathrm{i}}\frac{2e^{\mathrm{i}k_z z}}{K^2 - \frac{\omega^2}{c^2}\epsilon_t(K,\omega)}, \quad \beta(z) = \int_{-\infty}^{\infty}\frac{dk_z}{2\pi\mathrm{i}}\frac{2k_z e^{\mathrm{i}k_z z}}{K^2 - \frac{\omega^2}{c^2}\epsilon_t(K,\omega)} \tag{D.5}$$

with $K^2 = k^2 + k_z^2$ and $\epsilon_{t/l}$ is the longitudinal or transversal permittivity, respectively.

APPENDIX E

Non-Markovian Heat Bath in small Nanoparticles

As introduced in section 2.2, besides atom-like objects without any internal dissipation channels, one can consider more complex systems including dissipation. Such a system needs a sufficiently large amount of internal degrees of freedom, mimicking a heat bath. If the number of internal degrees of freedom is too small, one still may find an interesting complex response of the "heat bath", but also a finite Poincaré recurrence time, which would not be sufficient to describe actual dissipation effects. A rather interesting and peculiar object class are nanoparticles [299]. These nanoparticles can exhibit colored noise. As Hänggi and Jung stated in [94]: "In the theoretical treatment of such systems it is often the case that strongly colored internal noise emerges as the result of coarse graining over a hidden set of slow variables.". Therefore, we attempt to appropriately describe the nanoparticle response by incorporating the much slower electron-phonon relaxation. Especially, we follow the argument of López et al. [158] that in sufficiently small nanoparticles one phonon mode dominantly couples to the dipole moment. Besides the coupling between the dipole oscillation and the phonon — and the phonon oscillation itself —, we have to take care of the phonon's lifetime. The lifetime is determined by the coupling to the far detuned other phonon modes within the heat bath, which is the same bath as the dipole moment couples to. But since the dynamics of the dipole oscillations and the phonon happen on very different time scales ($\tau_{\mathrm{ph-ph}} \approx 100\,\mathrm{ps}$ $\tau_{\mathrm{e-ph}} \approx 1 - 5\,\mathrm{ps}$, whereas $\tau_{\mathrm{e-e}} \lesssim 500\,\mathrm{fs}$[300–303]), it is reasonable to assume that the relaxation mechanisms approximately decouple and can be described by separated heat baths $\mathcal{B}$ and $\tilde{\mathcal{B}}$. With this assumption, the equations of motion can be solved analytically. We start by setting up the Hamiltonian of the nanoparticle

$$\hat{\mathcal{H}} = \hat{\mathcal{H}}_{\mathbf{d}\mathcal{B}} + \hat{\mathcal{H}}_{\boldsymbol{\pi}\tilde{\mathcal{B}}} + \hat{\mathcal{H}}_{\mathbf{d}\pi}\,. \tag{E.1}$$

The three terms refer to the dipole plus its bath, the phonon plus its bath and the coupling between dipole and phonon. If we apply the independent oscillator model as done by Ford et

al. [304], we find

$$\hat{\mathcal{H}}_{\mathbf{d}\mathcal{B}} = \frac{\hat{\mathbf{p}}_{\mathbf{d}}^2}{2m_{\mathbf{d}}} + \frac{m_{\mathbf{d}}}{2}\omega_{\mathbf{d}}^2\hat{\mathbf{x}}_{\mathbf{d}}^2 + \sum_j \left[\frac{\hat{\mathbf{p}}_j^2}{2m_j} + \frac{m_j}{2}\omega_j^2\left(\hat{\mathbf{q}}_j - \hat{\mathbf{x}}_{\mathbf{d}}\right)^2\right] \tag{E.2}$$

$$\hat{\mathcal{H}}_{\boldsymbol{\pi}\tilde{\mathcal{B}}} = \frac{\hat{\mathbf{p}}_{\pi}^2}{2m_{\boldsymbol{\pi}}} + \frac{m_{\boldsymbol{\pi}}}{2}\omega_{\boldsymbol{\pi}}^2\hat{\mathbf{x}}^2 + \sum_j \left[\frac{\hat{\tilde{\mathbf{p}}}_j^2}{2\tilde{m}_j} + \frac{\tilde{m}_j}{2}\tilde{\omega}_j^2\left(\hat{\tilde{\mathbf{q}}}_j - \hat{\mathbf{x}}_{\boldsymbol{\pi}}\right)^2\right] \tag{E.3}$$

$$\hat{\mathcal{H}}_{\mathbf{d}\pi} = g\hat{\mathbf{x}}_{\mathbf{d}}^{\intercal}\hat{\mathbf{x}}_{\boldsymbol{\pi}} \tag{E.4}$$

where g is the coupling constant between the dipole and the phonon. The $\hat{\mathbf{q}}_j$ and $\hat{\mathbf{p}}_j$ (or with tilde, respectively) represent the bath modes. We can now extract the different equations of motion from the complete Hamiltonian of equation (E.1). First, analogously to Ford et al. [73] we find the equation of motions of the $\mathcal{B}$ bath's degrees of freedom

$$\ddot{\hat{\mathbf{q}}}_j(t) + \omega_j^2\hat{\mathbf{q}}_j(t) = \omega_j^2\hat{\mathbf{x}}_{\mathbf{d}}(t), \tag{E.5}$$

which is solved by

$$\hat{\mathbf{q}}_j(t) = \hat{\mathbf{q}}_j^{\text{free}}(t) + \int_{t_{\text{in}}}^{\infty} \mathrm{d}t_1\theta\left(t - t_1\right)\omega_j \sin\left[\omega_j\left(t - t_1\right)\right]\hat{\mathbf{x}}_{\mathbf{d}}\left(t_1\right) \tag{E.6}$$

$$\hat{\mathbf{q}}_j^{\text{free}}(t) = \hat{\mathbf{q}}_j(t_{\text{in}})\cos(\omega_j t) + \hat{\mathbf{p}}_j(t_{\text{in}})\frac{\sin(\omega_j t)}{m_j\omega_j}. \tag{E.7}$$

This can be done in complete analogy with respect to the $\tilde{\mathcal{B}}$ heat bath by substituting $\mathbf{d} \to \boldsymbol{\pi}$ and $\hat{\mathbf{q}}_j, \hat{\mathbf{p}}_j \to \hat{\tilde{\mathbf{q}}}_j, \hat{\tilde{\mathbf{p}}}_j$. Using the quantities

$$\mu_{\mathbf{d}}(t) = \theta(t)\sum_j \frac{m_j}{m_{\mathbf{d}}}\omega_j^2\cos\left[\omega_j t\right], \quad \hat{\mathbf{F}}_{\mathbf{d}}(t) = \sum_j \frac{m_j}{m_{\mathbf{d}}}\omega_j^2\hat{\mathbf{q}}_j^{\text{free}}(t), \tag{E.8}$$

we construct the equation of motion of the phononic mode

$$\ddot{\hat{\mathbf{x}}}_{\boldsymbol{\pi}}(t) + \int_{-\infty}^{\infty} \mathrm{d}t_1\,\mu_{\boldsymbol{\pi}}(t - t_1)\dot{\hat{\mathbf{x}}}_{\boldsymbol{\pi}}(t) + \omega_{\boldsymbol{\pi}}^2\hat{\mathbf{x}}_{\boldsymbol{\pi}}(t) = \hat{\mathbf{F}}_{\boldsymbol{\pi}}(t) - g\hat{\mathbf{x}}_{\mathbf{d}}(t) \tag{E.9}$$

which is solved in frequency domain by

$$\hat{\mathbf{x}}_{\boldsymbol{\pi}}(\omega) = \alpha_{\boldsymbol{\pi}}(\omega)\left(\hat{\mathbf{F}}_{\boldsymbol{\pi}}(\omega) - g\hat{\mathbf{x}}_{\mathbf{d}}(\omega)\right) \quad \text{with} \quad \alpha_{\boldsymbol{\pi}}(\omega) = \left(\omega_{\boldsymbol{\pi}}^2 - \omega^2 - i\omega\mu_{\boldsymbol{\pi}}(\omega)\right)^{-1}. \tag{E.10}$$

Combining the fluctuation force and the memory kernel of the phononic mode and the dipole mode as follows

$$\hat{\mathbf{F}}(\omega) = \hat{\mathbf{F}}_{\mathbf{d}}(\omega) - g\alpha_{\boldsymbol{\pi}}(\omega)\hat{\mathbf{F}}_{\boldsymbol{\pi}}(\omega), \quad \mu(\omega) = \mu_{\mathbf{d}}(\omega) + g^2\frac{\alpha_{\boldsymbol{\pi}}(\omega)}{i\omega}, \tag{E.11}$$

we retrieve the familiar Langevin form of equation (1.48)

$$-\omega^2 \hat{\mathbf{x}}_{\mathbf{d}}(\omega) - i\omega\mu(\omega)\hat{\mathbf{x}}_{\mathbf{d}}(\omega) + \omega_{\mathbf{d}}^2 \hat{\mathbf{x}}_{\mathbf{d}}(\omega) = \hat{\mathbf{F}}(\omega) \tag{E.12}$$

Here, the new quantities $\hat{\mathbf{F}}$ and μ still fulfill the fluctuation-dissipation theorem (see section 1.2). If we assume Ohmicity of the separated heat baths $\mathcal{B}$ and $\tilde{\mathcal{B}}$, i.e. $\mu_{\mathbf{d}}(\omega) = \gamma_{\mathcal{B}} = \text{const.}$ and $\mu_{\boldsymbol{\pi}}(\omega) = \gamma_{\tilde{\mathcal{B}}} = \text{const.}$, we arrive at the following memory kernel

$$\mu(\omega) = \gamma_{\mathcal{B}} + \frac{g^2}{\mathrm{i}\omega(\omega_{\boldsymbol{\pi}}^2 - \omega^2 - \mathrm{i}\omega\gamma_{\tilde{\mathcal{B}}})}, \tag{E.13}$$

with

$$\mathrm{Re}\{\mu(\omega)\} = \gamma_{\mathcal{B}} + \frac{g^2\gamma_{\tilde{\mathcal{B}}}}{(\omega_{\boldsymbol{\pi}}^2 - \omega^2)^2 + \omega^2\gamma_{\tilde{\mathcal{B}}}^2}, \quad \mathrm{Im}\{\mu(\omega)\} = \frac{-g^2(\omega_{\boldsymbol{\pi}}^2 - \omega^2)}{\omega[(\omega_{\boldsymbol{\pi}}^2 - \omega^2)^2 + \omega^2\gamma_{\tilde{\mathcal{B}}}^2]}. \tag{E.14}$$

With equation (E.13) we obtain a modified, but probably more realistic, description of a nanoparticle's memory kernel. To comply with the expression in equation (2.30) one has to substitute $\gamma_{\mathcal{B}} \to \gamma$, $\gamma_{\tilde{\mathcal{B}}} \to \gamma_{\mathrm{phon}}$ and $\omega_{\boldsymbol{\pi}} \to \omega_{\mathrm{phon}}$. The value of the various parameters can be found in comparison with other phenomenological models as described in [158].

APPENDIX F

Non-retarded Limit and Near-field Approximation

As argued in the main text in section 3.3, we can use the near-field limit of our system to simplify the results drastically. However, we need to be clear about the meaning of the near-field limit. Thus, in the following we like to present, how exactly this very useful asymptotic behavior is extracted and what restricts its range of validity. During the derivation we strongly depend on the non-relativistic limit. In order to do so, we want to start with equation (4.5). For $\hbar\omega \gg k_\mathrm{B}T$ the $\Theta_{T=0}(\omega + k_x v, \omega)$ becomes $-\theta(-\omega - k_x v)$ and yields the relation

$$-k_x v \geq \omega \,. \tag{F.1}$$

As shown in equation (4.5), we solely integrate over positive ω and thus only negative k_x values contribute. By using spherical coordinates, we find

$$kv \geq k|\cos\varphi|v \geq \omega \,. \tag{F.2}$$

Since we only investigate non-relativistic velocities, $v \ll c$ immediately leads to

$$k \geq \frac{\omega}{v} \gg \frac{\omega}{c} \,, \tag{F.3}$$

telling us that at least for one of the two contributing Green's tensors, solely evanescent waves contribute to the non-contact friction. In the following we will treat $\omega_+ = \omega + k_x v$ simply as if it was ω, since the statements we achieve remain the same. The above relation already enables us to approximate $\kappa = \sqrt{k^2 - \omega^2/c^2} \to k$. For κ or k respectively, we notice another feature. The exponential function in the Green's tensor is strongly damping κ values much larger than $1/(2z_a)$. With this information we find

$$\frac{1}{2z_a} \gtrsim k \geq \frac{\omega}{v} \gg \frac{\omega}{c} \,, \tag{F.4}$$

which gives us the estimated upper bound

$$\omega \lesssim \frac{v}{2z_a}\,. \tag{F.5}$$

The $\lesssim$ relation expresses the upper bound, but recognizes that values of $k \ll 1/(2z_a)$ are also suppressed. The suppression of very small values of k is due to the leading $k^{n>1}$ polynomial in the Green's tensor. With this inequality the first length scale enters the investigation, namely the distance of the particle to the surface. The reflection coefficients contain besides the κ also a $\kappa_\epsilon = \sqrt{k^2 - \epsilon(\omega)\omega^2/c^2}$. The latter is the crucial term of a near-field approximation in our setup. To clarify, we exemplary substitute the response of a semi-infinite Drude material, which was introduced in equation (2.93). We obtain using the above relations

$$\kappa_\epsilon^2 = k^2 - \frac{\omega^2}{c^2} + \frac{1}{\lambda\!\!\!^{-2}_{\mathrm{p}}(1 - \mathrm{i}\gamma/\omega)} \overset{v\ll c}{=} k^2 + \frac{1}{\lambda\!\!\!^{-2}_{\mathrm{p}}(1 - \mathrm{i}\gamma/\omega)} \tag{F.6}$$

This relation brings up two comparisons: ω compared to γ and k compared to the inverse plasma wavelength $\lambda\!\!\!^{-}_{\mathrm{p}} = c/\omega_{\mathrm{p}}$. The first comparison decides if a strongly damped ($\omega \ll \gamma$) or in nearly undamped ($\omega \gg \gamma$) regime is considered. The second comparison tells, if either propagating ($k \ll 1/\lambda\!\!\!^{-}_{\mathrm{p}}$) or evanescent ($k \gg 1/\lambda\!\!\!^{-}_{\mathrm{p}}$) contributions prevail the fields in the material. While the propagating fields can be sensed far off the material's surface, the evanescent fields are closely bound to the surface. Combining this with the information that $k \lesssim 1/(2z_a)$ yields the comparison of the two lengths z_a and $\lambda\!\!\!^{-}_{\mathrm{p}}$. Thus, if $\lambda\!\!\!^{-}_{\mathrm{p}} \ll 2z_a$ we can speak of the far field regime, which is governed by propagating fields, whereas $\lambda\!\!\!^{-}_{\mathrm{p}} \gg 2z_a$ represents the near-field with its dominant evanescent fields. To make statements independent of the (local) material model we define $\lambda\!\!\!^{-}_{\epsilon}(\omega) = c/(\omega\sqrt{\epsilon(\omega)})$. For the respective reflection coefficients we can identify following evanescent asymptotes [305]

$$r^p(\omega,k) = \frac{\epsilon(\omega)\kappa - \kappa_\epsilon}{\epsilon(\omega)\kappa + \kappa_\epsilon} = \begin{cases} \dfrac{\epsilon(\omega)-1}{\epsilon(\omega)+1} & \text{for} \quad k \gg 1/|\lambda\!\!\!^{-}_{\epsilon}(\omega)| \gg \omega/c \quad \text{(near field)} \\[2ex] 1 + \mathrm{i}\dfrac{2}{\sqrt{\epsilon(\omega)}}\dfrac{\omega}{ck} & \text{for} \quad 1/|\lambda\!\!\!^{-}_{\epsilon}(\omega)| \gg k \gg \omega/c \quad \text{(far field)} \end{cases}, \tag{F.7}$$

$$r^s(\omega,k) = \frac{\kappa - \kappa_\epsilon}{\kappa + \kappa_\epsilon} = \begin{cases} \big(\epsilon(\omega)-1\big)\dfrac{\omega^2}{4c^2k^2} & \text{for} \quad k \gg 1/|\lambda\!\!\!^{-}_{\epsilon}(\omega)| \gg \omega/c \quad \text{(near field)} \\[2ex] -1 + \mathrm{i}\dfrac{2}{\sqrt{\epsilon(\omega)}}\dfrac{ck}{\omega} & \text{for} \quad 1/|\lambda\!\!\!^{-}_{\epsilon}(\omega)| \gg k \gg \omega/c \quad \text{(far field)} \end{cases}. \tag{F.8}$$

We like to emphasize again, that the field in the vacuum remains evanescent in our context, however, within the material both contributions are possible. Furthermore, it is worth noticing,

that in the context of the scattered Green's tensor (see equation (2.41)) the imaginary parts of the two polarizations are, when including their respective weight — either k^2 for p polarization, or ω_+^2/c^2 for s polarization —, equally contributing

$$k^2 r_I^p(\omega, k) \approx -\frac{\omega^2}{c^2} r_I^s(\omega, k)\,. \tag{F.9}$$

Eventually, we obtain the (imaginary) scattered Green's tensor expressions from equation (4.14) for a local material model in the near field

$$\int \frac{\mathrm{d}^2\mathbf{k}}{(2\pi)^2} \underline{G}_{\Im}(\omega_+, k) \overset{\text{near}}{=} \frac{1}{4\pi^2\epsilon_0} \int_0^\pi \mathrm{d}\varphi \int_0^\infty \mathrm{d}k\, k^2 e^{-2z_a k} r_I^p(\omega_+, k) \tag{F.10}$$

$$\times \left[\mathrm{diag} \begin{pmatrix} \cos^2\varphi \\ \sin^2\varphi \\ 1 \end{pmatrix} - \cos\varphi\, \underline{L}_y \right], \tag{F.11}$$

whereas we find in the far field

$$\int \frac{\mathrm{d}^2\mathbf{k}}{(2\pi)^2} \underline{G}_{\Im}(\omega_+, k) \overset{\text{far}}{=} \frac{1}{4\pi^2\epsilon_0} \int_0^\pi \mathrm{d}\varphi \int_0^\infty \mathrm{d}k\, e^{-2z_a k} k^2 r_I^p(\omega_+, k) \tag{F.12}$$

$$\times \left[\mathrm{diag} \begin{pmatrix} \cos(2\varphi) \\ -\cos(2\varphi) \\ 1 \end{pmatrix} - \cos\varphi\, \underline{L}_y \right], \tag{F.13}$$

where the reflection coefficients are set to the corresponding approximation. In the near-field limit the s contribution can be neglected, whereas in the far field both polarizations equally contribute. So far we only discussed to limits with respect to one integration over the Green's tensor. However, in equation (3.24) or equation (4.5) a second integration over another Green's tensor is hidden in the power spectrum $\underline{S}(\omega)$. In order to avoid confusion, we mark any integration variable of this second integration with a prime. Here, no Heaviside distribution is present. Nonetheless, the inequalities $\omega \lesssim v/(2z_a)$ remain, since it is the very same frequency in both Green's tensors. Moreover, the $\kappa' = \sqrt{k'^2 - \omega^2/c^2} \lesssim 1/(2z_a)$ originates again solely from the exponential. Due to the non-relativistic limit $v \ll c$ again solely real κ' contribute. Hence, in combination we find the relation

$$\frac{1}{(2z_a)^2} \approx \frac{1}{(2z_a)^2} + \frac{v^2}{c^2(2z_a)^2} \gtrsim \frac{1}{(2z_a)^2} + \frac{\omega^2}{c^2} \gtrsim k'^2\,. \tag{F.14}$$

Eventually, one can apply the same scheme as done for the first Green's tensor integration.

Acknowledgments/Danksagung

First of all, I want to thank Prof. Dr. Kurt Busch for giving me the opportunity to work on fluctuation-induced phenomena in the wonderful TO&P group full of wonderful people. Moreover, I want to thank Dr. Francesco Intravaia for an always open door, great scientific advise, and a three and a half years journey through nearly all the physics.

Also, I want to thank Prof. Dr. Claudia Eberlein and Prof. Dr. Stefan Scheel for kindly agreeing to review my thesis and Prof. Christoph T. Koch, PhD and Prof. Dr. Caterina Cocchi for completing my PhD committee.

Furthermore, I want to thank Gus Chan for sharing his beautiful picture for the cover of this thesis and Gerda Wolf for the lovely quokka illustration.

Diese Arbeit wäre ohne all die wundervollen Menschen, die mich in den letzten Jahren und darüber hinaus unterstützt und mir geholfen haben, wahrscheinlich nicht zustande gekommen.

Vielen Dank Daniel, für dein immer offenes Ohr, das Zurück-auf-den-Boden-Holen, wenn alles zu viel schien und den Hinweis, dass wahrscheinlich alle nur mit Wasser kochen.

Vielen Dank Christoph, für alle noch so diversen Themen, die du mir nahegebracht hast, für deine ehrlich Art und deine Energie, die Dinge begeistert zum Gutem zu verändern.

Vielen Dank Dan-Nha, dass ich mit dir Zeit, Büro und die Musik in unseren Köpfen teilen durfte. Und vielen Dank für die unzähligen Male, in denen ich mich mit allen Sorgen und Nöten an dich wenden konnte.

Vielen Dank Bettina, für unsere sehr wertvollen und ehrlichen Gespräche und das stetige Erinnern an die Worte meiner Oma.

Vielen Dank Simon, für deinen unerschütterlichen Optimismus und das gemeinsame Über-Mauern-Hüpfen.

Vielen Dank Christian, für deine fortwährende Kritik an meinem Kleidungsstil und unsere Freundschaft, die mich sehr bereichert hat.

Vielen Dank Paulin, für all die liebevolle Unterstützung und deinen neugierigen Blick, der jeden Tag auf mich aufpasst.

Vielen Dank Maria, für so unglaublich Vieles und dass ich mich schon so unfassbar lange immer auf dich verlassen kann.

Vielen Dank Lisa, für alles Wundervolle, was ich von dir lernen durfte und dass du mich auch in dunklen Momenten aufgefangen hast.

Vielen Dank Oma, dass du in allen Lebenslagen für mich da bist und für deine hilfreichen Worte “Nicht ärgern, nur wundern.”

Vielen Dank Sally, dass du die großartigste Schwester bist, die ich mir vorstellen kann und von der ich so viel gelernt habe.

Vielen Dank Mama und Papa, für die Sicherheit und Geborgenheit, die mich Tag für Tag begleitet und dafür, dass ihr immer für mich da seid, egal was ich mir noch so einfallen lasse. Und für den unerschöpflichen Vorrat an Tomatensuppe. “Schnauf, schnauf, keiner hält uns auf!”

Vielen, vielen Dank!

Bibliography

1. Wikimedia-Commons, “Mirror charge of a positive charge in front of a metal surface", `https://commons.wikimedia.org/wiki/File:Mirror_charge.svg`, 2008.
2. B. N. Narozhny and A. Levchenko, “Coulomb drag", Reviews of Modern Physics **88,** 025003 (2016).
3. L. Lin, “Adhesion and cohesion phenomena in pigment dispersion", Surface Coatings International **83,** 289 (2000).
4. P. Loskill *et al.,* “Macroscale adhesion of gecko setae reflects nanoscale differences in subsurface composition", Journal of The Royal Society Interface **10,** 20120587 (2013).
5. L. F. Boesel, C. Greiner, E. Arzt and A. del Campo, “Gecko-Inspired Surfaces: A Path to Strong and Reversible Dry Adhesives", Advanced Materials **22,** 2125.
6. S. Kim *et al.,* “Smooth Vertical Surface Climbing With Directional Adhesion", IEEE Transactions on Robotics **24,** 65 (2008).
7. A. Lambrecht, “Das Vakuum kommt zu Kräften: Der Casimir-Effekt", Physik in unserer Zeit **36,** 85 (2005).
8. S. K. Lamoreaux, “Casimir forces: Still surprising after 60 years", Physics Today **60,** 40 (2007).
9. F. Schwabl, *Quantenmechanik (QM I): Eine Einführung*, Seventh (Springer-Verlag, Berlin Heidelberg, 2007).
10. N. H. Bingham, “Studies in the history of probability and statistics XLVI. Measure into probability: from Lebesgue to Kolmogorov", Biometrika **87,** 145 (2000).
11. M. Chaichian and A. Demichev, *Path Integrals in Physics: Volume I Stochastic Processes and Quantum Mechanics*(CRC Press, 2001).
12. M. Kardar and R. Golestanian, “The “friction” of vacuum, and other fluctuation-induced forces", Reviews of Modern Physics **71,** 1233 (1999).
13. D. S. Lemons and A. Gythiel, “Paul Langevin’s 1908 paper “On the Theory of Brownian Motion” [“Sur la théorie du mouvement brownien,” C. R. Acad. Sci. (Paris) 146, 530–533 (1908)]", American Journal of Physics **65,** 1079 (1997).
14. J. B. Pendry, “Quantum friction–fact or fiction?", New Journal of Physics **12,** 033028 (2010).

15. J. D. van der Waals, *Over de Continuiteit van den Gas- en Vloeistoftoestand* (Universität Leiden, 1873).
16. F. London, “Zur Theorie und Systematik der Molekularkräfte", Zeitschrift für Physik **63,** 245 (1930).
17. H. B. G. Casimir and D. Polder, “The Influence of Retardation on the London-van der Waals Forces", Phys. Rev. **73,** 360 (1948).
18. H. B. G. Casimir, “On the Attraction Between Two Perfectly Conducting Plates", Indag. Math. **10,** 261 (1948).
19. E. M. Lifshitz, “The theory of molecular attractive forces between solids", Sov. Phys. JETP **2,** 73 (1956).
20. D. Tabor and R. H. S. Winterton, “Surface Forces: Direct Measurement of Normal and Retarded van der Waals Forces", Nature **219,** 1120 (1968).
21. E. S. Sabisky and C. H. Anderson, “Verification of the Lifshitz Theory of the van der Waals Potential Using Liquid-Helium Films", Physical Review A **7,** 790 (1973).
22. M. J. Sparnaay, “Measurements of attractive forces between flat plates", Physica **24,** 751 (1958).
23. S. K. Lamoreaux, “Demonstration of the Casimir Force in the 0.6 to 6 mm Range", Physical Review Letters **78,** 4 (1997).
24. U Mohideen and A. Roy, “Precision Measurement of the Casimir Force from 0.1 to 0.9 mm", Phys. Rev. Lett. **81,** 4 (1998).
25. S. A. Fulling and P. C. W. Davies, “Radiation from a moving mirror in two dimensional space-time: conformal anomaly", Proceedings of the Royal Society of London. A. Mathematical and Physical Sciences **348,** 393 (1976).
26. C. M. Wilson *et al.*, “Observation of the dynamical Casimir effect in a superconducting circuit", Nature **479,** 376 (2011).
27. L. S Levitov, “Van Der Waals’ Friction", Europhysics Letters (EPL) **8,** 499 (1989).
28. J. S. Høye and I. Brevik, “Casimir friction force and energy dissipation for moving harmonic oscillators", EPL (Europhysics Letters) **91,** 60003 (2010).
29. J. B. Pendry, “Shearing the vacuum - quantum friction", Journal of Physics: Condensed Matter **9,** 10301 (1997).
30. E. V. Teodorovich, “Contribution of macroscopic van der Waals interactions to friction forces", Soviet Physics Journal **19,** 1471 (1976).
31. V. Polevoi, “Tangential molecular forces caused between moving bodies by a fluctuating electromagnetic field", **71,** 1119 (1990).
32. V. E. Mkrtchian, “Interaction between moving macroscopic bodies: viscosity of the electromagnetic vacuum", Physics Letters A **207,** 299 (1995).
33. B. N. J. Persson and Z. Zhang, “Theory of friction: Coulomb drag between two closely spaced solids", Physical Review B **57,** 7327 (1998).

34. A. I. Volokitin and B. N. J. Persson, “Theory of friction: the contribution from a fluctuating electromagnetic field", Journal of Physics: Condensed Matter **11,** 345 (1999).

35. T. G. Philbin and U. Leonhardt, “No quantum friction between uniformly moving plates", New Journal of Physics **11,** 033035 (2009).

36. J. Mahanty, “Velocity dependence of the van der Waals force between molecules", Journal of Physics B: Atomic and Molecular Physics **13,** 4391 (1980).

37. W. L. Schaich and J. Harris, “Dynamic corrections to Van der Waals potentials", Journal of Physics F: Metal Physics **11,** 65 (1981).

38. M. S. Tomassone and A. Widom, “Electronic friction forces on molecules moving near metals", Phys. Rev. B **56,** 4938 (1997).

39. S. Scheel and S. Y. Buhmann, “Casimir-Polder forces on moving atoms", Phys. Rev. A **80,** 042902 (2009).

40. G. Barton, “On van der Waals friction: I. Between two atoms", New Journal of Physics **12,** 113044 (2010).

41. J. Høye and I. Brevik, “Casimir friction in terms of moving harmonic oscillators: equivalence between two different formulations", The European Physical Journal D **64,** 1 (2011).

42. G. V. Dedkov and A. A. Kyasov, “The relativistic theory of fluctuation electromagnetic interactions of moving neutral particles with a flat surface", Physics of the Solid State **45,** 1815 (2003).

43. F. Intravaia *et al.,* “Friction forces on atoms after acceleration", Journal of Physics: Condensed Matter **27,** 214020 (2015).

44. D. Reiche, D. A. R. Dalvit, K. Busch and F. Intravaia, “Spatial dispersion in atom-surface quantum friction", Phys. Rev. B **95,** 155448 (2017).

45. J. Klatt, M. B. Farías, D. A. R. Dalvit and S. Y. Buhmann, “Quantum friction in arbitrarily directed motion", Phys. Rev. A **95,** 052510 (2017).

46. M. Oelschläger, K. Busch and F. Intravaia, “Nonequilibrium atom-surface interaction with lossy multilayer structures", Physical Review A **97,** 062507 (2018).

47. F. Intravaia, M. Oelschläger, D. Reiche, D. A. R. Dalvit and K. Busch, “Quantum Rolling Friction", Physical Review Letters **123,** 120401 (2019).

48. S. M. Rytov, *Theory of Electric Fluctuations and Thermal Radiation* (Electronics Research Directorate, Air Force Cambridge Research Center, Air Research and Development Command, U.S. Air Force, 1959).

49. A. I. Volokitin and B. N. J. Persson, “Comment on ‘No quantum friction between uniformly moving plates’", New Journal of Physics **13,** 068001 (2011).

50. A. I. Volokitin and B. N. J. Persson, “Dissipative van der Waals interaction between a small particle and a metal surface", Phys. Rev. B **65,** 115419 (2002).

51. G. V. Dedkov and A. A. Kyasov, “Electromagnetic and fluctuation-electromagnetic forces of interaction of moving particles and nanoprobes with surfaces: A nonrelativistic consideration", Physics of the Solid State **44,** 1809 (2002).

52. V. A. Golyk, M. Krüger and M. Kardar, “Linear response relations in fluctuational electrodynamics", Phys. Rev. B **88,** 155117 (2013).

53. V. A. Golyk, *Non-equilibrium fluctuation induced-phenomena in quantum electrodynamics*, Thesis (Massachusetts Institute of Technology, 2014).

54. G. V. Dedkov and A. A. Kyasov, “The dynamical Casimir-Polder force in relativistic atomic motion near the surface of a thick plate", Physics of the Solid State **54,** 834 (2012).

55. G. Pieplow and C. Henkel, “Fully covariant radiation force on a polarizable particle", New Journal of Physics **15,** 023027 (2013).

56. G. Pieplow and C. Henkel, “Cherenkov friction on a neutral particle moving parallel to a dielectric", Journal of Physics: Condensed Matter **27,** 214001 (2015).

57. F. Intravaia, R. O. Behunin and D. A. R. Dalvit, “Quantum friction and fluctuation theorems", Phys. Rev. A **89,** 050101 (2014).

58. F. Intravaia, R. O. Behunin, C. Henkel, K. Busch and D. A. R. Dalvit, “Non-Markovianity in atom-surface dispersion forces", Phys. Rev. A **94,** 042114 (2016).

59. A. I. Volokitin and B. N. J. Persson, “Noncontact friction between nanostructures", Physical Review B **68,** 155420 (2003).

60. K. A. Milton, J. S. Høye and I. Brevik, “The Reality of Casimir Friction", Symmetry **8,** 29 (2016).

61. C. M. Bender and S. A. Orszag, *Advanced Mathematical Methods for Scientists and Engineers I* (Springer New York, New York, NY, 1999).

62. R. Kubo, “The fluctuation-dissipation theorem", Reports on Progress in Physics **29,** 255 (1966).

63. W. Nolting, *Grundkurs Theoretische Physik 7: Viel-Teilchen-Theorie* , Seventh (Springer Spektrum, 2009).

64. G. Giuliani and G. Vignale, *Quantum Theory of the Electron Liquid*(Cambridge University Press, 2005).

65. S. S. Jha, “Nonlinear response theory—I", Pramana **22,** 173 (1984).

66. H. Nyquist, “Thermal Agitation of Electric Charge in Conductors", Physical Review **32,** 110 (1928).

67. H. B. Callen and T. A. Welton, “Irreversibility and Generalized Noise", Phys. Rev. **83,** 34 (1951).

68. R. Kubo, “Statistical-Mechanical Theory of Irreversible Processes. I.", Journal of the Physical Society of Japan **12,** 570 (1957).

69. P. C. Martin and J. Schwinger, “Theory of Many-Particle Systems. I", Physical Review **115,** 1342 (1959).

70. A. Einstein, “Über die von der molekularkinetischen Theorie der Wärme geforderte Bewegung von in ruhenden Flüssigkeiten suspendierten Teilchen", Annalen der Physik **322,** 549 (1905).

71. A. Khintchine, “Korrelationstheorie der stationären stochastischen Prozesse", Mathematische Annalen **109,** 604 (1934).

72. R. P. Feynman and F. L. Vernon, “The Theory of a General Quantum System Interacting with a Linear Dissipative System", Annals of Physics **281,** 547 (2000).

73. G. W. Ford, J. T. Lewis and R. F. O’Connell, “Quantum Langevin equation", Phys. Rev. A **37,** 4419 (1988).

74. G. W. Ford and M. Kac, “On the quantum langevin equation", Journal of Statistical Physics **46,** 803 (1987).

75. G. W. Ford, J. T. Lewis and R. F. O’Connell, “Independent oscillator model of a heat bath: Exact diagonalization of the Hamiltonian", Journal of Statistical Physics **53,** 439 (1988).

76. J. R. Anglin, J. P. Paz and W. H. Zurek, “Deconstructing decoherence", Physical Review A **55,** 4041 (1997).

77. Y. Subaşı, C. H. Fleming, J. M. Taylor and B. L. Hu, “Equilibrium states of open quantum systems in the strong coupling regime", Physical Review E **86,** 061132 (2012).

78. M. Perarnau-Llobet, H. Wilming, A. Riera, R. Gallego and J. Eisert, “Strong Coupling Corrections in Quantum Thermodynamics", Physical Review Letters **120,** 120602 (2018).

79. H. Liu, C. Wang, L.-Q. Wang and J. Ren, “Strong system-bath coupling induces negative differential thermal conductance and heat amplification in nonequilibrium two-qubit systems", Physical Review E **99,** 032114 (2019).

80. G. Katz and R. Kosloff, “Quantum Thermodynamics in Strong Coupling: Heat Transport and Refrigeration", Entropy **18,** 186 (2016).

81. T. Dittrich, P. Hänggi, G. L. Ingold, G. Schön and W. Zwerger, *Quantum Transport and Dissipation*(Wiley-VCH, Weinheim ; New York, 1997).

82. N. van Kampen, “Derivation of the quantum Langevin equation", Journal of Molecular Liquids **71,** 97 (1997).

83. T. Yu and J. H. Eberly, “Phonon decoherence of quantum entanglement: Robust and fragile states", Physical Review B **66,** 193306 (2002).

84. H. Mori, “Transport, Collective Motion, and Brownian Motion", Progress of Theoretical Physics **33,** 423 (1965).

85. N. G. van Kampen, “Itô versus Stratonovich", Journal of Statistical Physics **24,** 175 (1981).

86. R. Graham and F. Haake, *Quantum Statistics in Optics and Solid-State Physics*, 1st (Springer-Verlag, Berlin Heidelberg, 1973).

87. E. Geva, E. Rosenman and D. Tannor, “On the second-order corrections to the quantum canonical equilibrium density matrix", The Journal of Chemical Physics **113,** 1380 (2000).

88. V. Romero-Rochin and I. Oppenheim, “Relaxation properties of two-level systems in condensed phases", Physica A: Statistical Mechanics and its Applications **155,** 52 (1989).

89. C. Aslangul, N. Pottier and D. Saint-James, “Time behavior of the correlation functions in a simple dissipative quantum model", Journal of Statistical Physics **40,** 167 (1985).

90. N. V. Kampen, *Stochastic Processes in Physics and Chemistry (Third Edition)*, Third Edition (Elsevier, Amsterdam, 2003).

91. S. Chakravarty and A. J. Leggett, "Dynamics of the Two-State System with Ohmic Dissipation", Physical Review Letters **52,** 5 (1984).

92. P. Hänggi and G.-L. Ingold, "Fundamental aspects of quantum Brownian motion", Chaos: An Interdisciplinary Journal of Nonlinear Science **15,** 026105 (2005).

93. R. Zwanzig, "Nonlinear generalized Langevin equations", Journal of Statistical Physics **9,** 215 (1973).

94. P. Hänggi and P. Jung. *Advances in Chemical Physics* 239 (John Wiley & Sons, Ltd, 2007).

95. I. Sokolov, "Ito, Stratonovich, Hänggi and all the rest: The thermodynamics of interpretation", Chemical Physics **375,** 359 (2010).

96. J. D. Jackson, *Classical Electrodynamics*, 3rd (Wiley, 1999).

97. W. Nolting, *Grundkurs Theoretische Physik 3: Elektrodynamik*, Tenth (Springer Spektrum, 2013).

98. R. E. Raab and O. L. de Lange, *Multipole Theory in Electromagnetism: Classical, quantum, and symmetry aspects, with applications*(Oxford University Press, 2004).

99. V. V. Gobre, *Efficient modelling of linear electronic polarization in materials using atomic response functions*, PhD thesis (Technischen Universität Berlin, 2016).

100. A. Liebsch, "Second-Harmonic Generation at Simple Metal Surfaces", Physical Review Letters **61,** 1233 (1988).

101. D.-N. Huynh, *Nonlinear optical phenomena within the discontinuous Galerkin time-domain method*, PhD thesis (Humboldt-Universität zu Berlin, 2018).

102. R. W. Boyd, *Nonlinear Optics*, 3rd (Elsevier, 2003).

103. J. Lee *et al.,* "Giant nonlinear response from plasmonic metasurfaces coupled to intersubband transitions", Nature **511,** 65 (2014).

104. R. L. Peterson, "Formal Theory of Nonlinear Response", Reviews of Modern Physics **39,** 69 (1967).

105. M. Battiato, G. Barbalinardo, K. Carva and P. M. Oppeneer, "Beyond linear response theory for intensive light-matter interactions: Order formalism and ultrafast transient dynamics", Physical Review B **85,** 045117 (2012).

106. S. Y. Buhmann, D. T. Butcher and S. Scheel, "Macroscopic quantum electrodynamics in nonlocal and nonreciprocal media", New Journal of Physics **14,** 083034 (2012).

107. H. T. Dung *et al.,* "Electromagnetic-field quantization and spontaneous decay in left-handed media", Physical Review A **68,** 043816 (2003).

108. W. Eckhardt, "First and second fluctuation-dissipation-theorem in electromagnetic fluctuation theory", Optics Communications **41,** 305 (1982).

109. W. Eckhardt, "Macroscopic theory of electromagnetic fluctuations and stationary radiative heat transfer", Phys. Rev. A **29,** 1991 (1984).

110. S. A. R. Horsley and T. G. Philbin, “Canonical quantization of electromagnetism in spatially dispersive media", New Journal of Physics **16,** 013030 (2014).

111. L. Knöll, S. Scheel and D.-G. Welsch, *QED in Dispersing and Absorbing Media Coherence and statistics of photons and atoms* (ed J. Perina) (Wiley, 2001).

112. S. Scheel and S. Y. Buhmann, “Macroscopic Quantum Electrodynamics - Concepts and Applications", Acta Physica Slovaca **58,** 675 (2008).

113. B. Huttner and S. M. Barnett, “Quantization of the electromagnetic field in dielectrics", Phys. Rev. A **46,** 4306 (1992).

114. L. G. Suttorp and M. Wubs, “Field quantization in inhomogeneous absorptive dielectrics", Physical Review A **70,** 013816 (2004).

115. K. Fujikawa and H. Terashima, “Fluctuation-dissipation theorem and quantum tunneling with dissipation at finite temperature", Physical Review E **58,** 7063 (1998).

116. S. Y. Buhmann and D.-G. Welsch, “Dispersion forces in macroscopic quantum electrodynamics", Progress in Quantum Electronics **31,** 51 (2007).

117. W. Heitler and F. London, “Wechselwirkung neutraler Atome und homöopolare Bindung nach der Quantenmechanik", Zeitschrift für Physik **44,** 455 (1927).

118. S. Y. Buhmann, L. Knöll, D.-G. Welsch and H. T. Dung, “Casimir-Polder forces: A nonperturbative approach", Physical Review A **70,** 052117 (2004).

119. K. A. Milton, “Casimir-Polder forces in inhomogeneous backgrounds", JOSA B **36,** C41 (2019).

120. M. Chaichian, G. L. Klimchitskaya, V. M. Mostepanenko and A. Tureanu, “Thermal Casimir-Polder interaction of different atoms with graphene", Physical Review A **86** (2012).

121. K. A. Milton *et al.,* “Negative entropies in Casimir and Casimir-Polder interactions", Fortschritte der Physik **65,** 1600047 (2017).

122. D. Reiche, K. Busch and F. Intravaia, “Quantum Thermodynamics of Overdamped Modes in Local and Spatially Dispersive Materials", arXiv:1805.11353 [quant-ph] (2018).

123. J. R. Zurita-Sánchez, J.-J. Greffet and L. Novotny, “Friction forces arising from fluctuating thermal fields", Physical Review A **69,** 022902 (2004).

124. *Near-Field Optics and Surface Plasmon Polaritons* (ed S. Kawata) (Springer-Verlag, Berlin Heidelberg, 2001).

125. P. W. Milonni, J. R. Ackerhalt and W. A. Smith, “Interpretation of Radiative Corrections in Spontaneous Emission", Physical Review Letters **31,** 958 (1973).

126. R. Zhao, A. Manjavacas, F. J. García de Abajo and J. B. Pendry, “Rotational Quantum Friction", Physical Review Letters **109,** 123604 (2012).

127. A. Manjavacas and F. J. García de Abajo, “Vacuum Friction in Rotating Particles", Phys. Rev. Lett. **105,** 113601 (2010).

128. K. Joulain, R. Carminati, J.-P. Mulet and J.-J. Greffet, “Definition and measurement of the local density of electromagnetic states close to an interface", Physical Review B **68,** 245405 (2003).

129. G. V. Dedkov and A. A. Kyasov, “Fluctuation-electromagnetic interaction under dynamic and thermal nonequilibrium conditions", Physics-Uspekhi **60,** 559 (2017).

130. A. I. Volokitin and B. N. J. Persson, “Quantum Friction", Phys. Rev. Lett. **106,** 094502 (2011).

131. Wikimedia-Commons, “A 3D visualization of a caffeine molecule", `https://commons.wikimedia.org/wiki/File:Caffeine_Molecule.png`, 2006.

132. F. Enguehard. *Thermal Nanosystems and Nanomaterials* (ed S. Volz) 151 (Springer Berlin Heidelberg, Berlin, Heidelberg, 2009).

133. L Fortunato, “All transformations of coordinates that separate the center of mass kinetic energy, their group structure and geometry", Journal of Physics A: Mathematical and Theoretical **43,** 065301 (2010).

134. A. Ashkin, “Optical trapping and manipulation of neutral particles using lasers", Proc. Natl. Acad. Sci. USA **94,** 4853 (1997).

135. R. S. Dutra, P. A. M. Neto, H. M. Nussenzveig and H. Flyvbjerg, “Theory of optical-tweezers forces near a plane interface", Physical Review A **94,** 053848 (2016).

136. M. Born and R. Oppenheimer, “Zur Quantentheorie der Molekeln", Annalen der Physik **389,** 457 (1927).

137. G. Czycholl, *Theoretische Festkörperphysik*, 3rd (Springer, Berlin, 2008).

138. C. Kittel, *Introduction to Solid State Physics*, Eighth (Wiley, 2004).

139. *NIST Standard Reference Simulation Website*(eds V. Shen, D. Siderius, W. Krekelberg and H. Hatch) (National Institute of Standards and Technology, Gaithersburg MD, 2019).

140. J. S. D’Arrigo, “Screening of membrane surface charges by divalent cations: an atomic representation", American Journal of Physiology-Cell Physiology **235,** C109 (1978).

141. N. A. Campbell, *Biology Concepts & ConnectionsHardcover*, 4 edition (San Francisco Pearson Education, Inc., publishing as Benjamin Cummings, 2003).

142. O. Romero-Isart, M. L. Juan, R. Quidant and J. I. Cirac, “Toward quantum superposition of living organisms", New Journal of Physics **12,** 033015 (2010).

143. D. E. Chang *et al.,* “Cavity opto-mechanics using an optically levitated nanosphere", Proceedings of the National Academy of Sciences **107,** 1005 (2010).

144. V. Jain *et al.,* “Direct Measurement of Photon Recoil from a Levitated Nanoparticle", Physical Review Letters **116,** 243601 (2016).

145. N. Kiesel *et al.,* “Cavity cooling of an optically levitated submicron particle", Proceedings of the National Academy of Sciences **110,** 14180 (2013).

146. P. Asenbaum, S. Kuhn, S. Nimmrichter, U. Sezer and M. Arndt, “Cavity cooling of free silicon nanoparticles in high vacuum", Nature Communications **4,** 2743 (2013).

147. J. Gieseler, B. Deutsch, R. Quidant and L. Novotny, “Subkelvin Parametric Feedback Cooling of a Laser-Trapped Nanoparticle", Physical Review Letters **109,** 103603 (2012).

148. T. Li, S. Kheifets and M. G. Raizen, “Millikelvin cooling of an optically trapped microsphere in vacuum", Nature Physics **7,** 527 (2011).

149. P. F. Barker and M. N. Shneider, “Cavity cooling of an optically trapped nanoparticle", Physical Review A **81,** 023826 (2010).

150. B. T. Draine and J. Goodman, “Beyond Clausius-Mossotti - Wave propagation on a polarizable point lattice and the discrete dipole approximation", The Astrophysical Journal **405,** 685 (1993).

151. L. Novotny, R. X. Bian and X. S. Xie, “Theory of Nanometric Optical Tweezers", Physical Review Letters **79,** 645 (1997).

152. B. T. Draine, “The discrete-dipole approximation and its application to interstellar graphite grains", The Astrophysical Journal **333,** 848 (1988).

153. W. T. Doyle, “Optical properties of a suspension of metal spheres", Physical Review B **39,** 9852 (1989).

154. H. Grabert, P. Nalbach, J. Reichert and M. Thorwart, “Nonequilibrium Response of Nanosystems Coupled to Driven Quantum Baths", The Journal of Physical Chemistry Letters **7,** 2015 (2016).

155. H. E. Sauceda and I. L. Garzón, “Structural Determination of Metal Nanoparticles from their Vibrational (Phonon) Density of States", The Journal of Physical Chemistry C **119,** 10876 (2015).

156. T. Sanghi, R. Bhadauria and N. R. Aluru, “Memory effects in nanoparticle dynamics and transport", The Journal of Chemical Physics **145,** 134108 (2016).

157. H. Lamb, “On the Vibrations of an Elastic Sphere", Proceedings of the London Mathematical Society **s1-13,** 189 (1881).

158. A. E. R. López, “Internal quantum dynamics of a nanoparticle in a thermal electromagnetic field: A minimal model", Physical Review B **98,** 155405 (2018).

159. Q. C. Sun *et al.,* “Spectroscopic Determination of Phonon Lifetimes in Rhenium-Doped MoS_2 Nanoparticles", Nano Letters **13,** 2803 (2013).

160. A. Yaghjian, “Electric dyadic Green’s functions in the source region", Proceedings of the IEEE **68,** 248 (1980).

161. B. Amorim, P. a. D. Gonçalves, M. I. Vasilevskiy and N. M. R. Peres, “Impact of Graphene on the Polarizability of a Neighbour Nanoparticle: A Dyadic Green’s Function Study", Applied Sciences **7,** 1158 (2017).

162. J. Avelin *et al.,* “Electric fields in the source region: the depolarization dyadic for a cubic cavity", Electrical Engineering **81,** 199 (1998).

163. G. Pieplow, H. R. Haakh and C. Henkel, “A note on longitudinal fields in the weyl expansion of the electromagnetic green tensor", International Journal of Modern Physics: Conference Series **14,** 460 (2012).

164. J. E. Sipe, “New Green-function formalism for surface optics", JOSA B **4,** 481 (1987).

165. J. M. Wylie and J. E. Sipe, “Quantum electrodynamics near an interface", Phys. Rev. A **30,** 1185 (1984).

166. J. E. Sipe, “The dipole antenna problem in surface physics: A new approach", Surface Science **105,** 489 (1981).

167. S. Pekar, “The Theory of Electromagnetic Waves in a Crystal in which Excitons are Produced", Sov. Phys. JETP **6,** 785 (1958).

168. J. J. Hopfield and D. G. Thomas, “Theoretical and Experimental Effects of Spatial Dispersion on the Optical Properties of Crystals", Physical Review **132,** 563 (1963).

169. K. L. Kliewer and R. Fuchs, “Anomalous Skin Effect for Specular Electron Scattering and Optical Experiments at Non-Normal Angles of Incidence", Phys. Rev. **172,** 607 (1968).

170. P. J. Feibelman, “Surface electromagnetic fields", Progress in Surface Science **12,** 287 (1982).

171. W. L. Mochán, R. Fuchs and R. G. Barrera, “Surface contribution to the optical properties of nonlocal systems", Physical Review B **27,** 771 (1983).

172. G. W. Ford and W. H. Weber, “Electromagnetic interactions of molecules with metal surfaces", Physics Reports **113,** 195 (1984).

173. E. A. Muljarov and R. Zimmermann, “Exciton polariton including continuum states: Microscopic versus additional boundary conditions", Physical Review B **66,** 235319 (2002).

174. G. S. Agarwal, D. N. Pattanayak and E. Wolf, “Structure of electromagnetic fields in spatially dispersive media of arbitrary geometry", Physical Review B **11,** 1342 (1975).

175. K. Henneberger, “Additional Boundary Conditions: An Historical Mistake", Physical Review Letters **80,** 2889 (1998).

176. R. Schmidt and S. Scheel, “Local density of states near spatially dispersive nanospheres", Physical Review A **93,** 033804 (2016).

177. R. Schmidt and S. Scheel, “Radiative heat transfer between spatially nonlocally responding dielectric objects", Journal of Physics B: Atomic, Molecular and Optical Physics **51,** 044003 (2018).

178. G. Toscano *et al.,* “Resonance shifts and spill-out effects in self-consistent hydrodynamic nanoplasmonics", Nature Communications **6,** 1 (2015).

179. M. R. Foreman, “Field Correlations in Surface Plasmon Speckle", Scientific Reports **9,** 8359 (2019).

180. C. Genet, A. Lambrecht and S. Reynaud, “Casimir force and the quantum theory of lossy optical cavities", Physical Review A **67,** 043811 (2003).

181. W. L. Mochán, M. del Castillo-Mussot and R. G. Barrera, “Effect of plasma waves on the optical properties of metal-insulator superlattices", Phys. Rev. B **35,** 1088 (1987).

182. R. Esquivel, C. Villarreal and W. L. Mochán, “Exact surface impedance formulation of the Casimir force: Application to spatially dispersive metals", Phys. Rev. A **68,** 052103 (2003).

183. E. Hecht, *Optik*, Sixth (De Gruyter, Berlin, Boston, 2014).

184. G. Floquet, “Sur les équations différentielles linéaires à coefficients périodiques", Annales scientifiques de l’École Normale Supérieure **12,** 47 (1883).

185. F. Bloch, “Über die Quantenmechanik der Elektronen in Kristallgittern", Zeitschrift für Physik **52,** 555 (1929).

186. D. A. G. Bruggeman, “Berechnung verschiedener physikalischer Konstanten von heterogenen Substanzen. I. Dielektrizitätskonstanten und Leitfähigkeiten der Mischkörper aus isotropen Substanzen", Annalen der Physik **416,** 636 (1935).

187. A. Poddubny, I. Iorsh, P. Belov and Y. Kivshar, “Hyperbolic metamaterials", Nature Photonics **7,** 948 EP (2013).

188. P. P. Debye and E. Hückel, “Zur Theorie der Elektrolyte", **24,** 185 (1923).

189. N. F. Mott and H. Jones, *The Theory of the Properties of Metals and Alloys*(Dover Publications, 1936).

190. V. P. Silin, “Theory of a degenerate electron liquid", JETP **33,** 495 (1957).

191. G. Baym and C. Pethick, *Landau Fermi-liquid theory: concepts and applications*(Wiley, New York, 1991).

192. N. R. Arista and W. Brandt, “Dielectric response of quantum plasmas in thermal equilibrium", Physical Review A **29,** 1471 (1984).

193. P. Nozieres and D. Pines, *Theory Of Quantum Liquids*(CRC Press, 2018).

194. R. F. Fox, “Contributions to Nonequilibrium Thermodynamics. II. Fluctuation Theory for the Boltzmann Equation", Physics of Fluids **13,** 2881 (1970).

195. J. Logan and M. Kac, “Fluctuations and the Boltzmann equation. I", Physical Review A **13,** 458 (1976).

196. J. Lindhard, *On the Properties of a Gas of Charged Particles*(Dan. Mat. Fys. Medd., Copenhagen, 1954).

197. N. D. Mermin, “Lindhard Dielectric Function in the Relaxation-Time Approximation", Phys. Rev. B **1,** 2362 (1970).

198. D. Pines, *Elementary Excitations in Solids*(CRC Press, Boca Raton, 1963).

199. J. Bardeen and D. Pines, “Electron-Phonon Interaction in Metals", Physical Review **99,** 1140 (1955).

200. P. Nozières and D. Pines, “Electron Interaction in Solids. The Nature of the Elementary Excitations", Physical Review **109,** 1062 (1958).

201. D. Pines, “A Collective Description of Electron Interactions: IV. Electron Interaction in Metals", Physical Review **92,** 626 (1953).

202. L. D. Landau, “On the vibrations of the electronic plasma", J.Phys.(USSR) **10,** 25 (1946).

203. J. Dawson, “On Landau Damping", The Physics of Fluids **4,** 869 (1961).

204. P. Drude, “Zur Elektronentheorie der Metalle", Annalen der Physik **306,** 566 (1900).

205. V. B. Svetovoy and R. Esquivel, “Nonlocal impedances and the Casimir entropy at low temperatures", Physical Review E **72,** 036113 (2005).

206. H. R. Haakh and C. Henkel, “Magnetic near fields as a probe of charge transport in spatially dispersive conductors", The European Physical Journal B **85,** 46 (2012).

207. D. Reiche, *Equilibrium and non-equilibrium atom-surface interaction and the influence of spatial dispersion*, Master’s Thesis (Humboldt-Universität zu Berlin, 2016).

208. J. Heinrichs, “Hydrodynamic Theory of Surface-Plasmon Dispersion", Physical Review B **7,** 3487 (1973).

209. C. Ciracì, J. B. Pendry and D. R. Smith, “Hydrodynamic Model for Plasmonics: A Macroscopic Approach to a Microscopic Problem", ChemPhysChem **14,** 1109 (2013).

210. N. Crouseilles, P.-A. Hervieux and G. Manfredi, “Quantum hydrodynamic model for the nonlinear electron dynamics in thin metal films", Physical Review B **78,** 155412 (2008).

211. W. Klassmann, “Eine hydrodynamische Beschreibung des Plasmas im Rahmen der BBGKY-Hierarchie", Zeitschrift für Physik **204,** 83 (1967).

212. G. Barton, “Some surface effects in the hydrodynamic model of metals", Reports on Progress in Physics **42,** 963 (1979).

213. P. Halevi, “Hydrodynamic model for the degenerate free-electron gas: Generalization to arbitrary frequencies", Physical Review B **51,** 7497 (1995).

214. V. Mkrtchian, V. A. Parsegian, R. Podgornik and W. M. Saslow, “Universal Thermal Radiation Drag on Neutral Objects", Physical Review Letters **91,** 220801 (2003).

215. A. I. Volokitin and B. N. J. Persson, “Near-field radiative heat transfer and noncontact friction", Rev. Mod. Phys. **79,** 1291 (2007).

216. D. Polder and M. Van Hove, “Theory of Radiative Heat Transfer between Closely Spaced Bodies", Phys. Rev. B **4,** 3303 (1971).

217. I. A. Dorofeyev, “The force of attraction between two solids with different temperatures", Journal of Physics A: Mathematical and General **31,** 4369 (1998).

218. J. M. Obrecht *et al.,* “Measurement of the Temperature Dependence of the Casimir-Polder Force", Physical Review Letters **98,** 063201 (2007).

219. M. F. Maghrebi, R. L. Jaffe and M. Kardar, “Spontaneous Emission by Rotating Objects: A Scattering Approach", Physical Review Letters **108,** 230403 (2012).

220. M. F. Maghrebi, R. Golestanian and M. Kardar, “Quantum Cherenkov radiation and noncontact friction", Physical Review A **88,** 042509 (2013).

221. J. S. Høye and I. Brevik, “Casimir friction at zero and finite temperatures", The European Physical Journal D **68,** 61 (2014).

222. F. Intravaia, R. O. Behunin, C. Henkel, K. Busch and D. A. R. Dalvit, “Failure of Local Thermal Equilibrium in Quantum Friction", Phys. Rev. Lett. **117,** 100402 (2016).

223. D. Reiche, K. Busch and F. Intravaia, “Non-Additivity of Nonequilibrium Atom-Surface Forces", arXiv:1910.08484 [quant-ph] (2019).

224. G. E. Uhlenbeck and L. S. Ornstein, “On the Theory of the Brownian Motion", Phys. Rev. **36,** 823 (1930).

225. A. Caldeira and A. Leggett, “Path integral approach to quantum Brownian motion", Physica A: Statistical Mechanics and its Applications **121,** 587 (1983).

226. J. Bass, W. P. Pratt and P. A. Schroeder, “The temperature-dependent electrical resistivities of the alkali metals", Reviews of Modern Physics **62,** 645 (1990).

227. N. W. Ashcroft and N. D. Mermin, *Festkörperphysik* , Reprint 2014 (De Gruyter, Berlin, Boston, 2001).

228. R. Estrada and S. A. Fulling, “How singular functions define distributions", Journal of Physics A: Mathematical and General **35,** 3079 (2002).

229. G. Ford and R. O’Connell, “Radiation reaction in electrodynamics and the elimination of runaway solutions", Physics Letters A **157,** 217 (1991).

230. F. Intravaia, R. Behunin, P. W. Milonni, G. W. Ford and R. F. O’Connell, “Consistency of a causal theory of radiative reaction with the optical theorem", Physical Review A **84,** 035801 (2011).

231. F. Intravaia, “Vacuum Incalescence", arXiv:1604.02990 (2016).

232. K. Yasutake *et al.,* “Velocity spectrometer for a neutral atomic beam:", Applied Physics B **71,** 787 (2000).

233. J. D. Perreault and A. D. Cronin, “Observation of Atom Wave Phase Shifts Induced by Van Der Waals Atom-Surface Interactions", Physical Review Letters **95,** 133201 (2005).

234. J. Plemelj, “Ein Ergänzungssatz zur Cauchyschen Integraldarstellung analytischer Funktionen, Randwerte betreffend", Monatshefte für Mathematik und Physik **19,** 205 (1908).

235. D. A. Steck, *Alkalidata* tech. rep. (Oregon Center for Optics and Department of Physics, University of Oregon).

236. D. Reiche, M. Oelschläger, K. Busch and F. Intravaia, “Extended hydrodynamic description for nonequilibrium atom-surface interactions", JOSA B **36,** C52 (2019).

237. R. E. Camley and D. L. Mills, “Collective excitations of semi-infinite superlattice structures: Surface plasmons, bulk plasmons, and the electron-energy-loss spectrum", Phys. Rev. B **29,** 1695 (1984).

238. B. L. Johnson, J. T. Weiler and R. E. Camley, “Bulk and surface plasmons and localization effects in finite superlattices", Phys. Rev. B **32,** 6544 (1985).

239. J. M. Pitarke, V. M. Silkin, E. V. Chulkov and P. M. Echenique, “Theory of surface plasmons and surface-plasmon polaritons", Reports on Progress in Physics **70,** 1 (2007).

240. S. Kalusniak, S. Sadofev and F. Henneberger, “ZnO as a Tunable Metal: New Types of Surface Plasmon Polaritons", Phys. Rev. Lett. **112,** 137401 (2014).

241. G. Isić, S. Vuković, Z. Jasic and M. Belic, “Tamm plasmon modes on semi-infinite metallodielectric superlattices", Sci Rep **7,** 3746 (2017).

242. I. Pirozhenko and A. Lambrecht, “Influence of slab thickness on the Casimir force", Phys. Rev. A **77,** 013811 (2008).

243. J. Klatt, R. Bennett and S. Y. Buhmann, “Spectroscopic signatures of quantum friction", Phys. Rev. A **94,** 063803 (2016).

244. F. Intravaia *et al.,* “Friction forces on atoms after acceleration", Journal of Physics: Condensed Matter **27,** 214020 (2015).

245. G. Barton, “On van der Waals friction. II: Between atom and half-space", New Journal of Physics **12,** 113045 (2010).

246. R. Alicki, “The Markov master equations and the Fermi golden rule", International Journal of Theoretical Physics **16,** 351 (1977).

247. D. Barchiesi and T. Grosges, “Fitting the optical constants of gold, silver, chromium, titanium, and aluminum in the visible bandwidth", Journal of Nanophotonics **8,** 083097 (2014).

248. P. Berini, “Plasmon-polariton waves guided by thin lossy metal films of finite width: Bound modes of symmetric structures", Phys. Rev. B **61,** 10484 (2000).

249. N. G. Van Kampen, “On the theory of stationary waves in plasmas", Physica **21,** 949 (1955).

250. M. V. Nezlin, “Negative-energy waves and the anomalous Doppler effect", Soviet Physics Uspekhi **19,** 946 (1976).

251. V. L. Ginzburg, “Certain theoretical aspects of radiation due to superluminal motion in a medium", Soviet Physics Uspekhi **2,** 874 (1960).

252. P. A. Čerenkov, “Visible Radiation Produced by Electrons Moving in a Medium with Velocities Exceeding that of Light", Physical Review **52,** 378 (1937).

253. Y. Oi Nakamura, “Spin quantum number of surface plasmon", Solid State Communications **39,** 763 (1981).

254. D. O’Connor, P. Ginzburg, F. J. Rodríguez-Fortuño, G. A. Wurtz and A. V. Zayats, “Spin–orbit coupling in surface plasmon scattering by nanostructures", Nature Communications **5,** 5327 (2014).

255. K. Y. Bliokh, D. Smirnova and F. Nori, “Quantum spin Hall effect of light", Science **348,** 1448 (2015).

256. M. Galassi *et al., GNU Scientific Library*, Release 2.6 (2019).

257. C. I. Sukenik, M. G. Boshier, D. Cho, V. Sandoghdar and E. A. Hinds, “Measurement of the Casimir-Polder force", Physical Review Letters **70,** 560 (1993).

258. A. Manjavacas, F. J. Rodríguez-Fortuño, F. J. García de Abajo and A. V. Zayats, “Lateral Casimir Force on a Rotating Particle near a Planar Surface", Physical Review Letters **118,** 133605 (2017).

259. W. H. Zurek. *Quantum Decoherence: Poincaré Seminar 2005* (eds B. Duplantier, J.-M. Raimond and V. Rivasseau) 1 (Birkhäuser Basel, Basel, 2007).

260. E. J. Zeman and G. C. Schatz, “An accurate electromagnetic theory study of surface enhancement factors for silver, gold, copper, lithium, sodium, aluminum, gallium, indium, zinc, and cadmium", The Journal of Physical Chemistry **91,** 634 (1987).

261. P. Sonnentag and F. Hasselbach, “Measurement of Decoherence of Electron Waves and Visualization of the Quantum-Classical Transition", Physical Review Letters **98,** 200402 (2007).

262. L. Valdes, “Resistivity Measurements on Germanium for Transistors", Proceedings of the IRE **42,** 420 (1954).

263. C. Slowe, L. Vernac and L. V. Hau, “High flux source of cold rubidium atoms", Review of Scientific Instruments **76,** 103101 (2005).

264. P. R. Berman, *Atom Interferometry* (Academic Press, 1997).

265. J. Gillot, A. Gauguet, M. Büchner and J. Vigué, “Optical pumping of a lithium atomic beam for atom interferometry", The European Physical Journal D **67,** 263 (2013).

266. C. Brand *et al.,* “Coherent diffraction of hydrogen through the 246 pm lattice of graphene", New Journal of Physics **21,** 033004 (2019).

267. P. Schwerdtfeger and J. K. Nagle, “2018 Table of static dipole polarizabilities of the neutral elements in the periodic table", Molecular Physics **117,** 1200 (2019).

268. M. E. Wieser and T. B. Coplen, “Atomic weights of the elements 2009 (IUPAC Technical Report)", Pure and Applied Chemistry **83,** 359 (2010).

269. P. Haslinger *et al.,* “Attractive force on atoms due to blackbody radiation", Nature Physics **14,** 257 (2018).

270. A. Miffre, M. Jacquey, M. Büchner, G. Trénec and J. Vigué, “Measurement of the electric polarizability of lithium by atom interferometry", Physical Review A **73,** 011603 (2006).

271. J. D. Perreault, A. D. Cronin and T. A. Savas, “Using atomic diffraction of Na from material gratings to measure atom-surface interactions", Physical Review A **71,** 053612 (2005).

272. T.-I. Jeon and D. Grischkowsky, “Nature of Conduction in Doped Silicon", Physical Review Letters **78,** 1106 (1997).

273. M. van Exter and D. Grischkowsky, “Optical and electronic properties of doped silicon from 0.1 to 2 THz", Applied Physics Letters **56,** 1694 (1990).

274. T.-I. Jeon and D. Grischkowsky, “Observation of a Cole–Davidson type complex conductivity in the limit of very low carrier densities in doped silicon", Applied Physics Letters **72,** 2259 (1998).

275. P. E. Schmid, “Optical absorption in heavily doped silicon", Physical Review B **23,** 5531 (1981).

276. R. A. Maniyara *et al.,* “Tunable plasmons in ultrathin metal films", Nature Photonics **13,** 328 (2019).

277. E. J. H. Skjølstrup, T. Søndergaard and T. G. Pedersen, “Quantum spill-out in nanometer-thin gold slabs: Effect on the plasmon mode index and the plasmonic absorption", Physical Review B **99,** 155427 (2019).

278. S. Lepoutre *et al.,* "Dispersive atom interferometry phase shifts due to atom-surface interactions", EPL (Europhysics Letters) **88,** 20002 (2009).

279. J. Klatt, *The Casimir-Polder Effect and Quantum Friction Across Timescales*, PhD thesis (Albert-Ludwigs-Universität, 2017).

280. V. Sandoghdar, C. I. Sukenik, E. A. Hinds and S. Haroche, "Direct measurement of the van der Waals interaction between an atom and its images in a micron-sized cavity", Physical Review Letters **68,** 3432 (1992).

281. A. D. Cronin, J. Schmiedmayer and D. E. Pritchard, "Optics and interferometry with atoms and molecules", Reviews of Modern Physics **81,** 1051 (2009).

282. C. Brand *et al.,* "An atomically thin matter-wave beamsplitter", Nature Nanotechnology **10,** 845 (2015).

283. K. Hornberger, S. Gerlich, P. Haslinger, S. Nimmrichter and M. Arndt, "Colloquium: Quantum interference of clusters and molecules", Reviews of Modern Physics **84,** 157 (2012).

284. M. Arndt and K. Hornberger, "Testing the limits of quantum mechanical superpositions", Nature Physics **10,** 271 (2014).

285. A. I. Volokitin, "Casimir frictional drag force between a SiO_2 tip and a graphene-covered SiO_2 substrate", Physical Review B **94,** 235450 (2016).

286. *Dark matter in cosmology, qantum measurements and experimental gravitation: 1996, January 20-27, Les Arcs, Savoie ; proceedings of the XXXIst Rencontres de Moriond, series: Moriond workshops, Les Arcs, Savoie, France, January 20 - 27, 1996* (eds R. Ansari and Rencontre de Moriond) (Editions Frontieres, Gif-sur-Yvette Cedex, 1996).

287. L. Viotti, M. Belén Farías, P. I. Villar and F. C. Lombardo, "Thermal corrections to quantum friction and decoherence: A closed-time-path approach to atom-surface interaction", Physical Review D **99,** 105005 (2019).

288. S. Scheel and S. Y. Buhmann, "Path decoherence of charged and neutral particles near surfaces", Physical Review A **85,** 030101 (2012).

289. F. C. Lombardo and P. I. Villar, "Quantum friction imprints on the geometric phase of a moving atom in front of a dielectric plate", Journal of Physics: Conference Series **880,** 012035 (2017).

290. A. Howie, "Addressing Coulomb's singularity, nanoparticle recoil and Johnson's noise", Journal of Physics: Conference Series **522,** 012001 (2014).

291. A. Howie, "Mechanisms of decoherence in electron microscopy", Ultramicroscopy. *Special Issue: J. Spence's 65th birthday* **111,** 761 (2011).

292. P. J. Beierle, L. Zhang and H. Batelaan, "Experimental test of decoherence theory using electron matter waves", New Journal of Physics **20,** 113030 (2018).

293. J. C. H. Spence. *Compendium of Quantum Physics* (eds D. Greenberger, K. Hentschel and F. Weinert) 188 (Springer Berlin Heidelberg, Berlin, Heidelberg, 2009).

294. C. Jönsson, “Elektroneninterferenzen an mehreren künstlich hergestellten Feinspalten", Zeitschrift für Physik **161,** 454 (1961).

295. F. Impens, R. O. Behunin, C. C. Ttira and P. A. M. Neto, “Non-local double-path Casimir phase in atom interferometers", EPL (Europhysics Letters) **101,** 60006 (2013).

296. R. Estrada and R. P. Kanwal, *Asymptotic Analysis: a Distributional Approach*(Birkhäuser Boston, Boston, MA, 1994).

297. W. Rosenheinrich, “Tables of some indefinite integrals of Bessel functions of integer order,", `http://web.eah-jena.de/~rsh/Forschung/Stoer/besint.pdf`, 2019.

298. F. Intravaia and K. Busch, “Fluorescence in nonlocal dissipative periodic structures", Phys. Rev. A **91,** 053836 (2015).

299. V. Amendola, R. Pilot, M. Frasconi, O. M. Maragò and M. A. Iatì, “Surface plasmon resonance in gold nanoparticles: a review", Journal of Physics: Condensed Matter **29,** 203002 (2017).

300. M. Perner *et al.*, “Optically Induced Damping of the Surface Plasmon Resonance in Gold Colloids", Physical Review Letters **78,** 2192 (1997).

301. S. Link, C. Burda, M. B. Mohamed, B. Nikoobakht and M. A. El-Sayed, “Femtosecond transient-absorption dynamics of colloidal gold nanorods: Shape independence of the electron-phonon relaxation time", Physical Review B **61,** 6086 (2000).

302. S. Link and M. A. El-Sayed, “Optical Properties and Ultrafast Dynamics of Metallic Nanocrystals", Annual Review of Physical Chemistry **54,** 331 (2003).

303. C. Voisin, N. Del Fatti, D. Christofilos and F. Vallée, “Ultrafast Electron Dynamics and Optical Nonlinearities in Metal Nanoparticles", The Journal of Physical Chemistry B **105,** 2264 (2001).

304. G. W Ford, J. T Lewis and R. F O’Connell, “Quantum oscillator in a blackbody radiation field II. Direct calculation of the energy using the fluctuation-dissipation theorem", Annals of Physics **185,** 270 (1988).

305. C. Henkel, S. Pötting and M. Wilkens, “Loss and heating of particles in small and noisy traps", Applied Physics B **69,** 379 (1999).